Application of upstream wind tunnel model mounting to the investigation of lobe-mixing geometries for road vehicle drag reduction

Thesis submitted for the degree of
Doctor of Philosophy

by

Aleksandra Anna Rejniak

Department of Mechanical and Aerospace Engineering

Brunel University London

February 2021

Abstract

The aerodynamics of road vehicles is an important topic at the centre of scientific effort to reduce the transport's impact on climate change. Commercial vehicles are among the least efficient, contributing approximately 18% of the transport emissions, while accounting for only 5% of total vehicle miles. In typical operating conditions, the aerodynamic drag generated by these vehicles can be responsible for up to 50% of total fuel consumption. The base region contributes a significant amount of aerodynamic drag and remains particularly difficult to optimise. This area is the focus of this thesis.

Wind tunnels have been an important tool used in the aerodynamic design of ground vehicles and remain the most popular choice for this application. The development of low-drag concepts requires highly accurate testing environments. This work utilises a wind tunnel to investigate the effects of moving ground on the unsteady base wake of a commercial vehicle model. The results show that the wake dynamics are markedly affected by the varying condition, making moving ground an important aspect for correct aerodynamic representation. Additionally, a new approach of upstream model mounting is evaluated. This technique is shown to combine the benefits and minimise the deficiencies of the typical supports from the top and sides and is, therefore, proposed to be a suitable alternative for low-interference flow-field characteristics at the model base.

The second part of this thesis investigates the use of lobed-mixing geometries for base drag reduction. Lobed mixers are a popular device for mixing enhancement within the aerospace industry. In this work a similar concept is applied to a boat-tailed model, with further investigations including the integration of the geometries directly into the base trailing edges. This concept is demonstrated to produce significant drag reductions of up to 7% at high aspect ratios, highlighting the possibility that such devices may be used to improve the fuel efficiency while minimising the impact on internal trailer space.

In this work, the experiments are conducted on two 1/24th-scale models representative of a commercial vehicle, at a width-based Reynolds number of up to 2.8×10^5. Load and base pressure are measured for different configurations, with hot-wire anemometry used to interrogate the flow-field. Results are considered from both time-averaged and time-dependent perspectives.

Acknowledgements

Firstly, I would like to thank my supervisor, Dr Alvin Gatto, for his advice, commitment, and generous practical help throughout the course of the project. The assistance of technical staff, in particular Mr Kevin Robinson, is also greatly appreciated.

I would also like to thank my closest friends and family who provided ample amounts of emotional support. My Mother and Maciek deserve a special thanks for the amount of work they have contributed to my every little success. Thank you for always being there to help with anything, for pushing me forward, and for being excellent role models – without you, I would have not been where I am now.

Finally, I am forever grateful to Connor for the incredible emotional, technical, and editorial support which he has given me. Thank you for tolerating me, for believing, encouraging, and supporting me, and most importantly for always being there when needed. I simply could have not done this without you.

Contents

Published works

Journal articles:

Rejniak, A. A. and Gatto, A. (2019) ‘Application of Lobed Mixers to Reduce Drag of Boat-Tailed Ground Vehicles’, *Journal of Applied Fluid Mechanics*, 12(6), pp. 1729–1744. doi: 10.29252/jafm.12.06.29742

Rejniak, A. A. and Gatto, A. (2020) ‘Influence of Rotating Wheels and Moving Ground Use on the Unsteady Wake of a Small - Scale Road Vehicle’, *Flow, Turbulence and Combustion*, 106(1), pp. 109–137. doi: 10.1007/s10494-020-00180-8

Rejniak, A. A. and Gatto, A. (2020) ‘Upstream wind tunnel model mounting: The forgotten method for road vehicle aerodynamics’, *Proceedings of the Institution of Mechanical Engineers, Part D: Journal of Automobile Engineering*. doi: 10.1177/0954407020978017

Rejniak, A. A. and Gatto, A. ‘On the drag reduction of road vehicles with trailing edge-integrated lobed mixers’ (in review)

Conferences:

Rejniak, A. A. and Gatto, A. (2019) ‘Influence of moving ground use on the unsteady wake of a small-scale commercial road vehicle’, Presented at *UK Fluids Conference 2019*, University of Cambridge

List of figures

List of tables

Nomenclature

Roman symbols		**SI Unit**
A	model frontal area	m^2
A_C	test section cross-sectional area	m^2
A_f	combined frontal area of model and mounting	m^2
A_T	trailer frontal area	m^2
b	boat-tail length normal to base	m
C	lobe geometry dependent constant	
C_D	drag coefficient	
C_{Dfm}, C_{Df}	measured and corrected drag coefficient based on A_f	
C_{DM}, C_{DT}	model and trailer drag coefficients	
C_{DTb}	trailer base drag coefficient	
Cp	pressure coefficient	
C_{pb}	average base pressure coefficient	
D	drag force	N
D_M, D_T	total model and trailer drag forces	N
E_x	Power Spectral Density of variable x	dB/Hz
e	statistical uncertainty of rms fluctuating variable	
F	force	N
F_R	rolling resistance	N
F_T	total force	N
f	frequency	Hz
G	tractor-trailer gap	m

G_C	ground clearance	m
h	crest-trough height of lobed mixer profile	m
H	model height	m
H_{BL}	boundary layer shape factor	
H_C	test section height	m
K	turbulent kinetic energy normalised by $1/(U_\infty)^2$	
$\overline{K}$	plane-averaged K	
k_1, k_2	yaw coefficients of the hot-wire probe	
L	model length	m
L_f	combined length of model and mounting	m
l	initial interface length	m
N	sample size	
P_T	total power	W
p	pitch of lobed mixer profile	m
p', p_∞	instantaneous and freestream static pressures	Pa
q, q_m	corrected and measured dynamic pressure	Pa
r_{opt}	optimum front radius	m
Re	Reynolds Number	
s	sample standard deviation	
S_{1-1}, S_{2-2}	auto spectra of signals 1 and 2	
S_{1-2}	cross-spectrum of signals 1 and 2	
S_C	test section shape factor	
St	Strouhal Number	
T	measured ambient temperature	°C

T_o	ambient temperature at probe calibration	°C
T_w	temperature of wire sensor	°C
t	time	s
u, v, ω	streamwise, lateral and vertical velocity components	m/s
$(u'^2)^*$	normal Reynolds stress normalised by U_∞^2	
$(u'v')^*, (u'\omega')^*$	Reynolds shear stresses normalised by U_∞^2	
U	vehicle speed	m/s
U_{C1}, U_{C2}	velocity magnitude from calibration for sensors 1 and 2	m/s
U_∞	freestream velocity	m/s
$\bar{U}$	axial velocity at lobe exit	m/s
V_f	combined volume of model and mounting	m^3
W	model width	m
W_C	test section width	m
x_r	mean recirculation region length	m
z	critical value of chi-squared distribution	

Greek symbols

α	boat-tail angle	deg
β	penetration angle	deg
γ, γ_{corr}	measured and corrected voltage	V
$\gamma_{1\text{-}2}^2$	coherence of signals 1 and 2	
Γ	circulation	m^2/s
δ^{99}	boundary layer thickness	m
δ^*	boundary layer displacement thickness	

Δ	change	
ε_m	mechanical efficiency	
η	Mercker wake blockage coefficient	
θ	boundary layer momentum thickness	
λ	statistical uncertainty of mean variable	
μ	air dynamic viscosity	N s/m^2
ν	air kinematic viscosity	m^2/s
ρ	air density	kg/m^3
Σ	sum	
τ	critical value of t-distribution	
ϕ_{1-2}	phase angle between signals 1 and 2	deg
Ψ	vorticity magnitude	1/s
Ω	vorticity magnitude normalised by W/U_∞ ($\Psi W/U_\infty$)	
$\overline{\Omega}$	average vorticity magnitude	1/s

Subscripts

H, L, W	based on body height, length, and width
X, Y, Z	streamwise, lateral, and vertical directions
rms	root-mean-square

Superscripts

*	normalised by model width W (e.g. $x^* = X/W$) or freestream velocity (e.g. $u^* = u/U_\infty$)

Abbreviations

2D	Two-dimensional
3D	Three-dimensional
BT	Boat-tail
BTT	Boat-tail taper
CFD	Computational Fluid Dynamics
CNC	Computer Numerical Control
GHG	Greenhouse Gas
GSR	Ground Separation Region
GTS	Ground Transportation System
HGV	Heavy Goods Vehicle
JBT	Jet Boat-Tail
LB1-3	Lobed Boat-Tails 1-3
LBT	Lobed trailing edge
MG	Moving Ground
POD	Proper Orthogonal Decomposition
RMS	Root Mean Square
RSB	Reflectional Symmetry Breaking
SG	Stationary Ground
VG	Vortex Generator

Chapter 1

Introduction

In the last 140 years of global temperature record, the last 19 since 2001 were among the hottest 20 years **(NASA, 2020)**. As shown in **Fig. 1.1**, the surface temperature is constantly rising, with this warming being attributed to the increasing amount of greenhouse gas (GHG) in Earth's atmosphere. This growth is considered to be caused by general human activity; from farming large amounts of cattle to burning fossil fuels. The latter is the staple of nearly every industrial process, providing heat as well as electrical and mechanical power. Under the EU climate action, one of the targets is a 40% reduction in GHG emissions by 2030, and an 80% - 95% cut by 2050, compared with the levels of 1990 **(European Commission, 2018a)**. Although the UK will soon cease to be under the EU jurisdiction, it will remain a

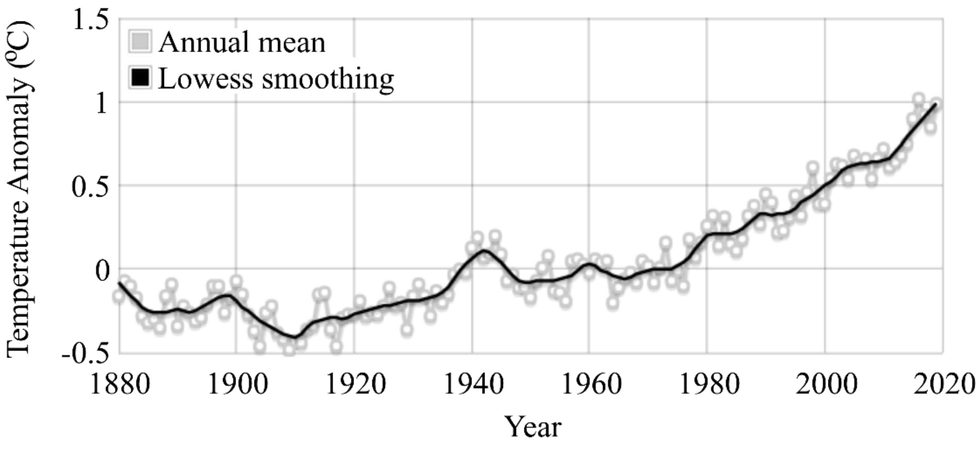

Fig. 1.1 Global surface temperature change from the average temperatures between 1951 and 1980 (source: NASA (2020))

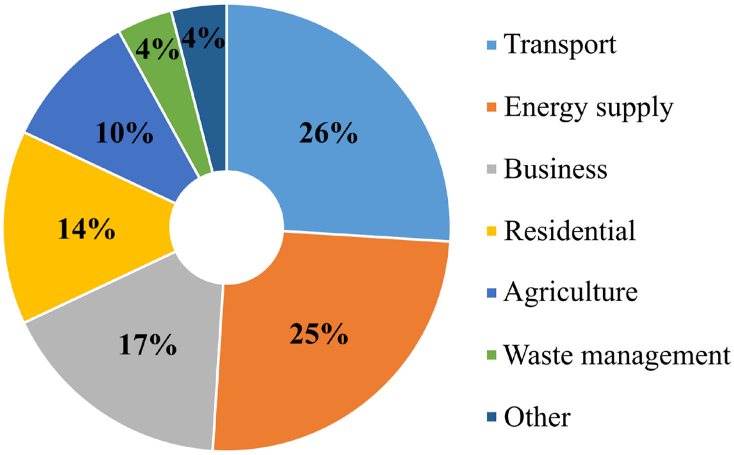

Fig. 1.2 2016 UK GHG emissions by sector (data from Department for Business Energy & Industrial Strategy (2016))

member of the UN Framework Convention on Climate Change **(CIFOR, 2016)**. As a signatory to the Paris Agreement[1], aiming to keep the global average temperature at less than 2°C above the pre-industrial levels, the UK is more than likely to work toward targets similar to those of the EU.

In the UK, transport is a major contributor to the overall GHG emissions. **Figure 1.2** presents the percentage breakdown of the 2016 emissions by sector. Carbon dioxide (CO_2) is, by far, the largest component of GHG, with every litre of diesel burnt producing approximately 2.64 kg **(Ecoscore, 2018)**. Thus, the vehicle efficiency is an important factor influencing the carbon footprint. In 2016, among other forms of road transport, Heavy Goods Vehicles (HGVs) used around 9.6 billion litres of fuel **(Department for Transport, 2017a, b)**, representing up to 25.2 million tonnes of CO_2 emitted into the atmosphere. This type includes all vehicles of gross weight over 3.5 tonnes **(Department for Transport, 2003)**. The poor fuel consumption of these vehicles is evident in **Fig. 1.3**, which shows that, despite accounting for only 5% of total vehicle miles travelled by all road transport, HGVs remain the second largest emission contributor (18%). If the climate targets are to be met, engineers must focus on reducing the fuel consumption of road vehicles. The most effective way to achieve the goal is to centre the efforts on the least efficient type – the HGV.

---

[1] The global climate deal agreed by 195 countries at the Paris climate conference (COP21) in December 2015 (European Commission, 2018b).

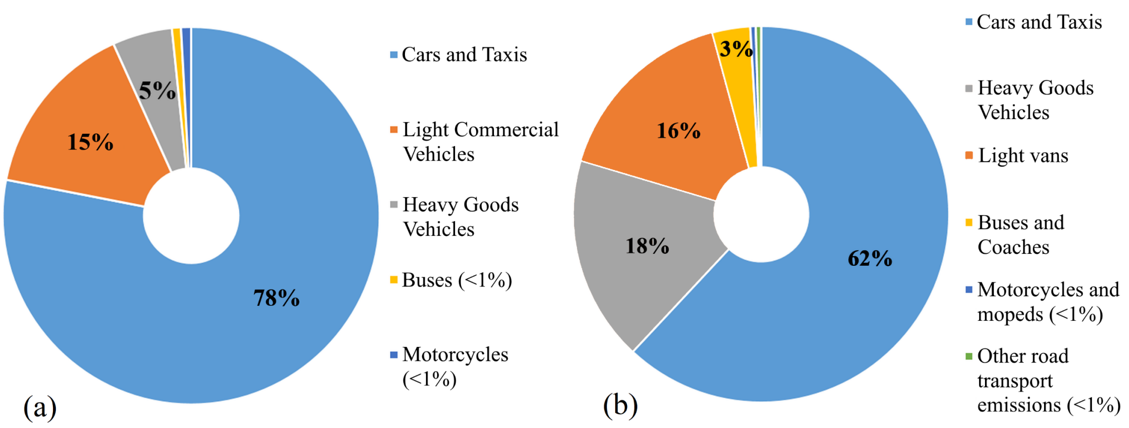

Fig. 1.3 (a) 2016 UK vehicle miles travelled by type of motor vehicle (data from (Department for Transport, 2017a)) (b) 2015 UK CO_2 emissions of all road transport (data from Department for Transport (2018))

The inefficiency of HGVs stems mainly from their bluff geometry. The first concepts to improve the shape and aerodynamic performance were proposed as early as 1914, but it was only sporadic until the oil crisis in 1970, which encouraged the advancement of various devices to be installed on existing vehicles **(Saltzman and Meyer, Jr., 1999)**. Prior to World War II, one of the first successful experiments was the Canadian Labatt Brewing Company's streamlined truck released in 1937. The truck's cruising speed increased from 35 to 50 miles per hour (mph), all the while carrying 150% of the original load **(Cooper, 2004)**. Over the years, the motivation for aerodynamic development has evolved; from increasing cruising speeds, through maximising load capabilities, to minimising fuel consumption.

In order to understand the fuel consumption, one should consider the sources of power requirement in the system. The total power required by the vehicle's engine, excluding the energy needed to drive the supplementary equipment (power steering pump, cooling system etc.) can be expressed as **(Drollinger, 1987)**:

$$P_T = \frac{1}{\varepsilon_m} F_T U \qquad (1.1)$$

where ε_m is the mechanical efficiency of the engine, F_T, the total force on the vehicle, and U, the speed of the vehicle relative to the road. The fuel efficiency, which is normally expressed in miles per gallon (MPG), can be estimated based on the power requirement through the relationship in equation 1.2 **(Drollinger, 1987)**:

$$MPG = k \frac{U}{P_T} = k \frac{\varepsilon_m}{F_T} \qquad (1.2)$$

where k is a constant based on estimates of thermal efficiency of the engine and the energy content of the fuel used. Equation 1.2 emphasises the important relationship between fuel efficiency and total forces on the vehicle; the larger the forces, the more fuel consumed per mile. The total force is a sum of forces due to road inclination, rolling resistance (F_R) and the aerodynamic drag force. On a level road (no inclination), the total force can be estimated using:

$$F_T = \frac{1}{2}\,\rho\,U^2 A\,C_D + F_R \qquad (1.3)$$

where ρ is the density of air, A, the vehicle frontal area, C_D, the drag coefficient, and F_R, a function of the vehicle's speed and gross weight. Applying these simplifications, allows to present the fuel efficiency as a function of speed and drag coefficient. Drollinger **(1987)** reported that for typical operating conditions, the aerodynamic drag and rolling resistance become equal at around $U = 58$ mph. This means that the aerodynamic drag becomes responsible for 50% of the power requirement (excluding the supplementary systems). At higher speeds, it increases further, exceeding the rolling resistance.

Although it is increasingly likely that in the next few decades, all vehicles will be replaced by electric alternatives, the need for energy conservation through reduction of aerodynamic drag will remain. Research into novel aerodynamic drag reduction methods, as well as focusing on a better understanding of the vehicle's flow characteristics is vital to the continuing progress in the field. Over the years, a considerable amount of effort has been placed on the front of the vehicle, making this area the most developed. For this reason, particular interest now resides in the base region[2], or rear of the trailer, which accounts for between 25% and 35% of the total vehicle aerodynamic drag **(Wood, 2006; Pankajakshan, Hilbert and Whitfield, 2010; van Raemdonck and van Tooren, 2010)**. Locally, the fixed separation from the trailing edges produces a large low-pressure wake directly downstream of the base. Various base drag reduction concepts have been developed over time, focusing mainly on the reduction of the base wake size or energising the separating flow. One such concept within the aerospace industry is the lobed mixer. This device provides a popular method for mixing enhancement through the generation of supplementary vorticity; however, its application to ground vehicles remains rather uncommon. Part of this thesis

---

[2] Further explanation in Section 2.2.3.

therefore focuses on the evaluation of lobed-mixing geometries for base drag reduction of ground vehicles.

Critical to correct evaluation of any flow control devices is the accurate representation of the typical vehicle aerodynamics. Ground vehicle studies normally utilise computational, road, or wind tunnel testing techniques for this purpose. Instances of high turbulence and complex unsteady motions can be particularly difficult to model computationally. While road testing may arguably produce the most realistic results, it is normally expensive, with the repeatability and detailed assessment of the flow often compromised. Wind tunnel testing remains the most popular method because it is typically associated with lower costs, particularly for sub-scale testing, and provides a good correlation to real conditions. A high-veracity experimental environment is essential to the quality of aerodynamic design. One of the aims of this thesis is to optimise the experimental setup to provide the best environment for developing low-drag concepts. This includes the assessment of ground simulation effects on the unsteady aspects of the base wake and evaluation of the upstream mounting approach for this application.

Chapter 2

Literature Review

This chapter opens by discussing ground vehicle aerodynamics, followed by a review of past studies on various types of flow control devices specific to the most common type of heavy vehicle. Existing methods for other applications are also considered in terms of their potential benefit for the automotive field. Finally, experimental techniques common to the automotive studies are reviewed.

2.1 Types of Heavy Goods Vehicles

There exist three main types of Heavy Goods Vehicles: rigid, articulated and drawbar. Simplified schematics of these are presented in **Fig. 2.1**. Rigid class is representative of most larger vans and smaller trucks, and in some cases, these are equipped to tow an additional trailer to form what is known as the drawbar configuration. Articulated vehicles remain popular in long haulage for their large payload capacity, meaning they are most likely to travel at steady motorway speeds where the aerodynamic drag plays a big part in the overall fuel efficiency. For this reason, the work presented in this thesis focuses on the articulated vehicle configuration, but most flow characteristics, and therefore, drag-reduction techniques, apply also to other types.

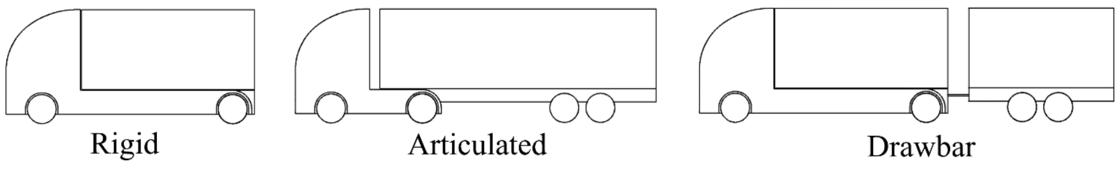

Fig. 2.1 Heavy goods vehicle configurations

2.2 Sources of aerodynamic drag

The aerodynamics of HGVs can be complex. Over the years of research, the vehicle has been split into four core areas: tractor, tractor-trailer gap, underbody, and trailer base (**Fig. 2.2**). Each area generates drag for different reasons, and together they contribute to the total vehicle aerodynamic drag. The following sections discuss, in detail, the mechanisms responsible for drag generation in each of the indicated areas.

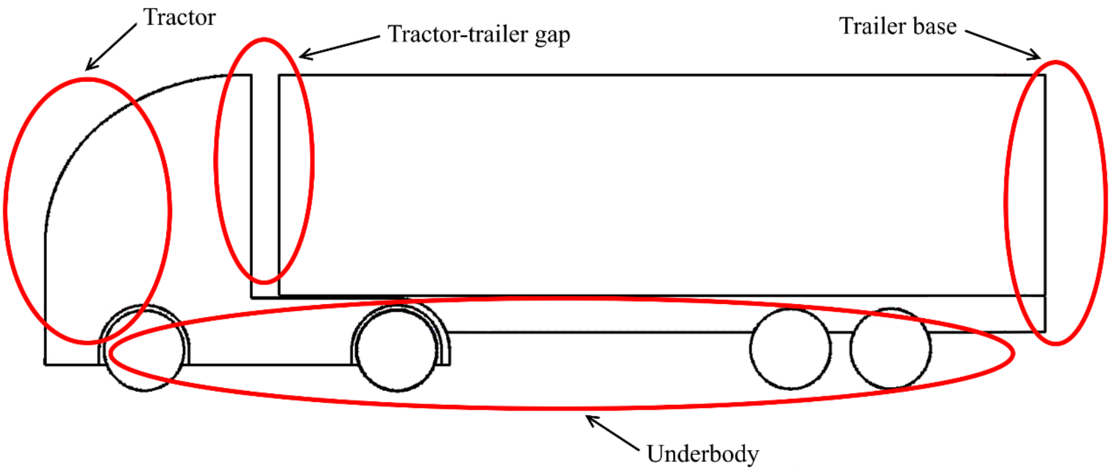

Fig. 2.2 Sources of aerodynamic drag on HGVs

2.2.1 The tractor and tractor-trailer gap

The main source of drag on the tractor originates from its shape. Under UK law, the maximum permitted length for an articulated HGV, encompassing both the tractor and trailer, is 16.5 meters **(Butcher, 2009)**. Manufacturers hoping to maximise the cargo space must compromise on the tractor size, resulting in the flat-nose squared shape seen on the roads today. The flow stagnation on the front face accounts for approximately 25% of the total aerodynamic drag **(Wood, 2006)**. The drag of the tractor can be reduced by minimising the flow separation at the vertical front edges. However, full streamlining can result in the loss of interior cab space and thus remains unpopular. Similar reductions can be achieved through corner rounding (applying radii to the sharp edges) **(Mason and Beebe, 1978)**. This technique can also be supplemented by the use of turning vanes, which effectively guide the flow around the cab corner promoting attachment at the tractor sides **(Heisler, 2002)**. Other sources of tractor drag are normally attributed to fine details such as side mirrors.

Another significant source of drag for articulated vehicles is the tractor-trailer gap, where the detached flow becomes trapped. Hammache and Browand **(2004)** showed the effects of gap clearance (G) on the gap flow features and total drag in symmetric flow conditions. Given A is the vehicle's frontal area, they report the following:

- $0.1 \lesssim G/\sqrt{A} \lesssim 0.5$ – the flow within the gap consists of steady and symmetric counter-rotating vortices, resulting in low pressure on the trailer front face and minimum total drag coefficient;
- $G/\sqrt{A} \approx 0.5$ – at this critical value, the symmetry breaks down resulting in a rise in the trailer and subsequently total drag;
- $G/\sqrt{A} \approx 1$ – the symmetry is restored; turbulent structures in the gap are wake-like in behaviour, and the tractor and trailer act as independent components.

Castellucci and Salari **(2005)** showed a similar trend for drag with increasing G in non-negligible crosswinds (see **Section 2.5.2.4**). They also reported a significant increase in drag when at 6° yaw the $G/\sqrt{A}$ value is increased from 0.35 to 0.65. At this angle, the region of constant drag coefficient ($0.1 \lesssim G/\sqrt{A} \lesssim 0.5$) found by Hammache and Browand **(2004)** was not noted. Instead, the drag coefficient was shown to increase with increasing gap throughout this range. Additionally, the tractor-trailer configuration, as well as increasing G can affect the pressure distribution on the trailer base; changing it from near-uniform across, to decreasing in the bottom base half **(Mason and Beebe, 1978)**.

Mason and Beebe **(1978)** showed that to achieve the lowest forebody drag (tractor and tractor-trailer gap), the tractor should not be treated separately and attempted to be streamlined, but rather aerodynamically sized to match the trailer. In this method, the double-stagnation flow field (stagnation on the tractor and stagnation on the trailer front) is changed to a single-stagnation flow field; stagnation occurs once on the tractor and the separated streamlines are "matched" to attach smoothly to the trailer. The authors reported the total drag to reduce by approximately a third **(Mason and Beebe, 1978)**. Similar conclusions were drawn by Götz and Mayr **(1998)** who showed a drag reduction with increasing frontal area (A) by increasing the height of the trailer behind a box-shaped tractor in symmetrical flow conditions. The principle of this concept is as presented in **Fig. 2.3**.

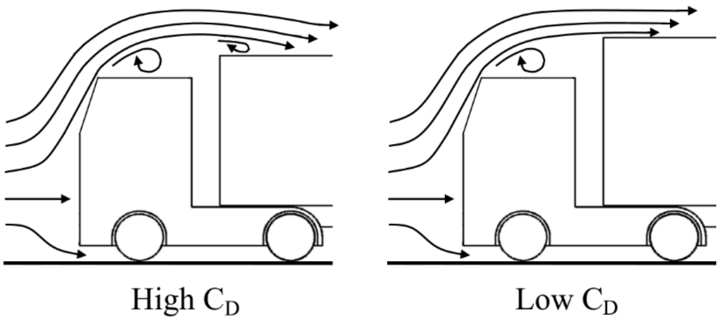

Fig. 2.3 Changes in forebody flow-field with increasing trailer height

Forebody is one of the most aerodynamically advanced areas of the vehicle, with tractor devices being developed to achieve the single-stagnation flow field without changing the vehicle geometry, one of most popular being a roof deflector. Berta and Bonis **(1980)** showed the effects of various types of wind-deflecting devices with the most effective, an expanded 3D device concerned with the flow over the top as well as the sides, reducing drag by up to 34.1% in symmetric flow conditions. Götz and Mayr **(1998)** also reported a comparable drag benefit (30%) for a similar device. While an inexpensive flat deflector was also shown to reduce drag substantially (28%), the drag generated in crosswinds was greater than the more advanced designs, making it less feasible.

Alternative methods of forebody drag reduction include modifications at the trailer front. Götz and Mayr **(1998)** reported a reduction of up to 9% with vortex stabilisers, which reduce the flow in the tractor-trailer gap in crosswinds. More recently, Salati, Cheli and Schito **(2015)** studied a device designed to move the flow separation point at the front of the trailer to a more suitable location above the trailer's surface, achieving a drag reduction of approximately 3.55%, despite the 10% increase in the frontal area. This concept was also found to reduce the turbulence over the trailer top owing to the reduced separation.

A study by Saltzman and Meyer, Jr. **(1999)** found that drag reductions at the forebody level often result in increases at the rear. This inverse relationship highlights the importance of continuing work on the base pressure drag reduction and the potential of maximising the benefits by combining methods typical to different vehicle areas.

2.2.2 The underbody

Within the underbody region the flow characteristics can be complex, with many factors from this area contributing to the overall increases in vehicle drag. One of the important aspects affecting the underbody flow is proximity to the ground, with total drag normally increasing with increasing ground clearance (G_C) **(Allan, 1981; Barlow, Guterres and Ranzenbach, 2001)**. With a typical HGV ground clearance in the range of $0.36 \leq G_C/W \leq 0.50$ **(Allan, 1981)**, where W is body width, higher drag is expected relative to other ground vehicles. Barlow, Guterres and Ranzenbach **(2001)** also showed that the drag increases with exposure to underbody surface area, with lower body aspect ratios (H^2/A – where H is body height) normally resulting in higher drag. The importance of this relationship becomes ever more significant considering the fine details of the undercarriage. Several bluff bodies located in this area, such as the fuel tank, wheel axles or bumpers, normally result in further increases in drag, with the level of detail of the underbody also shown to affect the flow at the vehicle base. Vallina Garcia and Babinsky **(2018)** showed increases in underbody roughness can result in a redistribution of the momentum within the base wake relative to a smooth underbody. Similarly, Perry **(2016)** reported redistribution in the base pressure and base wake balance with increasing underbody roughness, showing growing impact of the lower wake vortex and a consequent vertical shift in the base stagnation point (explained further in **Section 2.2.3**).

Methods for underbody drag reduction normally focus on minimising the exchange of flow within the region by shielding the area, with side-skirts proven to be a successful means of achieving this aim. Stephens and Babinsky **(2016)** showed that the effects of side-skirts vary with distance from the ground. Around the middle of the vehicle, skirts minimise the outflow from the underbody close to the ground and prevent freestream from being entrained in the upper underbody portions. Additionally, at the rear of the vehicle long skirts can contribute to a stronger base wake.

Van Raemdonck and van Tooren **(2010)** showed a drag reduction of up to 8% using side-skirts, with further benefits of up to 12% achieved by covering the wheels. More recently, a study by Hwang et al. **(2016)**, investigating the effects of different skirt shapes, showed a drag reduction of up to 5.3% with skirts comprising 45° inward bent flaps downstream of the vehicle's wheels. The reduction was attributed to a drop in pressure difference between positions upstream and downstream of the rear wheels, as well as the decrease of streamwise momentum loss and turbulent kinetic energy in the underbody region. The sharp front edges of side-skirts can often result in a local flow separation, negating their benefits. To minimise this effect, van Raemdonck and van Tooren **(2010)** produced a skirt with an aerofoil profile incorporated into the front edge, reporting a drag reduction of up to 14% in symmetric flow conditions, and 17% at 8° yaw.

2.2.3 The trailer base

The trailer base region accounts for 25% - 35% of the total vehicle aerodynamic drag **(Wood, 2006; Pankajakshan, Hilbert and Whitfield, 2010; van Raemdonck and van Tooren, 2010)**. In this area, the separation from the blunt trailing edges forms a large wake immediately behind the vehicle, producing lower static pressures acting to resist vehicle motion. Mason and Beebe **(1978)** showed that in a tractor-trailer HGV configuration, the pressure across the base decreases from top to bottom, remaining uniform spanwise. The region of minimum pressure at the base is attributed to the large wake vortex situated in the lower portions **(Mason and Beebe, 1978; McArthur et al., 2016; Lo and Kontis, 2017)**. Lo and Kontis **(2017)** reported that the structure is formed from the 'coiled-up' lower shear layer and extends over approximately 75% of the base height. Comparisons between the instantaneous and time-averaged flow fields showed the large lower vortex was steady in terms of both position and time **(McArthur et al., 2016)**. Besides the lower vortex, McArthur et al. **(2016)** showed the wake to contain an upper vortex and a pair of side vortices. The wake is normally symmetric in the vertical centreline, however, due to the positions of the upper and lower vortices, asymmetry is typically observed in the horizontal

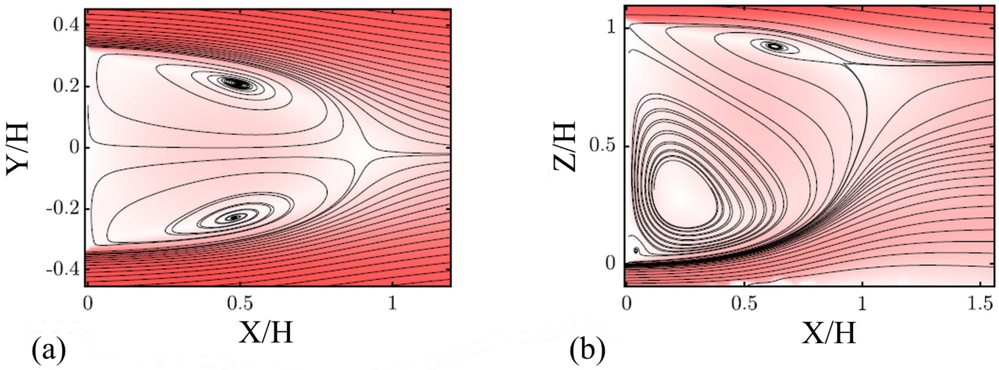

Fig. 2.4 Streamlines outlining the four main vortical structures in the base wake: (a) side vortices (lateral central view), (b) top and bottom vortices (vertical central view) (adapted from McArthur et al. (2016))

centreline. McArthur et al. **(2016)** suggested the four main structures in the wake, as presented in **Fig. 2.4**, form a larger toroidal vortex, tilted streamwise such that its upper part is placed further downstream. Spanwise, the upper and lower structures are seen to be distinct over most of the base width, with the flow passing between the two stagnating on the base close to the top trailing edge. This point of flow impingement corresponds to the position of the maximum base pressure.

Flow fluctuations are a significant characteristic of the wake as they define its unsteadiness. The most velocity fluctuations and turbulence are found to stem from the upper and side shear layers, which ultimately bound the recirculation region **(McArthur et al., 2016; Lo and Kontis, 2017)**, with moderate root-mean-square (RMS) values seen within the wake itself. McArthur et al. **(2016)** reported that the upper and side shear layers exhibit Kelvin-Helmholtz vortices, with this instability suggested to be inhibited in the lower shear layer due to its centrifugal acceleration towards the low-pressure core of the lower wake vortex. Furthermore, Lo and Kontis **(2017)** reported that the interaction between the lower wake vortex and upper shear layer results in an energy transfer from the former to the latter, generating weak streamwise vortices locally.

Another important aspect of the base wake is its downstream propagation. Duell and George **(1999)** defined the mean recirculation length as the distance between the base and the free stagnation point in the wake, which they determined to be approximately 1.1H. It was suggested that increases in the mean recirculation length can be related to decreases in drag due to the shifting of the low-pressure wake downstream and away from the base.

2.2.3.1 Time-dependent aspects

Duell and George **(1999)** attempted to characterise the unsteady base wake of a square-back body, establishing an important phenomenon of wake pumping, which is associated with the breakdown of vortical structures in the rear stagnation point. As the shear layers entrain the ambient fluid, the wake grows downstream, moving the free stagnation point further away from the base. When a critical length is reached, vortices are shed from the stagnation point, balancing the amount of entrained fluid. Consequently, the stagnation point moves back towards the base to repeat the cycle. The frequency of the pumping is described as the frequency of shedding at the free stagnation point. The vortices shed in the shear layers at separation are observed to pair as they travel downstream towards the free stagnation point, which results in the downstream decrease of the fluctuations' frequency. Duell and George **(1999)** suggested the relationship which characterises this process to be given by the following:

$$f_{downstream} = f_{upstream} / 2^{n} \qquad (2.1)$$

where f is the frequency and n, integer multiple of 2. The authors reported the normalised frequency (Strouhal number, St) corresponding to the shear layer vortex shedding at the trailing edges to be:

$$St_H = \frac{f\ H}{U_\infty} = 1.157 \qquad (2.2)$$

where U_∞ is the freestream velocity of the flow. Subsequently, the frequency associated with wake pumping was observed to be $St_H \approx 0.069$. Similar wake pumping frequency ($St_W \approx 0.08$, based on body width, W) was also reported at lower Reynolds numbers (Re – see **Section 2.5.2.1**) by McArthur et al. **(2016)**.

Recent research shows that the symmetrical toroidal-like structure pervading the near wake is a result of long-time-averaging. Grandemange, Cadot and Gohlke **(2012)** showed various states of the evolution of a laminar square-back body wake with small-step increases in the Reynolds number ($Re_H < 400$, based on body height). A lateral reflectional

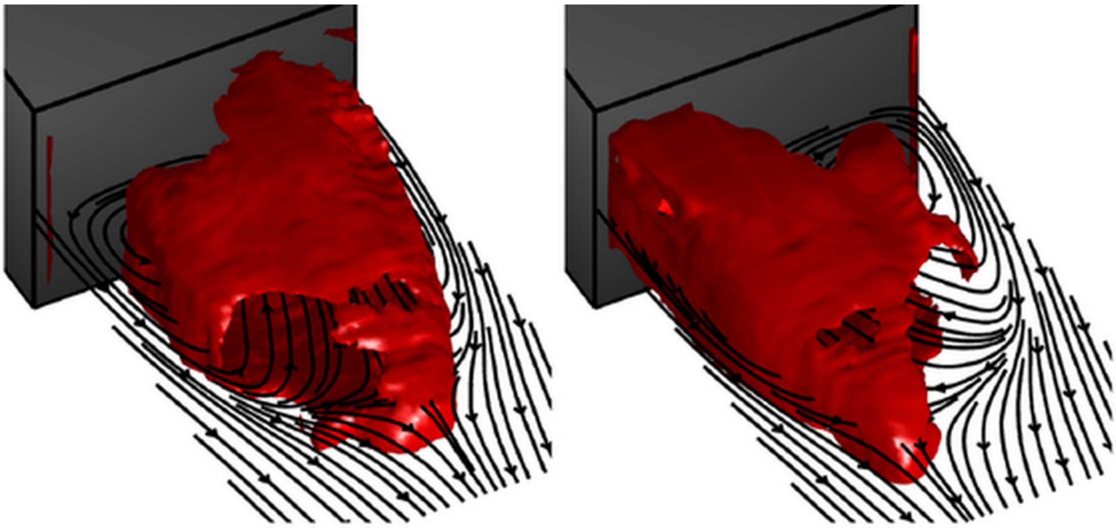

Fig. 2.5 The two asymmetric modes of a bi-stable wake; isosurfaces of $u/U_\infty=0.1$ (adapted from Volpe, Devinant and Kourta (2015))

symmetry breaking (RSB) mode was identified, whereby the symmetrical state becomes unsteady and triggers the wake to switch to a preferable asymmetric lateral position. Further increases in the Reynolds number ($Re_H > 415$) additionally destabilise the asymmetric state, leading to a bi-stable behaviour of the wake. This phenomenon is characterised by wake switching between the reflectional symmetry breaking positions at random. The asymmetric states (see **Fig. 2.5**) are equiprobable, which results in a statistically symmetric organisation when time-averaged over long periods.

The bi-stability was subsequently demonstrated at Reynolds numbers of up to Re ≈ 2.5×10^6 **(Grandemange, Gohlke and Cadot, 2013b)** and is said to be independent of its value in turbulent regimes. Position switches are associated with long time scales of the order of $t \approx 10^3 H/U_\infty$. Simultaneously, at shorter time scales ($t \approx 5H/U_\infty$), the wake exhibits much weaker coherent oscillations in the lateral and vertical directions, which are, respectively, related to side-side and top-bottom shear layer interactions. The characteristic

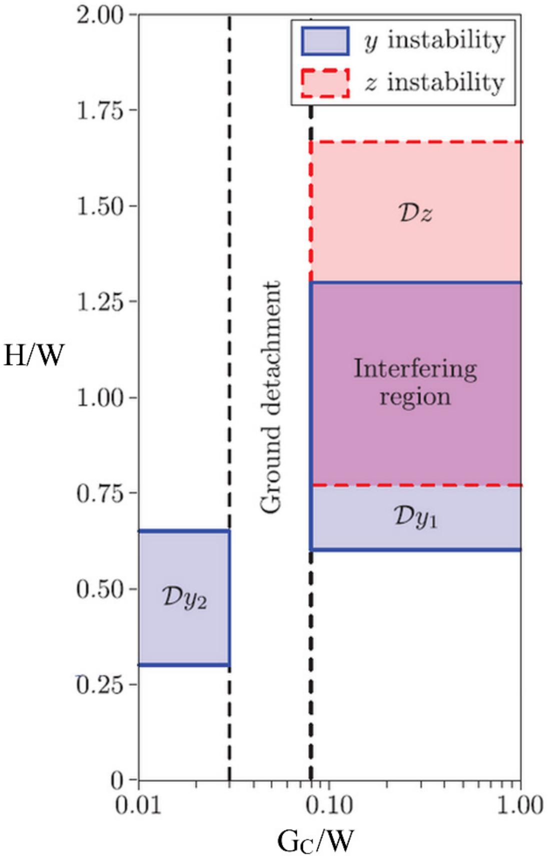

Fig. 2.6 Predicted domains of development of instabilities in the wake with respect to H/W and G_C; here "y" and "z" correspond to the lateral and vertical directions respectively (adapted from Grandemange, Gohlke and Cadot (2013a), with the permission of AIP Publishing)

frequencies of these oscillations were reported to be $St_H = 0.127$ (lateral) and $St_H = 0.174$ (vertical). It is worth noting that when normalised by the distances between the respective shear layers (H or W), both frequencies reduce to $St \approx 0.17$, which is identical to the value identified by McArthur et al. **(2016)** as the lateral shedding frequency. Grandemange, Gohlke and Cadot **(2013)** found no evidence of the wake pumping motion reported by Duell and George **(1999)**. In contrast, Volpe, Devinant and Kourta **(2015)**, who also identified the wake's bi-stable behaviour alongside the two short time-scale oscillation modes ($St_H = 0.13$ and $St_H = 0.19$), indicated a lower frequency mode ($St_H = 0.08$) coherent with periodic shrinking and expansion of the recirculation region.

The wake's bi-stability is strongly dependent on the geometrical aspects of the body. Grandemange, Gohlke and Cadot **(2013a)** showed that, in cases of base aspect ratios where $W>H$, bi-stability is lateral, meaning that the asymmetric modes exist in the horizontal axis. Alternatively, when $W<H$, the instabilities occur along the vertical axis. The influence of ground clearance on the development of bi-stability is another key aspect, with the instability found to ensue only at $G_C/W < 0.03$ and $G_C/W > 0.08$. Between these values, the ground proximity forces a detachment from the wall, which prevents the development of the unsteady state. The lower end of this spectrum ($G_C/W < 0.03$) is suggested to be equivalent to $G_C = 0$, whereby the body behaves as a symmetrical half of a full figure out of ground proximity, but through the physical limitation of the ground can only experience lateral instability. Through similar reasoning, the higher values ($G_C/W > 0.08$) enable the existence of bi-stability as the ground influence weakens. In this case, both lateral and vertical modes can occur. **Figure 2.6** presents the domains of the development of these instabilities with respect to the body H/W and G_C as predicted by Grandemange, Gohlke and Cadot **(2013a)**. It is worth noting that the area denoted as "interfering region" marks the geometrical configurations, which allow the occurrence of both lateral and vertical instability. Nevertheless, only one mode can exist at any time and it is highly likely that the dominant direction will be one corresponding to the larger length (height or width). Grandemange, Gohlke and Cadot **(2013b)** highlighted the importance of the underbody flow on the bi-stability's development. With minimal ground clearance, or when the flow is restricted by the underbody supports, asymmetric states may not be observed. They also suggested that any asymmetry of the experimental setup can result in the wake favouring one of the RSB modes.

Naturally, the unsteadiness of the near wake affects the base pressure distribution. The effects of bi-stability on the average base pressure coefficient (C_{pb}) become clear through cross-referencing of **Fig. 2.6** and **Fig. 2.7**. At the typical HGV's ground clearance ($0.36 \leq G_C/W \leq 0.50$ **(Allan, 1981)**), the occurrence of bi-stability in the wake is evident, along with a relatively low base pressure resulting in higher drag of these bodies. Grandemange, Gohlke and Cadot **(2013b)** suggested that the lateral and vertical oscillations, induced by the interaction between opposing shear layers, have low energy and thus, their impact on the base pressure is rather limited. However, the process of random switching between preferred asymmetric modes induces some unsteady side force, which may result in increases of the instantaneous drag and degradation of the vehicle's stability. Through statistical symmetry, however, the long-time-averaged force appears balanced, highlighting the importance of studying the unsteady as well as time-averaged aspects when concentrating on drag reduction.

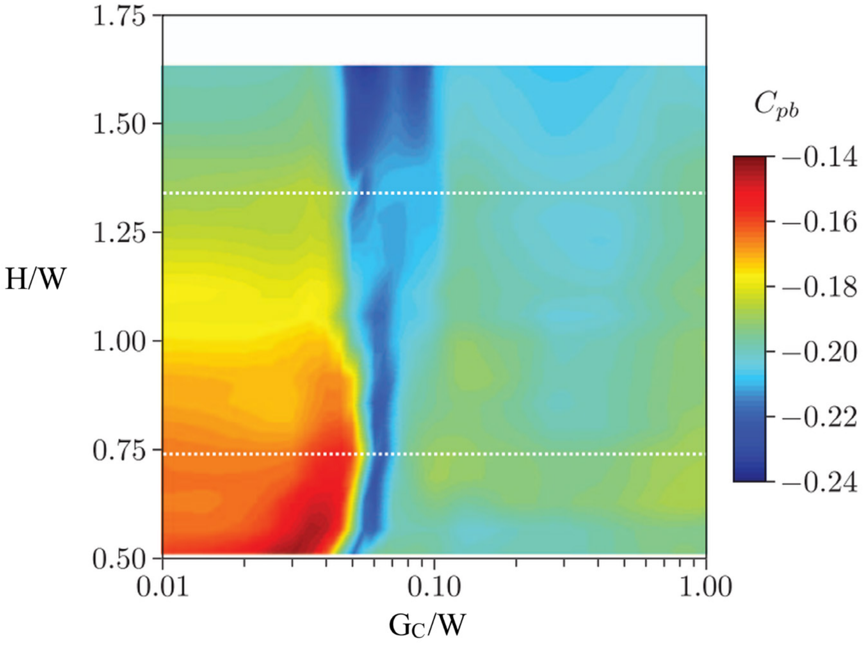

Fig. 2.7 Effects of the base height/width and ground clearance on the average base pressure coefficient (C_{pb}) (adapted from Grandemange, Gohlke and Cadot (2013a), with the permission of AIP Publishing)

2.3 Current flow control methods for trailer base

Trailer rear, which accounts for 25% - 35% of total vehicle drag **(Wood, 2006; Pankajakshan, Hilbert and Whitfield, 2010; van Raemdonck and van Tooren, 2010)** is the focus of this work. The following sections discuss, in detail, the development of the base flow control methods over the past years. Base pressure drag reduction techniques are normally classed as either passive or active. The latter typically requires external energy input, while the former focuses on forms of geometry modifications. Only passive methods are considered in this thesis.

2.3.1 Boat-tails

Early in the development of bluff body flow control, boat-tailing became a popular method for the base pressure drag reduction. This legacy concept uses a fitted extension with reducing cross-sectional area to better streamline the rear of the vehicle. Full-length boat-tails (**Fig. 2.8(a)**) have shown a vehicle drag reduction of up to 35% **(Saltzman and Meyer, Jr., 1999)**. However, hampered by regulatory requirements limiting vehicle length, a revised truncated boat-tail (**Fig. 2.8(b)**) appeared thereafter, reducing drag by almost the same amount (34%). Similar results were obtained by Muirhead **(1976)** experimenting on 1/10th-scale (38%) and Peterson **(1981)** on full-scale (31%). This configuration offered potentially less hazards for the following vehicles and was consequently favoured. Though the results showed promise, in practice, such cumbersome extensions were difficult to implement. The focus, therefore, turned to searching for methods, which could result in similar flow

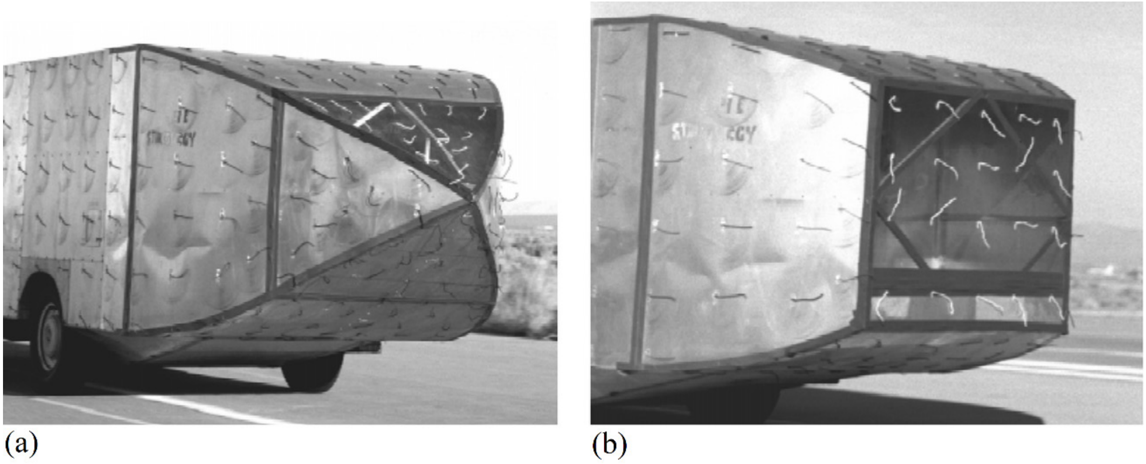
(a) (b)

Fig. 2.8 Photographs of the early: (a) full-length boat-tail, and (b) truncated boat-tail (adapted from Saltzman and Meyer, Jr. (1999))

characteristics, while providing simpler technical solutions. The relevant concepts, which became a part of this effort are considered in the following subsections.

2.3.1.1 Straight cavity

One of the first attempts to optimise a boat-tail was the employment of straight-walled base cavities, whose drag reduction mechanism is attributed to the shift of the low-pressure region away from the base. Mason and Beebe **(1978)** reported a potential of up to 5% drag reduction when using a three-sided (top and sides) straight-walled cavity, fixed flush to the base edges. More recent experiments also included inboard offset cavities. Lanser, Ross and Kaufman **(1991)** conducted a full-scale wind tunnel analysis of such devices (see **Fig. 2.9**), reporting the principal effect as entrapment of vortices in the offset corners of the cavity. A reduction of up to 9.8% in the wind-averaged drag coefficient (yaw range of ±15°) was shown with the top and sides offset inboard by 0.06W, and a streamwise length of 0.36W. Although the outer base edges were found to experience reduced surface pressures, the pressure within the cavity was increased, resulting in a net benefit. Storms et al. **(2001)** added that, along the vertical plane of symmetry, the base pressure distributions in the upper half remain essentially unchanged, however, they are increased in the bottom base half. A similar device was also studied by Khalighi et al. **(2001)**, both experimentally and through computational simulations, with drag reduction of 18 – 20% depending on the method. These results compared well with the 19% drag reduction found by Storms et al. **(2001)** with the top and side inboard offset of approximately 0.05W, and a streamwise length 0.29W. The base

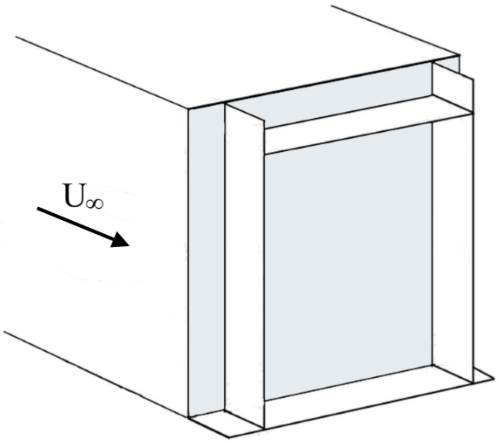

Fig. 2.9 Schematic of a straight-walled cavity studied by Lanser, Ross and Kaufman (1991), Storms et al. (2001) and Khalighi et al. (2001)

pressure distributions also agreed with those presented by Lanser, Ross and Kaufman **(1991)**; reduced outside and increased inside the cavity, with a net increase. Wake pumping peaks at $St_H \approx 0.07$ were found in the base pressure and velocity spectra for the baseline (no device). Adding the device, reduced the energy of pressure fluctuations at $St_H \approx 0.07$ by approximately 40%, with the same peaks in velocity spectra effectively completely suppressed **(Khalighi et al., 2001)**. The cavity was shown to stabilise the near wake by suppressing large-scale vortical structures, with reductions in turbulence intensity at the base and higher upward momentum of the underbody exiting flow. Khalighi et al. **(2001)** also suggested that the boat-tailing effect of the device is manifested by a narrower recirculation region.

More recently, other, less conventional, variations of the straight cavities also appeared. Howell et al. **(2012)** examined the effects of ventilating the cavity walls, conducting the study using a square-back Ahmed body (see **Section 2.5.3** for details) at a length-based Reynolds number of 1.8×10^6 in a wind tunnel with a fixed ground. The configuration with cavity and ventilation slots is presented in **Fig. 2.10**. The results showed that, although ventilated cavities reduce drag compared to the baseline, the benefit is smaller than when using sealed cavities. The authors also reported that through ventilation, the maximum possible drag reduction can be achieved at shorter cavity lengths. This was true for all cavities but was particularly important for the case of top and side ventilation with the bottom kept sealed. For this configuration with the cavity length in the range of $0.15W < b < 0.23W$, drag reduction was marginally larger than that of the fully sealed cavity. The study also showed ventilated cavities to have increased sensitivity to elongation. For sealed cavities, drag typically reduces with elongation up to a maximum beyond which it remains near-constant. Elongating ventilated cavities past the maximum, however, resulted in sharp

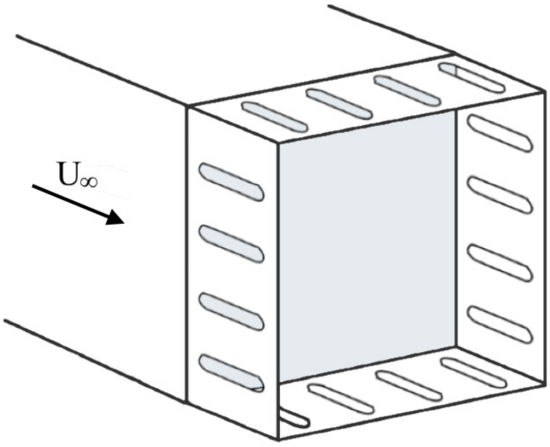

Fig. 2.10 Cavity with ventilation slots as studied by Howell et al. (2012)

increases in drag reaching values higher than the original drag of the baseline. Finally, the unsteady pressures in the upper shear layer decreased with both, sealed and ventilated cavities, with the latter producing larger reductions.

Martín-Alcántara et al. **(2014)** studied the influence of cavities in the base of two-dimensional (2D) bluff bodies within a computational domain, testing the baseline, a typical single cavity, and multi-cavity consisting of two sub-cavities, as shown in **Fig. 2.11**. A significant drag reduction of 23% for the multi-cavity was observed at lower cavity lengths ($b < 0.2H$). When increasing the length, the multi-cavity's performance degraded, while the single cavity persisted, achieving a drag reduction of up to 30% at $b=0.3H$. In either case, the addition of cavities significantly stabilised the base wake. The authors found that the temporal evolution of the drag coefficient of the baseline consisted of two superimposed signals: one of low frequency and high amplitude ($St_H \leq 0.2$), as well as one of high frequency and low amplitude ($St_H \approx 0.5$). The low frequency peak arose close to the value found by Khalighi et al. **(2001)** in the three-dimensional (3D) case; that is $0.05 \lesssim St_H \lesssim 0.07$. The addition of either cavity appeared to suppress the low-frequency component, with it being nearly inhibited in case of the multi-cavity. The multi-cavity also produced secondary small vortices inside the cavity, whose sense of rotation was opposite to the corresponding trailing edge vortices, which resulted in the weakening of the latter.

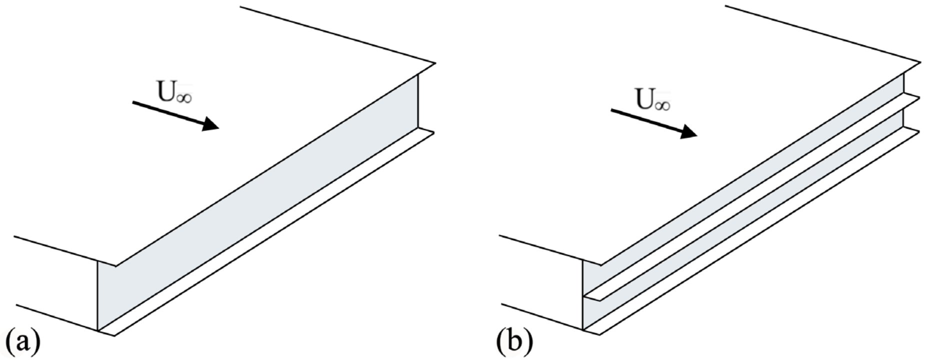

Fig. 2.11 2D bluff body with a single cavity (a) and multi-cavity (b), as studied by Martín-Alcántara et al. (2014)

2.3.1.2 Boat-tail with cavity

Both, tapering as for the original boat-tail, and presence of a cavity at the base showed to produce drag benefits separately, therefore, combining the two became commonplace in many boat-tail studies. The devices now, typically, consist of trailing edge panels angled inboard to provide reduction in cross-sectional area, as well as a hollow space within (**Fig. 2.12(a)**). Browand, Radovich and Boivin **(2005)** conducted full-scale field tests on partial (three-sided; no bottom panel) boat-tails of this type. Fuel savings of up to 1.63 litre/100km were found with a streamwise length of b = 0.25W and a boat-tail angle of $\alpha = 13°$ (**Fig. 2.12(b)**). Similar results were reported by Grover and Visser **(2006)** showing potential fuel savings of up to 10% with $\alpha = 15°$ for the top and sides, and $\alpha = 7°$ for the bottom panel. The authors suggested that, the necessity for reduced angle at the bottom edge is generated by additional turbulence from the rotating wheels. Cooper **(1985)** showed that the optimum boat-tail angle lies generally within $10° < \alpha < 15°$, depending on various aspects such as vehicle configuration and panel length, with flat panels normally better than curved.

Whether the bottom panel of a boat-tail is at all necessary for enhanced drag reduction became an important aspect of these studies. Through a combination of numerical, wind tunnel, and field tests, van Raemdonck and van Tooren **(2010)** achieved the best drag reduction, up to 12%, with the bottom panel utilised and $\alpha = 10°$. The same configuration in the full-scale field tests resulted in fuel consumption reductions of up to 2 litre/100km. Similarly, Pankajakshan, Hilbert and Whitfield **(2010)** showed that omitting the bottom panel may reduce the drag benefit by over 50%. While van Raemdonck and van Tooren **(2010)**, Pankajakshan, Hilbert and Whitfield **(2010)**, and Kehs et al. **(2013)**, all agreed that the optimum position for the bottom panel is at the level of the base bottom trailing edge, Schaut and Sengupta **(2015)** suggested the panel should be located little above the edge, reducing the distance to the base centre. The authors reported a 13% fuel consumption improvement with the optimum configuration of varying panel angles.

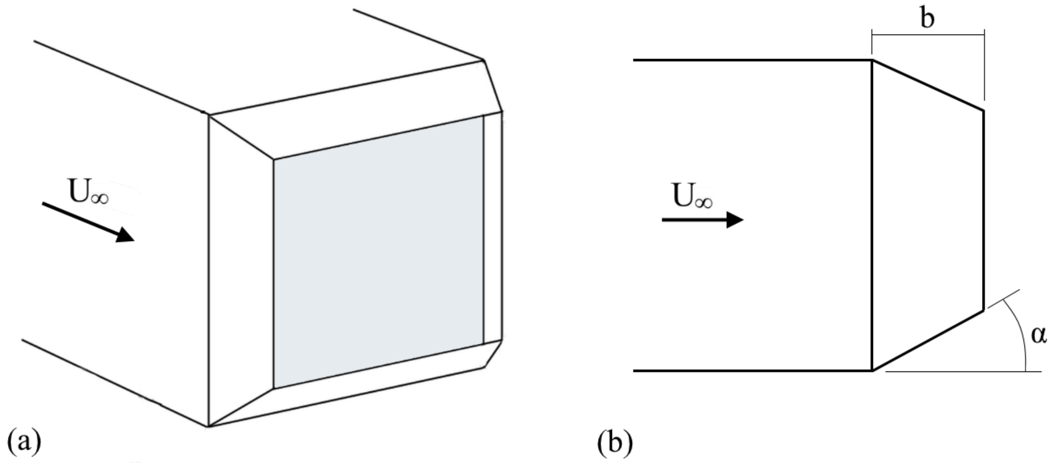

Fig. 2.12 Schematic of a standard boat-tail with cavity: (a) isometric view, (b) side view

Using boat-tails of α = 12°, Kehs et al. **(2013)** studied the effects of the streamwise length (b) on drag, showing this relationship to be near-quadratic in nature. The drag was shown to reduce with increasing length near-linearly up to approximately b = 0.4W, where the gradient experienced a sudden decrease, with no benefit from further elongation past b > 0.5W. Kehs et al. **(2013)** attributed the reduction in drag to the increased base pressure. On the contrary, Salati, Cheli and Schito **(2015)** reported the best drag reduction (9.068%) with a significantly longer boat-tail of b = 0.8W (α = 12°) though a shorter option (b = 0.1W) was noted to result in equally significant benefits (8.620%). While it is suggested that boat-tails normally have little effect on the flow upstream of the base **(Kehs et al., 2013)**, their performance can depend on the upstream geometry **(Schaut and Sengupta, 2015)**. Schaut and Sengupta **(2015)** showed that modifying the extent of underbody skirting can alter the drag's response to increasing boat-tail length, with partial skirting found to allow greater lengths.

As discussed, the complexity of the boat-tail stems from the varying performance of the device's key features such as bottom panel position, streamwise length and most importantly, boat-tail angle. Yi **(2007)** described, in more detail, the flow structures over a boat-tail's surface with varying α, which may offer an explanation as to why certain angles perform better than others. Four main regimes, which affect the device's efficiency were identified. In regime I (0°< α <5°), the angle is small enough for the flow from the trailer to follow onto the device without early separation; the main separation occurs at the trailing edge of the device, and drag reduction is proportional to the increasing angle. In regime II (5°< α <15°), a small separation bubble is produced at the leading edge of the device, and the strong momentum of the flow at reattachment delays the main separation to the trailing edge of the device; the maximum drag reduction is obtained in this range. In regime III (16°< α <19°), in addition to the separation bubble, side longitudinal vortices associated with the side edges of the slanted surfaces are generated; total drag increases with higher angles due to the rise in induced drag. Finally, in regime IV (20° ≤ α), the angle becomes too large, causing the main separation to occur at the leading edge of the device and thus, all benefit is lost.

Overall, the literature suggests that boat-tails with cavities result in larger drag benefits than straight cavities, as well as being more effective than rigid boat-tails **(Choi,**

Lee and Park, 2014). Past studies of these devices have shown that, in order to maximise the drag benefit:

- the bottom device panel is necessary, and the bottom panel boat-tail angle should usually be less than that of sides and top;
- it is usually sufficient for the boat-tail length to not exceed b = 0.4W;
- the optimum boat-tail angle is normally within the range of 10°< α <15°.

Despite the compelling benefits, boat-tails remain unpopular due to the vehicle length restrictions in Europe **(The Council of The European Union, 1996)**. Other, more subtle, and practical geometry modifications are now sought after, with boat-tails serving as a good basis for performance evaluation.

2.3.1.3 Individual panels

Grandemange et al. **(2013)** studied the effects of modifying flow orientation at separation using individual rectangular panels fixed to the top and bottom base edges of the square-back Ahmed body. They showed that the optimisation process is a careful balance of three inter-dependent aspects. The reduction in drag is largely associated with the reduction in wake size (width and height), which is characterised by a linear relationship. This effect, however, is counteracted by additional drag components induced by the lift changes generated by the flaps, as well as development of streamwise vorticity at the flap's side edges. The latter is similar to the effect produced by high-angle boat-tailed cavities. More

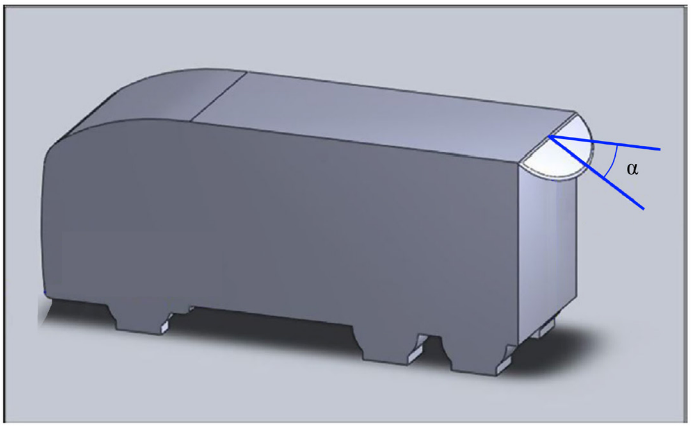

Fig. 2.13 Elliptical flap studied by Altaf, Omar and Asrar (2014)
(adapted from Altaf, Omar and Asrar (2014))

recently, Altaf, Omar and Asrar **(2014)** studied different variations of top-edge single flaps at the base of a simplified vehicle, investigating rectangular, triangular and elliptical geometries. A drag reduction of up to 11.1% was achieved with the latter fixed at an inboard angle of $\alpha = 50°$ (**Fig. 2.13**), resulting in the highest base pressure and reduction in the wake's size, with distinct tapering from the top. The panel enhanced downward momentum close to the top trailing edge and isolated regions of the wake. Additionally, all flaps, irrespective of the shape, were found to minimise the spanwise vorticity from the model's sides.

2.3.2 Trailer tapering

A more radical version of boat-tailing focuses on reshaping of the original squared trailer to achieve a similar tapered tail. Littlewood and Passmore **(2010)** showed that a satisfactory base pressure recovery can be achieved with the top trailing edge tapers, reporting an aerodynamic drag reduction of up to 2.7% with angles as small as 4°, with significantly higher slants of 12° offering reductions of up to 4.4%. Perry, Passmore and Finney **(2015)** showed that much more severe rear tapering only increases the drag benefit marginally, with a drag reduction of approximately 5% achieved with top and bottom inboard tapers of 16° and 6°, respectively. In contrast, inboard tapering of the side vertical edges of 12° can yield a drag reduction of up to 7%. The primary mechanism responsible for improved base pressure recovery was identified to be the increase in the size of the side portions of the toroidal vortical structure within the base wake. The same mechanism occurs for both, horizontal and vertical trailing edge tapering **(Perry, Passmore and Finney, 2015)**.

While for passenger vehicles the rear tapering is a part of the design process mainly affecting the aesthetics, the important aspect to consider when this is applied to HGVs is the potential loss of payload space. The streamlining method allows for maximum length within the restrictions, but the trailer volume is normally reduced. Hirz and Stadler **(2013)** considered this alongside the respective drag benefits of different degrees of taper. From their results, it is evident that there exists a practical limit to drag reduction achieved with top edge tapering, whereby beyond it any further decrease in cargo space results in only marginal, if any, drag reductions. Their results also suggest that tapering of the side edges is more effective, with higher drag benefits achieved at significantly lower payload penalties. This may be related to the increases in the size of the side vortical structures reported by

Perry, Passmore and Finney **(2015)**. Overall, the data presented by Hirz and Stadler **(2013)** implies that the optimisation process is a careful balance of the drag reduction and cargo space penalty, which, for best results, should be adjusted to the individual needs and requirements.

2.3.3 Jet boat-tail

In recent years, a new concept was developed intended to provide the flow-field characteristics of boat-tailing without the typical extensions fixed to the base periphery. Jet boat-tail (JBT) is a passive concept aiming to reduce the size of the base wake by injecting accelerated flow at the base edges. The principal action is the capturing of upstream flow, sending it through a converging duct, and subsequently ejecting a higher momentum fluid at the base; this is presented in the schematic in **Fig. 2.14(a)**. Studies conducted on this method focus mainly on its application to a car wing mirror **(Bartow et al., 2014; Wang et al., 2014; Yang et al., 2015, 2020)**, but the concept has also been suggested for a ground vehicle's base **(Hirst et al., 2015)**.

JBT was found to reduce the wake size, with the larger inlet area associated with smaller wakes, owing to the higher mass flow rate through the duct **(Bartow et al., 2014)**. Consequently, the higher mass flow rate was also linked to greater drag benefits **(Wang et al., 2014)**. The interactions of the high-speed jet with the free shear layer instigate vortex pairing, enhancing the flow entrainment towards the wake centreline **(Yang et al., 2015)**. Stronger entrainment was also found to increase the turbulent kinetic energy close to the base trailing edges and past the wake closure **(Yang et al., 2020)**. Additionally, Hirst et al. **(2015)** also showed that for a short square cylinder, dominated by flow separation along the sides, the JBT aids flow reattachment by strong entrainment at the duct inlet. JBT was reported to increase the static pressure near the base, with drag reductions between 15 – 26% **(Wang et al., 2014; Hirst et al., 2015; Yang et al., 2015, 2020)**.

More recently, Mohammadikalakoo, Schito and Mani **(2020)** proposed the concept of rear linking tunnels. Similar to the JBT, the principle of this method lies in the flow upstream of the base being captured and sent through a converging duct, to be expelled at the base (**Fig. 2.14(b)**). However, this method appears less invasive, with individual tunnels incorporated into the base corner, as opposed to the separate fixture around the edges, as seen with the JBT. Mohammadikalakoo, Schito and Mani **(2020)** reported drag reductions of up to 3% with a downstream shift and size reduction in the wake vortices, facilitating better pressure recovery.

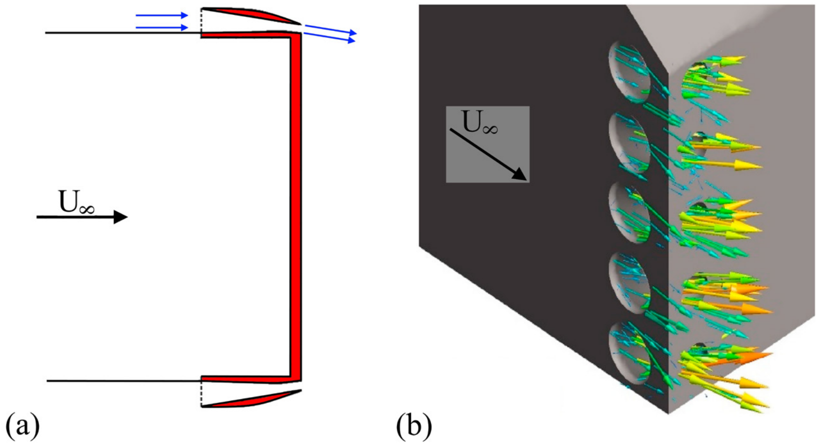

Fig. 2.14 Schematics of: (a) jet boat-tail and (b) rear linking tunnels (adapted from Mohammadikalakoo, Schito and Mani (2020))

2.3.4 Passive base bleed and ventilation

Passive base bleed techniques typically focus on connecting the opposing high- and low-pressure regions at the front and base of the body, respectively. This is normally achieved using a connecting duct allowing a transfer of energy between the regions. Early ventilation concepts for drag reduction of bluff bodies concentrated on simple 3D shapes, such as a sphere **(Suryanarayana, Pauer and Meier, 1993)**. With promising results, there began a shift to more specific applications. Falchi et al. **(2006)** reported drag reductions of up to 20% on a ventilated bullet-like model with a fully turbulent boundary layer profile at the trailing edge. The benefit was shown to be a consequence of reduction and increase in the wake width and length, respectively, as well as the redistribution of kinetic energy and Reynolds stress within. Irving Brown, Windsor and Gaylard **(2010)** studied similar passive base bleed on a sport utility vehicle, showing, in combination with a rear cavity, a drag reduction of up to 2% with the bleed applied to appropriate base portions. The authors, however, noted these benefits to be disproportionally small relative to the workload involved in duct installation. Additionally, such ducts appear to be rather impractical for real vehicles.

A more realisable configuration may be the one described by Gatto and Babinsky **(2018)**. While the principle of operation remains similar – allowing communication between regions of high and low pressure, this method considers the internal trailer space as the plenum chamber, with the configuration consisting of porous trailer sides and base. With various porosity ratios examined, considerable drag reductions of up to 12% at zero yaw, and 6% at 10.5° yaw were reported **(Gatto and Babinsky, 2018)**. The maximum drag benefits were related to the highest pressure drop between the outside and inside of the trailer. While increases in the porosity of the sides were found to have adverse effects, the opposite was true for the base porosity, with higher levels resulting in further drag reductions. Similar results were also reported by Howell, Sheppard and Blakemore **(2003)**, with base passive porosity levels of 50 – 70% resulting in drag reductions of up to 7.5%.

2.3.5 Surface treatment

Another group of passive drag reduction concepts focuses on various surface treatments indented to modify the boundary layer. Bauer and Wood **(2001)** proposed a porous layer covering the base and rear portions of the sides and top for flow control of ground vehicles. The authors showed weaker separation and a reduced recirculation region resulted in drag benefits of up to 6%. Porous surfaces have also been studied on Ahmed body variations with different configurations and coverage **(Bruneau and Mortazavi, 2008; Bruneau, Mortazavi and Gilliéron, 2008a, 2008b; Bruneau et al., 2012)**. Bruneau and Mortazavi **(2008)** reported a drag reduction of up to 40% on a square-back Ahmed body with the treatment applied to the top surface. The modifications were found to reduce the wake size and rear vorticity, resulting in increases in local static pressure **(Bruneau, Mortazavi and Gilliéron, 2008b)**.

Better base pressure recovery has also been reported using some more exotic concepts inspired by animal aerodynamics. Feuvrier, Mazellier and Kourta **(2013)** showed a drag benefit of up 22% using porous, self-adaptive (passive) flaps fixed to a square cylinder's sides, designed to mimic a bird's plumage.

2.3.6 Vortex generators

Another popular method for base drag reduction concentrates on the injection of supplementary vorticity into the separating flow. Vortex generators (VGs) are commonly studied for applications where fixed flow separation produces adverse pressure gradients. Streamwise vortices induced by such devices have been found to energise the boundary layer, which delays the separation and therefore, in many cases, the associated drag is reduced.

Normally characterised simply as a type of protrusion on a body's surface, VGs come in various shapes. Park et al. **(2006)** reported reductions in base pressure drag of a 2D bluff body with simple rectangular tabs fixed at the trailing edges, as those in **Fig. 2.15(a)**. The optimum configuration was found to increase the base pressure by up to 33%. Streamwise vortices generated at the adjacent sides of each tab decelerated the flow near the device, with increases in the streamwise velocity at positions between the tabs. The characteristic frequency of baseline trailing edge vortex shedding identified as $St_H \approx 0.25$, in agreement with Martín-Alcántara et al. **(2014)**, was found to increase ($St_H \approx 0.27$), with the energy peak suppressed at different locations downstream of the base. As a result of this vortex dislocation, the Kármán vortex shedding was suppressed immediately behind the body and reappeared further downstream, thereby increasing the vortex formation length and base pressure.

Another popular geometry for VGs is a cylinder (**Fig. 2.15(b)**). Duriez, Aider and Wesfried **(2006)** studied their effects on the control of the boundary layer. The separation was significantly delayed directly downstream of the VG, and marginally advanced in-between, with the net effect being a reduction in the separation region of approximately 20%. The pattern was caused by pairs of counter-rotating streamwise vortices, whereby

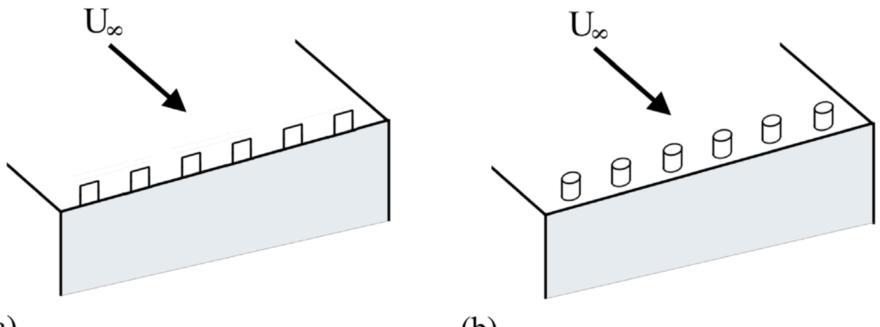

(a) (b)

Fig. 2.15 Schematic of rectangular tabs (a) and cylindrical (b) vortex generators directly downstream of the VG, the direction is towards the surface (inflow region), with the opposite true for the areas located in-between (outflow region). This velocity imbalance is similar to the effects of rectangular tabs discussed earlier **(Park et al., 2006)**. Duriez, Aider and Wesfried **(2006)** defined three spatial regions (in the streamwise direction) behind the cylindrical VG: 1) between the VG and the first critical position, the flow is dominated by the recirculation bubble caused directly by the physical existence of the VG; 2) between the end of recirculation bubble (the first critical position) and the second critical position (also marked as characteristic length), the counter-rotating streamwise vortices begin to reorganise and accelerate the mean flow; 3) beyond the characteristic length, the streamwise vortices are well organised and the acceleration of the flow causes the mean boundary layer thickness to be significantly smaller than that of the baseline at the same location. Thus, the principal action of induced counter-rotating streamwise vortices is a substantial increase in the velocity gradient in the boundary layer, which leads to its thinning and delayed flow separation. Pujals, Depardon and Cossu **(2010)** reported a drag reduction of up to 10% with cylindrical VGs lower than the upstream boundary layer thickness. The base pressure was found to increase irrespective of the VG size, leading to the conclusion that increasing drag benefit was solely a result of reducing the element of induced drag through smaller VG diameter. Evrard et al. **(2017)** also studied the influence of such cylindrical VGs on a full-scale hatchback vehicle. They reported notable increases in the separated shear layer thickness associated with, and expected from, the secondary vorticity. However, globally, the drag of the car was found to increase, suggesting that the local benefits to the base region were outweighed by the additional induced drag.

In truth, vortex generators are often found to produce additional drag as a result of the devices' local pressure drag. This effect can be lessened by reducing their frontal area perpendicular to the upstream flow. One such example is the delta VG, similar to the

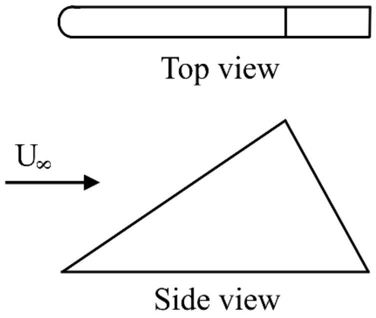

Fig. 2.16 Schematic of a simple delta vortex generator

schematic presented in **Fig. 2.16**. Koike, Nagayoshi and Hamamoto **(2004)** reported a drag reduction of up to ΔC_D=-0.006 on a sedan car using an array of delta VGs upstream of the normal fixed separation point on the roof. The optimal device was fixed at a 15° yaw to the oncoming flow and of height close to the upstream boundary layer thickness, with sub boundary layer VGs generally more common for their lower induced drag. The results showed that the separation point was shifted downstream with the use of the VGs, increasing the pressure on the back-slanted window **(Koike, Nagayoshi and Hamamoto, 2004)**. Similar delta VGs placed at the base of a tractor-trailer HGV configuration were reported to increase the velocity near the trailing edges **(Lav, 2013)**. As a result, the wake was found to be subtly tapered and the vorticity within stronger, with reported drag reductions of up to 9.1% **(Lav, 2013)**.

The frontal area perpendicular to the flow can also be reduced with the use of vane-like thin VGs. The individual vanes can be fixed in different positions to create various configurations, for instance, to produce co-rotating or counter-rotating vorticity. Sirenko, Pavlovs'ky and Rohatgi **(2012)** reported a drag reduction of up to 1.24% with an array of equally spaced delta-shaped vane VGs fixed parallel to the freestream. A small increase in drag was recorded with a configuration consisting of pairs of vanes placed alternately at 15° and -15° yaw to form a dihedral angle. A similar arrangement was also studied by Evrard et al. **(2017)**, who reported an array of counter-rotating vorticity, which was found to have a significant impact on the flow-field at the vehicle's base. The increase in flow entrainment resulted in enhanced mixing and growth of the shear layer thickness, with the wake size

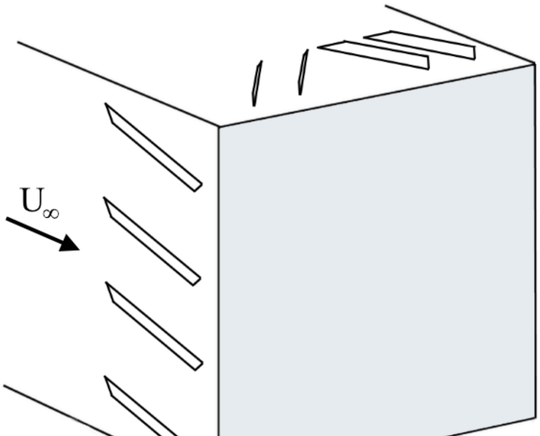

Fig. 2.17 Vortex strake device (VSD) as studied by Wood (2006)

significantly reduced. Overall, similar results were reported, with significant reductions in base pressure and global increases in drag.

Specifically for HGVs, Wood **(2006)** studied a so-called Vortex Strake Device, presented in **Fig. 2.17**. The concept consists of long and narrow vanes added, in sets, to the near-base sections of the sides and top of the trailer. The vanes were applied at the angle of 30°; on the sides – leading edge up, on the top – leading edge inboard, creating a chevron pattern. The concept was reported to produce vortices, which energised the flow near the trailing edge and stabilised the near wake. Wood **(2006)** reported a 1 – 5% improvement in the fuel economy.

Similar fuel savings (2 – 5%) are offered by Aeroserve Technologies Ltd. **(2019)** with the use of their commercially available VG called Airtab®. The device is advertised for a range of vehicles from relatively small hatchbacks to HGVs and tankers. Each individual VG is wishbone-shaped (**Fig. 2.18**) and suggested to be used in closely-fixed arrays. Varshney and Guru **(2017)** studied the concept in the numerical domain, with groups of aligned Airtabs® along the trailing edges of the trailer, as well as the tractor of a HGV configuration; a drag reduction of up to 1.7% was reported.

Many reports on vortex generators are found to be contradicting. While it is clear that the generated vorticity aids in base pressure recovery, some studies show that the additional induced drag outweighs these benefits and the industry continues to have mixed opinions on the matter **(North American Council for Freight Efficiency, 2016)**.

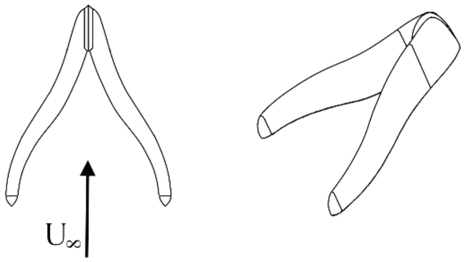

Fig. 2.18 Schematic of Airtab® vortex generator

2.3.7 Edge serrations

Flow characteristics similar to those produced by typical VGs have also been found for some 2D trailing edge modifications. Rodriguez **(1991)** studied such edges with squared segmentation and a combination with additional triangles placed in the wave troughs (**Fig.**

2.19) on a thick, flat plate with a sharp leading edge. A drag reduction of over 40% was reported, with streamwise vortices generated at the longitudinal segment edges. The vortical structures shed from the troughs were found to lag behind those generated at the crests.

Comparable results on a similar plate model were also found by Tombazis and Bearman **(1997)** with a sinusoidal wave disturbance. The authors reported different shedding modes, with a vortex dislocation occurring between the structures shed at the troughs and crests; shedding frequency behind the trough was shown to be higher ($St_H \approx 0.29$) relative to the peak ($St_H \approx 0.24$). The modifications were found to increase the base pressure and produce drag reductions in the range of 10 – 34%, dependent on the specific pitch and height of the waveform, with larger heights and smaller pitches associated with more significant pressure recovery. For similar wavy trailing edge profiles, Cai, Chng and Tsai **(2008)**, and Bearman and Owen **(1998)** related the base drag reductions to suppression of the vortex shedding modes, with Cai and Chng **(2009)** also noting reductions in drag fluctuations.

More recently, similar trailing edge serrations applied to a jet engine nacelle were also reported to produce favourable trust augmentation **(Zaman, Bridges and Huff, 2011)**. The streamwise vorticity shed from such edges was found to increase the surface pressure on the engine nozzle, thereby reducing the local drag.

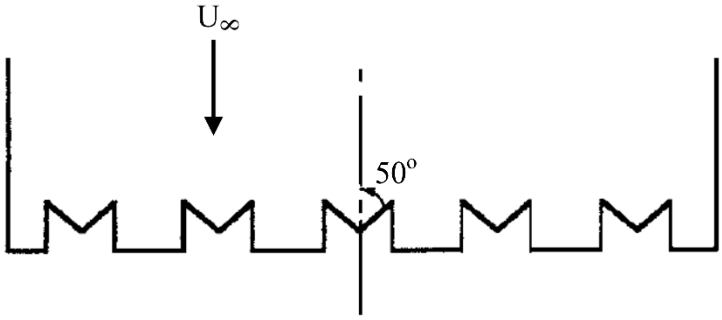

Fig. 2.19 Schematic of the segmented edge studied by Rodriguez (1991) (adapted from Rodriguez (1991))

2.4 The lobed mixer

In the aerodynamic research, it is often useful to consider advancements outside the field of interest, with many mechanisms offering favourable results in various applications. One such example is considered in this section.

The lobed mixer is a device commonly used to efficiently mix two coflowing fluid streams. It first became popular in the aeronautic field as a method for mixing enhancement for jet engine noise reduction **(Crouch, Coughlin and Paynter, 1977)**. The lobed mixer's success stemmed from its unique ability to decrease noise levels while providing thrust augmentation. Since then, the range of applications has expanded to include studies of efficient fuel injectors **(McCormick and Bennett, 1994; Smith et al., 1997; Waitz et al., 1997; Yu and Yip, 1997; Mao, Yu and Chua, 2006; Mao et al., 2009; Depuru Mohan, Prakash and Panchapakesan, 2015)**. More recently, similar devices were also explored for modifying the reattachment length within transonic and supersonic flows **(Bolgar et al. 2016; Schreyer and Taskin 2018**). The following sections discuss, in detail, the lobed mixer's principles of operation as well as typical configurations and results.

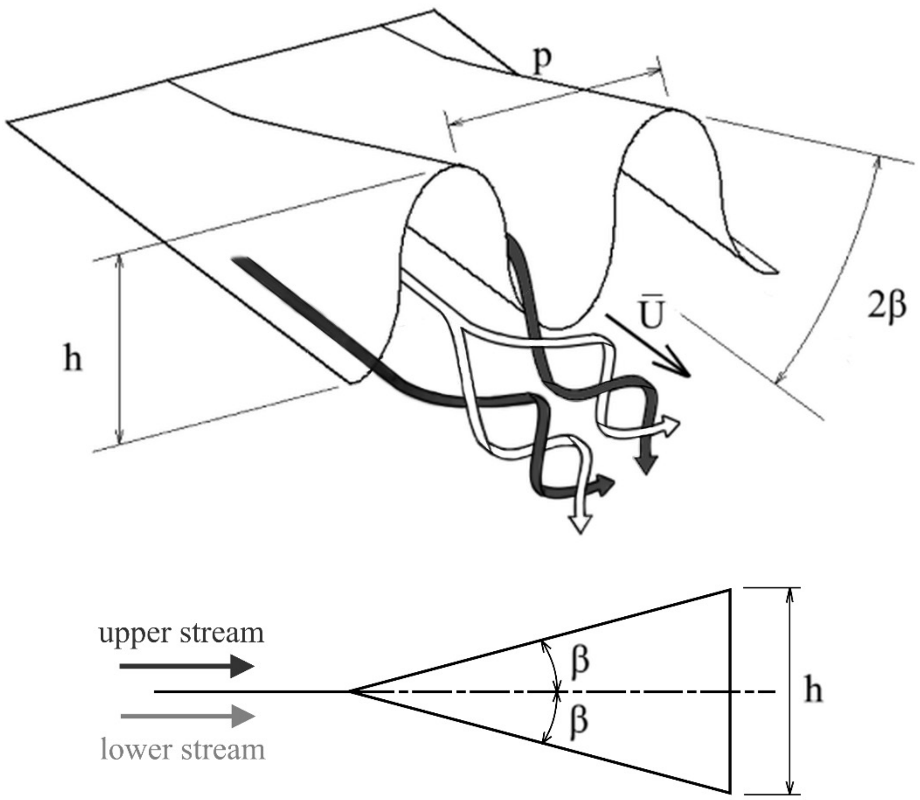

Fig. 2.20 Schematic of a typical lobed mixer

2.4.1 Overview

A lobed mixer is normally characterised as a three-dimensional, convoluted splitter plate; a basic schematic of such a geometry is presented in **Fig. 2.20**. The device is typically mounted upstream at the flat edge, with the two streams to be mixed each occupying one side of the plate. The crests and troughs of the lobes diverge from the streamwise direction at the penetration angle, denoted as β in **Fig. 2.20**. The principle of mixing augmentation resides in an increase in the interface area as well as the interfacial area gradients through strain. The interface length is initially extended solely through lengthening of the trailing edge by adding the lobed profile. For profiles which are approximately squared, the initial interface length increases by around 2h per lobe, relative to a typical straight splitter. In such cases, the initial interface length (l) can be estimated as **(Waitz et al., 1997)**:

$$l = 2h + p \qquad (2.3).$$

In contrast, for a normal straight-edge splitter encompassing the same transverse distance, the initial interface length would be equivalent to p. Mixing of the two streams is amplified in this way due to the increase in the net surface area of flow interaction; equivalent to mixing the same volume of fluid over a larger surface.

A further effect of the lobed mixers is the introduction of strong streamwise vorticity. The streamwise vorticity is generated through an inviscid process due to the non-uniform aerodynamic loading along the mixer's span, which is provided by the non-zero penetration angle **(Skebe et al., 1988)**. This action is equivalent to that typically observed on a finite wing, with the boundary layer over the lobe peak normally thinner relative to that in the trough **(Qiu, 1992)**. The vortices are generated within the lobes and subsequently shed at the trailing edges **(Waitz et al., 1997)**, with the structures seen at the lobe exit normally arranged in counter-rotating pairs (**Fig. 2.20**). The circulation produced in a lobe segment, as indicated by the red dotted lines in **Fig. 2.21**, can be estimated from experimental results through contour integration within the plane perpendicular to the streamwise direction **(Barber, Paterson and Skebe, 1988)**. Barber, Paterson and Skebe **(1988)** also showed that

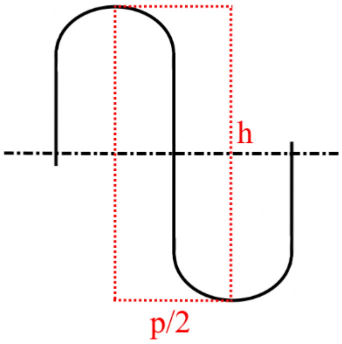

Fig. 2.21 Schematic representation of a lobe segment

the circulation can be approximated through inviscid analysis, in which case, for any lobe profile shape, it is given by:

$$\Gamma_X = 0.5\, C\, \bar{U}\, h \tan\beta \qquad (2.4)$$

where C is a profile-dependent constant, and $\bar{U}$, the axial velocity at lobe exit. For $\bar{U}$, Waitz et al. **(1997)** suggested using the average of upstream velocities either side of the mixer. The estimate presented in equation 2.4 is derived by assuming the fluid exits the lobe at the penetration angle and that the penetration angles of the adjacent lobes are equal. The average vorticity per lobe segment (**Fig. 2.21**) can then be calculated as **(Barber, Paterson and Skebe, 1988)**:

$$\bar{\Omega}_X = \frac{\Gamma_X}{0.5\, h\, p} = \frac{C\, \bar{U} \tan\beta}{p} \qquad (2.5).$$

The scale of the exiting vortices is of the same order as one lobe segment. After being shed into the flow, the vortices grow downstream through turbulent diffusion, eventually decaying completely as they diffuse into the adjoining counter-rotating neighbours **(Waitz et al., 1997)**. The streamwise vortices provide further mixing augmentation by wrapping the interface area, ultimately elongating it further and inducing higher gradients through strain. The downstream growth of the interface surface area is approximately linear and proportional to the circulation.

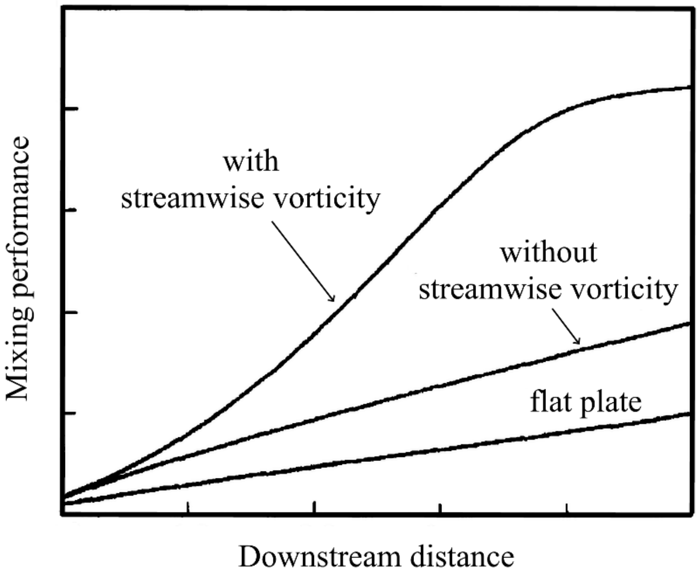

Fig. 2.22 Effects of streamwise vorticity on mixing performance as a function of downstream distance (adapted from Waitz et al. (1997))

Waitz et al. **(1997)** isolated the effect of the initial increase in interface area through the trailing edge geometry (no penetration angle) on mixing. This was compared to the result obtained with streamwise vorticity, as presented in **Fig. 2.22**. In both cases, mixing was improved in comparison with the straight-edge splitter. The isolated influences of geometry and vorticity are shown to be of similar magnitude, however, the combination of both evidently maximises the benefits.

In addition to the streamwise vortices, the typical flow topology at the lobe exit contains other structures. The flow wrapping around the upstream portions of a lobe may result in the appearance of a small horseshoe vortex at the exit, as shown in **Fig. 2.23**. These structures however, have little impact on the overall mixing processes **(Waitz et al., 1997)**. Upstream of the trailing edge, the mixer isolates the above flow from the flow located underneath. In cases where the flow velocities are identical either side of the mixer, the velocity ratio is equal to one and the magnitude at the lobe exit is the same as upstream. However, in cases of non-singular velocity ratios, additional transverse vortices, caused by wrapping of the imbalanced layers (Kelvin-Helmholtz instability), can appear in the near wake **(McCormick and Bennett, 1994; Waitz et al., 1997; Yu and Yip, 1997)**. Waitz et al. **(1997)** showed that, with the boundary layer over the lobe's peak and sides being up to five times thinner relative to the undisturbed flow upstream of the mixer, the transverse vortices' scale is small in comparison with the streamwise vortices. The latter are the largest scale structures for the downstream distance of 3p – 10p behind the trailing edges. McCormick and Bennett **(1994)**, and Yu and Yip **(1997)** reported that the strong streamwise

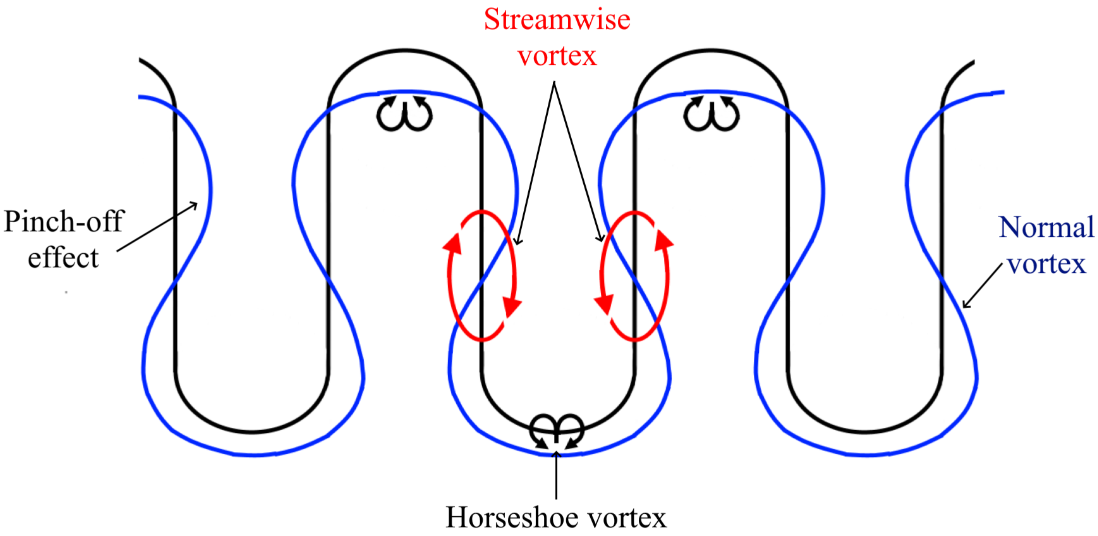

Fig. 2.23 Flow topology downstream of lobed mixer exit

counter-rotating vorticity can act to deform the Kelvin-Helmholtz structures, whereby they appear to be “pinched-off” around the midsection, similar to the schematic in **Fig. 2.23**. This deformation quickens the breakdown of the transverse structures, ultimately enhancing mixing through local increases in small-scale turbulence. Mao et al. **(2009)** showed that the shedding of the Kelvin-Helmholtz vortices is not uniform along the lobe profile, with higher shedding frequency near the peak and lower along the lobe sides. Furthermore, increasing the frequency reduces the wavelength of these vortices, resulting in an improved mixing performance. While the production of streamwise vortices remains essentially unaffected by changes in the velocity ratio, non-unity ratios are reported to produce higher frequency Kelvin-Helmholtz vortices. This is therefore why, while not impacting the strength of streamwise vorticity, the velocity ratio can affect the overall mixing performance **(Mao et al., 2009)**.

Downstream mixing augmentation is approximately proportional to the shed circulation **(Qiu, 1992)**. From equation 2.4, it is evident that increasing the penetration angle can maximise the resulting initial circulation, however, this is limited by flow separation within the troughs. For low fluid velocities Qiu **(1992)** suggested an upper limit of β=20°. This agrees with the results of Yu, Hou and Chan **(2000)** (β=22°), with O’Sullivan et al. **(1996)** also reporting no further vorticity benefit past $\beta = 30°$. Though beyond this limit, the vorticity will not cease to be generated, the effective lobe height and penetration angle will decrease as the thickening boundary layer introduces local blockage, diminishing the vortex strength. Skebe et al. **(1988)** showed that for angles up to β=22°, values estimated using equation 2.4, compare to within 5% of those obtained through numerical simulations. The parameter directly related to penetration angle is the lobe height, with equation 2.4 indicating larger values for stronger circulation. Qiu **(1992)** however suggested that for a given penetration angle, increasing the ratio of h/p may reduce the rotation speed at the lobe trailing edge, which results in weaker growth of the initial interface, decreasing the contribution of streamwise vortices to overall mixing augmentation. Qiu **(1992)** recommended $h/p \approx 1$ or lower.

Profile pitch is another key parameter, with Barber, Paterson and Skebe **(1988)** indicating that very small lobe spacing is not desirable. In such cases, the boundary layers from the opposite lobe sides may merge, producing viscous losses and weaker circulation. In contrast, however, as seen in equation 2.5, large pitches will result in reduced average

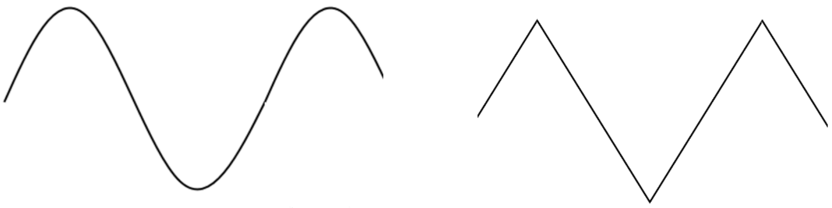

Sinusoidal Triangular

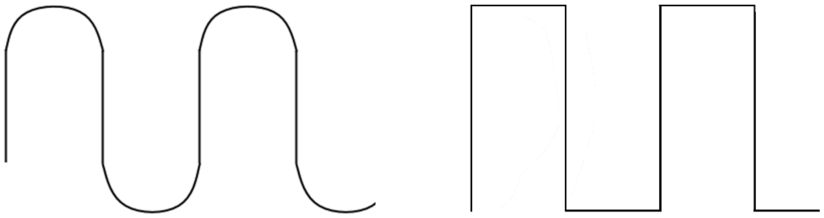

Parallel Squared

Fig. 2.24 Typical lobed mixer profiles

lobe vorticity. Furthermore, the specific profile geometry has also been shown to affect the generated vorticity. The two most common variations of lobe profile are sinusoidal and parallel (**Fig. 2.24**), with Skebe et al. **(1988)** suggesting the strongest secondary flow is produced by the latter. For sinusoidal geometries, the performance is hindered by the boundary layer blockage within the troughs, which decreases the effective penetration angle. This is eliminated with parallel profiles, which offer increased space in the trough, and prevent side boundary layers from merging. Similar conclusions were drawn by Waitz et al. **(1997)** and Mao et al. **(2009)**, with Smith et al. **(1997)** also noting higher strain rates in comparison with sinusoidal lobes. These differences are best reflected in the value of C in equations 2.4 and 2.5. Barber, Paterson and Skebe **(1988)** estimated those experimentally, showing $C \approx 4$ and $C \approx 2.5$ for parallel and sinusoidal profiles, respectively. In other words, for a given penetration angle and lobe height, the circulation produced by parallel lobes will be 60% higher.

Practically, due to manufacturing limitations, other simpler profiles may be preferred. The interest normally lies with the simplified versions of the standard profiles; triangular and squared (**Fig. 2.24**). Mao et al. **(2009)** compared these geometries to the parallel lobe. They reported that, while the squared profile results in Kelvin-Helmholtz vortices of lower frequencies, the generated streamwise vorticity is marginally higher, which, overall, balances and amounts to a similar mixing performance. The Kelvin-

Helmholtz vorticity shed from the triangular profile was also characterised by lower frequencies. However, as a result of a significant boundary layer blockage in the trough, this particular profile was found to produce only 60% of the parallel-lobe initial streamwise vorticity, resulting in severely degraded performance **(Mao et al., 2009)**. This is also in agreement with estimations of Barber, Paterson and Skebe **(1988)**, who indicated $C \approx 2$ for triangular lobes, or a 50% reduction in initial circulation relative to an equivalent parallel profile.

Other, more atypical, lobe profiles also exist, the scarfed and scalloped lobes being two examples (**Fig. 2.25**). The former is created by removing a part of the penetration area, and the latter, by removing sections of the lobe sides. Mao et al. **(2009)** reported both geometries to have very little effect on the Kelvin-Helmholtz spanwise structures. No improvement in performance was found for the scarfed lobe, which effectively reduced the lobe height. In contrast, the scalloped lobes tend to increase the initial streamwise vorticity, which is attributed to the production of additional small streamwise vortices at the four notches created by removing parts of the lobe **(Yu, Hou and Chan, 2000; Mao et al., 2009)**.

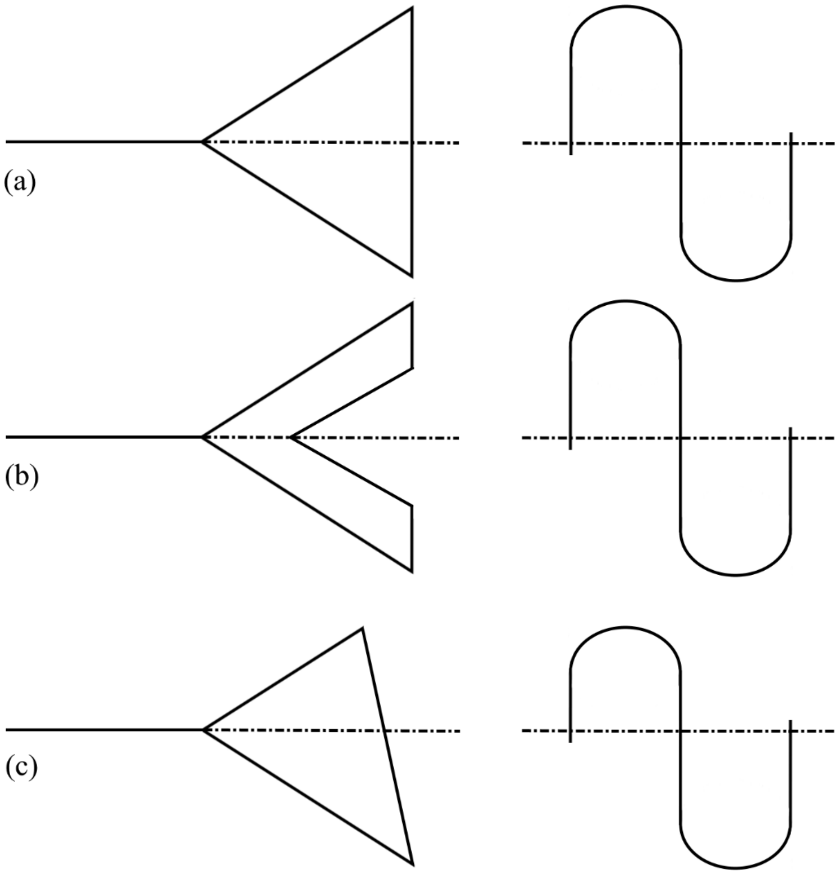

Fig. 2.25 Side (left) and front (right) profiles of lobed mixer geometries: (a) normal, (b) scalloped, (c) scarfed

The added vortices rotate in the same direction as the main vortex on the corresponding side and merge further downstream, causing an overall more diffused structure due to their like sense of rotation. The result is a faster decay of streamwise vorticity in comparison with an unaltered lobe. Mao et al. **(2009)** reported the scalloped lobe to improve mixing marginally. Additionally, Yu, Hou and Chan **(2000)** noted that scalloping may aid the suppression of flow separation and consequently enable the extension to higher penetration angles.

2.4.2 Results in various applications

Smith et al. **(1997)** conducted a study of lobed mixers in application to fuel injectors; lobed mixers were found to improve mixing over a standard flat injector by more than 30%. For lobed jets, the centreline velocity decay was found to be significantly faster, relative to a smooth circular jet, resulting in shorter core lengths **(Hu et al., 2000; Depuru Mohan, Prakash and Panchapakesan, 2015)**. This is typically a result of a higher entrainment velocity due to the secondary flow, with Hu et al. **(2000)** also noting reductions in the scale of Kelvin-Helmholtz structures. Depuru Mohan, Prakash and Panchapakesan **(2015)** showed that, through the early introduction of streamwise vorticity, the lobed jets performed a significant amount of mixing in the near field, increasing local levels of mixedness by up to 83% relative to standard jets.

McCormick and Bennett, **(1994)** and Hu et al. **(2001, 2002)** confirmed that the most intense mixing with the use of lobed mixers occurs in the short downstream distances from the trailing edges. Hu et al. **(2001)** characterised this process using the downstream evolution of turbulent kinetic energy in the flow. The early breakdown of transverse structures by streamwise vorticity increased the level of turbulent kinetic energy significantly. For this reason, within the downstream distance equivalent to 8 lobe heights ($X/h<8$), the turbulence of a lobed jet was substantially higher relative to a normal smooth trailing edge; these results are presented in **Fig. 2.26**. Beyond $X/h=8$, the reverse is true. Due to the strong initial mixing, further downstream, the shear layer of a lobed mixer is expected to be weaker (smaller velocity ratio) relative to a normal jet. The more rapid mixing also results in quicker pressure recovery within the mixing layer past vortex breakdown **(Waitz et al., 1997)**.

Eckerle, Sheibani and Awad, **(1990)** showed that, while the generation of streamwise vorticity by the lobes is an inviscid process, the subsequent downstream evolution of the

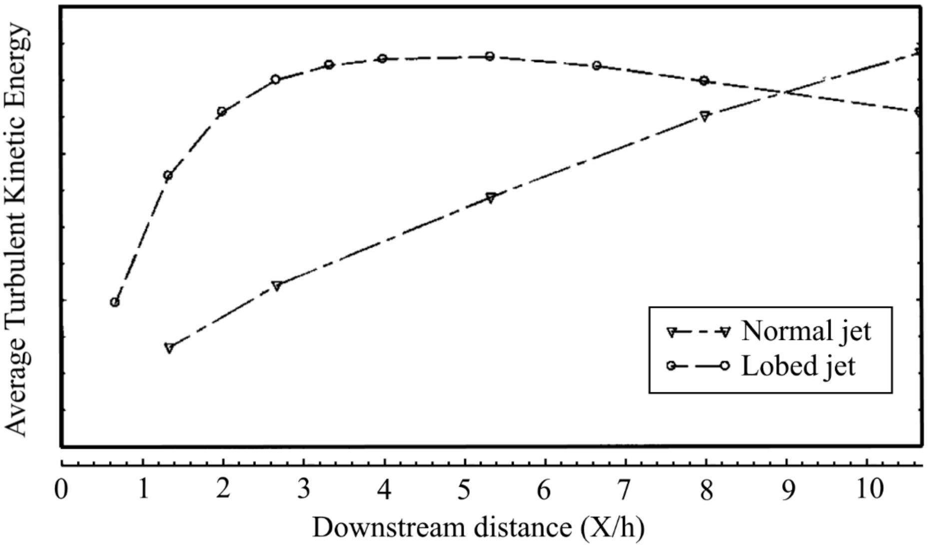

Fig. 2.26 Turbulent kinetic energy evolution downstream of normal and lobed jets (adapted from Hu et al. (2001), with the permission of AIP Publishing)

structures is typically affected by viscous forces. Varying velocity ratios result in different vorticity decay. Additionally, the authors observed asymmetry in the strength of the counter-rotating vortex pairs at non-unity velocity ratios, with subtly higher anticlockwise magnitudes. Such characteristics result in turbulence increases across the mixing layer, with the breakdown occurring at variable downstream positions.

Characteristic streamwise vorticity produced by lobed mixers was found to improve mixing and suppress the wake of aerofoils when fixed to the trailing edges **(Hunter, Delore and Presz, 1991)**. Hunter, Delore and Presz **(1991)** reported the vorticity to interact with the wing-tip vortex, suggesting that such devices may be useful for the tip vortex dispersion in marine vehicles. The same physics have also been found to enhance heat transfer in heat exchanger devices **(Tsui et al., 2000)**. In such cases, the streamwise vortex flow was shown to enhance convection between high and low temperature regions downstream of the lobes. The superb mixing characteristics of these geometries also proved useful for low-power-loss infra-red signature suppression in helicopters **(Zhang, Pan and Shan, 2014)**.

The enhanced flow entrainment produced by the lobed geometries has also been exploited for reduction in rear separation area and reattachment length in subsonic, as well as transonic **(Bolgar, Scharnowski and Kähler, 2016)** and supersonic conditions **(Chao, Huanli and Jian, 2020; Fang et al., 2020)**. Feng et al. **(2015)** showed that a similar topology, including streamwise vorticity, "pinched-off" transverse structures, and velocity ratio-dependent decay rates, is also characteristic in supersonic mixing layers, as observed in lower-speed environments. Bolgar, Scharnowski and Kähler **(2019)** showed up to 80% reduction in reattachment length downstream of a 2D backward-facing step with lobe-like geometries along the top trailing edge. This reduction is equivalent to decreases in wake size with faster pressure recovery along the reattachment surface. The effects were primarily attributed to higher flow entrainment into the shear layer within short downstream distances. The protruding lobes were found to produce additional aerodynamic loads. This was suggested to be minimised through the removal of these top parts, keeping only the body-penetrating lobes. Similar configurations, resembling trailing edge longitudinal grooves, were shown to reduce reattachment length by up to 66% **(Lin, Howard and Selby, 1990)**.

Deere and Hunter **(1999)** also reported reductions in the separation region with protruding convoluted contouring placed ahead of a boat-tailed aircraft fuselage afterbody model. Additionally, while no overall drag reduction was recorded for the boat-tail angle of 15°, at 22°, drag was reduced by up to 36%. This disparity was attributed to the latter having a generally larger separation region, and therefore higher capability for improvement. All drag reductions were found at subsonic speeds, with no appreciable effects in supersonic conditions. Similar grooves within the afterbody of a projectile-like shape have also been shown to produce small drag reductions by Howard and Goodman **(1985)**. Paterson et al. **(1989)** suggested lobe-like trailing edge grooves to be an effective method for drag reduction of many different types of bluff bodies. However, there are no exact data underpinning the mechanisms responsible for the potential drag reduction, possible benefit levels, or optimal configurations.

Overall, the literature suggests that the use of lobed-mixing geometries at the base of bluff bodies may result in shorter and smaller wakes, better pressure recovery and potential drag reductions. With the characteristic enhancement of flow entrainment across the mixing layer, the lobed mixer appears to be a promising method, which may be able to combine the effectiveness of a vortex generator without the additional drag induced by standard protrusions. Additionally, the preference for high penetration angles suggests the technique may be effective for maximising the benefits of steep boat-tails and tapers, normally dominated by premature flow separation. Many questions remain unanswered, including how such a configuration may affect the characteristics of a 3D base wake in ground proximity.

2.5 Experimental techniques

Having reviewed the aerodynamic characteristics typical to ground vehicles, as well as various drag reduction concepts, it is important to understand the ways in which this data may be obtained. In the research of ground vehicle aerodynamics, various methods can be used, belonging to the main two groups of experimental and computational (Computational Fluid Dynamics – CFD) testing. The latter remains a useful and popular tool **(Krajnović and Davidson, 2004; Strachan, Knowles and Lawson, 2004; Lav, 2013)** due to key advantages such as relatively low costs as well as easy manipulation of ground condition, scale, blockage, incident angles, and dynamic similarity. That said, all CFD-obtained results must typically be experimentally validated, with cases of high turbulence and unsteady flow motions, like those found in the base wake of a HGV, remaining particularly difficult to model computationally **(Cyr, Ih and Park, 2011)**. An accurate reproduction often requires very large grids, which can be difficult to set up, making this a time and labour intensive technique **(Bayraktar and Bayraktar, 2006)**, with some characteristics still found dissimilar to experimental flow **(Hinterberger, Garcia-Villalba and Rodi, 2004; Ortega et al., 2004)**. For this reason, experimental methods remain the prevalent choice among many designers and researchers. The following sections discuss the aspects of road and wind tunnel testing.

2.5.1 Road testing

A common ground vehicle experimental technique is road or track testing. Arguably, this method provides the most accurate results; typically using full-scale, geometrically detailed vehicles. The realistic environment allows the freestream turbulence and on-road conditions to be correctly replicated. The drag or fuel economy are normally evaluated through steady state **(Coon and Visser, 2004; Browand, Radovich and Boivin, 2005; Grover and Visser, 2006; Surcel, Michaelsen and Provencher, 2008; Kehs et al., 2013)** or coastdown tests **(Buckley, 1995; Le Good et al., 1998; Howell et al., 2002)**. The former typically involves comparisons of fuel consumption during constant velocity journeys, and the latter, measuring the velocity and deceleration of the vehicle as it coasts from a set speed down to stop. Though the aerodynamic performance may be accurately estimated, this technique precludes detailed flow-field studies, with other disadvantages also including difficulty to control ambient conditions, resulting in low repeatability, and high costs.

2.5.2 Wind tunnel

Wind tunnel testing remains the most popular experimental technique for studies of ground vehicles. Originally designed to serve the aerospace industry, wind tunnel facilities quickly evolved to accommodate the needs of ground vehicles and have informed their design for many decades. There exist two main types of wind tunnel circuits: closed and open return. Closed circuits rely on the same volume of air being continuously recirculated during operation, whereas open circuit wind tunnels intake air, which is subsequently expelled at the outlet. The latter are normally located in closed buildings to ensure a monitored environment **(Tropea, Yarin and Foss, 2007)**. Irrespective of the circuit type, the key components of all wind tunnels are the contraction ratio and diffuser, which allow to create a uniform flow across the connecting test section. There are many types of test sections: open, closed, slotted, streamlined and adaptive. Owing to lower costs, however, the most common are the open and closed sections. While there are many aspects which ought to be considered carefully, the main difference between the two is the variation in the displacement of the airstream boundary around the test body. The open test section normally results in a wider (compared with free flow) boundary, whereby the fluid close to the body is minimally slower than would be expected in free flow. In contrast, in closed sections, the flow is constrained by the walls, resulting in a narrower boundary and higher speeds **(Tropea, Yarin and Foss, 2007)**.

The following subsections discuss the aspects pertinent to all wind tunnels, which must be considered when designing such experiments.

2.5.2.1 Dynamic similarity

Although some wind tunnels allow full-scale experiments, these typically result in high costs, making sub-scale models far more popular. In these cases, the similarity to full-scale vehicles can be achieved through the dynamic similarity of the flows. This means that ideally Reynolds numbers of the sub and full-scale flows are matched, where Reynolds number is defined as

$$\mathrm{Re} = \frac{\rho U_\infty d}{\mu} \qquad (2.6)$$

where d is the characteristic length (e.g., body length or width), and μ, the dynamic viscosity of air. In the UK, the motorway speed limit for HGVs is 60 mph, resulting in typical width-based Reynolds numbers of approximately $Re_W \approx 4 \times 10^6$. The exact dynamic similarity, therefore, is not always possible, particularly at very small scales, where increasing speeds can result in compressibility issues. For this reason, most studies are conducted at lower than critical Reynolds numbers, which is deemed acceptable so long as the non-dimensional parameter sought after, such as the drag coefficient, has reached a constant value (it no longer varies with increasing Reynolds number).

Physically, dynamic similarity is concerned with the accurate representation of the boundary layer profile along the model's surface. Reynolds numbers which are not sufficiently high may cause a laminar flow separation at the model leading edges and result in degraded downstream flow. The correct boundary layer profile can be critical for studies concerned with the aerodynamic drag reduction. Wood **(2015)** outlined the difficult relationship between Reynolds number and boat-tail angle, whereby different absolute optima were found at varying flow conditions. Storms et al. **(2001)** investigated the Reynolds number's effect on the vehicle's drag coefficient. In the range of $3 \times 10^5 < Re_W < 2 \times 10^6$, the trend showed the drag coefficient (C_D) to decrease up to $Re_W \approx 1 \times 10^6$. For $Re_W > 1 \times 10^6$, the drag coefficient plateaued ($C_D \approx 0.25$) and the variations thereafter were marginal. Overall, within the examined Re_W range, while the drag coefficient varied significantly, the base pressure changes were limited to 2%. This led to the conclusion that the discrepancy in drag measurements between higher and lower Re studies is mostly caused by varying flow conditions at the forebody, i.e., separation/reattachment at the front corners, and that the Reynolds number has little effect on the flow characteristics at the base.

While it is commonplace to present Reynolds numbers based on the vehicle width or length (d=W, d=L), some sources emphasise the importance of the relationship between the Reynolds number and the radii of the leading edges **(Tropea, Yarin and Foss, 2007; Wood, 2015)**. Normally, larger radii (more streamlined front) result in lower critical Reynolds numbers, therefore, it is important to consider this relationship to ensure correct flow-field representation.

2.5.2.2 The influence of blockage

A wind tunnel environment normally produces several interference effects. Typical of closed test sections is the confinement of the flow, or solid blockage, resulting in increases in the velocity along the model sides. The local flow acceleration modifies the boundary layer on the model's surface, affecting the size of the rear wake, which gives rise to the wake blockage component. Additionally, as the flow travels along the section, the boundary layer on the test section walls grows and may accelerate the flow further. This effect, known as horizonal buoyancy, is normally considered during wind tunnel design, with most closed test sections including a small divergence in the streamwise direction. Although most interferences arise from the transverse boundaries, for bluff bodies characterised by large rear wakes, small streamwise distances between the model base and the test section end may result in reductions in the measured drag. This is further explored in **Section 2.5.4.6**.

When the wind tunnel interferences are sufficiently high, the resulting pressure distribution modifications become non-negligible and the effects must be considered. The most common result of high blockage is a false increase in drag coefficient **(Yang and Schenkel, 2010; Yang, Nastov and Schenkel, 2013)**, with HGV models remaining particularly affected due to their size and aerodynamic characteristics. Over the years, several correction techniques have been developed. However, to maintain high levels of accuracy, the recommended solid blockage limit for comparative studies is 15%, with the corrections not exceeding 30% of the measured drag coefficient **(SAE International, 2012)**.

One of the first correction methods developed for bluff bodies in closed test sections was that of Maskell **(1965)**, based on studies of flow separation over normal flat plates. This method used momentum balance and assumed that the solid constraint of the test section walls does not influence the pressure distribution. While this was suggested to be appropriate for solid blockage ratios of up to 21% **(Cooper, 1998)**, the method may not be suitable for setups exceeding this value. Additionally, Cooper **(1998)** reported that the method may only be accurate for drag correction, with the remaining forces being typically overcorrected due to the disproportionately high dynamic pressure correction value.

With Maskell's **(1965)** method found to generally overcorrect, other improved approaches based on this principle emerged **(Cooper, 1998)**. Hackett and Cooper **(2001)** presented an extended version, denoted as Maskell III, and developed using a flat plate at various incident angles. The new approach divided the correction into two steps, separating the dynamic pressure and incremental drag components, reducing the tendency to overcorrect for higher blockage ratios. Another variation of Maskell's **(1965)** method was presented in the work of Söderblom, Elofsson and Hyvärinen **(2016)**. In this adaptation, the correction includes the influence of the vehicle's length, making it particularly suitable for long models at high blockage ratios, such as HGVs. This method was found to produce data in good agreement with the open road results **(Söderblom, Elofsson and Hyvärinen, 2016)**.

Another group, denoted as pressure signature methods, includes techniques which use supplementary pressure measurements to generate adequate corrections **(Hackett, Wilsden and Lilley, 1979; Cooper, 1998; Söderblom, Elofsson and Hyvärinen, 2016)**. Static pressure on the wind tunnel wall is typically measured and used for the correction of the dynamic pressure. These methods can produce accurate results, with the ability to reflect changes from small geometrical variations, however, they often require multiple measurement points along the test section, making the setups complex, and testing labour intensive **(Söderblom, Elofsson and Hyvärinen, 2016)**.

Mercker **(1986)** developed a method specifically for ground vehicles characterised by rear separation. The new approach was based on earlier solid blockage and wake blockage analyses of Glauert **(1933)**, Maskell **(1965)** and others **(Cooper, 1998)**. Mercker's **(1986)** method remains particularly useful for ground vehicles as it accounts for various interferences. The dynamic pressure correction includes the influence of body volume, as well as the projected area and length, considering the flow-field modifications due to non-zero yaw.

Söderblom, Elofsson and Hyvärinen **(2016)** conducted an extensive investigation of several techniques in application to HGVs of varying front radii, showing that the accuracy of the correction methods is dependent on the specific vehicle shape. Corrections including volume dependency, such as that of Mercker **(1986)**, are especially advantageous for long models with high solid blockage ratios. Furthermore, Cooper **(1998)** reported that for simplified ground vehicle models, data corrected using Mercker's **(1986)** technique were in good agreement with those obtained through one of the pressure signature methods.

2.5.2.3 Ground simulation

A common condition of most wind tunnels is the forced movement of air over a stationary model. This characteristic is rather atypical to reality and the resulting generation of additional boundary layers on the wind tunnel floor can be problematic. This is particularly important if they are allowed to interact with the model, adversely impacting attempts to replicate true aerodynamic performance. To counter these effects, velocity profile on the floor is usually adjusted using raised ground planes **(Garry, 1981; Hammache and Browand, 2004; Van Raemdonck and Van Tooren, 2008a; Lo and Kontis, 2017)**, raised models **(Coon and Visser, 2004; Krajnović and Davidson, 2004; Strachan, Knowles and Lawson, 2004; Storms and Ross, 2006)**, upstream suction and tangential blowing **(Tropea, Yarin and Foss, 2007)**, as well as moving ground. These methods (**Fig. 2.27**) aim to either fill in the velocity deficit or make the profile fuller.

Arguably, among the most accurate methods is the use of a moving ground, normally provided by a rolling belt. Such facilities impose floor motions relative to the model consistent with the freestream flow to prevent boundary layer formation **(Burgin, Adey and**

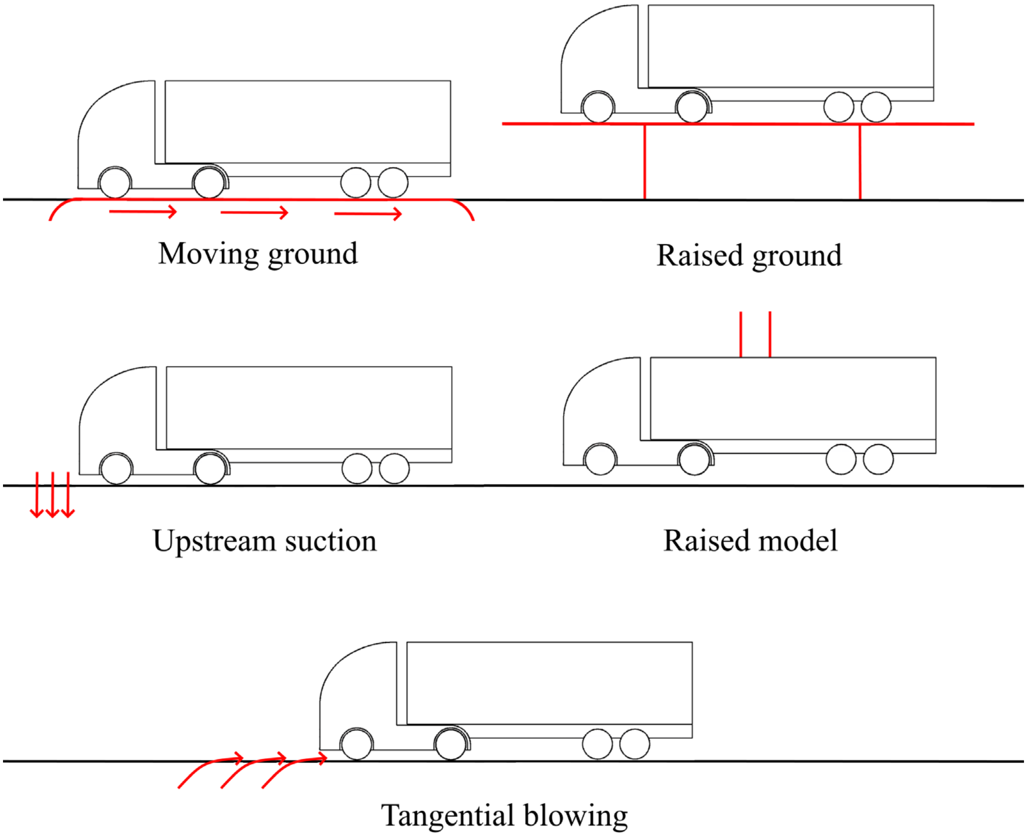
Moving ground
Raised ground
Upstream suction
Raised model
Tangential blowing

Fig. 2.27 Common methods of ground simulation

Beatham, 1986; Wiedemann and Potthoff, 2003). While the use of moving ground remains common within the motorsport and automotive industries, they are rarely adopted for HGV aerodynamic design. This is partly due to the cost and difficult implementation, but also the general perception that accurate ground simulation is not needed, given their larger ride height, with Fago, Lindner and Mahrenholtz **(1991)** reporting drag insensitivity beyond $G_C/H>0.1$. Over the years, the necessity for moving ground has been broadly interrogated, with many studies reporting that substantial differences exist between flow-fields simulated in moving and stationary ground conditions for various configurations, including HGV models. This subsequently leads to questions of the validity of omitting proper ground simulation on the basis of elevated ride height.

Reports are generally inconclusive, with multiple studies noting reductions in drag **(Sardou, 1986; Fago, Lindner and Mahrenholtz, 1991; Le Good et al., 1998; Krajnović and Davidson, 2005)**, and others showing drag increases **(Burgin, Adey and Beatham, 1986; Strachan, Knowles and Lawson, 2007; Söderblom et al., 2009; Leuschen, 2013; Zhang et al., 2014)** with the use of moving ground relative to stationary ground. Zhang et al. **(2014)** suggested that increasing drag is a result of the prevention of viscous underbody blockage (from the boundary layer formation), increasing local velocities. A similar interpretation was provided by Leuschen **(2013)**, who also reported the sensitivity of certain tractor drag-reduction devices. In contrast, Geropp and Odenthal **(2000)** demonstrated the ground simulation effects to be Reynolds number dependent.

Literature shows that the ground condition can also affect the surrounding flow-field. Lajos, Preszler and Finta **(1986)** reported that moving ground increases momentum flux within the underbody, which is responsible for the generation of additional downward

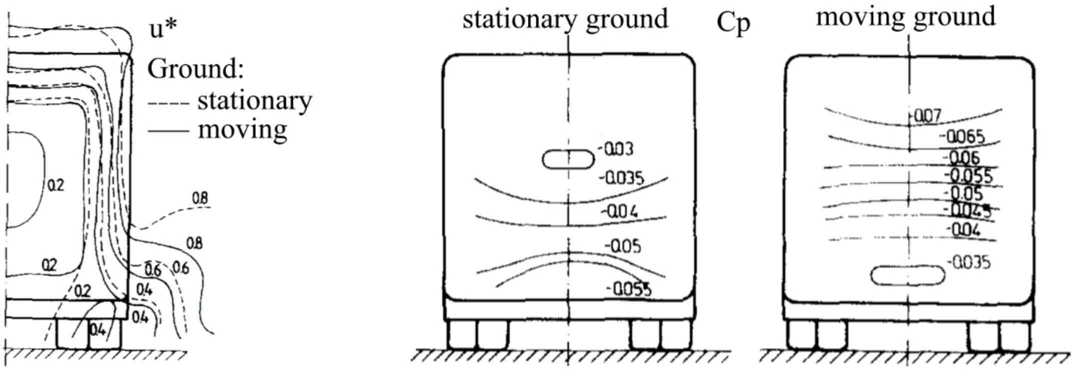

Fig. 2.28 Contours of streamwise velocity (u*) and base pressure coefficient (Cp) with stationary and moving ground use as reported by Lajos, Preszler and Finta (1986) (adapted from Lajos, Preszler and Finta (1986))

momentum along the model sides and rear; this is evident in the streamwise velocity contours (u*, normalised by U_∞) presented in **Fig. 2.28**. With stationary ground, the underbody region is dominated by strongly impeded flow, which promotes side outflow. Additionally, substantial changes in the wake flow-field were also observed with moving ground, constituting a shift of the base stagnation point from the upper to the bottom base half, and complete redistribution of the base pressure coefficient (Cp), as shown in **Fig. 2.28**. In a similar work, Duell and George **(1993)** also identified base pressure modifications, with a 2 – 8% (ground clearance dependent) change in the average pressure coefficient.

Another important aspect, directly related to moving ground, is the wheel rotation. Despite reports showing it is important for accurate reproduction of realistic flow conditions **(Burgin, Adey and Beatham, 1986; Wickern, Zwicker and Pfadenhauer, 1997; Wäschle, 2007; Söderblom et al., 2009, 2012)**, it is still largely omitted in HGV studies. One of the effects of including rotating wheels is relative drag reduction **(Le Good et al., 1998; Willemsen et al., 2011; Devesa and Indinger, 2012)**. Söderblom et al. **(2009, 2012)** noted reductions in static pressure within the wheel housing, showing also that the consequent local flow modifications close to a rotating wheel result in further modified structures downstream. Additionally, the injection of momentum with a moving wheel surface normally results in higher velocities, with Anbarci et al. **(2013)** noting a reduced size of the wheel wake.

Other important questions regarding correct ground simulation for HGVs appear to have not yet been answered. For instance, the influence on the unsteady base wake aspects, such as bi-stability, pumping or shedding, remains largely unresolved.

2.5.2.4 Influence of crosswinds

On the road, the aerodynamics of a vehicle are affected not only by its forward velocity but also the relative wind, which is eliminated in wind tunnel experiments where the uniform flow typically creates zero-crosswind conditions. Such environments can significantly alter the vehicle's drag. Driving and crosswind speeds can, however, be combined to produce a single resultant air speed whose magnitude and direction can be used to replicate such conditions in the wind tunnel by varying the yaw angle. Understandably, this is limited by the difficulty to predict all possible real-life crosswind conditions. Götz and Mayr **(1998)** however, used a database of wind conditions at international airports consisting of frequencies, directions, and strengths of winds, to estimate the appropriate magnitude and yaw. The authors found that stronger wind forces of Beaufort 4 – 5 (12.5-24mph) occur relatively rarely, with the lighter wind being dominant for most of the year, establishing an adequate range of yaw angle to test the drag of HGVs to be within 0° – 14°. Based on such experiments at different yaw angles, the standard drag coefficient C_D can be replaced by a wind-averaged drag coefficient $\overline{C}_D$, which considers the probability of certain crosswinds. The appropriate method for estimating the wind-averaged drag coefficient is outlined within the SAE standard J1252 **(SAE International, 2012)**.

2.5.3 Typical models

The models used for automotive wind tunnel testing can generally be divided into three categories: simple bodies, basic car shapes, and production cars **(Le Good and Garry, 2004)**. The first two are mostly popular for general research purposes, with the latter typically used for more specific investigations. Simplified ground vehicle models typically reflect the overall vehicle silhouettes while omitting geometrical details. Over the years, the simplified models have proven incredibly useful, benefitting the research with uncomplicated setups and facilitation of rapid geometry modifications. These reference models have informed ground vehicle aerodynamics for many decades, being instrumental in building much of the current understanding of the governing phenomena **(Le Good and Garry, 2004)**. This section describes the three most popular simple body models used in ground vehicle research.

The Rover, or Windsor, model (**Fig. 2.29(a)**) was designed for investigations of principal shape effects on the flow-field and drag, encompassing most passenger car configurations **(Le Good and Garry, 2004)**. The adjustable base geometry allows backlight angle variations in the range of 0° – 40° with 5° increments, offering the possibility for both hatchback and sedan features to be investigated. With the long, slanted nose and relatively short roof, this model's aerodynamic characteristics at the forebody and base are normally closely correlated **(Perry, 2016)**, reflective of typical passenger cars. The disadvantage of this dependency, however, is that the isolation of the effects at different body levels may become difficult.

The dependency between upstream and downstream flow features can be alleviated by using the Ahmed body (**Fig. 2.29(b)**). First introduced by Ahmed, Ramm and Faltin **(1984)**, the Ahmed body is a squared cylinder with round front edges as well as a relatively long and straight forebody. This geometry allows the isolation of the front and rear effects, making it particularly useful for studying base wake characteristics and local drag reduction concepts. Similar to the Windsor body, typical backlight angles vary between 0° – 40° to facilitate various base configurations, such as hatchback or fastback, offering a possibility to investigate a wide range of rear flow-field characteristics **(Strachan, Knowles and Lawson, 2004)**. Extensive experimental evidence describing the aerodynamic features of the Ahmed reference model has also been shown to be useful for validation and development of appropriate numerical methods **(Le Good and Garry, 2004; Strachan, Knowles and Lawson, 2004)**.

The square-back variation of Ahmed body (0° backlight angle) has also been widely used to investigate the base wake characteristics typical to HGVs, resulting in the identification of many important phenomena. Nevertheless, in comparison to common automotive shapes, commercial vehicles differ significantly through inherently larger body lengths; an aspect which should not be ignored. This can be accommodated with the use of

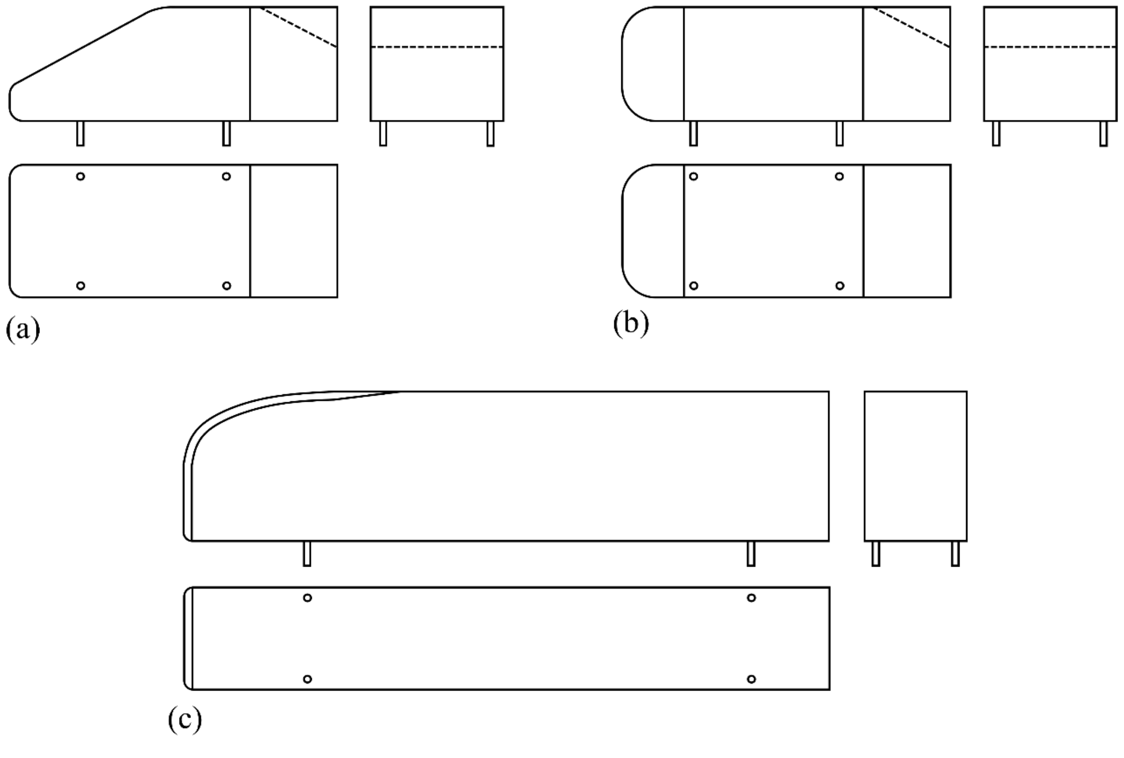

Fig. 2.29 Schematics of typical reference models: (a) Windsor body, (b) Ahmed body, (c) Ground Transportation System

the Ground Transportation System (GTS; **Fig. 2.29(c)**). In comparison with Windsor and Ahmed bodies, this model incorporates a less rounded front with a long body and square blunt base. It has been shown to produce flow-field features most typical to HGVs, with studies of Storms et al. **(2001)**, Ortega et al. **(2004)** and McArthur et al., **(2016)** all identifying many complex base wake characteristics, both experimentally and through computational simulations using this body.

2.5.4 Model mounting

A typical wind tunnel where moving air is forced over a stationary model produces a requirement for some form of mounting whose main purpose is to resist the generated loads. While they can often be helpful in measuring the forces on the body, their presence can also introduce some undesirable uncertainties. Among the most common effects are atypical changes to the surrounding flow-field, such as those occurring at the support-model junction, where the strut intersects the model's surface **(Simpson, 2001)**. Simpson **(2001)** studied such junction flows between planar surfaces and various obstructions, showing the stagnation at the leading edge of the obstruction to provoke the upstream surface boundary layer to separate. The subsequent rolling of the separated layer results in generation of horseshoe vortices, which wrap around the junction and propagate downstream. These vortices are normally smaller than the boundary layer thickness, with their strength increasing with the bluntness of the obstacle **(Simpson, 2001)**. Additionally, a secondary separation may also occur at the trailing edge of the obstacle, with Hetherington **(2006)**, who investigated similar effects on various mounting configurations, noting a significant localised momentum wake deficit caused by the support. This effect can be minimised through the use of aerodynamically streamlined struts. Reductions in strength of the horseshoe vortex can also be achieved by introducing fillets at the leading and trailing edges of the strut, or creating a small depression upstream **(Hetherington and Sims-Williams, 2004)**. Nevertheless, the distorted flow typically affects the model aerodynamics through increases in pressure and friction drag **(Hetherington, 2006)**.

Hetherington **(2006)** emphasised that the total forces measured on the model in the presence of a support strut are different from the measurements on a lone model, with similar logic also applicable to the loads on the support structure. Furthermore, the forces measured on the entire system, i.e., model with support, are usually higher than the sum of the individual components. These interference effects are normally corrected by means of separate model load measurements with the supports disconnected but remaining in close proximity **(Hetherington, 2006; Miao, Mack and Indinger, 2015; Wittmeier et al., 2016)**. Other methods also include combining wind tunnel and computational simulations to provide similar estimates **(Zhang et al., 2013)**.

Over the years, many different methods have been developed, each having their own advantages and disadvantages, with a particular technique normally selected based on its suitability for individual conditions and goals. Testing ground vehicles to the utmost fidelity is particularly unique, normally requiring both relative ground movement and wheel rotation, which tends to limit available options. Among the most popular model-mounting configurations are top, side, or ventral supports. These are discussed in the following sections, with other, less common, concepts considered thereafter. Finally, the last subsection considers the aspects of mounting position relative to the test section.

2.5.4.1 Top

One of the most common concepts is mounting from above **(Duell and George, 1993; Geropp and Odenthal, 2000; Hetherington and Sims-Williams, 2004, 2006; Strachan, Knowles and Lawson, 2004, 2007; Garry and Le Good, 2005; Strachan et al., 2012)**. This method typically consists of an aerodynamically streamlined strut, often aerofoil-shaped, fixed to the model's roof; as presented in **Fig. 2.30**. The implementation is generally uncomplicated, with such struts normally easily connected to an internal or external measurement balance. One of the important aspects of this arrangement is the ability to facilitate both full-width moving ground use and wheel rotation, making this technique popular within the motorsport industry. Among the disadvantages is typically high flow interference within the upper model portions, and subsequent contamination of the downstream flow-field. Directly ahead and behind of a top strut on the model's roof, Page et al. **(2002)** showed erroneous modifications to the pressure coefficient of up to $\Delta Cp = -0.1$, reflecting the upstream and downstream separation forced by the junction flow. Additionally, on an Ahmed body with a 25° backlight angle, Strachan, Knowles and Lawson **(2004)** noted a significant velocity deficit ($u^{*} \approx 0.95$) extending up to one model length downstream of the model base. Likewise, on a similar model, Strachan, Knowles and

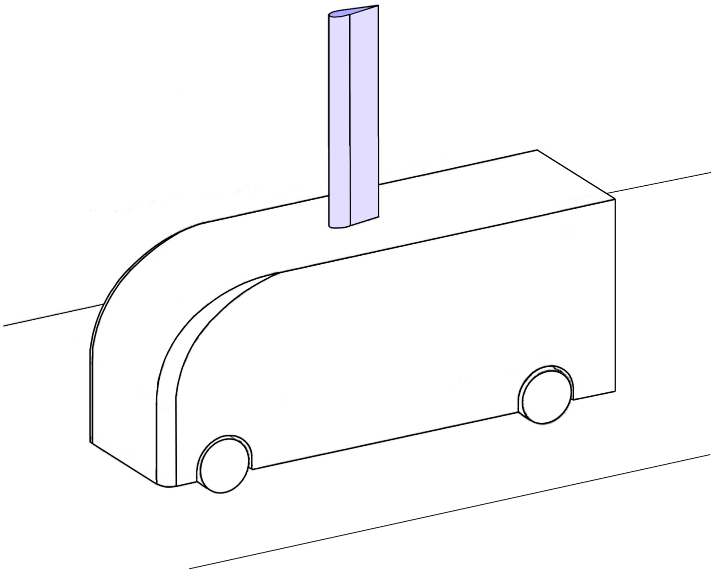

Fig. 2.30 Schematic of a setup using a top aerodynamic strut

Lawson **(2007)** showed the top strut's wake to reduce the suction in the backlight region, resulting in the generation of weaker (C-pillar) corner vortices and premature bursting of the separation bubble. The authors also noted a local central increase in downwash, attributed to the strut-model horseshoe vortex and preventing normal boundary layer development downstream of the support. Similar variations in the trailing edge separation features were also reported by Hetherington **(2006)** on a passenger car model, with results also showing changes to the rear deflector performance. In this case, the deflector was found to both decrease drag in the absence of the top strut, and increase it when the support was used.

Overall, Hetherington and Sims-Williams **(2006)** showed hatchback passenger car configurations to be particularly sensitive to these effects, with up to 7.5% and 28.2% increases in drag and lift coefficients, respectively. Notchback, fastback and motorsport configurations were shown less susceptible, with drag and lift changes limited to within 1 – 3% **(Hetherington, 2006; Miao, Mack and Indinger, 2015)** and 5% **(Hetherington and Sims-Williams, 2006)**, respectively. Hetherington and Sims-Williams **(2006)** also showed the primary source of these changes to vary between model configurations, with the increase in drag for notchback vehicles originating largely from the junction flow, while for hatchbacks the support wake and consequent interactions with downstream flow were the principal contributor.

Furthermore, the aerofoil-like cross-section of typical overhead struts can incorrectly alter the direction of the exiting flow when yawed **(Page et al., 2002)**, forcing it to be strut-parallel and thus, introducing additional uncertainties. Increasing projected frontal area with increasing yaw angle would also result in higher loads, making them less suitable for these types of studies. Haque et al. **(2017)**, who conducted similar investigations using various strut geometries and variable yaw, indicated the use of a diamond-shaped strut to be most beneficial for minimising the impact on the lift coefficient.

2.5.4.2 Side

Another popular mounting type is from the sides. These supports normally consist of lateral struts fixed to the wheel hubs **(Hetherington and Sims-Williams, 2004, 2006; Christoffersen, Landström and Walker, 2010; Mack et al., 2012)**, with some cases of underbody fixtures **(Walter et al., 2012; Gleason et al., 2015; Guzman et al., 2017)**; examples presented in **Fig. 2.31**. As with the top support, the main advantages of this method include the facilitation of a full-width moving ground use and wheel rotation. Additionally, this method has been shown to have less effect on model drag **(Hetherington, 2006)**. Miao, Mack and Indinger **(2015)** reported drag coefficient increases on a notchback passenger car model with both fixed and moving ground use limited to 2%. For the hatchback configuration and stationary ground, drag increased by 1.4%, with results using a moving ground only marginally more significant (1.7%). The influence of front and rear wheel strut pairs was also found not additive, suggesting further interactions occur between the two **(Miao, Mack and Indinger, 2015)**. The small influence on drag was attributed by Hetherington and Sims-Williams **(2006)** to the position of the side struts, being typically located in an already highly turbulent flow where the local effects, such as junction flow, are minimised.

Nevertheless, for motorsport configurations, which remain sensitive to lift and downforce, increases in the lift coefficient of up to 8.3% have been reported **(Hetherington and Sims-Williams, 2006)**. For notchback passenger cars, likewise, Hetherington and Sims-Williams **(2004)** showed lift discrepancies of up to 4.1%. The authors also showed the front wheel strut pair to contribute less to the lift increase (1%) in comparison with the rear pair (2.4%), as well as highlighting the influences not to be additive. Additionally, Miao, Mack and Indinger **(2015)** reported these variations in the lift to be dependent on the ground simulation, resulting in lift and downforce increases with stationary and moving ground use, respectively.

Hetherington **(2006)** conducted a detailed investigation of such setups and concluded that the significant impact on vehicle lift originates from the side strut's wake impinging on the model's sides and affecting the pressure at the underbody. Along the upper vehicle portions, no significant impact on the flow-field was also identified **(Hetherington, 2006; Hetherington and Sims-Williams, 2006)**. Further, more localised, flow-field modifications were also noted in the study of an isolated wheel mounted on a lateral strut by Knowles, Saddington and Knowles **(2002)**, who found the vortex normally shed at the wheel hub to be suppressed on the side on the mounting. Additionally, on a Formula One car model with hub-fixed struts, Knowles, Saddington and Knowles **(2013)** showed notable reductions in the areas of high turbulence intensity within the wheel wake, weakening local diffusion and mixing further downstream.

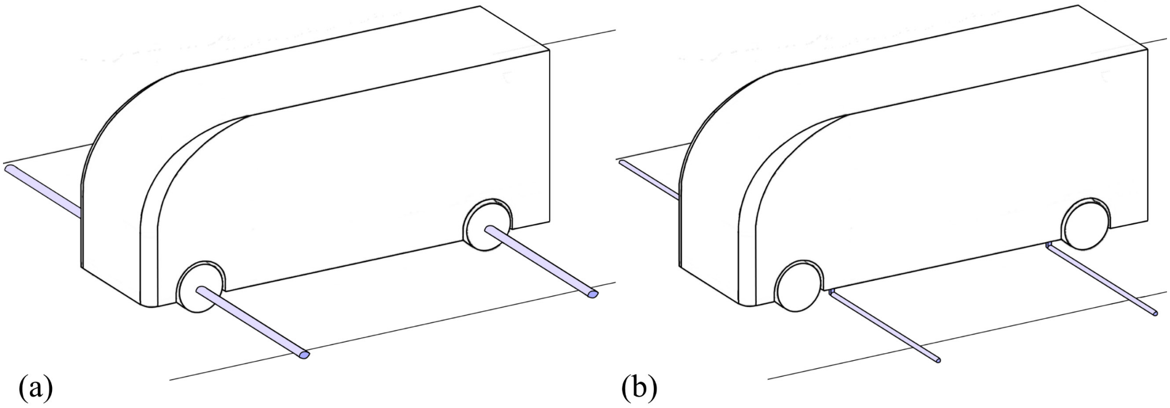

Fig. 2.31 Schematics of side mounting fixed to: (a) wheel hubs, (b) underbody

Combinations of both, top and side struts (**Fig. 2.32**) have also been popular **(Burgin, Adey and Beatham, 1986; Page et al., 2002; Hetherington and Sims-Williams, 2004, 2006; Christoffersen, Landström and Walker, 2010; Mack et al., 2012)**. These are usually used in cases where the wheels are not part of the body, with the top strut supporting the chassis, and the side struts, the wheels. For this reason, such configurations are typically associated with complex experimental setups and difficulty testing at variable yaw **(Page et al., 2002)**. Hetherington and Sims-Williams **(2006)** showed the influence of such a setup on drag and lift variations to extend to 6.9% and 15.8%, respectively. Interestingly, the effects of such a combination were shown to not be summative (top and sides separately) for most vehicle configurations, reflecting additional interactions which occur under such conditions and the necessity to examine the full setup for correct evaluation **(Hetherington, 2006)**. Additionally, Mack et al. **(2012)** also observed increases in static pressure of up to ΔCp=0.008 along the test section centreline upstream and downstream of the vehicle in a similar configuration.

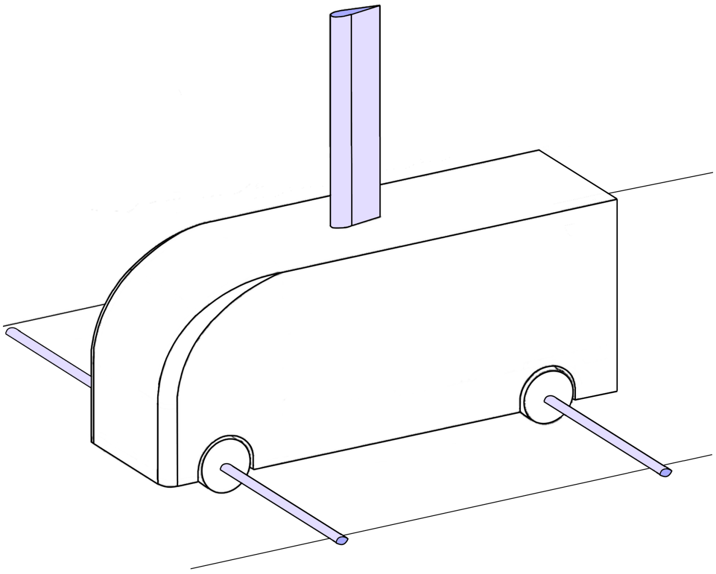

Fig. 2.32 Schematic of a setup combining the use of top and side mounting struts

2.5.4.3 Ventral

Mounting from underneath (**Fig. 2.33**) is especially popular in studies of commercial vehicles **(Fago, Lindner and Mahrenholtz, 1991; B. L. Storms et al., 2001; Coon and Visser, 2004; Storms et al., 2005; Van Raemdonck and Van Tooren, 2008; McArthur et al., 2016; Lo and Kontis, 2017)**. This method allows for easy measurements of vehicle forces and moments, with the bottom support typically fixed directly to an underfloor balance. One significant advantage of this technique is better facilitation of variable yaw studies, with the body normally fixed to a built-in turntable **(Storms et al., 2001)**, and little effect on the resultant flow. Far less material exists regarding the effects of ventral techniques on the flow-field. This is perhaps due to the general understanding that their effects on the overall model aerodynamics are minimised since they are placed in an already turbulent region of the body. Logically however, this technique is not suitable for studies concerned with underbody flow features. Additionally, the method normally precludes the use of moving ground and is commonly used in combination with the raised model setup (shown in **Fig. 2.27**). In some cases, where the supports can be placed further apart, narrow belts are used **(Leuschen, 2013)**, but these naturally span less than the model's width, compromising the accuracy of the results **(Hetherington, 2006)**. In those instances, isolated wheel rotation may also be provided through internal or external drivers **(Le Good et al., 1998; Elofsson and Bannister, 2002; Christoffersen, Landström and Walker, 2010)**. More recent setup configurations also include multi-belt facilities **(Wiedemann and Potthoff, 2003; Wittmeier et al., 2016)**, which combine the central narrow belt with smaller strips located underneath the wheels. In such cases however, the support struts are typically positioned in line with the wheels, making assessments of this area particularly difficult **(Tortosa et al., 2017)**. In the study by Tortosa et al. **(2017)**, a facility was described, where this can be alleviated by means of shifting the longitudinal position of the restraint posts between upstream and downstream of the wheel, depending on the needs. For HGVs, however, this is less suitable given their inherently large lengths.

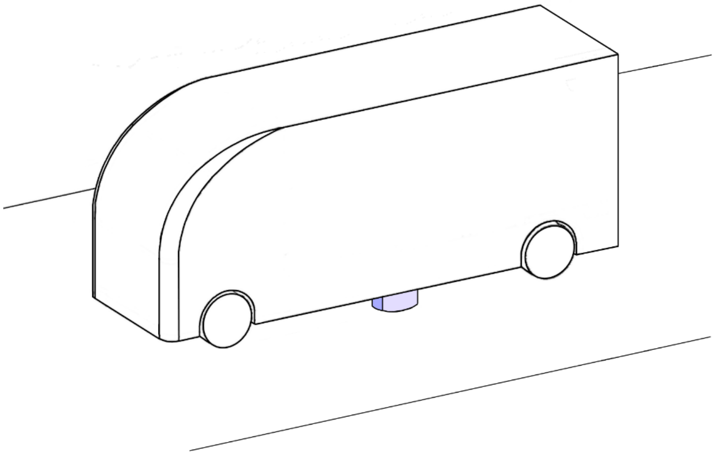

Fig. 2.33 Schematic of a ventral mounting configuration

2.5.4.4 Rear

Within the aerospace industry, types of tail mounting are some of the most popular support methods. However, they can be difficult to implement due to the proximity to some important control surfaces. The horizontal tail may be particularly affected, with the adjacent support sting altering the pressure distribution and resulting in incorrectly predicted pitching moments **(Cartieri et al., 2010; Ocokoljić, Rašuo and Kozić, 2017; Waldmann, Lutz and Krämer, 2018)**. Mercker and Knape **(1989)** showed that ground vehicles may also be adversely impacted in a similar way. On a passenger car model, a similar back sting entering at an angle through the rear window was shown to reduce model drag by up to 4% **(Mercker and Knape, 1989)**. Page et al. **(2002)** however, argued the opposite, suggesting a horizontal rear sting (**Fig. 2.34**) to be advantageous for evaluating time-averaged aerodynamic data, with changes in the base pressure coefficient limited to $|\Delta Cp| = 0.005$. Minimal flow interference was inferred as a result of placing the support in the highly turbulent base wake **(Page et al., 2002)**. Nevertheless, while this technique may be suitable for passenger or motorsport car configurations **(Page et al., 2002)**, the base wakes of square-back geometries are dominated by large-scale unsteady structures, which are often critical to determining the performance of many flow control concepts. Such stings, therefore, appear too intrusive for accurate reproduction of the normal base wake dynamics. Important aspects including vortex shedding and shear layer interaction are expected to be adversely affected.

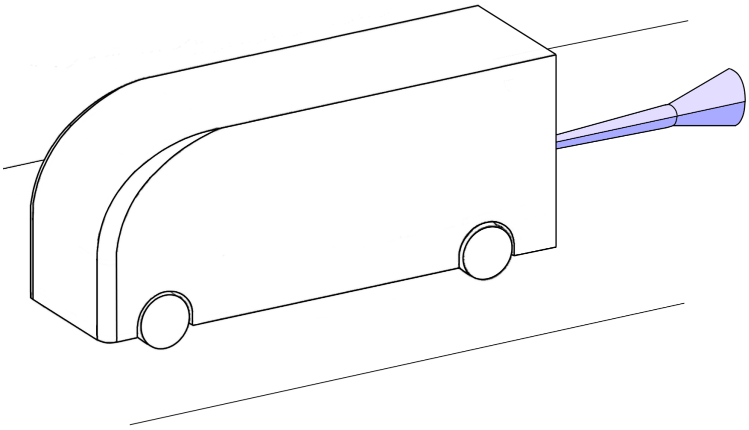

Fig. 2.34 Schematic of a horizontal rear sting mounting

2.5.4.5 Other techniques

More exotic concepts also exist but, for various reasons, they remain outside the mainstream use. One example is the concept of using magnetic levitation to suspend a model in air without a physical connection to the test section walls. Such systems began to appear over 50 years ago, with some early examples including the support of bullet-like rotating bodies **(Goodyer, Henderson and Judd, 1975)**. More recently, Muscroft, Sims-Williams and Cardwell **(2006)** successfully employed a similar system on a simplified body representative of a Formula One car chassis. Experimental details such as the inclusion of rotating wheels or moving ground, however, do not seem to be easily attainable. This technique appears very attractive, with the overwhelming advantage being the capability to rid the setup of any interference effects. In practice however, there continues to remain a lot of complications which prevent easy implementation, with some likely reasons for this method not having yet gained widespread use being the high initial cost and power requirements **(Kawamura and Mizota, 2013)**.

Another less common method is mounting at the front or upstream. One of the first examples of this technique was using a rigid aircraft towline to simulate free-flight **(Schneider, 1955)**. Nowadays however, this approach appears largely forgotten. Among the possible reasons for this, could be the expectation that a mounting sting placed upstream of the model may result in significant interference and contamination of the downstream flow. While this is of course a possibility, the research suggests that most mounting methods result in some types of adverse effects. From the literature, it can also be inferred that, with careful placement, the disturbances could be directed into the underbody where their influence would be minimised. For such a configuration, the possibility for moving ground use remains, as does the wheel rotation. Unhindered access to the base wake would also be available, allowing the interrogation of the region on which primary performance metrics fundamentally depend. Additionally, while other complex mounting systems may contribute significantly to the setup's solid blockage, a front sting is expected to minimise this influence. Placing the mounting structure at the front appears a promising method for ground vehicle studies, having the potential of providing a more favourable environment for the replication of true aerodynamic performance.

2.5.4.6 Model position

One requirement common to all mounting configurations is the provision of fixed model position. It is commonly accepted that laterally, ground vehicle models be placed along the test section centreline to prevent erroneous asymmetry in the flow conditions, however, the effects of the longitudinal position appear generally disregarded. This may be less important for low-blockage setups, where typically the model constitutes only a small portion of the test section volume and is normally placed in the centre. However, the effects may become more severe with increasing blockage ratios, common to many HGV studies.

Garry et al. **(1994)** investigated the relationship between the position of the model's base relative to the end of the test section, and the characteristics of the flow. Here, the end of the test section is marked by the leading edge of the diffuser. They reported that in cases where this distance is not sufficiently long, errors in the drag coefficient may be as high as 10 – 20%, depending on the specific model geometry. The differences are attributed to changes in the base pressure caused by the proximity to the diffuser's pressure field. The authors recommended that for a distance x between the base and test section end, the ratio of $x/\sqrt{\mathrm{A}}$, where A is the base area (or model frontal area), should ideally exceed 4, and most definitely not fall below 2.

Chapter 3

Thesis aims and objectives

The literature review revealed that most base pressure drag reduction concepts for ground vehicles remain unrealisable. For this reason, the base region continues to contribute a large portion of aerodynamic drag on most HGVs on roads today. A review of the characteristics of lobed mixers, typical of the aerospace field, suggests these geometries to have the potential for this application. The aim of this thesis, therefore, is to apply a lobed mixer geometry as a flow control method to be used for the base pressure drag reduction of ground vehicles. Additionally, the literature remains inconclusive regarding the accurate experimental setup arrangements for these types of vehicles. Part of this thesis aims to assess the need for moving ground and the appropriate mounting configuration for the model used.

Specific objectives include:

- Optimisation of the experimental setup, including:
  - Assessment of the moving ground facility
  - Assessment of appropriate wind tunnel model-mounting techniques
  - Baseline model geometry optimisation
- Initial assessment of lobed mixers for drag reduction of boat-tailed ground vehicles
- Detailed study of trailing edge-integrated lobed mixer geometries:
  - Assessment of the impact of lobe pitch
  - Assessment of the impact of penetration angle
  - Assessment of the effects of “non-linear” configurations
  - Identification of the mechanisms responsible for drag reduction

Chapter 4

Experimental setup and procedures

All results presented in this thesis are obtained through experimental wind tunnel testing. Throughout the experimental campaign, numerous variables are measured and compiled in order to meet the set objectives. Three main tools are selected for this purpose:

- load measurements – for the evaluation of drag forces of various configurations,
- hot-wire anemometry – for the assessment of velocities within the model flow-field,
- pressure measurements – for the assessment of surface pressures across the model base.

The following sections discuss in detail the methodology, procedures and parameters selected for the experiments.

4.1 Brunel University wind tunnel

All experiments are conducted in the Brunel University Ground Research Facility, presented in **Fig. 4.1**. It is an open-circuit wind tunnel with a closed test section measuring 1.3m long, 0.46m wide, and 0.36m high. Access to the test section is provided from the sides and top through removable acrylic windows. With an empty section, freestream velocities of up to U_∞ = 40m/s can be achieved. The wind speed is adjusted manually and monitored by a Furness Controls Ltd FCO510 micromanometer to within ±1m/s. Freestream uniformity, turbulence intensity, and heightwise velocity consistency at a central position within the empty test section are ±1%, 0.5%, and ±1%, respectively.

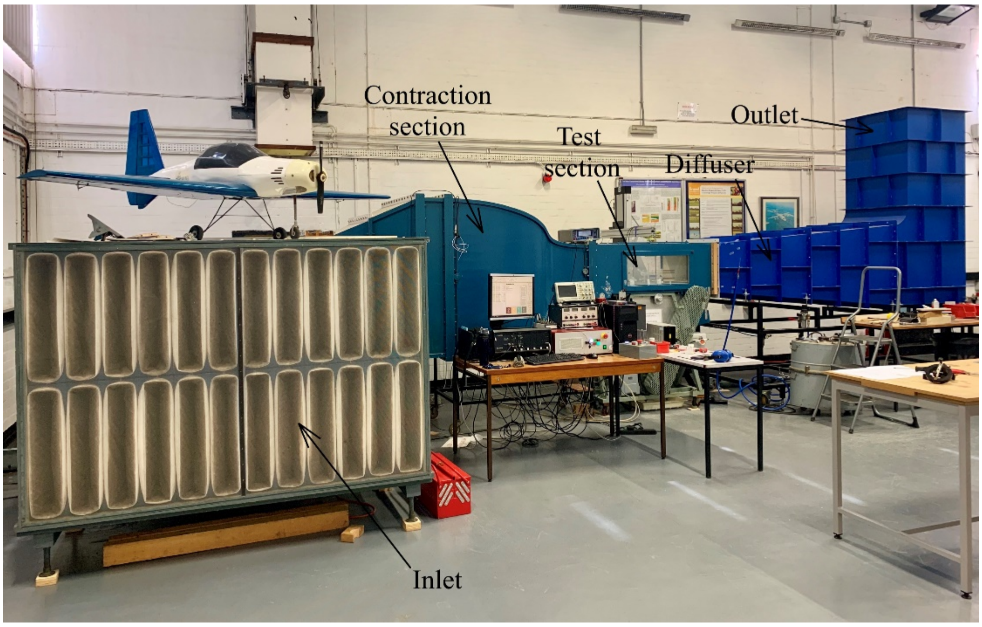

Fig. 4.1 Brunel University wind tunnel facility

4.1.1 Coordinate system

The coordinate system adopted for all experiments is such that the origin is placed along the test section centreline, on the floor, level with the model base. Streamwise, lateral and vertical directions are denoted by X, Y and Z, respectively (**Fig. 4.2**). All positions are presented in line with these coordinates and normalised by model width (W), such that x*=X/W, y*=Y/W and z*=Z/W. The velocity components corresponding to X, Y and Z directions are denoted as u, v and ω, respectively. Results are presented as velocities normalised by the freestream velocity of the flow (U_∞), such that $u^*=u/U_\infty$, $v^*=v/U_\infty$ and $\omega^*= \omega/U_\infty$.

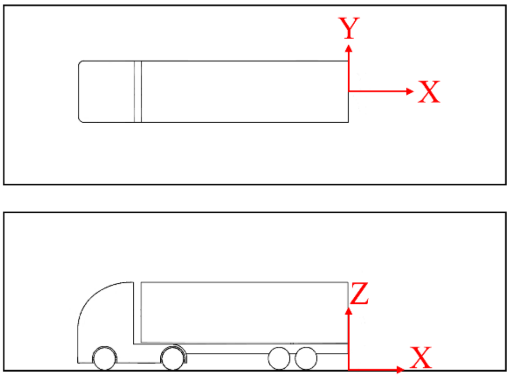

Fig. 4.2 Experimental coordinate system

4.1.2 Ground simulation

A rolling belt with a width of 0.36m is used to simulate the influence of moving ground and suppress the boundary layer formation on the test section floor; a schematic is shown in **Fig. 4.3**. When operating, the speed of the belt is manually matched to the freestream within ±1 m/s, with the moving ground precipitating rotation of the model's wheels (see **Section 4.2**). To prevent inadvertent lifting when operating, suction is applied through a perforated plate located underneath the moving belt; **Fig. 4.4(a)** shows the locations of the holes on the plate. The holes are connected to the vacuum through silicon tubing, as presented in **Fig. 4.4(b)**. The design of the setup allows the supply of suction to selected parts of the floor, with most suction directed to the sides and rear of the model. A steady stream of air is also applied directly underneath the model wheels to avoid premature belt damage; especially important during long periods of operation. To facilitate better heat rejection, cooling water is circulated throughout the perforated plate, as shown in **Fig. 4.4(a)**. The setup is driven by a 3kW AC motor and monitored by LabVIEW control software.

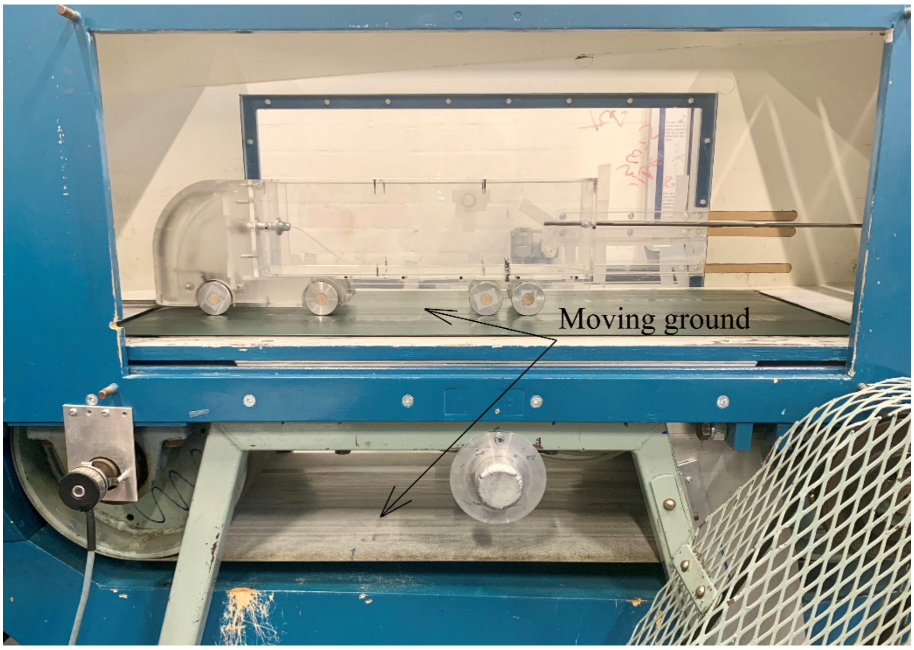

Fig. 4.3 Moving ground system in the Brunel University wind tunnel

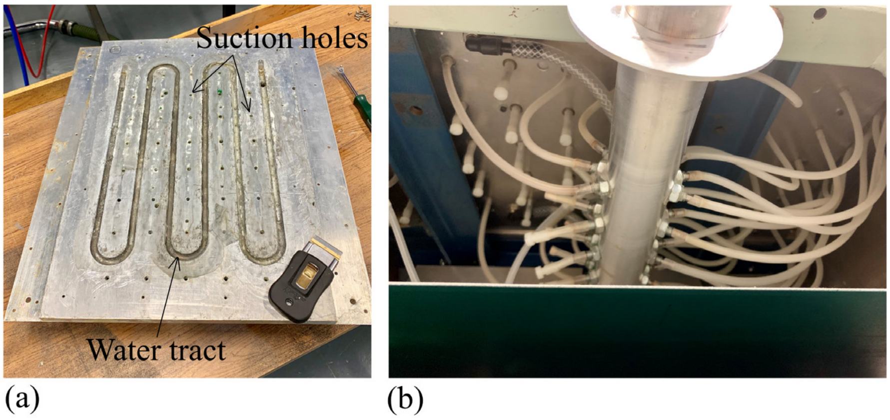

Fig. 4.4 Elements of the moving ground system: (a) bottom plate, (b) suction lines

The wind tunnel is also equipped with a front flow splitter installed in the test section to remove the upstream boundary layer. Perforated holes on the top splitter surface allow the application of suction to further aid boundary layer suppression. The resultant velocity profile in a central location of the empty test section is presented in **Fig. 4.5**, including the variation with both, moving and stationary ground conditions.

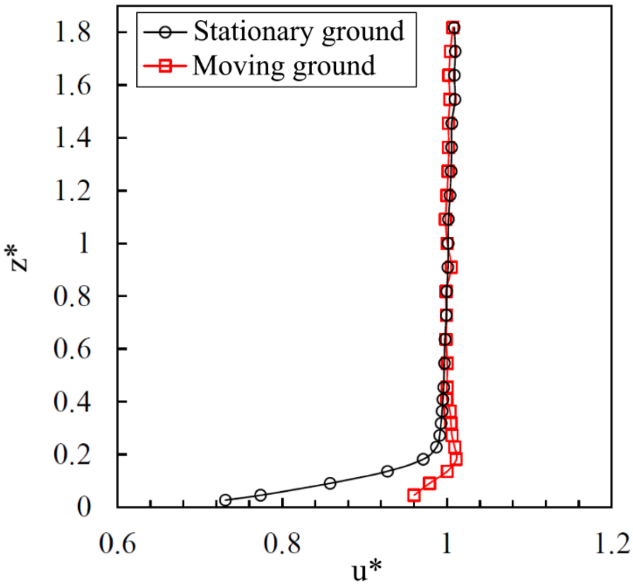

Fig. 4.5 Velocity profile at a central position in the empty test section of Brunel University wind tunnel

4.2 Baseline models

Over the course of the testing programme, two baseline models are used in the different experimental phases. The characteristics of both models are described in the following subsections.

4.2.1 Baseline 1

The first model used is a pre-existing simplified 1/24th-scale model shown in **Fig. 4.6**. This baseline profile is based on the GTS (see **Section 2.5.3**), representative of a HGV, neglecting fine details and incorporating a front face with round leading corners. The model is constructed in two parts: a tractor and trailer bottom section, and the trailer. Overall dimensions are 500mm long (L), 156mm high (H), and 110mm wide (W). The trailer is attached to the tractor as a separate section via a load cell and sliding contacts to allow the trailer to "free-float" on the bottom section. This particular configuration is selected to allow measurements of isolated drag of the trailer, and the tractor and trailer bottom. The tractor-trailer gap chosen is relatively small (0.13W) to minimise any possible development of significant unsteadiness unrelated to the base wake, which could contaminate the load cell signal. The model is made from Perspex and Aluminium with fully rotating wheels. All wheels are mounted on steel axles with installed bearings to ensure smooth rotation.

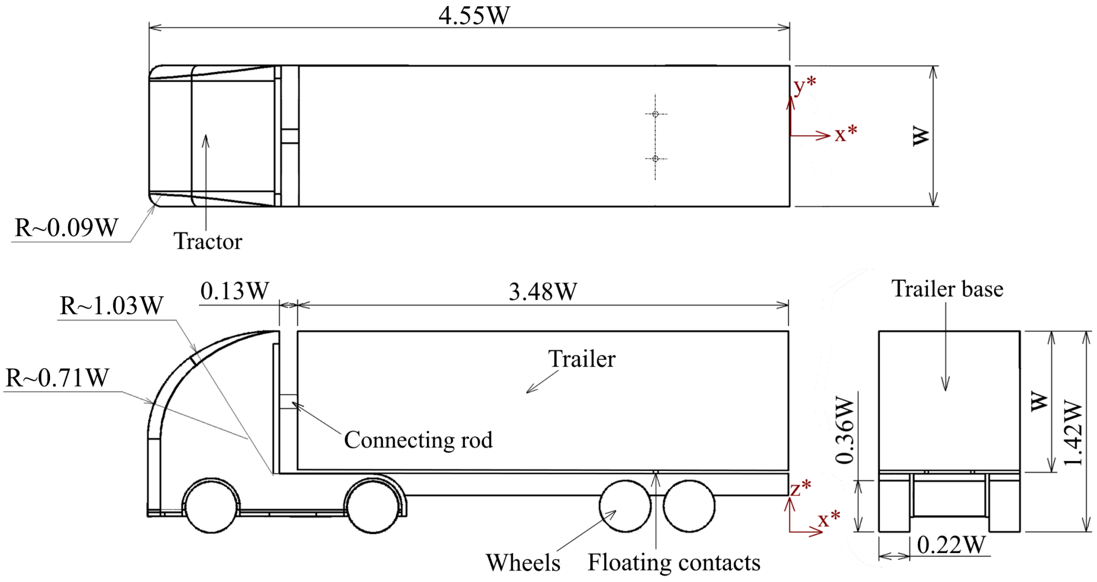

Fig. 4.6 Schematic of Baseline 1

This model is used as the baseline in the preliminary assessment of lobed mixers (**Chapter 7**). The same model is also employed in the assessment of the moving ground facility and model-mounting techniques (**Chapters 5** and **6**).

All tests using Baseline 1 are conducted at the maximum freestream velocity of $U_\infty = 30$ m/s, resulting in a Reynolds number based on body width of

$$Re_W = \frac{\rho U_\infty W}{\mu} = 2.3 \times 10^5 \qquad (4.1).$$

To ensure the utmost accuracy, a Reynolds number sensitivity study is conducted. Experiments on Baseline 1 include moving and stationary ground use; therefore, the results presented in **Fig. 4.7** show the variation for both conditions. **Figure 4.7** shows that beyond $Re_W = 2.0 \times 10^5$ the measured total (C_{DM}) and trailer (C_{DT}) drag coefficients are largely insensitive to further increases. Note that the drag coefficients presented in **Fig. 4.7** are not corrected for blockage effects (read more in **Section 4.8**).

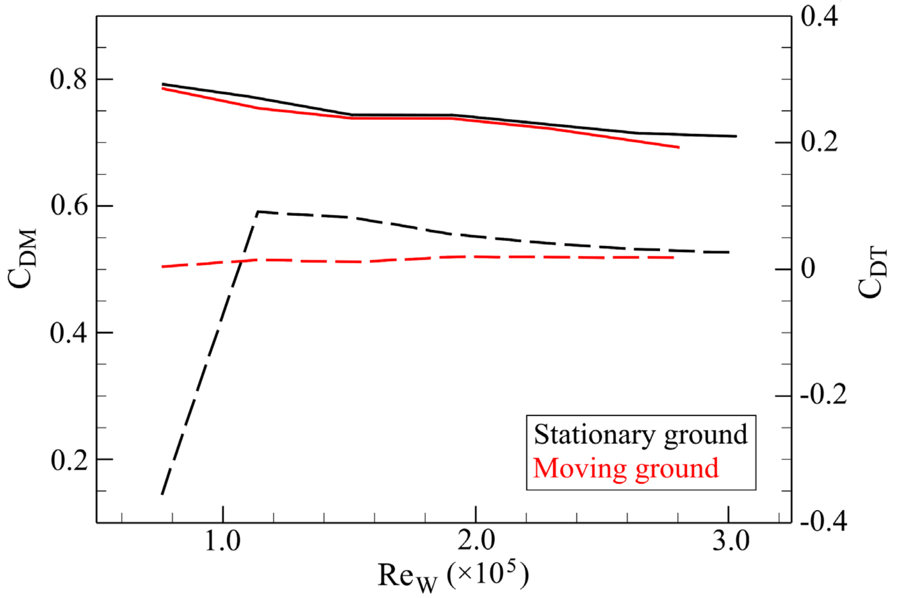

Fig. 4.7 Variation of drag coefficient with Reynold number for Baseline 1; C_{DM} (solid line), C_{DT} (dashed line)

Inside the test section, the model is positioned laterally in the centre with the front face 0.36m downstream of the upstream splitter. In this configuration, the distance from the model base to the end of the test section is 0.44m. This separation is sufficient ($x/\sqrt{A} = 3.34$ – see **Section 2.5.4.6**) to prevent any effects of the diffuser pressure field on the flow-field of the model **(Garry et al., 1994)**.

4.2.2 Baseline 2

A new model was designed and manufactured as part of the experimental setup optimisation. This baseline is used in the experiments conducted on the trailing edge-integrated lobed mixers (**Chapter 8**). While keeping the same scale and main body features, this revised model incorporates a more streamlined front profile in an effort to minimise the influence of any potential upstream flow separation on the conditions measured at the base.

4.2.2.1 Design process

The tractor of Baseline 2 is designed to the criteria described by Tropea, Yarin and Foss **(2007)**. They reported that for long bluff bodies, such as HGVs, the front corner radius has an optimum value, which is dependent on the Reynolds number of the flow. The relation which can help to either select an appropriate flow velocity, or based on available facility, adjust the front radius to optimum, has been derived as **(Tropea, Yarin and Foss 2007)**:

$$\mathrm{Re} = \frac{\rho U_{\infty} \times r_{opt}}{\mu} = 1.3 \times 10^{5} \qquad (4.2)$$

where r_{opt} is the minimum radius required to avoid upstream separation.

In order to keep the width and height of Baseline 2 identical to Baseline 1, the maximum achievable front corner radius for the revised tractor is estimated as $R^* = 0.44$, with the top radius of up to $R^* = 0.79$; these limits being imposed by the overall experimental constraints. Based on the relationship in equation 4.2, the optimum freestream velocity for such a model is $U_{\infty} \geq 40$ m/s. With this optimised model, freestream velocity of up to $U_{\infty} =$ 37 m/s is achievable. All experiments using Baseline 2 are conducted at this maximum velocity, resulting in a flow Reynolds number of $\mathrm{Re}_W = 2.8 \times 10^5$. Although this is marginally lower than the optimal $U_{\infty} = 40$ m/s indicated by equation 4.2, due to the solid blockage, the real velocity around the model profile is expected to reach $u = 41$ m/s. This is, therefore, anticipated to be sufficient to produce the desired characteristics (explored further in **Section 4.2.2.2**).

Baseline 2 is constructed in a similar way to Baseline 1, with the two main sections being the tractor and trailer bottom, and the trailer. **Figure 4.8** presents the model schematic with the overall dimensions: L = 535mm, H = 156mm and W = 110mm. The model chassis

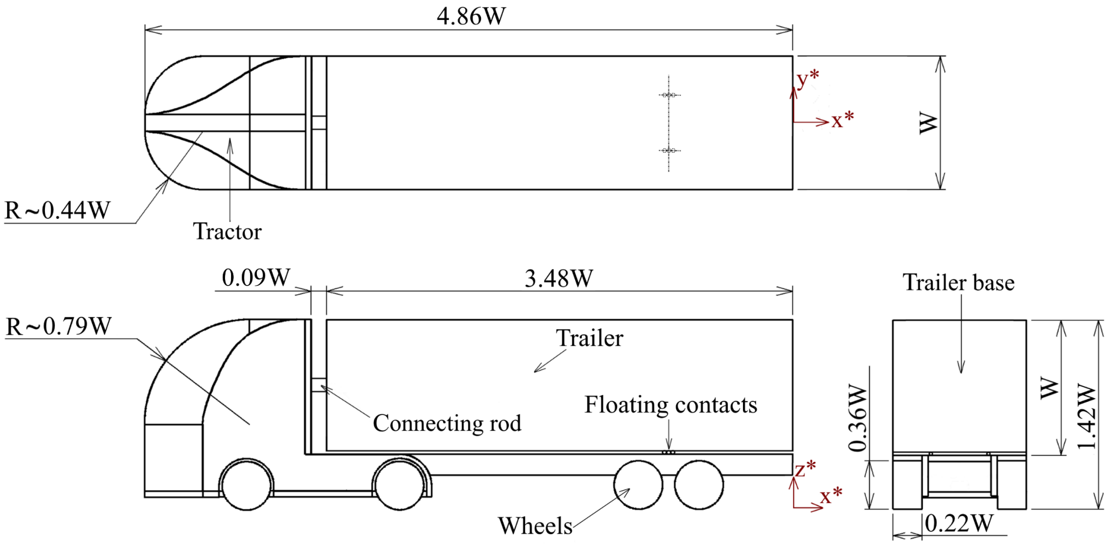

Fig. 4.8 Schematic of Baseline 2

components are designed using Computer Aided Design (CAD) software and manufactured out of Perspex, employing a combination of laser cutting and Computer Numerical Control (CNC) machining techniques. The new tractor is constructed as an empty shell consisting of five main parts: two symmetric sides with a joining centre-rib as well as bottom and back plates. This design, presented in **Fig. 4.9**, enables the placement of the primary load cell (**Section 4.5.1**) and accompanying electronics, as well as the mounting fixture (**Section 4.3.3**) inside the tractor.

Similar to Baseline 1, the trailer of Baseline 2 is attached to the tractor through a connecting rod fixed to the load cell located inside. The tractor-trailer gap remains small at 0.09W. The trailer is again "free-floating", with the sliding contacts toward the rear

Fig. 4.9 Photographs of the empty outside shell of the tractor of Baseline 2

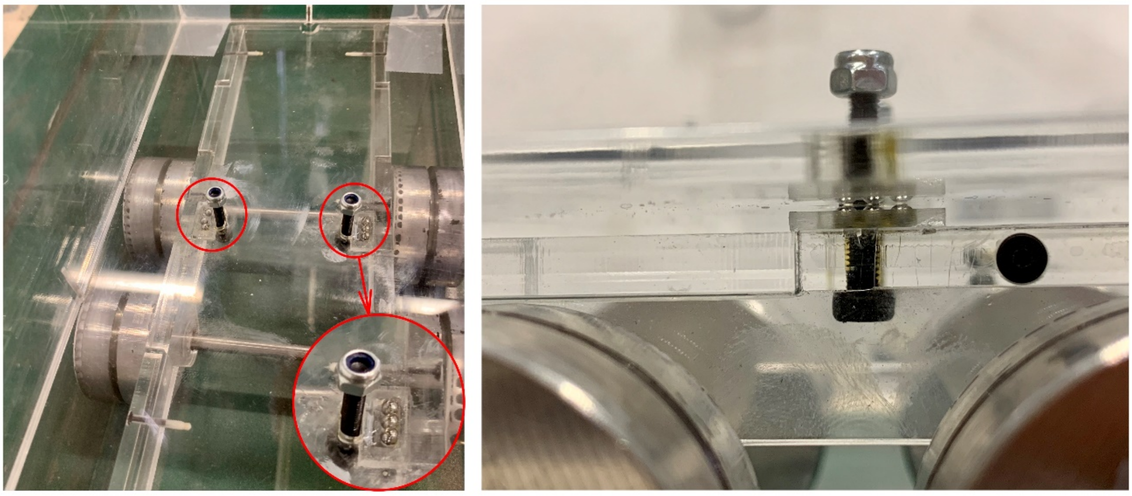

Fig. 4.10 Photographs of the new sliding contacts

improved for the new model. Each of the new sliding contacts consists of three steel ball bearings encased in a frame attached to the underbody section, with the trailer body resting on top (presented in **Fig. 4.10**). This design provides a minimum surface contact between the trailer and the bottom section, subsequently minimising any resistance on the trailer. The neighbouring bolts, seen in **Fig. 4.10**, extend up through the openings in the trailer bottom, making no contact with the surface. They are used to ensure the trailer remains in place in case of any crosswise instability inducing sideways movement. The final assembled model includes four sets of fully rotating aluminium wheels fixed on steel axels. All wheels are equipped with bearings. A photograph of Baseline 2 is presented in **Fig. 4.11**.

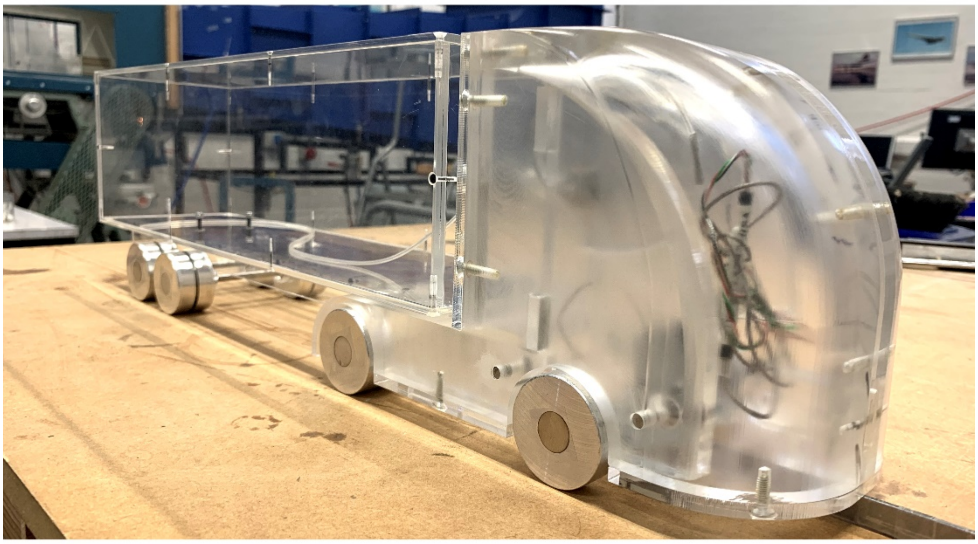

Fig. 4.11 Photograph of assembled Baseline 2

Baseline 2 is placed in the test section in the same position as Baseline 1; laterally central with the front face 0.36m downstream of the splitter. Although Baseline 2 is longer, the distance from its base to the end of the test section (0.405m) remains sufficiently large to prevent any adverse effects on the flow-field, with $x/\sqrt{A} = 3.07$ **(Garry et al., 1994)**.

4.2.2.2 Flow properties

Boundary layer profiles are assessed at central locations of the top and side (left and right) trailer surfaces, 5mm upstream of the trailing edges. Along the top, the closest measurement point is located $\Delta z^* \approx 0.018$ away from the surface, with $\Delta y^* \approx 0.036$ at both left and right sides. The resulting profiles are presented in **Fig. 4.12**. All three profiles show excellent agreement, indicating near-uniform flow around the trailer. These characteristics are further evaluated with the boundary layer thickness (δ^{99}), displacement thickness (δ^*), momentum thickness (θ) and shape factor (H_{BL}). The first is defined as the distance between the surface and point within the profile where the local velocity reaches 99% of the asymptotic velocity. The remaining parameters are calculated using equations 4.3, 4.4. and 4.5 for incompressible flow. Note that equations 4.3 and 4.4 account for the change in velocity in the Y-direction; applicable to the profiles along the sides of the trailer. For the boundary layer over the trailer roof, this is replaced by considering the variation along the Z-axis. The dy and dz steps used in the equations 4.3 and 4.4 are indicated in **Fig. 4.12**, with n=19 for the profiles at the trailer sides (**Fig. 4.12(b, c)**) and n=20 for the roof profile (**Fig. 4.12(a)**).

$$\delta^* = \int_0^\infty \left(1 - \frac{u(y)}{U_\infty}\right) dy \;\approx\; \sum_{i=1}^{n} \left(1 - \frac{u(y)}{U_\infty}\right) \cdot dy \tag{4.3}$$

$$\theta = \int_0^\infty \frac{u(y)}{U_\infty} \left(1 - \frac{u(y)}{U_\infty}\right) dy \;\approx\; \sum_{i=1}^{n} \frac{u(y)}{U_\infty} \left(1 - \frac{u(y)}{U_\infty}\right) \cdot dy \tag{4.4}$$

$$H_{BL} = \delta^* / \theta \tag{4.5}$$

Boundary layer properties for all three profiles (**Fig. 4.12**) estimated this way are presented in **Table 4.1**. The boundary layer thickness is shown to be consistent around the trailer profile at $\delta^{99}/W \approx 0.08 \pm 0.01$. Importantly, the low shape factor values in **Table 4.1** indicate all three profiles are those of a turbulent boundary layer. This confirms the flow remains attached over the trailer surfaces, with no strong pressure gradients prior to the fixed separation at the trailing edges. It is important to note that because these parameters are estimated using discrete measurements, the provision of the largest spatial step (dy and dz) in the area of highest velocity gradients (near-wall region) as well as the finite size of the subsequent steps will result in degraded accuracy. Other sources of error may originate from the uncertainty in the position with respect to the wall and the position of the boundary layer edge, as described by Titchener, Colliss and Babinsky **(2015)**. The authors showed that for typical experimental aerodynamics, the error in the boundary layer integral parameters may be significant (up to 5%), with the region between the wall and the first measurement accounting for up to 90% of this uncertainty. Nevertheless, the data in **Table 4.1** is not corrected for this error, with the estimated parameters (**Table 4.1**) used solely to indicate the general state of the local boundary layer and not for detailed comparisons to other setups.

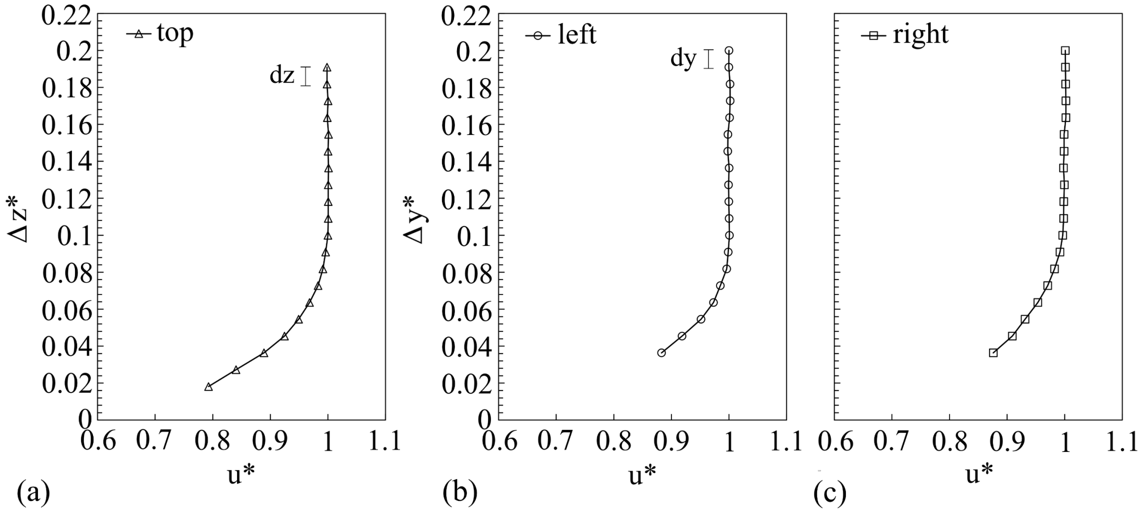

Fig. 4.12 Baseline 2 boundary layer profiles 5mm upstream of the trailing edges, along the centrelines of the three trailer surfaces: (a) top (roof), (b) left side and (c) right side

	δ^{99}	δ^*	θ	H_{BL}
top	0.08W	0.0079W	0.0067W	1.18
left	0.08W	0.0059W	0.0053W	1.11
right	0.09W	0.0069W	0.0062W	1.11

Table 4.1 Boundary layer properties for the three profiles presented in Fig. 4.12

A further assessment of the Baseline 2 characteristics is provided by the Reynolds number sensitivity study. Both, C_{DM} and C_{DT} within the range of $7.6 \times 10^4 < Re_W < 2.8 \times 10^5$ are presented in **Fig. 4.13**. All experiments conducted on Baseline 2 include the use of moving ground, therefore, the stationary ground condition is not considered in this Reynolds sweep. As can be seen, the study confirms that beyond $Re_W = 2.0 \times 10^5$ the drag coefficients of both total model and isolated trailer remain largely insensitive to further velocity increases.

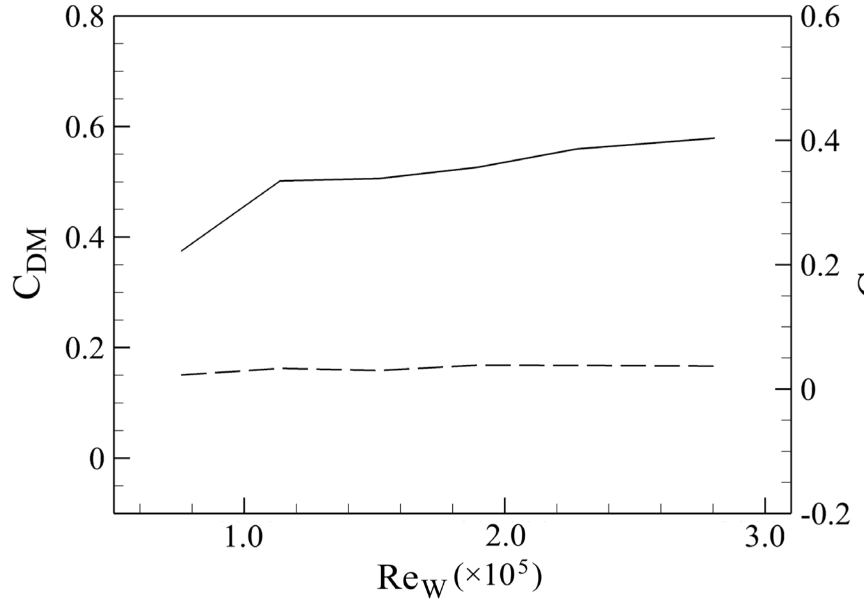

Fig. 4.13 Variation of drag coefficient with Reynold number for Baseline 2; C_{DM} (solid line), C_{DT} (dashed line)

4.3 Model mounting techniques

Throughout the experimental campaign, a total of four different model-mounting techniques are used. The following sections describe in detail the characteristics of each method and reasons for its use.

4.3.1 Side mounting

As part of the experimental setup optimisation, the effects of different mounting techniques on the model base flow-field are evaluated using Baseline 1. Among the commonly used methods discussed in **Section 2.5.4**, the side mounting appeared to be appropriate for similar ground vehicle models and was selected for this assessment. For this purpose, two steel rods of thickness = 0.03W are used to replace the front and aft wheel axles for sufficient model stability. Each rod is thin, resembling a square cylinder with rounded leading and trailing edges. This design is selected to minimise the total frontal area of the system as well as the size and strength of the wake shed from the supports. These struts extend horizontally from the wheel hubs to the test section side walls, where they are fixed to height-adjustable slots. This configuration is presented in **Fig. 4.14**. In this lateral support setup, the wheels remain fully rotating and connected to the model body. During the installation, the model is elevated marginally (0.01W) before being fixed in place. This ensures the wheels only make light contact with the ground, minimising the rolling resistance.

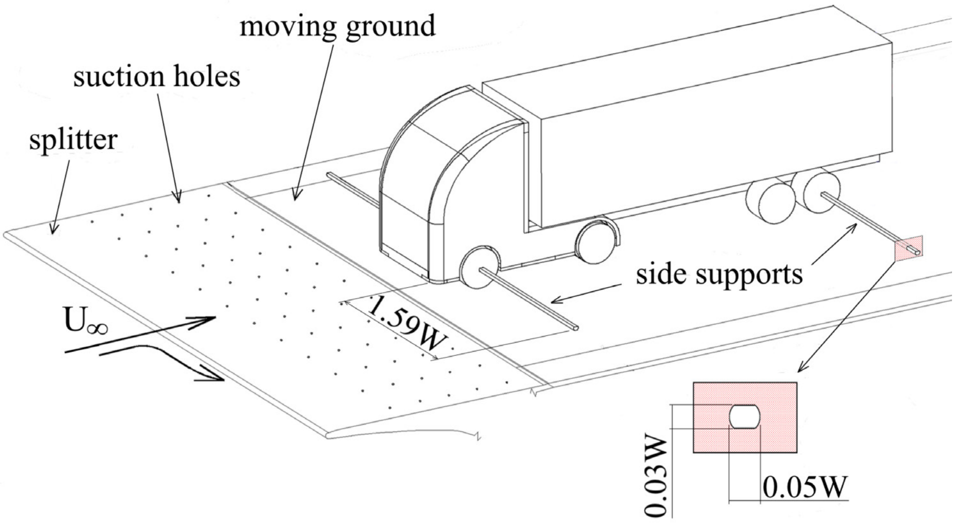

Fig. 4.14 Schematic of Baseline 1 in the side mounting configuration

4.3.2 Top mounting

Another model mounting method popular for studies of ground vehicles is from the top. In this thesis, a similar setup is considered and the effects on the base wake evaluated. Additionally, the top support configuration is also used for the assessment of the moving ground facility. This is selected to prevent the development of any possible near-floor interference interacting with the moving ground. In the top-mounted configuration, Baseline 1 is fixed inside the test section via a support strut affixed atop the trailer (**Fig. 4.15**). The support extends through the wind tunnel roof (length = 1.85W), where it is mounted externally to a horizontal substructure. The strut is aerodynamically streamlined to minimise the resulting wake and the potential horseshoe vortex developing at the support-model junction **(Hetherington, 2006)**. The aerofoil profile adopted is the same as that used by

Strachan, Knowles and Lawson **(2007)**, with the thickness-to-chord ratio of 0.25 (chord = 0.36W). The strut is positioned at the model centreline, Δx*=2.18 downstream of the tractor's front face. The entire support structure is height-adjustable, with the same positioning off the floor employed as that adopted for the side mounting.

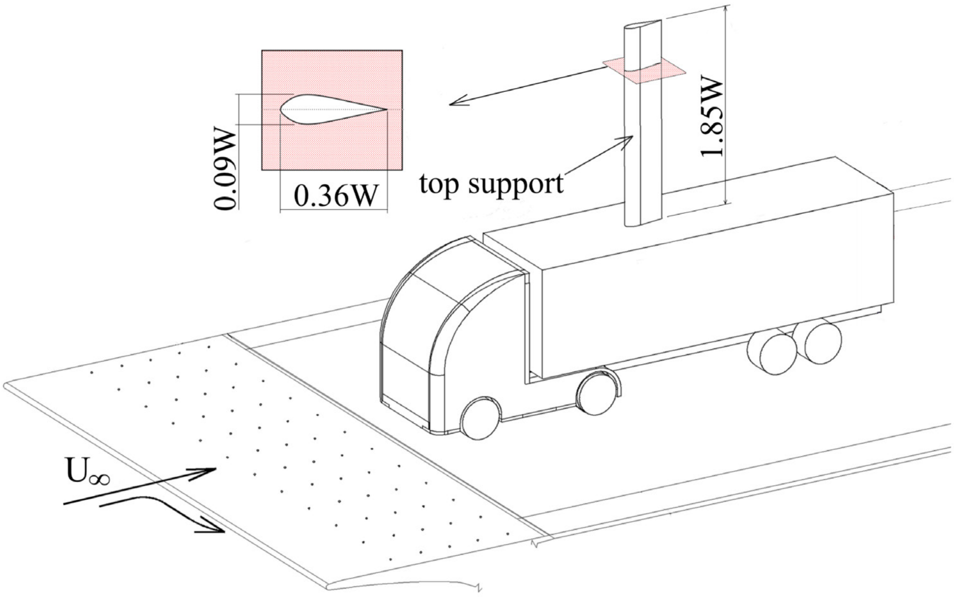

Fig. 4.15 Schematic of Baseline 1 in the top mounting configuration

4.3.3 Front mounting

A new method of upstream mounting is developed for the purpose of this thesis in an effort to minimise the impact of support interference on the base flow-field being studied. The review of the literature revealed that this method is not typical to ground vehicles, however, placing the support structure at the front appeared promising for studying the base wake. The first version of this technique is used in the initial assessment of lobed mixers (**Chapter 7**) in conjunction with Baseline 1. The design consists of two 90° steel supports mounted to the front of the tractor and fixed to the upstream flow splitter installed in the test section (see **Fig. 4.16**). Each sting is 0.02W wide and extends 1.05W in front of the model. The same off the floor installation technique is also maintained for this configuration.

Based on the excellent flow characteristic obtained in the initial assessment of lobed mixers (**Chapter 7**), the front mounting technique was developed further to consist of only a single steel support sting fixed centrally (**Fig. 4.17**). The support is attached to the underside of the tractor and extends out 1.05W in front of the model, where it is fixed to the test section floor. The sting is ensured to be sufficiently strong (thickness = 0.02W) while minimising the underbody blockage and model frontal area. The generation of upstream junction flow is minimised by situating the support within the area of upstream suction already utilised to prevent the development of the upstream boundary layer. The support sting is positioned close to the ground underneath the stagnation point on the tractor front to ensure normal frontal separation and undisturbed aerodynamics. Additionally, any disturbance produced is directed into the turbulent underbody flow where its influence may be minimised. For consistency, identical off-the-floor fixing procedure is also used with this mounting.

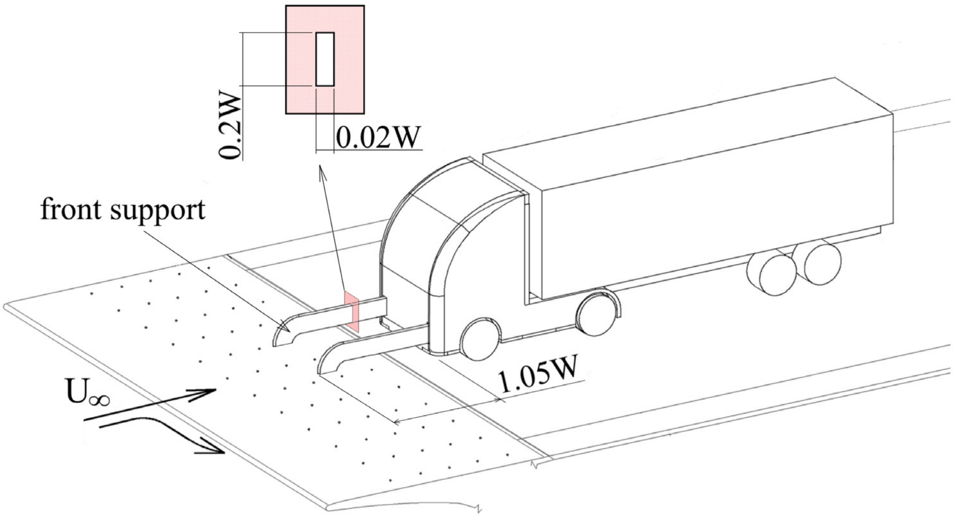

Fig. 4.16 Schematic of Baseline 1 in the double front mounting configuration

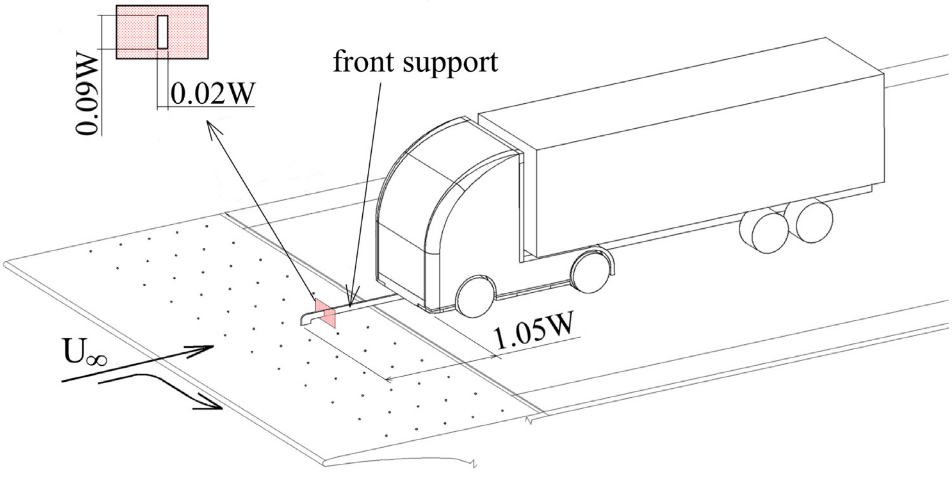

Fig. 4.17 Schematic of Baseline 1 in the single front mounting configuration

The proposed upstream mounting method is assessed against the popular mounting from the sides and top. This assessment is carried out using Baseline 1 and the results are discussed in **Chapter 6**. Subsequently, for all experiments with Baseline 2 (**Chapter 8**), the model is fixed in the test section using the single front mounting sting, with the installation position and procedures maintained. **Figure 4.18** presents photographs of Baseline 2 with the front sting, outside and fixed inside the test section. The sting itself is attached to the bottom plate of the tractor, allowing the fixture to be concealed inside when assembled (**Fig. 4.19**). The load cell connecting wire (**Section 4.5**) and silicon tubing used for pressure measurements (**Section 4.7**) are directed out of the tractor via a custom cut groove along the sting's side, as presented in **Fig. 4.19(b)**.

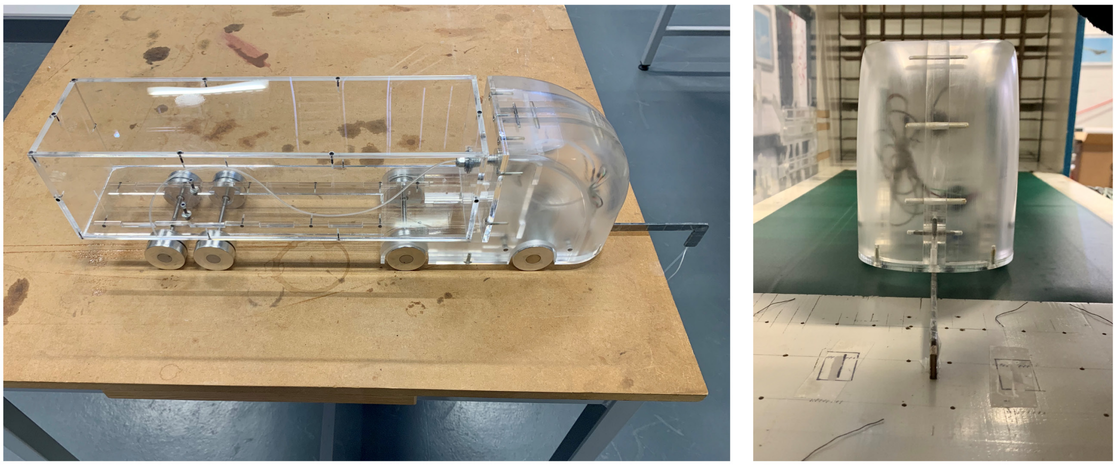
(a) (b)

Fig. 4.18 Photographs of Baseline 2 outside (a) and fixed inside (b) the test section

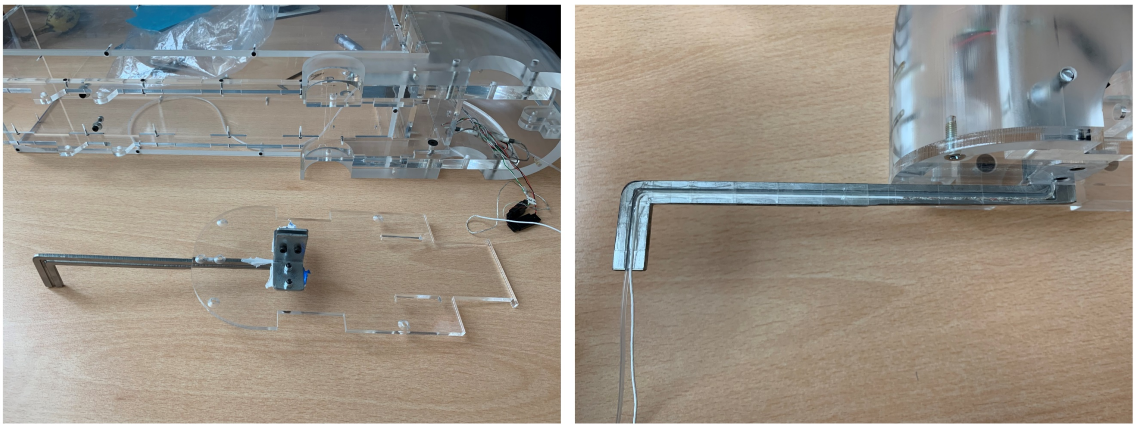
(a) (b)

Fig. 4.19 Photographs of the front support sting: (a) fixed to the bottom tractor plate, (b) with the tractor assembled

4.4 Low-drag configurations

4.4.1 Base inserts

For the initial assessment, the lobed mixers are incorporated into trailing edges of a common boat-tail. At this stage, three different lobe geometries are designed (LB1, LB2, LB3). For comparison, an unmodified boat-tail (BT) configuration is also used. These four devices are quantified in **Fig. 4.20** and **Table 4.2**. The configurations are designed and manufactured to be easily fixed to the removable base of the baseline model (Baseline 1). All inserts have blunt trailing edges and identical overall streamwise length, b=0.25W. Only lobed mixers with parallel sides are chosen for this study, owing to their potential for higher vorticity generation **(Skebe et al. 1988; Mao et al. 2009)**. For the three lobed profiles tested, pitch (p), crest-trough height (h), and penetration angle (β) are varied. Each of these parameters is common to at least two devices to facilitate the isolation of the influence on mixing and drag. A maximum boat-tail angle of α=17° is selected for all four inserts, allowing direct comparisons of performance. This angle is expected to be marginally higher than the optimum but not sufficiently steep to promote instant flow separation. Since one of the

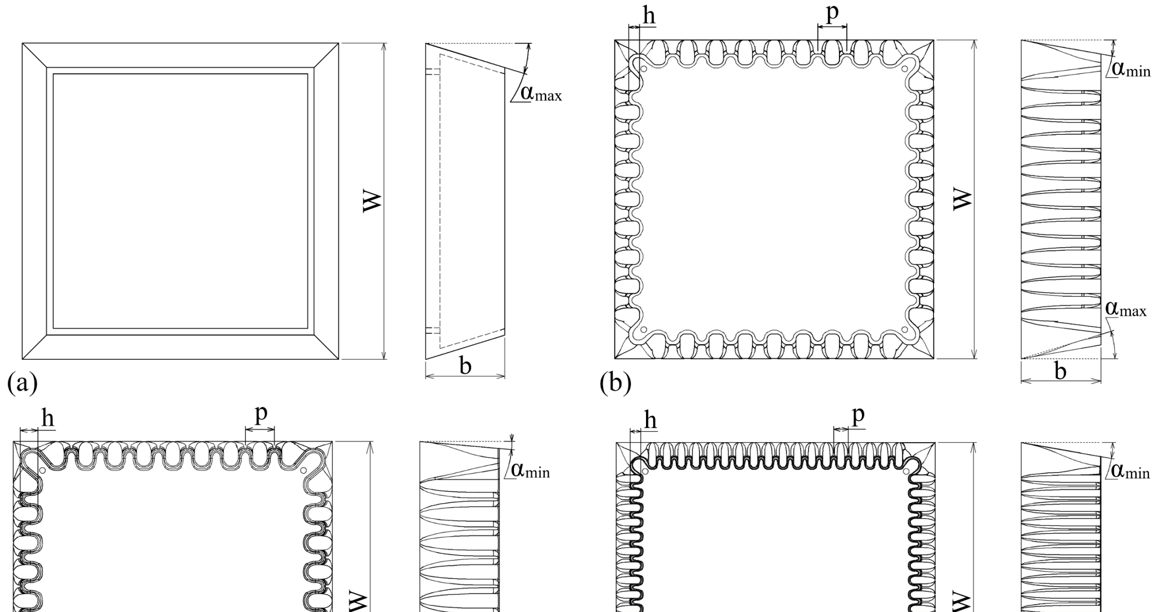

Fig. 4.20 Schematic of base inserts: (a) BT; (b) LB1; (c) LB2; (d) LB3

expected effects of the secondary flow produced by the lobed mixer is a delay in the flow separation, this is selected as an appropriate condition to evaluate its effectiveness.

All inserts are designed using CAD and 3D-printed. The techniques and material are common for all to ensure identical smooth surface finish. **Figure 4.21** presents photographs of BT and LB1 fixed to Baseline 1 as used in the experiments. Additionally, estimates are made of the added weight due to the inclusion of the lobed profiling at full-scale. Based on a gross vehicle mass of 44 tonnes **(Butcher, 2009)**, this is less than +0.4% relative to a standard boat-tail with the same overall dimensions and material specifications.

	b	p	h	α_{min}	α_{max}	β
BT	0.25W	-	-	-	17°	-
LB1	0.25W	0.091W	0.034W	10°	17°	3.5°
LB2	0.25W	0.091W	0.056W	5°	17°	6.0°
LB3	0.25W	0.045W	0.034W	10°	17°	3.5°

Table 4.2 Summary of the geometric parameters for the base inserts


(a) (b)

Fig. 4.21 Photographs of BT (a) and LB1 (b) fixed to Baseline 1

4.4.2 Trailing edge modifications

Following the initial assessment, a new lobed mixer configuration, consisting of integrating the lobed profiling directly into the vehicle's trailing edges, was developed to reach a more practical solution likely to be suitable for real applications. This profiling is achieved by

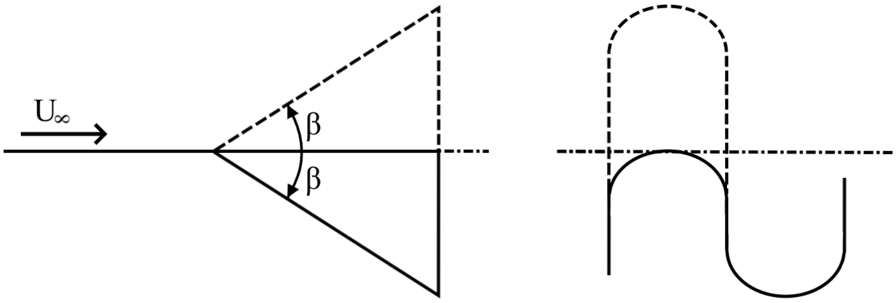

Fig. 4.22 Side (left) and front (right) profiles of the studied trailing edge lobes

cutting longitudinal grooves in the trailer rear edges. Each groove is cut at an inboard angle generating a desired penetration angle relative to the freestream flow. The profiling is such that the lobes which would normally be protruding (outboard penetration angle relative to the axial flow) are reduced to β = 0°, as presented in **Fig. 4.22**. Such trailing edge modifications ensure no change in the model overall length and width.

Thirty-nine different lobed mixer configurations (denoted LBT) are studied. Profiling varies in lobe pitch within $0.027 < p/W < 0.105$, and penetration angle between $5° < \beta < 30°$. For comparison, a range of conventional boat-tail tapers (denoted as BTT) between $5° < \alpha < 30°$ is also assessed. The summary of all configurations' geometric parameters is presented in **Fig. 4.23** and **Table 4.3**. All modifications, as presented in **Fig. 4.23**, are applied to each top and two side trailer faces, with the bottom edge unaltered. All profiling (LBT and BTT) is applied to identical portions of the side and top trailing edges, extending over 91% of the length, with the end portions kept unmodified to enable the assembly of the trailer. All profiling is designed with the same height (h), with h=0.045W

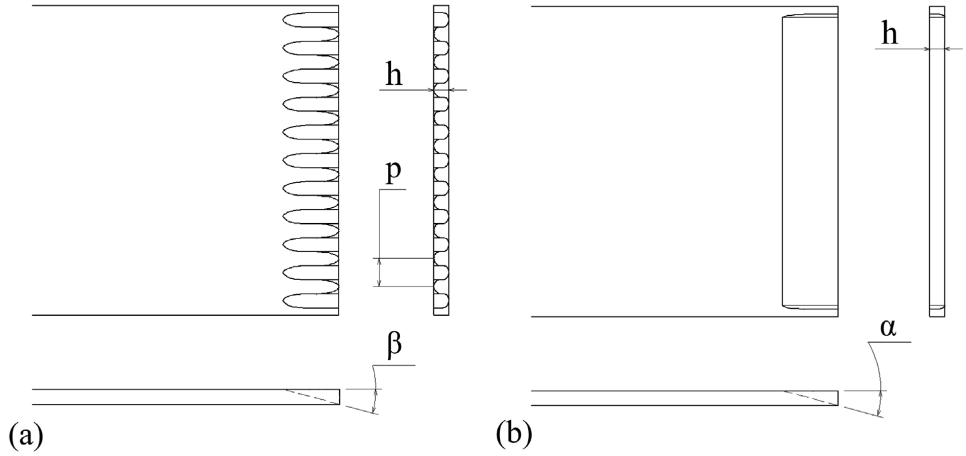

Fig. 4.23 Schematics of lobed trailing edge LBT (a)
and boat-tail taper BTT (b)

along the trailer sides and h=0.027W along the trailer top edge. The small height is selected to create high aspect ratio modifications, ensuring the effect of the geometry on the trailer volume is minimised, with h less than 5% of the model width.

Additionally, various non-linear variations of these configurations are also assessed. These include geometrical lobe changes, variable penetration angles and different combinations of sides and top edges. A detailed description of these modifications is provided in **Appendix A**.

	p	**h (sides)**	**h (top)**	**α / β**
BTT1 – 6	-	0.045W	0.027W	5° – 30°
LBT1 – 7	0.027W	0.045W	0.027W	5° – 30°
LBT8 – 14	0.044W	0.045W	0.027W	10° – 30°
LBT15 – 21	0.055W	0.045W	0.027W	5° – 30°
LBT22 – 27	0.067W	0.045W	0.027W	5° – 30°
LBT28 – 33	0.086W	0.045W	0.027W	10° – 25°
LBT34	0.095W	0.045W	0.027W	15°
LBT35 – 39	0.105W	0.045W	0.027W	5° – 25°

Table 4.3 Summary of the geometric parameters for the trailing edge modifications BTT and LBT

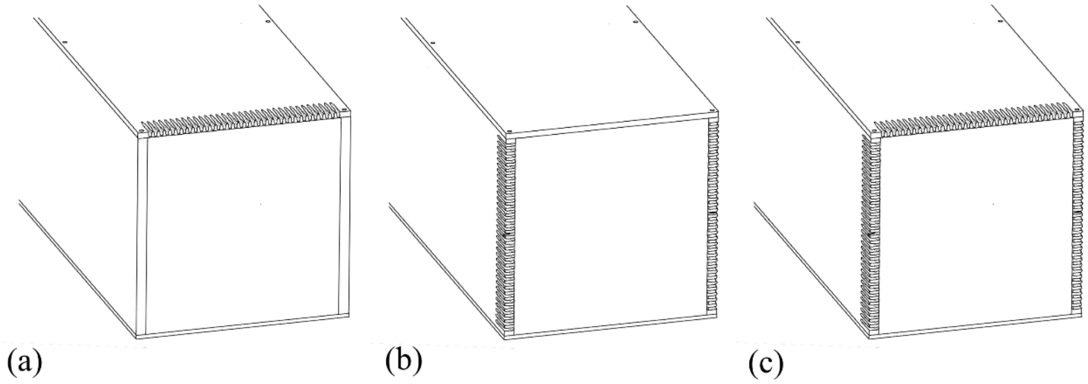

Fig. 4.24 Schematic of the different device arrangements: (a) top only, (b) sides only, (c) all top and sides

For each configuration, the isolated influence of the top and sides alone is also studied along with the combination of both. As a result, each design is tested in the three arrangements presented in **Fig. 4.24** (identical for BTT). For this purpose, the trailer of

Baseline 2 is made as a box with each of the three faces removable. All faces are cut out of Perspex sheets, with the trailing edge modifications added subsequently using CNC machining. All configurations are manufactured with an identical smooth surface finish. **Figure 4.25** presents photographs of the taper and lobed edge modification examples.

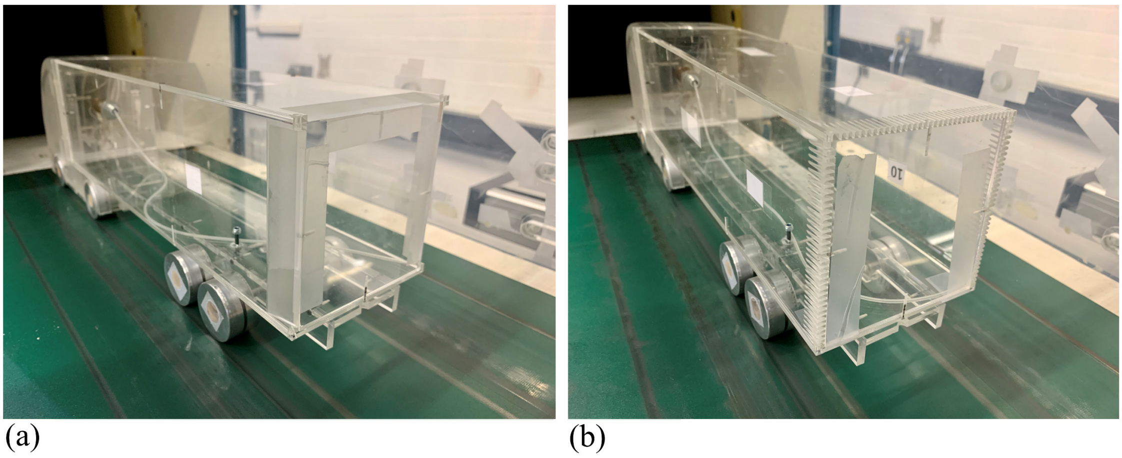
(a) (b)

Fig. 4.25 Photographs of configurations BTT3 (a) and LBT4 (b)

4.5 Load measurements

The load is measured to quantify the changes in drag for the different model configurations and Reynolds numbers. Across the experimental campaign, two load cells are used.

4.5.1 Load cell 1

The load cell used in all experiments is a Model 31 single axis tension/compression load cell by RDP Electronics with a full range capability of ±44N. Signal amplification is provided by an RDP Electronics S7DC amplifier. The cell is mounted on a plate inside the tractor with a connecting rod fixed to the front face of the trailer. This is presented in **Fig. 4.26** on Baseline 1, with an identical load cell configuration also used for Baseline 2. With the "free-floating" trailer, this particular setup allows the measurement of isolated trailer drag used for direct comparison of the various trailer arrangements.

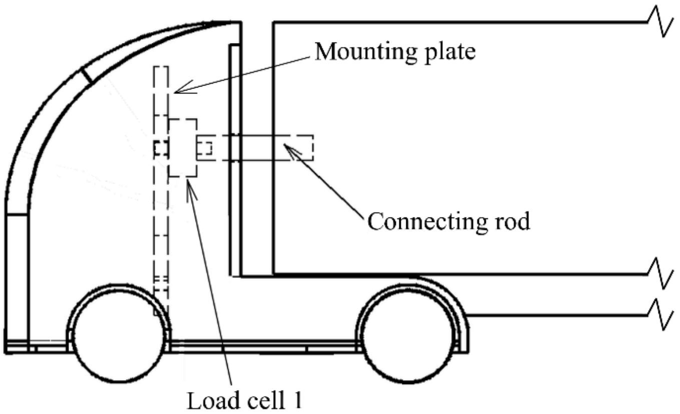

Fig. 4.26 Schematic of load cell 1 configuration of the example of Baseline 1 (identical for Baseline 2)

4.5.1.1 Estimates of total drag coefficient

This load cell is also used to estimate the total drag of the models in the front mounting configuration (**Section 4.3.3**). In a separate test, the model is secured in the test section using a steel rear sting as shown in **Fig. 4.27**. The sting is 5mm in diameter and fixed to the test section floor, 390mm downstream of the trailer base. In this arrangement, the compression measured by the load cell is equivalent to the drag exerted on the tractor and trailer bottom section of the model. This measurement is subsequently added to the measured trailer drag to obtain total model drag.

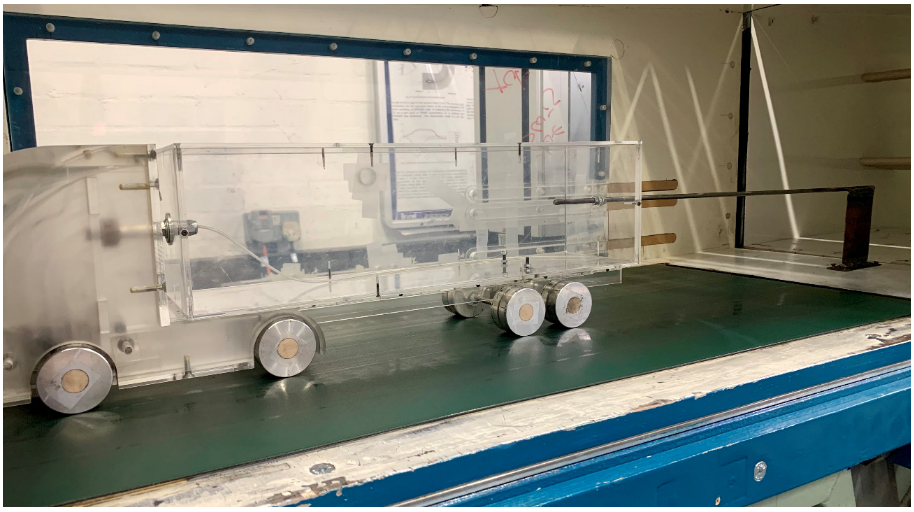

Fig. 4.27 Photograph of Baseline 2 fixed in the test section using a rear sting

To ensure that the various low-drag devices studied do not affect the drag of the tractor and trailer bottom section, similar tests are conducted with the use of selected trailer modifications. The results confirm such changes to be within the experimental uncertainty, limited to $\Delta C_{DM} = \pm 0.007$ (for C_{DM} see **Section 4.5.4**).

4.5.2 Load cell 2

A second load cell is used to measure total drag of Baseline 1 in the top mounting configuration (**Section 4.3.2**). This single point compression Tedea Huntleigh cell has a full range of 196N. It is affixed directly to the top strut and the horizonal support outside of the test section, as shown in **Fig. 4.28**. Similar signal amplification and conditioning electronics are used as for load cell 1.

This load cell is also used to measure the influence of the top support tare for corrections of model drag in this configuration. In this test, the drag of a dummy support extending down to, but not touching, the top of the trailer (<2mm separation) is measured, with the model secured by the same rear sting presented in **Fig. 4.27**.

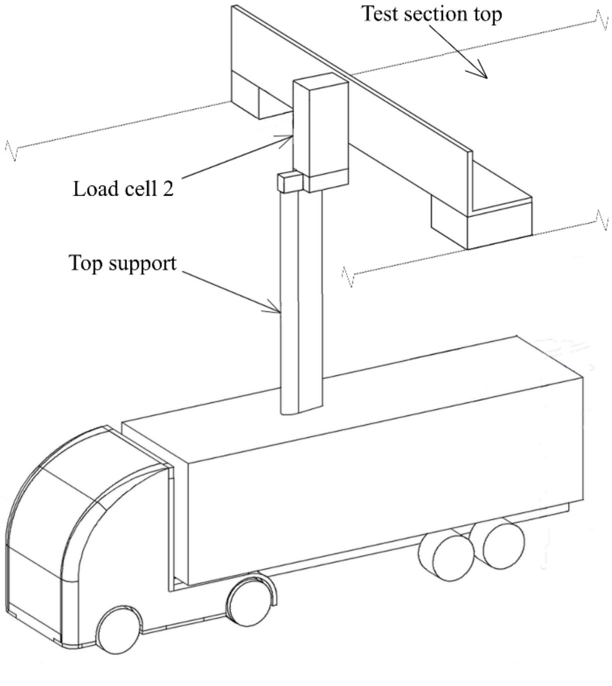

Fig. 4.28 Schematic of load cell 2 configuration

4.5.3 Load cell calibration

Both load cells are calibrated at regular intervals to ensure the accuracy of the recorded results. The load cell calibration is always performed in situ. For this purpose, a custom rig was designed and manufactured (**Fig. 4.29**), with a metal pulley affixed to the top to minimise the friction influence.

During the calibration, the rig is placed downstream of the model base in the wind tunnel test section. A string fixed to the trailer, coinciding with its central longitudinal axis (**Fig. 4.30(a)**), runs over the pulley and outside of the test section through an opening at the bottom (**Fig. 4.30(c)**). In the top mounting configuration, both load cells are calibrated simultaneously by attaching the string to the tractor and trailer bottom section, as shown in **Fig. 4.30(b)**. In all cases, the process consists of loading the free end of the string (**Fig. 4.30(d)**) with masses up to a selected maximum, followed by subsequent unloading.

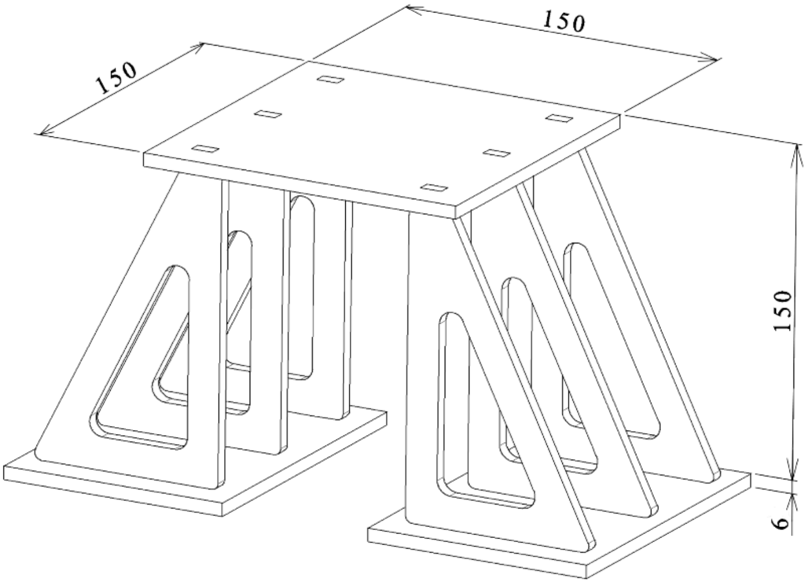

Fig. 4.29 Load cell calibration custom rig (dimensions in millimetres)

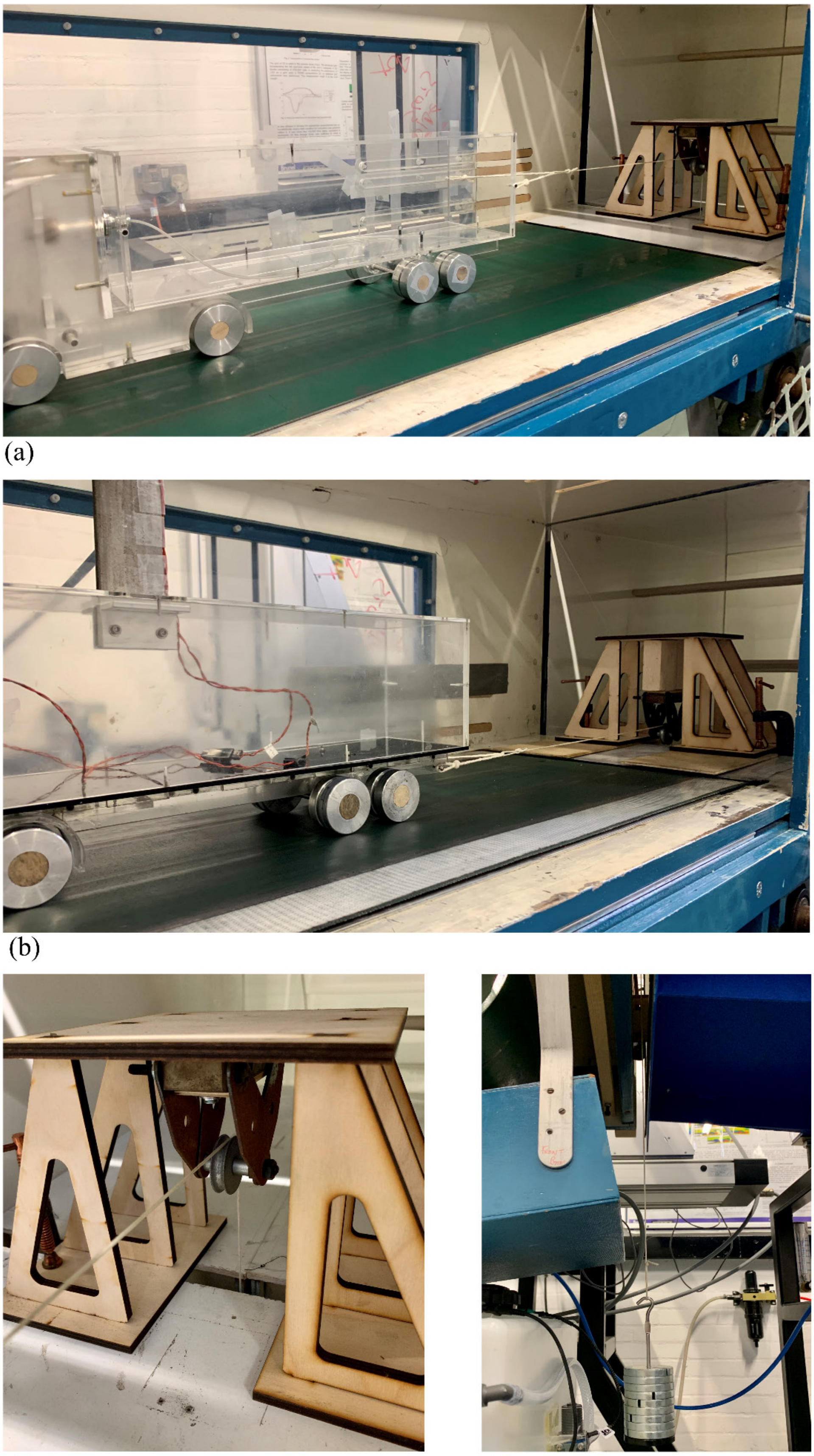

(a)

(b)

(c)

(d)

Fig. 4.30 Photographs of the in-situ load cell calibration: (a) front mounting configuration, (b) top mounting configuration, (c) calibration rig, (d) masses

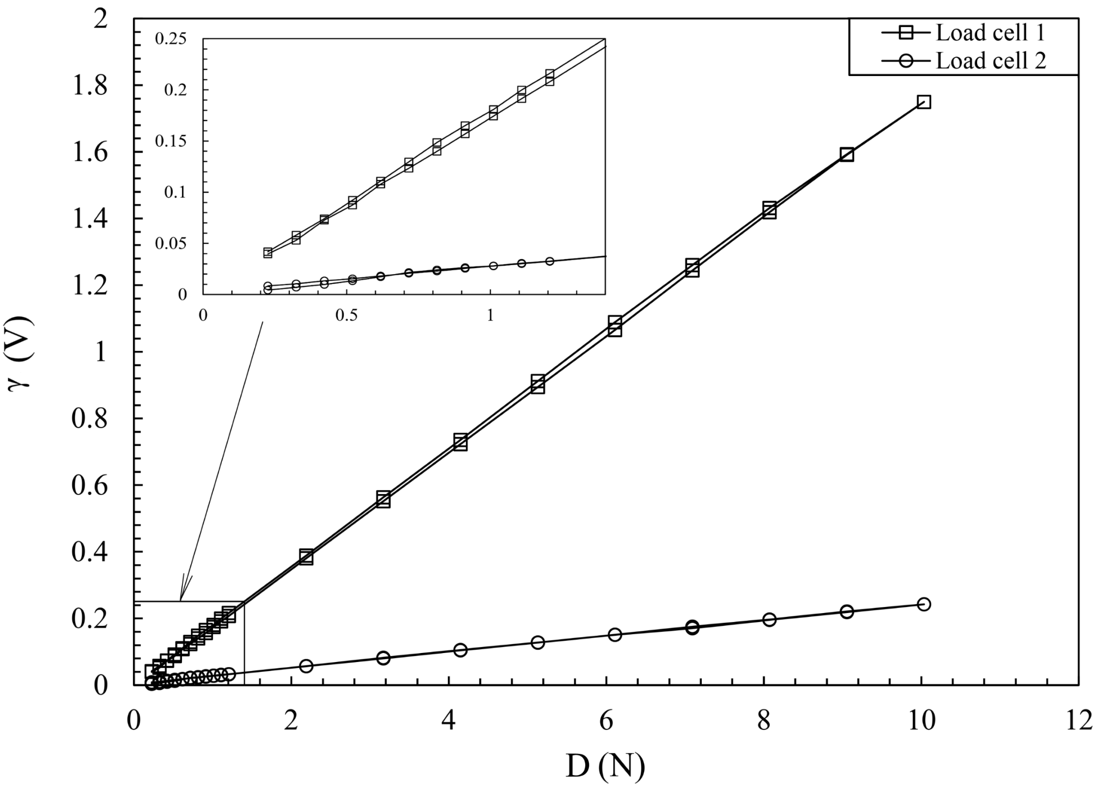

Fig. 4.31 Calibration curves for load cells 1 and 2

Both load cells are calibrated for a total load of up to 10N. To assess the low-load performance of the cells for measurements of trailer drag, eleven equally spaced increments up to 1.2N are applied initially. Beyond this load, a further nine equal steps up to 10N are applied for the total drag. For the subsequent unloading, this process is reversed. The selected calibration ranges are expected to coincide with the results. Each point is sampled at 20 kHz for 40 seconds and averaged. **Figure 4.31** presents sample calibration curves for both load cells.

For each calibration curve, the least squares regression line is found, with its gradient used as a constant for converting measured voltages to force. The resulting conversion equations are

$$\gamma / 0.17 = D \qquad (4.6)$$

for Load cell 1, and

$$\gamma / 0.024 = D \qquad (4.7)$$

for Load cell 2, where γ is the measured voltage, and D, the resultant drag force.

Analysis of the calibration curves produces the following characteristics for load cell 1:

- hysteresis: <1.3% of maximum load,
- non-linearity: <1.0% of maximum load,
- gradient repeatability between the calibrations: ±0.007,

and for load cell 2:

- hysteresis: <1.7% of maximum load,
- non-linearity: <1.6% of maximum load,
- gradient repeatability between the calibrations: ±0.0002.

4.5.4 Sampling

In the preliminary study of lobed mixers (**Chapter 7**), all load data are sampled at the rate of 1 kHz for 2 minutes using a dedicated LABView programme. Each result presented is an average of three separate measurements. In the experiments conducted as part of the assessments of moving ground facility and model-mounting techniques (**Chapters 5 – 6**), the load data are sampled simultaneously with the hot-wire anemometry measurements (discussed in **Section 4.6**). This is conducted at a rate of up to 25 kHz for a continuous period of 20 seconds and averaged from up to four measurements. A similar sampling rate and time is also used for the drag measurements of different trailing edge modifications (**Chapter 8**), taken independently of hot-wire tests, with results averaged from up to four measurements. For all tests, both the initial and final 'wind-off' (belt-on where moving ground used) measurements are taken and used for data correction. This allows the influence of the wind to be isolated, as recommended in SAE J1252 **(SAE International, 2012)**.

The recorded voltages are used to estimate the forces using equations 4.6 and 4.7. Subsequently, based on the atmospheric conditions (recorded daily) the model (C_{DM}) and trailer (C_{DT}) drag coefficients are calculated as follows:

$$C_{DM} = \frac{2\,D_M}{\rho\,U_\infty^2\,A} \qquad (4.8)$$

$$C_{DT} = \frac{2\,D_T}{\rho\,U_\infty^2\,A} \qquad (4.9)$$

where D_M, D_T, ρ, U_∞ and A are total model and trailer drag forces, ambient air density, freestream velocity, and model frontal area, respectively. Trailer drag (C_{DT}) is calculated based on the model frontal area (A) because it is always discussed as a relative portion of total model drag.

4.5.5 Error assessment

The following sections discuss the possible sources of error in the drag measurements. Throughout this thesis, drag measurements are used to evaluate differences between configurations, and not as absolute values. For this reason, only the error sources which are dependent on configuration, setup, or time are discussed in the following sections. All other errors are assumed to be constant for all tests and thus eliminated during comparison.

4.5.5.1 Model installation

With both load cells used for this thesis being linear and measuring forces in the streamwise direction, potential offsets in the yaw angle can result in erroneous measurements. The precision with which the position of the installed model is assessed is within ±1mm. Though any errors resulting from offsets within this range should be negligible, to ensure the utmost accuracy, the model remains installed in its position for the duration of the experimental phase where the drag results are to be compared. The only exception to this are the tests conducted as part of the assessment of different mounting methods.

4.5.5.2 Temperature changes

Variations in the drag measurements due to temperature changes are twofold. Firstly, the changes in the ambient temperature affect the “zero” reading of the load cell. To mitigate this, zero is adjusted on the amplifier daily. Additionally, for all tests, the initial and final “wind-off” measurements are taken to correct for tare. For the tests with the use of moving ground, these are taken with the belt on.

The second error which may arise due to temperature variations is directly related to the offset of “zero”. Where the drag is measured simultaneously with hot-wire runs for extended periods of time during which the ambient temperature rises, the time trace of the load cell reading can be seen to drift significantly from the original mean. For this reason, in these tests, the drag is evaluated only for the initial 200 seconds of the entire hot-wire run, effectively eliminating drift as an error source by substantially reducing the data collection period.

4.5.5.3 Rolling resistance and static friction

In all tests with moving ground, the measured drag is corrected for rolling resistance with the “zero” reading taken with running belt. Though the rolling resistance may change subtly during the actual wind-on run through natural lifting of the model, drag comparisons are made only between the measurements taken where the model installation position is constant, alleviating this issue. The only exceptions are the experiments conducted as part of the assessment of mounting techniques and moving ground. In these tests, the effects of rolling resistance variation are minimised by placing the model on a 1mm thick board during installation. When the mounting is fixed, the board is removed, and the model is allowed to drop under its weight; the weight of the model is always constant. Where drag is compared between moving and stationary ground conditions, the effects of static friction are minimised by careful adjustment of the vertical position of the model, such that the wheels only make light contact with the ground while still preventing any flow ingress between the wheels and the floor.

4.5.5.4 Signal noise

Random errors can be introduced into the data through electrical noise. The voltage of the input signal into the amplifier is very low and therefore, susceptible to interference. To minimise this effect, the cable connecting the load cell and the amplifier is kept as short as possible. The signal between the amplifier and the computer is much stronger and thus, not as vulnerable. For the equipment used for the purpose of this thesis, the average noise is evaluated from the time trace of the “zero” reading with a stationary ground, with the root-mean-square of this measurement being 0.01V – 0.9% of the voltage corresponding to the subsequent constant-velocity load measurement.

4.5.5.5 Repeatability

To mitigate random errors, all drag results presented in this thesis are averages of multiple runs (n), as outlined in **Section 4.5.4**. The process of measuring drag consists of:

1. Recording the initial “zero” with wind-off (belt-on where moving ground is used);
2. Measuring force with wind-on at a constant freestream velocity;
3. Recording the final “zero” with wind-off (belt-on where moving ground is used).

For each configuration, this process is then repeated n+1 times, with the first measurement always discarded (not included in the average). The first measurement is treated as a warm-up to prevent errors from load cell “sticking”. Overall, the variance within such measurements repeated under the same conditions is less than ±1%. Across all experimental phases, the maximum uncertainties for the total and trailer drag measurements are $\Delta C_{DM} = \pm 0.018$ and $\Delta C_{DT} = \pm 0.010$, respectively.

4.6 Hot-wire anemometry

Hot-wire anemometry (HWA) is used to measure the velocity within the model wake. The method is based on placing a heated metal element in a fluid flow. As the flow of lower temperature passes over the element, heat transfer takes place. The resistance of many metals is dependent on their temperature, hence, as the temperature changes, the relationship between resistance and actual fluid velocity can be obtained. Thermal anemometers offer high spatial resolution and have outstanding frequency response characteristics. In turbulent flows, such as a base wake, thermal inertia can introduce limitations and, for this reason, constant temperature anemometry is chosen for this work. As opposed to constant current

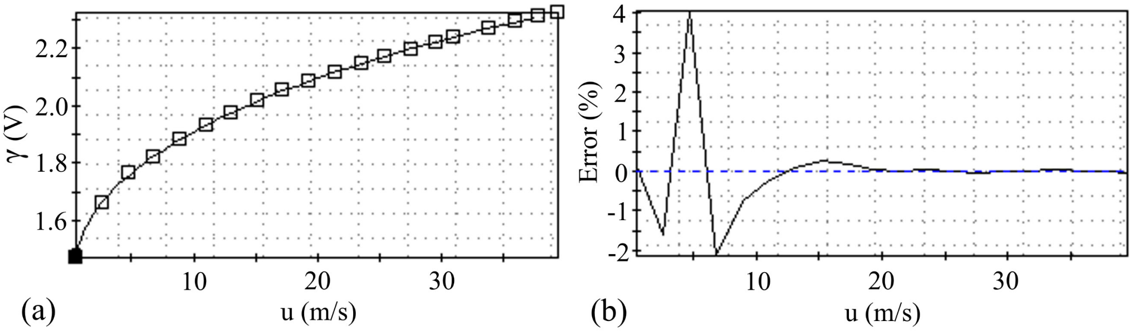

Fig. 4.32 Velocity calibration results for the x-wire probe: (a) velocity calibration curve for one of the probe sensors; (b) corresponding error curve

or voltage anemometers, it ensures that the electrical power is supplied at the same rate that the flow cools the heated element, thus, maintaining the wire temperature and removing the influence of specific heat or thermal conductivity.

4.6.1 Probe calibration

4.6.1.1 Velocity calibration

A dual-sensor (x-wire) probe type P61 by Dantec Dynamics is used to measure wake velocities in all three axes (X, Y, and Z), with probe calibration performed using a Dantec Dynamics Calibration Unit type 90H01/H02 and the entire system controlled by dedicated software (StreamWare Pro). Velocity calibration is done at the start of each test day and consists of measuring voltages in 20 points over the velocity range expected in the actual flow. Consequently, for the freestream of U_∞ = 30 m/s the chosen range is 0.5 – 40 m/s, and for U_∞ = 37 m/s, 0.5 – 45 m/s. In all cases, the probe is exposed to a known flow velocity established by the automatic calibrator at each point and the probe measured velocity is set to be estimated from 8 iterations **(Dantec Dynamics, 2013)**. Linear polynomial fitting is chosen to correlate the voltages and velocities due to improved accuracy. **Figure 4.32** presents sample results from one of the calibrations. The maximum calibration error is less than 4%, but below 1% for velocities higher than 10 m/s.

4.6.1.2 Directional calibration

Dual-sensor probes require yaw coefficients (k_1 and k_2) to decompose the measured velocity into its orthogonal components. For the preliminary study of lobed mixers (**Chapter 7**), default probe yaw coefficients are used ($k_1^2 = k_2^2 = 0.0225$ – Jørgensen **(2002)**). To ensure the highest possible accuracy, in the remaining experimental phases (**Chapters 5, 6, 8**), directional calibration is performed to determine the specific yaw factors of the probe used. The calibration process consists of placing the probe fixed to a yaw manipulator in an airstream of the flow unit (as presented in **Fig. 4.33**) and assessing the output voltage over the yaw range between -40° – 40° (5° increments) at a selected constant velocity (u). This process results in specific characteristics for each of the two probe sensors, as presented in **Fig. 4.34**, where **Fig. 4.34(a)** shows the velocity from calibration (U_C) for the two sensors

(1 and 2), and **Fig. 4.34(b)**, the resultant k_1 and k_2 for all recorded yaw angles. Each final yaw coefficient used for data reduction is the average of the values obtained across the angle sweep.

Fig. 4.33 The HWA probe directional calibration setup

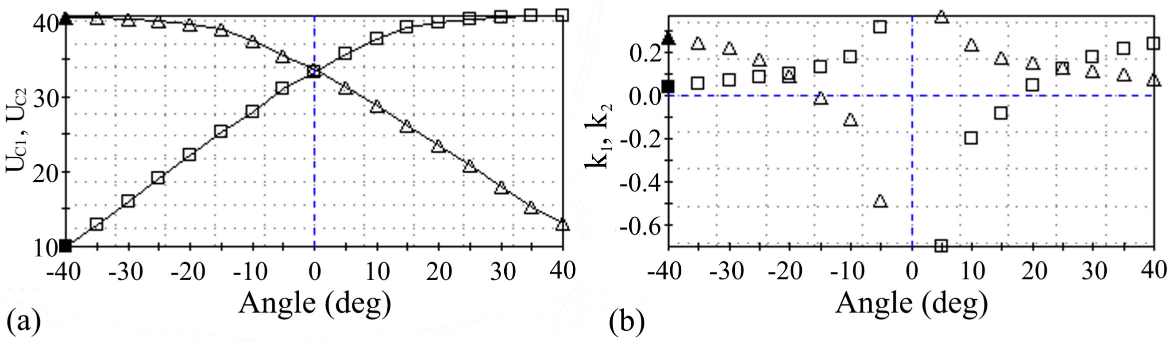

Fig. 4.34 Directional calibration results for the x-wire probe: (a) velocity from calibration for each probe sensor, (b) k_1 and k_2 at each yaw angle

The variation in the yaw coefficient values is first assessed over a wide range of velocities ($5 < u < 35$ m/s); **Fig. 4.35** presents this relationship. For $10 < u < 30$ m/s, the coefficient values remain near-constant. Beyond this range ($u = 35$ m/s) both, k_1 and k_2 are significantly increased. For data reduction of the results described in this thesis, the yaw coefficients used are those obtained at velocities equivalent to the middle of the range expected in the experiments: 20 m/s for freestream U_∞ = 30m/s, and 25m/s for freestream U_∞ = 37m/s; both within the constant region, as presented in **Fig. 4.35**.

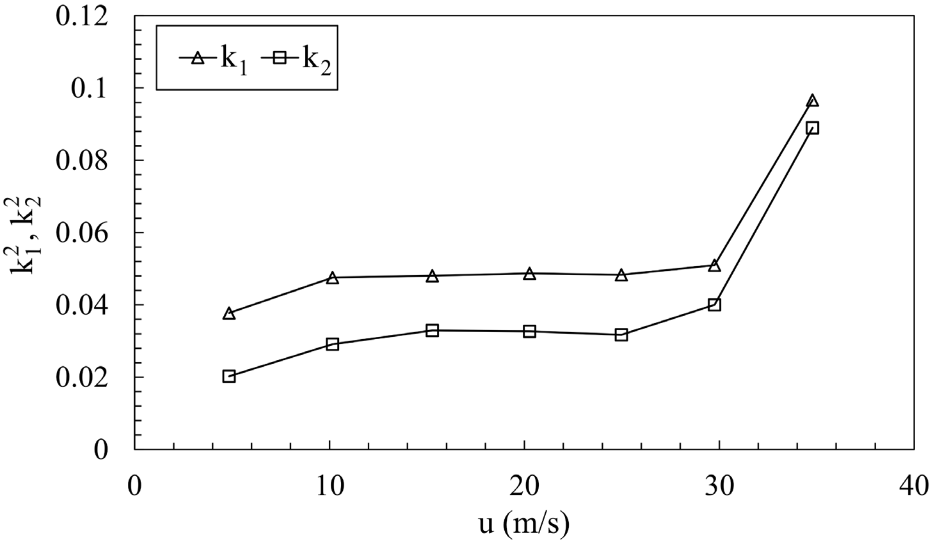

Fig. 4.35 Changes in probe yaw coefficients (k1 and k2) with flow velocity

4.6.2 Sampling

The hot-wire apparatus used is fully integrated and controlled, allowing automated data acquisition. In all experiments, the probe is automatically positioned by a 3D traverse system, with the recommended overheat ratio set to 0.8 **(Jørgensen, 2002; Dantec Dynamics, 2018)**. In the preliminary experimental phase (**Chapter 7**), all data are sampled at 1000 Hz with the signal lengths up to 5 seconds (N=5000 samples). To evaluate the suitability of these parameters, mean data convergence is assessed using up to 10000 samples (10 seconds). Velocity convergence to within 1% is achieved after 1800 samples, as presented in **Fig. 4.36**.

In the following experimental phases (**Chapters 5, 6, 8**), the sampling rate and time are increased to enable the analysis of time-dependent aspects. In those instances, the data are sampled at up to 25 kHz for 20 seconds (N=500000 samples at each position). The only exception is the data in planes TS1-3 (see **Section 4.6.3** for details), where the sampling time is reduced to 5 seconds to minimise testing times for high spatial resolution planes. **Figure 4.37** presents the power spectral densities of a streamwise velocity signal (E_u) for varying sampling times between 1 and 20 seconds. The variation in spectral trends for sampling times beyond 5 seconds is marginal, with magnitude convergence to within 1dB/Hz for $St_W < 0.2$, and 2dB/Hz for $St_W > 0.2$. The selected measurement rates and times are, therefore, suitable for evaluation of unsteady characteristics, with spectra comparisons only made between signals sampled for identical time periods.

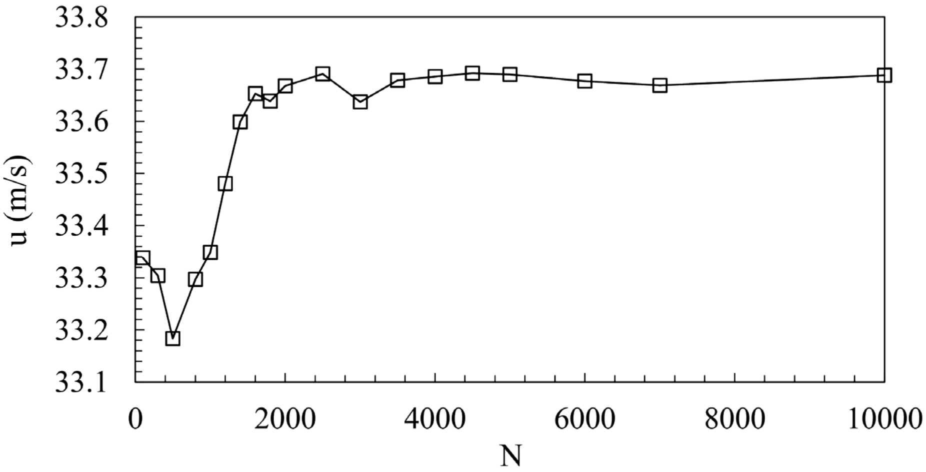

Fig. 4.36 Mean velocity convergence for data sampled at 1kHz

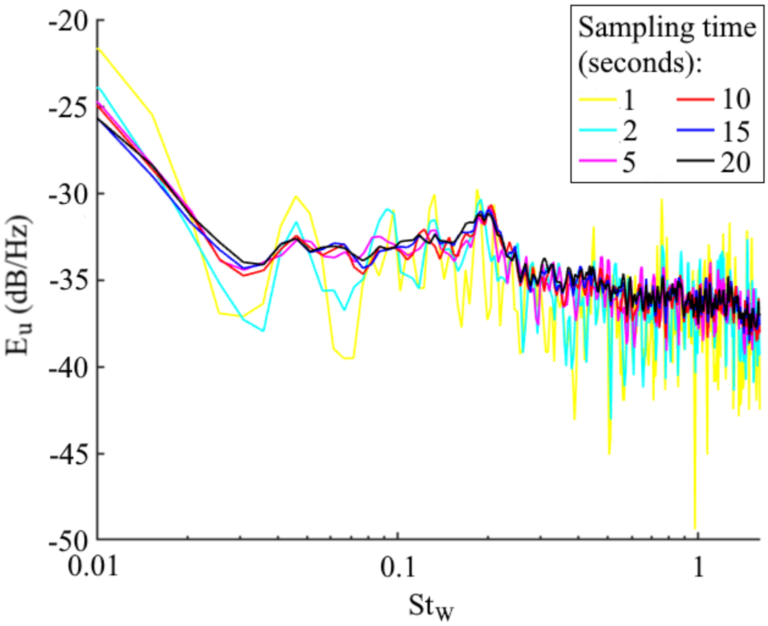

Fig. 4.37 Power spectral density of streamwise velocity signals sampled for different time periods between 1 and 20 seconds

4.6.2.1 Data reduction

All data are corrected for temperature variations with the temperature loading factor of 0.2, chosen for its smallest residual error. Each voltage measurement is corrected using the equation:

$$\gamma_{\mathrm{corr}} = \gamma_1 \left(\frac{T_w\text{-}T_o}{T_w\text{-}T_1}\right)^{0.5} \qquad (4.10)$$

where γ_1 and T_1 are the local voltage and temperature, respectively, T_w, the temperature of the wire sensor, and T_o, the ambient temperature at the probe velocity calibration. The coefficients of the quintic polynomial used to describe the velocity calibration curve (as in **Fig. 4.32(a)**) are thereafter applied to the corrected voltages for linearisation; this results in velocity magnitudes from calibration for both sensors 1 and 2 (U_{C1} and U_{C2}). To obtain the directional velocity components (u, v) the yaw coefficients (k_1 and k_2) are used in the following manner:

(step 1) $$U_1 = \frac{\sqrt{2}}{2}\sqrt{\left(1 + k_2^2\right)U_{C2}^2 - k_2^2U_{C1}^2} \qquad (4.11)$$

(step 1) $$U_2 = \frac{\sqrt{2}}{2}\sqrt{\left(1 + k_1^2\right)U_{C1}^2 - k_1^2U_{C2}^2} \qquad (4.12)$$

(step 2) $$u = \frac{\sqrt{2}}{2}U_1 + \frac{\sqrt{2}}{2}U_2 \qquad (4.13)$$

(step 2) $$v = \frac{\sqrt{2}}{2}U_1 - \frac{\sqrt{2}}{2}U_2 \qquad (4.14).$$

Based on the angular position of the x-wire probe, the same process is used to obtain the set of streamwise and heightwise velocity components (u, ω). Where there are two sets of the streamwise velocity component (u) for the same condition, the result presented are the average of these two sets.

The velocities obtained this way are subsequently post-processed using dedicated software (Tecplot 360) which enables the calculation of further variables, such as vorticity. The vorticity function uses the data for velocity and position from the measurement matrices uploaded to the software. Each component of vorticity (Ψ) about X, Y, and Z axes is calculated as the change in velocity in the plane perpendicular to the corresponding axis, as indicated in the equation 4.15 **(Tecplot Inc., 2013)**. For the results presented in **Chapter 7**, Ψ_Y and Ψ_Z are calculated without the X-direction component, meaning the streamwise variations in the crosswise/vertical velocities (∂v/∂x and ∂ω/∂x) are neglected, as only transverse planes are used (see **Section 4.6.3**).

$$\begin{bmatrix} \Psi_X \\ \Psi_Y \\ \Psi_Z \end{bmatrix} = \begin{bmatrix} \frac{\partial \omega}{\partial y} - \frac{\partial v}{\partial z} \\ \frac{\partial u}{\partial z} - \frac{\partial \omega}{\partial x} \\ \frac{\partial v}{\partial x} - \frac{\partial u}{\partial y} \end{bmatrix} \qquad (4.15).$$

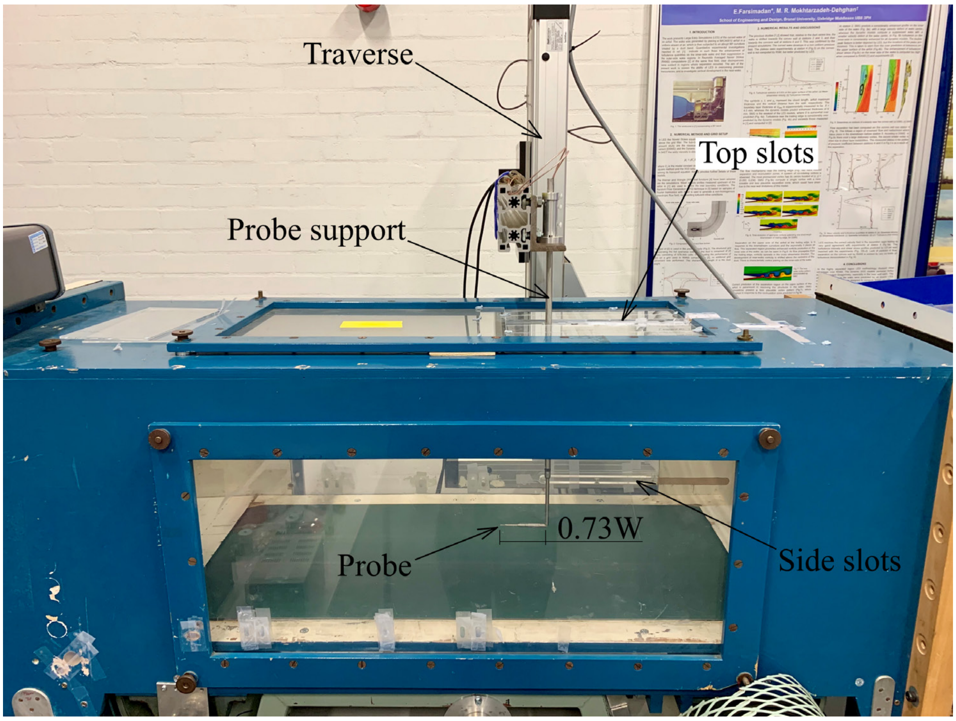

Fig. 4.38 Hot-wire anemometry setup

4.6.3 Measurement grids

In all HWA tests, the probe is fixed to the traverse via a support which enters the test section through custom slots cut into the test section’s top and side, as presented in **Fig. 4.38**. The probe’s sensor wires are located Δx*=0.73 upstream of the support to minimise any flow interference likely to affect the signal. Additionally, a lower limit of z*=0.091 is selected to prevent probe damage.

Throughout the experimental campaign, a total of eight main planes are used: four transverse planes (T1 – 4), three streamwise vertical planes (SV1 – 3), and one streamwise horizontal plane (SH1). The position and size of these planes are summarised in **Fig. 4.39** and **Table 4.4**. For the preliminary study of lobed mixers (**Chapter 7**), certain plane specifications vary, with these changes indicated in **Table 4.4** by an asterisk. Additionally, with the length of Baseline 2 increased, the relative streamwise distance from the base to the planes is reduced, with these specifications indicated by a double asterisk. In the preliminary study (**Chapter 7**), a uniform measurement point spacing is adopted, with 0.045W in T2 and 0.091W in T3. For the remaining experimental phases, measurement points are selected equally spaced at 0.091W for all planes, with a finer resolution (0.045W) applied to areas of particular interest, such as separated shear layers, to allow for a more detailed interrogation. Furthermore, grid spacing is also increased (0.18W) in other areas to minimise test duration where possible. These alternative point distributions are summarised in **Table 4.5**.

A further three transverse planes were also used directly downstream of the side trailing edge of Baseline 2, intended for a more detailed assessment of the flow-field downstream of the edge-integrated modifications. The size and position of these planes are specified in **Fig. 4.40** and **Table 4.6**. For these grids, the spacing is uniform throughout and significantly reduced for finer spatial resolution, with 0.009W for TS1-2 and 0.018W for TS3.

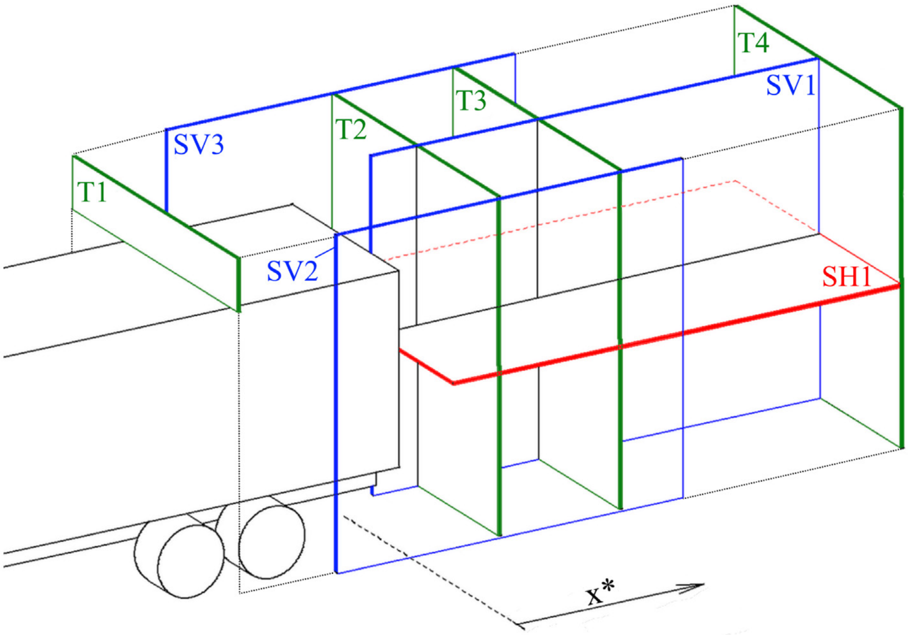

Fig. 4.39 Schematic of the main hot-wire measurement planes

In this thesis, all HWA results obtained in the described measurement grids are presented interpolated by a factor of two using Gaussian process regression to enhance feature detail.

	T1	T2	T3	T4	SV2	SV3	SV1	SH1
x*	-1.05	0.42 (0.38)*	1.11 (1.05)* (0.79)**	2.59	-0.48 – 1.43		0.14 – 2.59 (0.064 – 2.29)**	
y*	-0.76 – 0.76				-0.76	0.76	0	-0.76 – 0.76
z*	1.55 – 1.82	0.09 – 1.82 (0.09 – 1.69)*						0.92
Grid points	217	528 (1365)*	360		357		552 (504)**	552 (483)**

Table 4.4 Specifications for the main hot-wire planes (*specifications for results described in **Chapter 7**; **specifications for results described in **Chapter 8**)

Alternate grid spacing	**0.045W**	**0.18W**
T1	-0.59 < y* < 0.59 1.55 < z* < 1.81	-
T2	0.41 < |y*| < 0.59 0.45 < z* < 0.64 1.45 < z* < 1.64	-
SV1	0.09 < z* < 0.27 1.36 < z* < 1.55	1.55 < x* < 2.45 (1.34 < x* < 2.29)**
SV2-3	0.09 < z* < 0.45	0.43 < x* < 1.43 1.27 < z* < 1.81
SH1	0.59 < |y*| < 0.36	1.73 < x* < 2.45 (1.34 < x* < 2.29)**

Table 4.5 Specifications of the alternate grid spacing within the main hot-wire planes (**specifications for results described in **Chapter 8**)

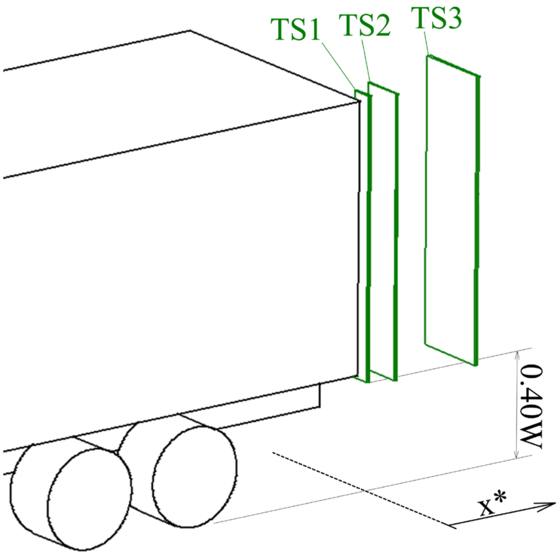

Fig. 4.40 Schematic of the edge hot-wire measurement planes used with Baseline 2

	TS1	TS2	TS3
x*	0.027	0.12	0.45
y*	-0.44 – -0.52	-0.39 – -0.55	-0.28 – -0.57
z*	0.40 – 1.45		0.40 – 1.46
Grid points	1160	2204	1003

Table 4.6 Specifications for the edge hot-wire planes TS1-3

4.6.4 Error assessment

It is common knowledge that HWA is unable to always measure accurately within recirculating flows. The nature of this technique means that the flow direction is indiscernible. Additionally, the accuracy of the measured magnitudes can reduce significantly in highly turbulent flows. In contrast however, the superior ability of this technique to provide high frequency spectral content, at reasonable cost, to small spatial resolution, makes it an excellent method for evaluating base wake dynamics. Where identical test methodology is used, mean velocity magnitudes can be used for direct comparison of various configurations and determining key wake features. Close to the model base and the rear free stagnation point, where mean velocity magnitudes are low and rms fluctuations high, the relative turbulence intensity can exceed $u_{rms}/u = 0.5$, suggesting only qualitative assessment should be made **(Chandrsuda and Bradshaw, 1981)**. Outside these areas, however, the data lie well within the maximum limit of $u_{rms}/u < 0.3$, specified by Chandrsuda and Bradshaw **(1981)**.

The following sections discuss, in detail, the possible errors which can be introduced into the HWA measurements. In the analysis, systematic and random errors are assumed independent of configuration, therefore, the same for all and not precluding direct comparison.

4.6.4.1 Position error

In all experiments, the HWA probe is positioned in the specified points of the measurement grids using an automated traverse system. The precision of the traverse is ±0.01mm. Based on the maximum number of points along any column/row of the selected measurement grids being 116, the resulting maximum position error is within ±1.16mm or ±0.011W.

4.6.4.2 Temperature changes

Changes in ambient temperature throughout the course of a single experiment can introduce errors into the velocity measurements. This is especially important for long tests, during which the temperature can vary significantly. As outlined in **Section 4.6.2.1**, in all experiments, the gathered data are post-processed to correct for these changes. Throughout the experiments, the variations of the ambient temperature are recorded using a dedicated temperature probe, located on the side of the wind tunnel, measuring the mean temperature at the HWA rate for every grid point with a precision of 0.001°C. In all experiments, the temperature probe and its position are kept constant to minimise any random errors arising from a non-uniform heat distribution.

4.6.4.3 Measured velocity uncertainty

At each position of the HWA measurement grid, the measured velocity is a mean of a number of independent samples collected at that point. The number of samples depends on the rate and time of sampling. Typically, increasing the number of independent samples reduces the uncertainty of the resulting mean velocity measurement, with the assumption that an infinite number of samples would yield the true result. At any point in the flow, therefore, the uncertainty of the measurement can be estimated statistically. The same method adopted by Duell **(1994)** is used here.

In this analysis, it is assumed that the collected velocity measurements are normally distributed. The sample standard deviation (s) at a single measurement point is calculated using the following equation:

$$s = \sqrt{\frac{\sum_{i=1}^{N} (u_i - \bar{u})^2}{N - 1}} \qquad (4.16)$$

where u is the local velocity measurement and N, the sample size. The uncertainty (λ) of the measurement can then be estimated using t-distribution in the following way:

$$\lambda = \frac{\tau\, s}{\sqrt{N}} \qquad (4.17)$$

where τ is the critical value of the t-distribution, dependent on the selected confidence level and degrees of freedom (df = N-1).

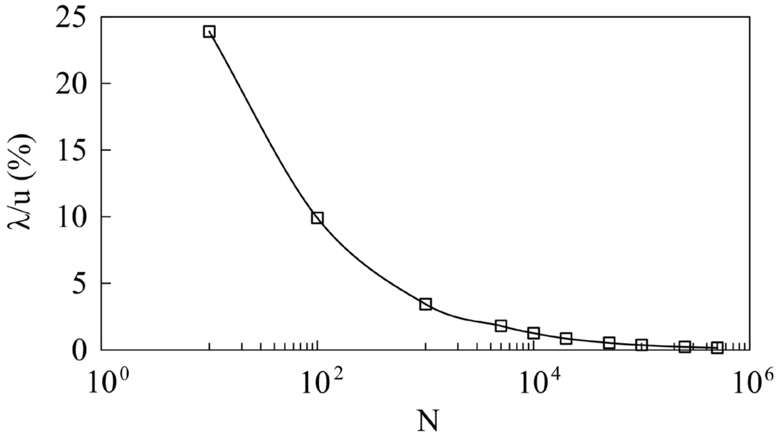

Fig. 4.41 Changes in statistical velocity uncertainty with increasing sample size close to the rear free stagnation point in the model base wake

The statistical velocity uncertainty will vary depending on positions within the flow. Of particular interest are the uncertainty values within the near wake of the model and outside in the freestream flow. The maximum local uncertainty is expected at a point of highest flow fluctuations and lowest mean velocity. For this reason, the uncertainty here is estimated close to the rear free stagnation point in the wake. Based on the number of samples $N = 500000$, the local sample standard deviation at the free stagnation point is calculated to be $s = 4.3983$m/s using equation 4.16. Subsequently, the resulting uncertainty in this position is $\lambda = \pm 0.012$m/s, based on equation 4.17 and $\tau = 1.96$ found in the statistical table for t-distribution and 95% confidence level. Based on the local mean velocity of $u = 7.5$m/s, this yields an approximate error of 0.16% (or 0.04% with respect to freestream velocity). In the same position, the change in measurement error with increasing sample size is determined for a range of $10 < N < 500000$; the results are presented in **Fig. 4.41**. It is important to note that for smaller sample sizes within the range, the critical τ value should be adjusted accordingly ($\tau = 2.262$ for $N=10$, $\tau = 1.984$ for $N=100$, $\tau = 1.96$ for $N > 600$). As can be seen in **Fig. 4.41**, the local error reduces sharply within the first 5000 samples, with the error of 1.8% at N=5000; beyond 20000 samples, the error decreases significantly below 1%. Using the same method, the mean velocity error within the steady freestream flow is estimated at 0.01%.

The statistical uncertainty of the rms fluctuating velocity (e) is estimated using the chi-squared distribution from the following equation:

$$N = 1 + 0.5\left(z + \sqrt{2(N-1)-1}\right)^2 (1-2e) \qquad (4.18)$$

where z is the critical value for the chi-squared distribution. For large sample sizes (N>100), the approximations are normally made using the normal distribution, resulting in $z = 1.96$ in equation 4.18 for 95% confidence level. Therefore, for N=500000, the error of the measured u_{rms} is less than 0.2% with 95% confidence.

During the experiments, the freestream flow velocity is set with the precision of ±1m/s. The overall uncertainty of the HWA velocity measurement will be, therefore, a sum of this precision and the previously estimated statistical uncertainty. Based on this, the resulting maximum uncertainty of the measured velocity is $\Delta u^* = \pm 0.034$ for $U_\infty = 30$m/s, and $\Delta u^* = \pm 0.027$ for $U_\infty = 37$m/s.

4.7 Pressure measurements

Surface pressures are measured on the trailer base at 64 equally spaced positions using a Scanivalve MPS-4264. The measurement positions, as presented in **Fig. 4.42**, are identical for both Baseline 1 and Baseline 2. Each surface tap is 0.8mm in diameter and connected to the port of the scanner via a 90 mm long (1 mm internal diameter) connecting silicon tubing. A wireless communication system mounted inside the trailer and connected to the scanner is configured to transmit data to a PC. This system comprises a Belkin N100 wireless access point connected to a battery power source. Data are sampled for a total of 60 seconds at 800 Hz, giving N=48000 samples for subsequent post-processing. In all tests, reference static pressure is measured at a port located on the side of the test section directly adjacent to the trailer base. A single pneumatic tube channelled out of the trailer and test section and connected to the port is used for this purpose. To obtain surface pressure maps on the base, multiple wind tunnel test runs are conducted. In total, three separate tests, each taken over 20 sec intervals and independently of HWA and drag measurements, are acquired and averaged. The results are presented in terms of the pressure coefficient (Cp) calculated using the following equation:

$$\mathrm{Cp} = \frac{2(\mathrm{p}' - \mathrm{p}_\infty)}{\rho \mathrm{U}_\infty^2} \qquad (4.19)$$

where p' and p_∞ are instantaneous and freestream static pressures, respectively. The rms fluctuating pressure coefficient (Cp_{rms}) is then obtained in the following way:

$$\mathrm{Cp}_{\mathrm{rms}} = \sqrt{\frac{\sum_{i=1}^{N}(\mathrm{Cp}_i - \overline{\mathrm{Cp}})^2}{N}} \qquad (4.20).$$

Comparisons between configurations are also made in terms of the average base pressure coefficient (Cp_b) and the trailer base drag coefficient with respect to the model frontal area A (C_{DTb}), which are calculated using the following equations:

$$\mathrm{Cp}_\mathrm{b} = \frac{\sum \mathrm{Cp}}{64} \qquad (4.21)$$

$$\mathrm{C}_{\mathrm{DTb}} = -\tfrac{1}{A}\int \mathrm{Cp}\cdot \mathrm{dA}_\mathrm{T} \approx -\tfrac{1}{A}\textstyle\sum_{i=1}^{64} \mathrm{Cp}\cdot \mathrm{dA}_\mathrm{T} \qquad (4.22)$$

where A_T is the frontal area of the trailer, and the dA_T segments are indicated in **Fig. 4.42**.

4.7.1 Error correction

The provision of silicon tubing connection between the tap on the model base and the corresponding port of the Scanivalve is expected to produce signal attenuation and resonance, distorting the actual measurement **(Sims-Williams and Dominy, 1998)**. To minimise these distortions, the connecting tubing length and internal diameter are kept minimal. For all ports, the tubing length also remains identical, allowing standardised correction to be applied prior to further processing of the data. The method used in this work is similar to that of Sims-Williams and Dominy **(1998)**, based on an experimentally derived function. For this purpose, prior to testing, the frequency response characteristics of the connecting tube are assessed against a Bruel and Kjaer 4133 laboratory standard microphone up to 400 Hz. The function is then applied to all presented data, correcting both the magnitude and phase of the recorded signal.

To mitigate random errors and assess the repeatability, three independent measurements are taken and subsequently averaged for each presented configuration. Additionally, data is also acquired for the initial and final “wind-off” states, used for spectral analysis of the pressure signals.

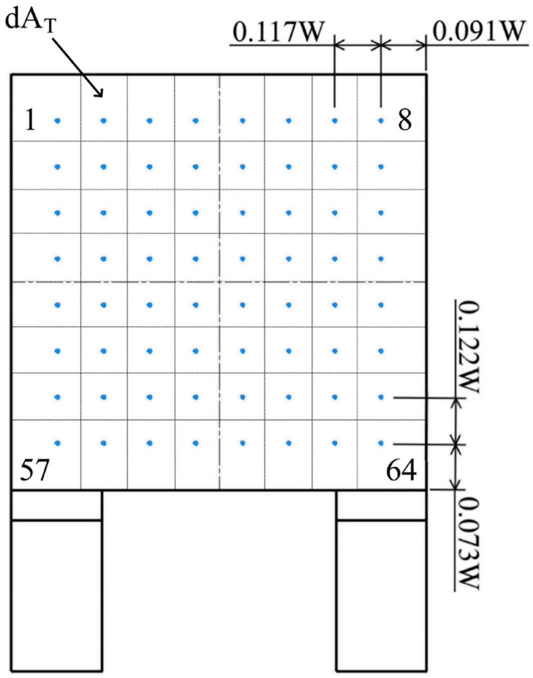

Fig. 4.42 Base pressure measurement positions

4.8 Blockage corrections

The solid blockage ratio of the model alone in the test section is 10.0%, for both Baseline 1 and Baseline 2 (identical A). With the top and side mounting struts in place, the ratio increases to 11.2% and 10.8%, respectively. The front mounting systems' small frontal areas result only in negligible increases in blockage; therefore, it is assumed unchanged. Though these blockage ratios are relatively high and can have a significant impact on the absolute magnitude of the results, where the blockage remains constant between compared configurations, no corrections are applied (**Chapters 5, 7**). In these cases, any blockage corrections would only serve to offset the results obtained equally, making little fundamental change to the findings. However, in cases where the configurations being compared have varying blockage ratios, application of corrections is necessary to ensure valid results. For this reason, in this thesis, blockage corrections are applied to all results described in the assessment of model-mounting techniques (**Chapter 6**). Additionally, results for the various trailing edge modifications (**Chapter 8**) are also corrected for blockage; Mercker's method **(Mercker, 1986)** is used throughout. Once adjusted for zero yaw conditions, the method corrects the dynamic pressure in the following way:

$$\frac{q}{q_m} = \left[1 + \frac{2S_C}{\sqrt{\pi}}\left(\frac{2A_f}{\sqrt{2L_f V_f}}\right)\left(\frac{2V_f}{(2A_C)^{3/2}}\right) + \frac{A_f}{A_C}\left(\frac{1}{4}C_{Dfm} + \eta\right)\right]^2 \qquad (4.23)$$

where A_f, L_f, V_f are the frontal area, length, and volume of the entire system, including the model and mounting struts, respectively, A_C, the cross-sectional area of the test section, and C_{Dfm}, the measured total model drag coefficient based on A_f. The shape factor of the test section (S_C) is defined as $S_C=0.36[(W_C/H_C)+(H_C/W_C)]$, where W_C and H_C are the width and height of the test section, respectively. The variable η denotes the Mercker wake blockage coefficient, with $\eta=0.41$ used as recommended by Cooper **(1998)**. Subsequently, the corrected drag coefficient (C_{Df}, based on A_f) is calculated using the following equation:

$$C_{Df} = \frac{C_{Dfm} + \frac{1}{4}C_{Dfm}^2\left(\frac{A_f}{A_C}\right)}{q/q_m} \qquad (4.24).$$

The coefficient corrected this way is then converted into the drag coefficient based on the model frontal area (A):

$$C_D = C_{Df}\,\frac{A_f}{A} \qquad (4.25).$$

Chapter 5

Assessment of the moving ground facility

One part of the experimental setup optimisation process focused on the assessment of the moving ground facility. The results of this investigation are detailed in this chapter. With some questions regarding ground simulation still unanswered, particularly with respect to higher ride-height vehicles, this investigation seeks to provide insight into how the different conditions and wheel rotation affect the unsteady wake of a HGV model. All experiments were conducted using Baseline 1 in the top mounting configuration (described in **Section 4.3.2**) to eliminate any possible support interference close to the ground. Differences between stationary and moving ground conditions for drag coefficients, base pressures, and wake dynamics are explored, with particular focus on the time-dependent characteristics.

The results presented in this chapter have been published as Rejniak and Gatto **(2020)** and are reproduced here with some changes under the Creative Commons Attribution 4.0 International License (https://creativecommons.org/licenses/by/4.0/).

5.1 Drag coefficients

First, the differences in mean drag coefficients obtained for both moving and stationary ground conditions (denoted MG and SG respectively) are assessed; **Table 5.1** summarises these results. With moving ground use, marginal reductions in both total (C_{DM}) and trailer (C_{DT}) drag measurements are evident, although the C_{DM} variation is noted to be within experimental uncertainty. Similar trends with ground simulation were also found by Sardou

(1986), Fago, Lindner and Mahrenholtz **(1991)**, Le Good et al. **(1998)**, Geropp and Odenthal **(2000)**, and Krajnović and Davidson **(2005)**. Overall, total drag results for both configurations are in good agreement with Allan **(1981)** ($C_{DM} \approx 0.75$).

Considering C_{DT} for each condition, the trailer itself is shown to make a small contribution to total drag for both. For the stationary ground case, this is representative of 5.6%, more than double that observed for moving ground (2.6%), with both being lower than expected at full-scale (≈25 – 35% - **Section 2.2.3**). Many factors can account for this result. As described in **Section 2.2.1**, the size of the tractor-trailer gap can have a significant influence on trailer drag. With small gaps, as is in the current setup, lower surface pressures are known to exist on the trailer front, resulting in overall reductions in trailer drag component **(Hammache and Browand, 2004)**. Frank and Turney **(2016)** also showed this effect can be significant, with a trailer absent any undercarriage/wheel contributions (similar to the current setup) being an overall negative contributor to total drag. Reynolds number and elevated solid model blockage ratio can also be further contributory factors **(Zdravkovich, 2003; Wood, 2015)**. It is important to note however, that these results do not preclude direct comparison between the two equally affected configurations.

	C_{DM} (±0.018)	**C_{DT}** (±0.010)
SG	0.729	0.041
MG	0.723	0.019

Table 5.1 Total model (C_{DM}) and trailer (C_{DT}) drag coefficients for stationary and moving ground conditions

5.2 Time-averaged base pressure

Figure 5.1 presents the mean (Cp) and rms (Cp_{rms}) static pressure coefficient distributions over the trailer base, with vehicle centreline ($y^* \approx 0$) relative difference (MG-SG) also included (**Fig. 5.1(c)**). In each case, Cp contours remain topologically similar. A large area of low pressure acting within $0.5<z^*<1.1$ as well as an isolated region of higher pressure located close to the top centreline position ($1.3<z^*<1.35$) are evident for both. These trends reflect a well-known topology typical to such vehicle configurations, in agreement with the

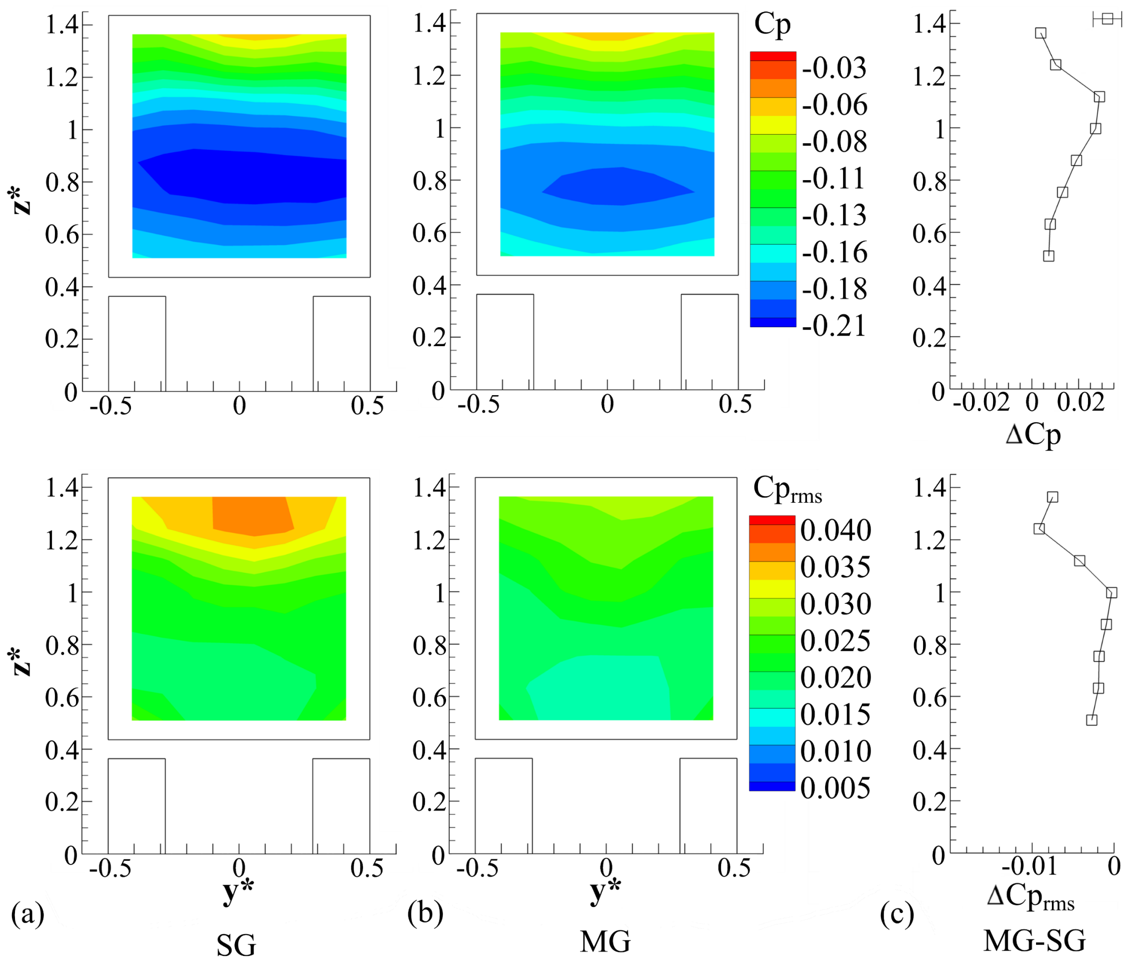

Fig. 5.1 Trailer base pressure coefficient results: (a) SG, (b) MG, (c) MG-SG difference along $y^*\approx0$

literature **(Gutierrez et al., 1996; McCallen et al., 1999; Storms et al., 2001; Bayraktar et al., 2005; Horrigan et al., 2007)**. It arises as a result of the recirculating wake encompassing a proximate bottom vortex core responsible for the minimum Cp magnitudes identified at $z^* \approx 0.7$-0.8, as well as upper recirculating flow impingement reflected in higher magnitudes adjacent to the top edge ($y^*\approx0$, $z^*\approx1.35$ – **(Perry, Pavia and Passmore, 2016; Castelain et al., 2018; Pavia, Passmore and Sardu, 2018)**). The former appears subtly more pronounced for the stationary ground case, suggesting a stronger influence. The implications of this finding will be discussed further in **Section 5.3**. In **Fig. 5.1(c)**, maximum variation of $\Delta Cp \approx 0.03$ is shown just above the base centre ($z^*\approx1.1$), signifying a local pressure increase with moving ground use. The reduction in C_{DT} (**Table 5.1**) for this condition supports this finding, as does the increase (9%) in the average base pressure coefficient (Cp_b), and the corresponding decrease in the trailer base pressure drag coefficient (C_{DTb}), indicated in **Table 5.2**. Additionally, a comparison of C_{DTb} (**Table 5.2**) and C_{DM}

(**Table 5.1**) shows that the influence of the tractor-trailer gap at reducing overall trailer drag is indeed significant as discussed in **Section 5.1**, with C_{DTb} alone responsible for between 14.8% (MG) and 16.2% (SG) of total drag.

	Cp_b (±0.006)	**C_{DTb}**
SG	-0.169	0.118
MG	-0.154	0.107

Table 5.2 Average base pressure (Cp_b) and trailer base pressure drag (C_{DTb}) coefficients for stationary and moving ground conditions

Results for Cp_{rms} show analogous trends, with similar general topologies accompanied by subtle magnitude differences. For the stationary ground case, a comparative increase in fluctuations near the top ($1<z^*<1.35$) is evident in **Fig. 5.1(c)**, reflective of a more intense unsteady flow impingement on the base **(Lajos, Preszler and Finta, 1986; McArthur et al., 2016; Perry, Pavia and Passmore, 2016; Pavia and Passmore, 2018; Wang et al., 2020)**. This implies moving ground use under these conditions imparts flow stability to the upper base portions (maximum $\Delta Cp_{rms} \approx -0.01$ at $z^* \approx 1.25$). This influence is seen to be very localised, with results below $z^* \approx 1$ exhibiting only a limited variation.

Further insight can be gained from the Cp crosswise and heightwise spatial gradient distributions presented in **Fig. 5.2**. At first inspection, $\partial Cp/\partial y$ topologies again show a lot of similarities, with regions subtending the top ($|y^*| \approx 0.1$-0.3, $z^* \approx 1.35$) and side edges ($|y^*| \approx 0.3$-0.4, $0.8<z^*<1.1$ - **Fig. 5.2(a-b)(i)**) exhibiting little change, suggesting insensitivity to moving ground use. Upon closer examination, however, subtle variations are observed for $\partial Cp/\partial y$ within locations directly above the wheels ($|y^*| \approx 0.3$-0.4, $0.5<z^*<0.6$), indicating marginally more wheel wake influence. The mechanism responsible for this result is discussed in **Section 5.3**.

In contrast, vertical Cp gradient distributions (**Fig. 5.2(a-b)(ii)**) appear decidedly less chaotic with a clear transition from negative, close to the bottom base edge, to positive magnitudes with increasing height. These trends are consistent with the significant heightwise base pressure variations caused by the proximate wake, with the low-pressure vortex core at the bottom shifting to a higher pressure flow impingement at the top **(Pavia**

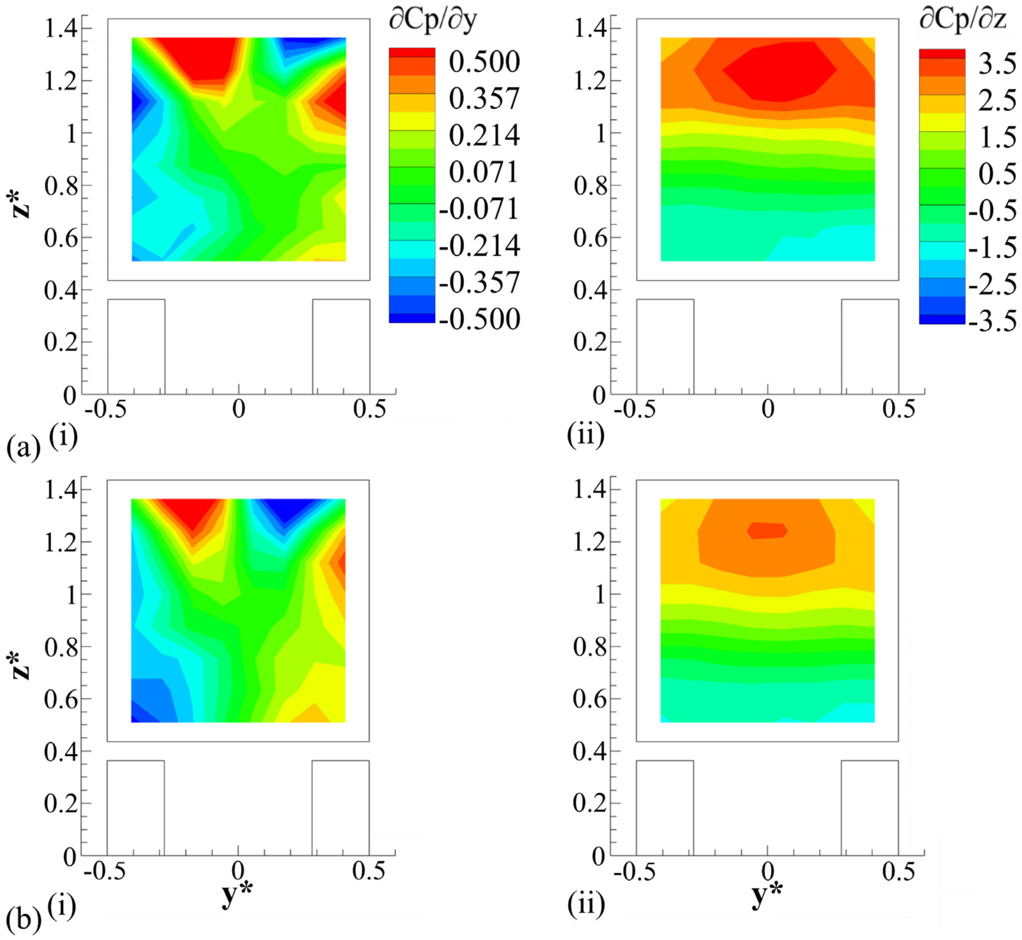

Fig. 5.2 Spatial base pressure coefficient gradients: (a) SG, (b) MG; (i) ∂Cp/∂y, (ii) ∂Cp/∂z

and Passmore, 2018; Wang et al., 2020). Additionally, the relative significance of the heightwise changes is manifested in ∂Cp/∂z magnitudes being an order higher than ∂Cp/∂y. Comparisons between the moving and stationary ground conditions show the upper base regions (z*>1) affected more for the latter (**Fig. 5.2(a)(ii)**), indicating the base impingement to be stronger for this case. Considering this result alongside Cp presented in **Fig. 5.1**, the development of a more compact wake with use of a stationary ground is inferred.

Figure 5.3 also provides the spatial gradients of Cp_{rms}. The crosswise gradient distributions (**Fig. 5.3(a-b)(i)**) capture the unsteady wheel wake signatures for both setups (|y*|≈0.35, z*≈ 0.55), indicating a general insensitivity to the ground condition. Some differences, however, are found in the upper base half (|y*|≈0.1-0.4, 1.1<z*<1.3), with more elevated $\partial Cp_{rms}/\partial y$ evident for the stationary ground case (**Fig. 5.3(a)(i)**) relative to **Fig. 5.3(b)(i)**. These differences are reflective of the rise in unsteadiness for the former as indicated in **Fig. 5.1(a)**. Within the same region, the $\partial Cp_{rms}/\partial y$ magnitudes for the moving ground case (**Fig. 5.3**) are found much weaker, more distributed, and displaced to lower positions (|y*|≈0.1-0.4, 1<z*<1.2). These results confirm a shift towards a more quiescent base flow under these conditions. Pavia and Passmore **(2018)** identified a similar stabilising effect on the wake of a Windsor body with rotating wheels.

The unsteady wheel wake signatures are also captured in the heightwise Cp_{rms} gradients (**Fig. 5.3(a-b)(ii)**) close to the bottom base corners (|y*|≈0.35, z*≈ 0.55). From this perspective, however, the influence appears more pronounced for the stationary ground case, indicating a weak heightwise sensitivity to moving ground use. The implications of this finding are discussed further in **Section 5.4.4**. Elevated magnitudes are also found in the top base half (1<z*<1.3). These results provide further support for the significant unsteadiness imparted to this region of the base.

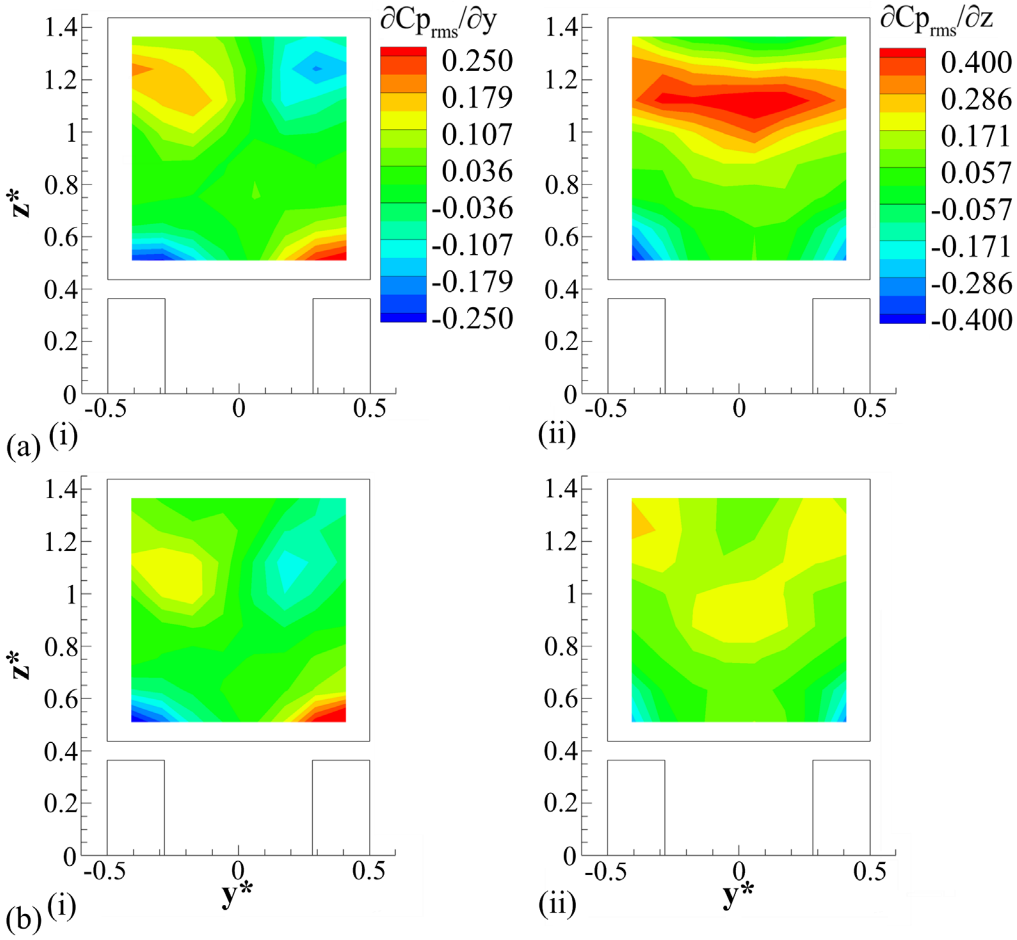

Fig. 5.3 Spatial base pressure coefficient gradients: (a) SG, (b) MG; (i) $\partial Cp_{rms}/\partial y$, (ii) $\partial Cp_{rms}/\partial z$

5.3 Time-averaged wake flow-field

The time-averaged results within the base wake are now considered, with streamwise velocity (u*) magnitudes from planes T2-T4 presented in **Fig. 5.4**. Across the three planes, lower u* contours can be used to map downstream wake development. The flow-field appears symmetric about $y^* \approx 0$, with little variation in wake height and bounding freestream flow around the model profile. Above $z^* \approx 1.5$, the influence of the overhead support strut is also captured ($y^* \approx 0$), most evident in T2 and T3 (**Fig. 5.4(a-b)(i-ii)**). The implications of this observation are discussed, in detail, in **Chapter 6**. At T2 regions of the lowest u* magnitude ($u^* < 0.35$) reside directly downstream of the trailer base and represent the measurements made within the recirculating flow. Magnitudes are seen to reduce from the top towards the floor, with the minima found in the bottom base half ($z^* < 0.8$) coinciding with the location of minimum Cp (**Fig. 5.1**), indicative of the central position of the lower wake vortex. At T3 the wake can be seen to extend to ground level, attaining closure by T4.

Comparisons of the different ground conditions (**Fig. 5.4(a-b)**) reveal several distinct disparities. As would be expected, for the stationary ground case, the presence of the ground boundary layer is significant. This is evident in the increasingly prominent area of lower u* magnitude fluid below $z^* \approx 0.25$ either side of the model ($|y^*| > 0.5$), becoming most obvious at T4 (**Fig. 5.4**(a)(iii)). In contrast, with moving ground, some remnants persist, but are found to impart significantly less impact to the surrounding flow-field. This effect is best reflected in the wake width close to the ground being more consistent (**Fig. 5.4(b)(iii)**).

Another distinctive characteristic evident with stationary ground use is the area of low u* magnitude developing beneath the trailer. This feature is most obvious in T2 and T3, between $|y^*| < 0.3$ and $z^* < 0.3$. A similar effect has been previously identified behind a car model with stationary ground use by Sardou **(1986)** as “Ground Delamination Bubble”. In this work, the name Ground Separation Region (GSR) will be adopted to indicate this region. McArthur et al. **(2016)** and Castelain et al. **(2018)** also described a similar phenomenon with reducing ground clearance and underbody mass flux, respectively. In all cases, the region develops as a result of strong ground adverse pressure gradients and produces enhanced upwash towards the base wake characterised by lower pressure. Here, this is reflected in the “arch-like” distortion in **Fig. 5.4(a)(i)** at $|y^*| < 0.4$ and $0.5 < z^* < 0.6$. At T2 (**Fig. 5.4(a)(i)**), the GSR dominates the lower wake regions ($|y^*| < 0.4$ at $z^* < 0.5$). Further downstream at T3 (**Fig. 5.4(a)(ii)**), it can be seen to merge with the base wake, having only limited impact at T4

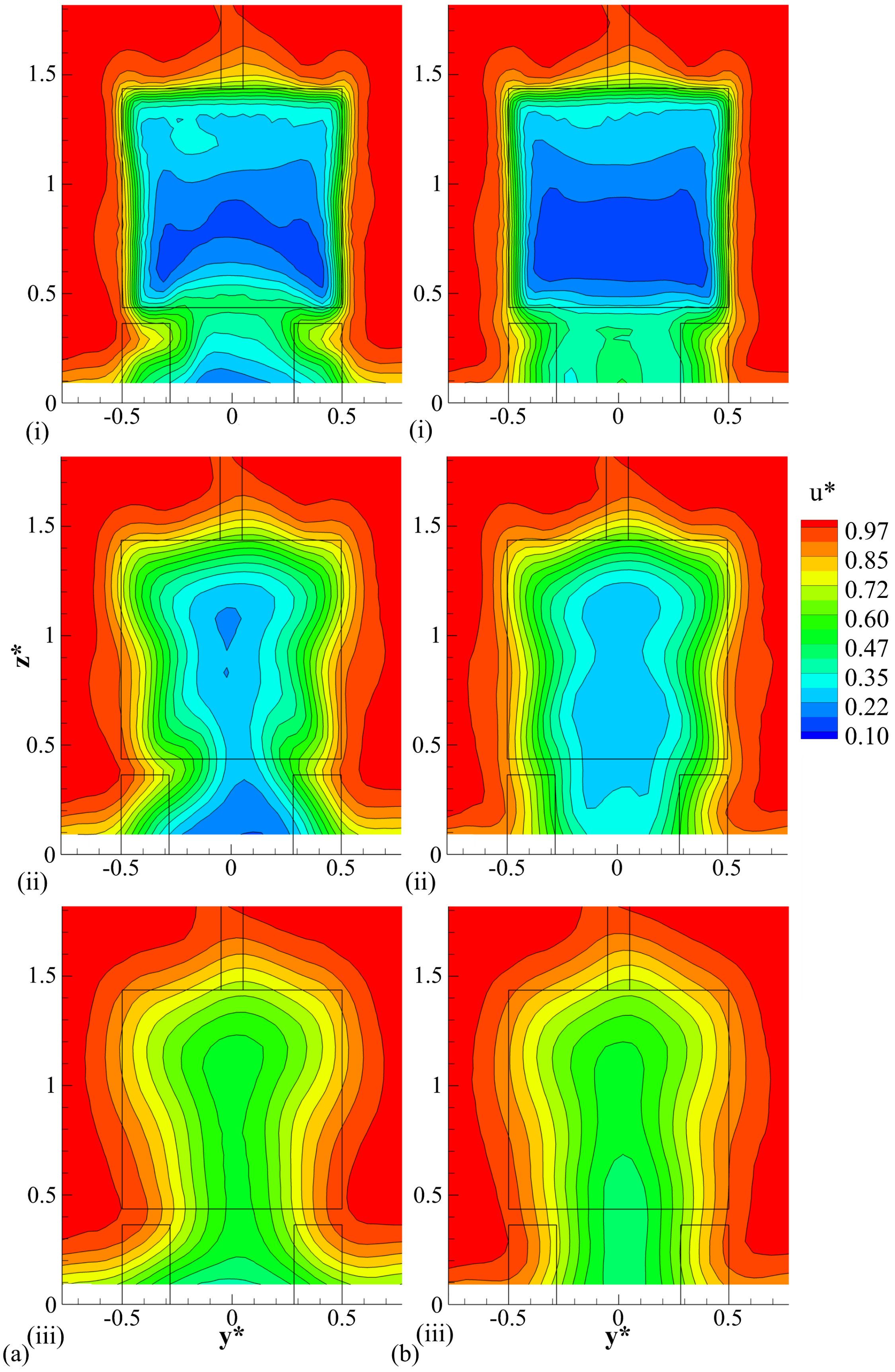

Fig. 5.4 Streamwise velocity (u*) contours with: (a) SG, (b) MG; (i) T2, (ii) T3, and (iii) T4

(y*≈0, z*≈0.1 – **Fig. 5.4(a)(iii)**). With moving ground use (**Fig. 5.4(b)(i-iii)**), there is no evidence of the GSR at any plane.

Further subtle variations can be identified when considering the wake width in T2. For the moving ground case, near constant wake width is shown in **Fig. 5.4(b)(i)**. With stationary ground use (**Fig. 5.4(a)(i)**), the flow within the wheel-trailer junction area can be seen to entrain more rapidly inboard, triggering a localised wake contraction at z*≈0.3. This originates from the flow around and in-between the rear wheels and bottom trailer surface, leading to the encroachment of higher velocity flow beneath each base bottom corner (|y*|≈0.4 at z*≈0.3 – **Fig. 5.4(a)(i)**). This feature offers an explanation for the reduced wheel wake influence identified with stationary ground use in **Fig. 5.2(a)(i)**. The contraction is found to persist downstream to T3 (**Fig. 5.4(a)(ii)**) and eventually T4 (**Fig. 5.4(a)(iii)**), where the wake exhibits markedly more inconsistent width with height.

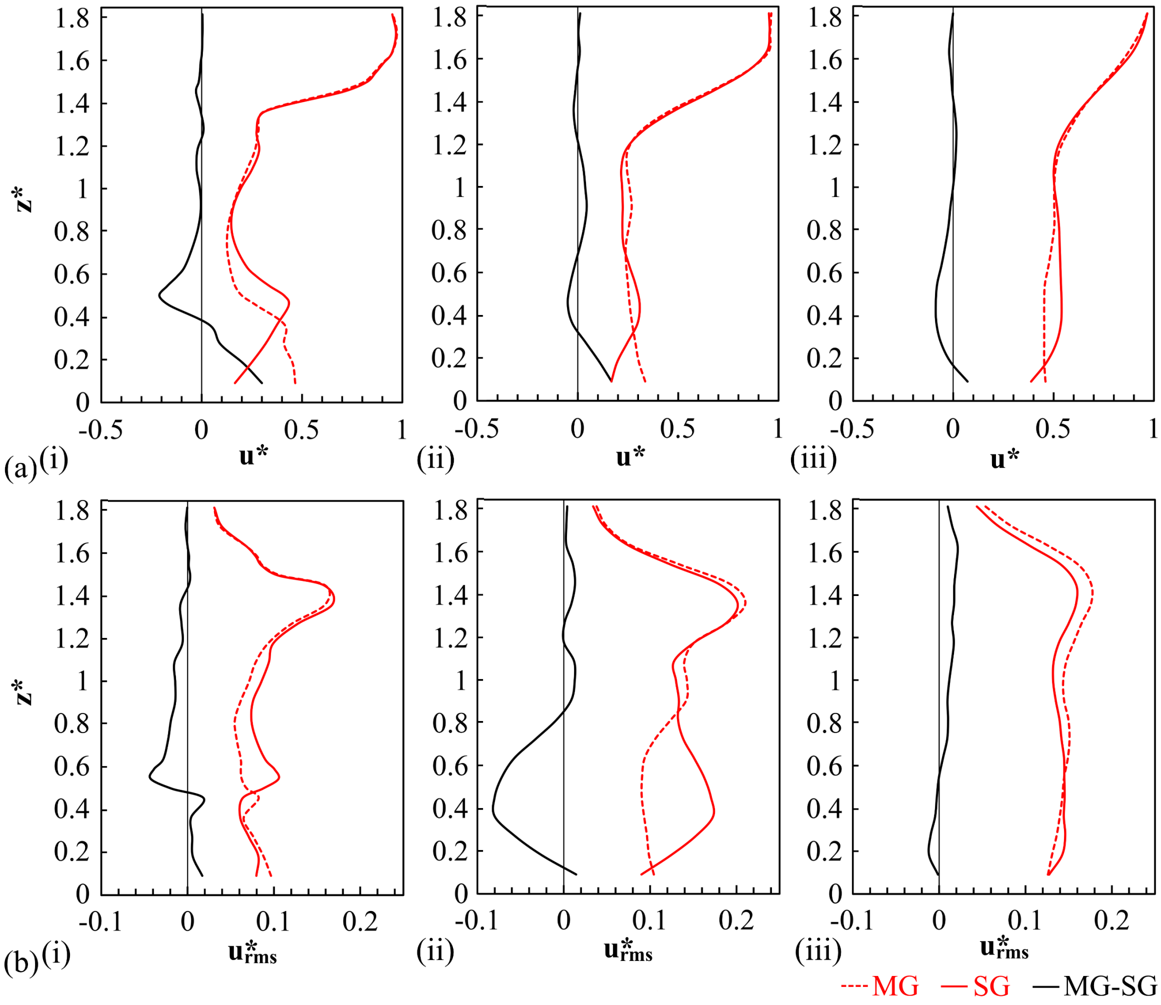

Fig. 5.5 Comparisons at y*≈0: (a) u* and (b) u_{rms}*; (i) T2, (ii) T3, (iii) T4

Figure 5.5 explores these differences further with local differences in u* and u_{rms}* in planes T2-T4. In **Fig. 5.5(a)(i)** (T2), while the trends remain near-identical in the upper portions, most variability can be observed below z*≈0.8. For the stationary ground case, the flow is faster at z*≈0.5 (Δu*≈-0.2), where the upwash emanating from the underbody entrains towards the base wake, consistent with the "arch-like" distortion identified in **Fig. 5.4(a)(i)**. Moving towards the ground, this trend is reversed at lower z* locations, with a maximum increase found at z*≈0.091 for moving ground, as the development of the GSR and boundary layer is suppressed. Further downstream (**Fig. 5.5(a)(ii-iii)**), this trend persists, though with notably diminishing magnitude differences (Δu* ≈ ±0.1 at T4).

The results for u_{rms}* are presented in **Fig. 5.5(b)**. At z*≈1.42, elevated u_{rms}* values map the top separated shear layer, which can be seen to gradually broaden with downstream development from T2 to T4. In both cases, the local trends remain similar, indicating little sensitivity to moving ground and suggesting no substantial disparity in boundary layer characteristics at the base edge upon separation between the two setups. Below z*≈0.8 at T3 (**Fig. 5.5(b)(ii)**), significant reductions in flow unsteadiness of up to Δu_{rms}*=-0.07 are evident for the moving ground case, with only limited sensitivity shown at the preceding (T2 - **Fig. 5.5(b)(i)**) and following (T4 - **Fig. 5.5(b)(iii)**) planes.

Figure 5.6 presents the differences in crosswise (v*) and heightwise (ω*) velocities within the wheel-trailer junction at z*≈0.3 (**Fig. 5.6(a)**) and y*≈-0.4 (**Fig. 5.6(b)** – red), as well as y*≈0 (**Fig. 5.6(b)** – black). As can be seen, maximum Δv* between the two

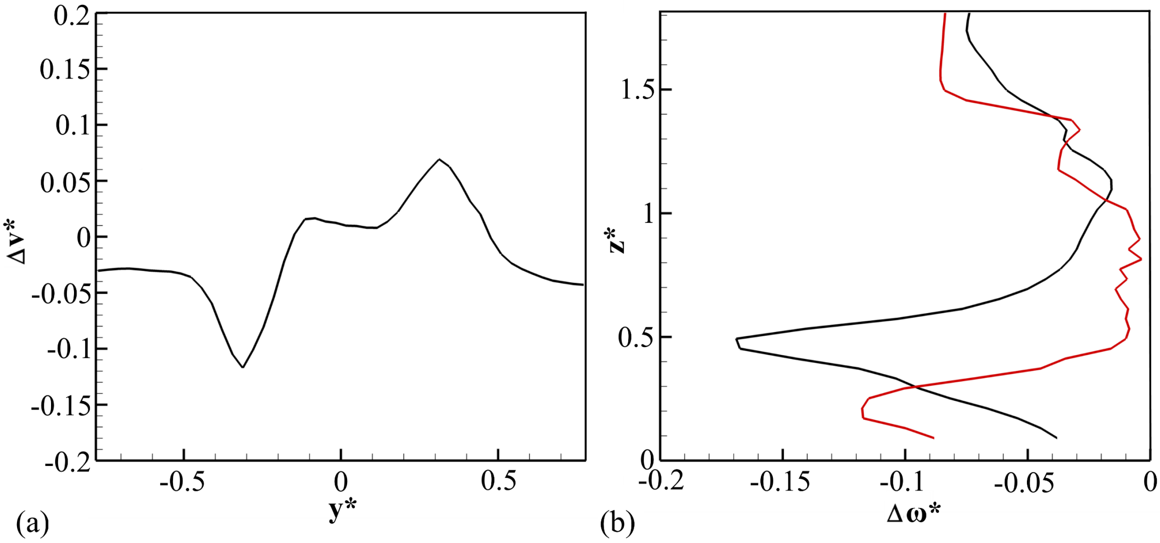

Fig. 5.6 Differences MG-SG at T2: (a) Δv* at z*≈0.3, (b) Δω* at y*≈0 (black) and y*≈-0.4 (red)

configurations in this area is significant, with Δv*≈0.07-0.11 (subtle asymmetry favouring the left side) higher directed inboard with stationary ground use. This is a consequence of the additional upwash generated locally, as quantified in **Fig. 5.6(b)**. At the vehicle centreline (**Fig. 5.6(b)** – black), the difference is comparable to that indicated for Δu* in **Fig. 5.5(a)(i)**, with up to Δω*≈-0.17. Moving outwards (**Fig. 5.6(b)** – red), this impact is found preserved, with up to Δω*≈-0.12 seen behind the rear wheel close to the ground (y*≈-0.4, z*≈0.2).

Further insight still, is provided by the contours of mean turbulent kinetic energy (K) in the plane T2 (**Fig. 5.7**). Firstly, for the stationary ground case (**Fig. 5.7(a)**), a similar inwardly skewed topology behind the wheels is again evident. Secondly, the results highlight significant variations in turbulence production dependent on ground simulation. For both conditions, **Fig. 5.7(a)** and **(b)** show elevated K downstream of the wheels. However, with stationary ground, significantly lower peak magnitudes are indicated, which is a result of the disturbance caused by the enhancement in local crossflow, as identified in **Fig. 5.6**. For the moving ground case, **Fig. 5.7(b)** shows more concentrated, elevated K in this region (|y*|≈0.4, z*≈0.2). Additionally, higher K is also found along the sides in the upper half (|y*|≈0.4-0.5, 0.7<z*<1.4) with stationary ground, indicating disparities in the flow unsteadiness within the shear layers, providing further support for the results discussed in **Section 5.2**.

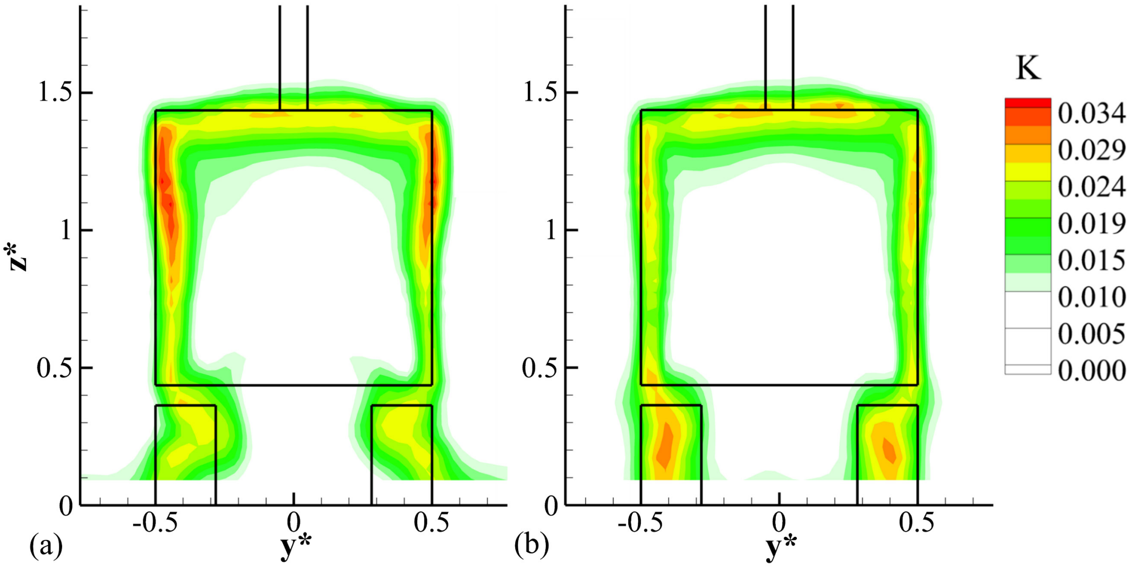

Fig. 5.7 Mean Turbulent Kinetic Energy (K) at plane T2 for: (a) SG and (b) MG

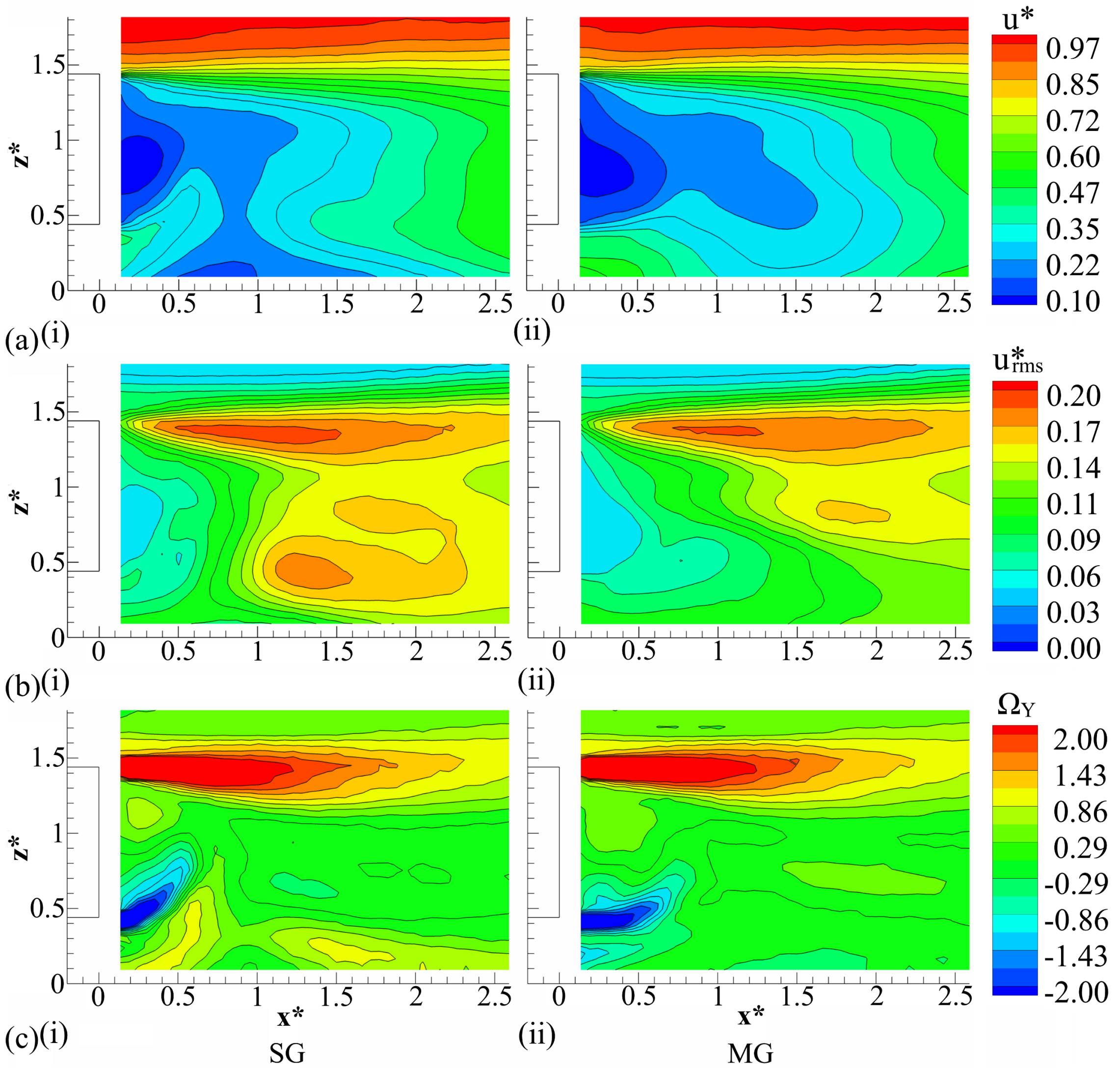

Fig. 5.8 Contours at SV1 for SG (i) and MG (ii) conditions: (a) u*, (b) u_{rms}*, and (c) Ω_Y

Results from the streamwise perspective (plane SV1) are now considered (**Fig. 5.8**). In **Fig. 5.8(a)**, the wake is again represented by lower u* magnitudes ($u^*<0.35$) directly behind the trailer and seen convecting downstream. For both conditions, lowest u* magnitudes are found adjacent to the base, close to $z^*\approx0.8$, as already identified in **Fig. 5.4**, with undisturbed freestream flow observed above model height ($z^*>1.6$). This perspective reveals the GSR to be centred at $x^*\approx0.75$ and affecting the region within $0.1<x^*<2.3$, $z^*<0.5$. The merging of the GSR and base wake is also shown, in agreement with the results from plane T3 (**Fig. 5.4(a)(ii)**), as is the area of significant upwash produced by the emanating underbody flow ($x^*\approx0.3$, $z^*\approx0.5$).

Topologies for u_{rms}* from the same perspective are also provided in **Fig. 5.8(b)**. The top separated shear layers can again be identified from these trends for both conditions, reflected in the elevated u_{rms}* downstream of the top trailer edge ($1.2<z^*<1.5$, $0.2<x^*<2.5$). These results agree with those presented in **Fig. 5.5(b)**, confirming limited sensitivity to ground simulation. Closer to the ground, **Fig. 5.8(b)(i)** also captures the GSR ($0.5<x^*<1.5$, $z^*<0.2$), which can be seen to precede a large region of elevated u_{rms}* ($1<x^*<2.55$, $z^*<0.7$). The maximum difference relative to the moving ground case is $\Delta u_{rms}^*\approx0.18$, found at $x^*\approx1.25$, $z^*\approx0.45$. Similar characteristics are also shown in **Fig. 5.5(b)(ii)**.

Figure 5.8(c) provides the results of crosswise vorticity Ω_Y. The strongest circulation is found within the top separated shear layer and the flow from beneath the trailer, with the direction indicating the tendency of the wake to achieve closure. Of particular interest are the regions of strong upwash for both conditions, where significant differences in characteristics are observed. With moving ground use, this area is seen markedly more horizontal (**Fig. 5.8(c)(ii)**). This is the expected consequence of more effective underbody flow and inhibition of the GSR, contributing to a shift in the wake balance. In the stationary ground case (**Fig. 5.8(c)(ii)**), regions of weaker co-rotating Ω_Y are also found directly up and downstream of the GSR ($x^*\approx0.5$, $z^*\approx0.2$ and $x^*\approx1.6$, $z^*\approx0.2$), being most probably generated by the preceding upwash and subsequent downwash.

Finally, **Fig. 5.9** presents the corresponding results from the horizontal perspective (plane SH1). At this position, the influence of moving ground appears much more subtle, with all results showing similar topologies. Again, the base wake is reflected in the lower u* magnitudes, with excellent flow symmetry evident for both conditions. The side separated shear layers are also captured in **Fig. 5.9(b)**, with coincident heightwise vorticity (Ω_Z) trends found very similar (**Fig. 5.9(c)**). In **Fig. 5.9(c)**, pockets of weak counter-rotating vorticity are also evident at $x^*\approx0.65$-0.75, $|y^*|\approx0.2$. Considering the results in **Fig. 5.9** qualitatively, trends of all, u*, u_{rms}* and Ω_Z, show evidence suggesting longer wake under moving ground conditions.

This hypothesis is considered more quantitatively in **Fig. 5.10**, with the streamwise evolution of u/u_{rms} ratio at $y^*\approx0$ in SH1. Duell and George **(1993, 1999)** show HWA measurements within the base wake can be used to determine the average position of the rear free stagnation point as the point of combined u minimum and u_{rms} maximum. The mean recirculation region length (x_r*) can then be estimated as the distance from the base to this location. The results in **Fig. 5.10** indicate the local minima of u/u_{rms} for both conditions, showing a 17% increase in the wake length from $x_r^*\approx1.19$ to $x_r^*\approx1.39$ with moving ground.

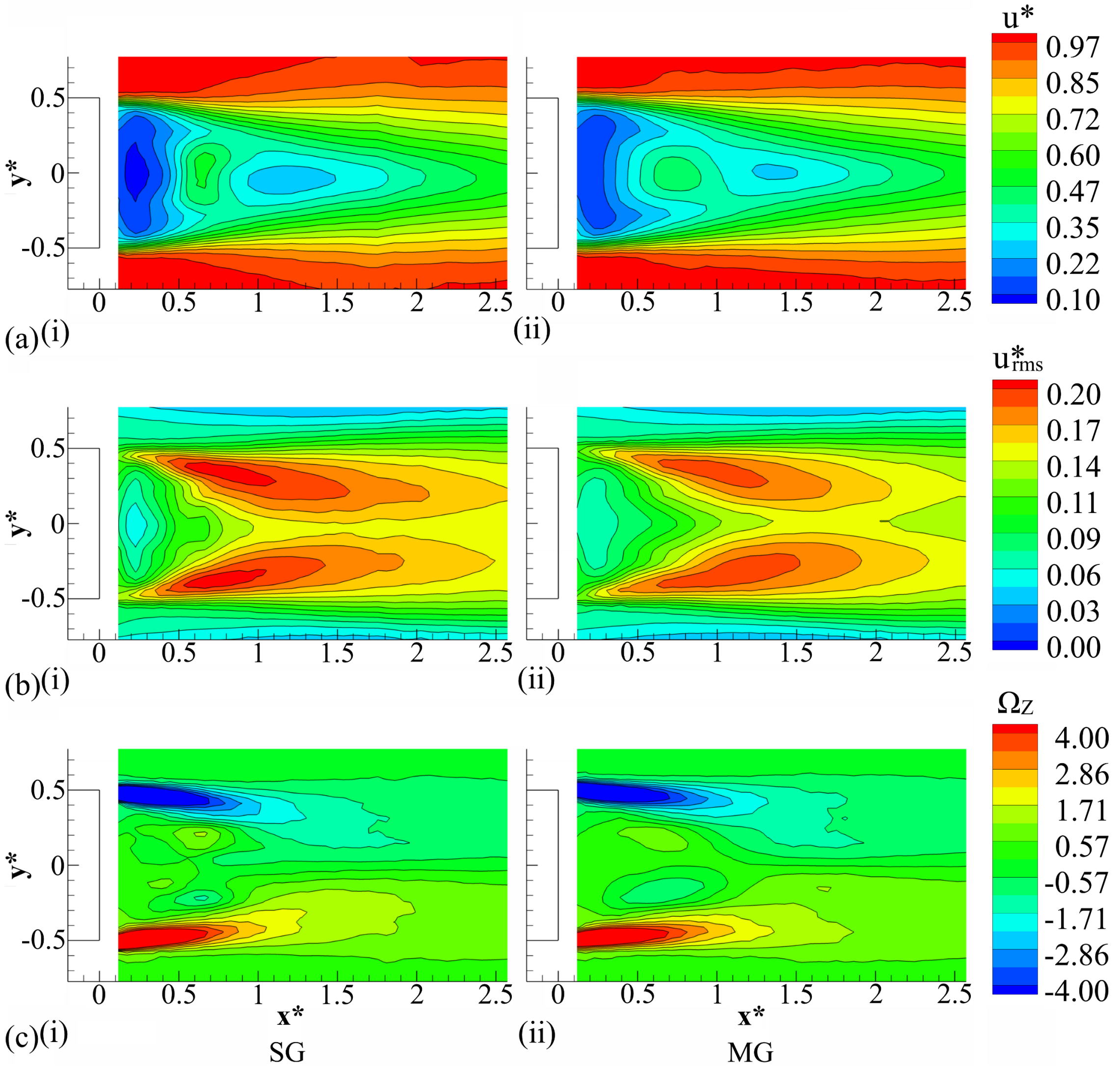

Fig. 5.9 Contours at SH1 for SG (i) and MG (ii) conditions: (a) u^*, (b) u_{rms}^*, and (c) Ω_Z

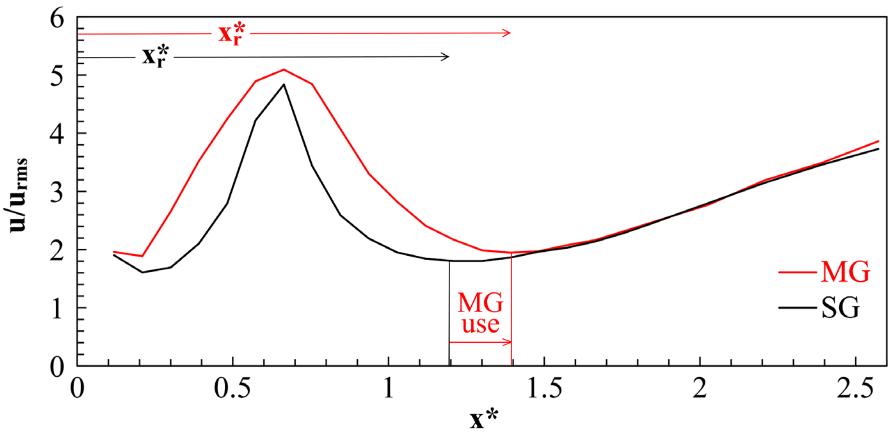

Fig. 5.10 Determination of x_r^*; plot of u/u_{rms} at $y^*\approx0$ in plane SH1

5.4 Time-dependent flow characteristics

Given some subtle differences in the time-independent results exist between the different ground conditions, the influence on the unsteady wake aspects is now evaluated. First, base pressure spectra are considered, followed by the general wake dynamics assessed from the velocity signals. Finally, velocity spectra within selected areas of interest are detailed. All pressure and velocity spectra were obtained from the average of 15 time segments (1.25s duration) and 39 time segments (0.5s duration), respectively, using a Hamming window and 50% overlap. All frequencies are normalised and presented as width-based Strouhal number (St_W), with bin widths of $\Delta St_W \approx 0.0014$ (pressure) and $\Delta St_W \approx 0.0022$ (velocity). In the following sections, selected results are presented with offset magnitudes to aid interpretation. This is indicated in the figure captions and text where necessary.

5.4.1 Base pressure spectra

Pressure spectra at selected locations on the base are presented in **Fig. 5.11**. Spectra of the signals recorded with the wind off (belt on for MG case) are also included at location 1. The results appear uniform, with little spanwise and heightwise variation, except for the positions directly above the rear wheels (57, 64). At 57 and 64, spectral magnitudes are notably higher for $St_W > 0.3$, reflective of the localised unsteadiness generated by the wheel wake for both conditions, as captured in **Fig. 5.2** and **Fig. 5.3**. Defined oscillatory behaviour is generally absent from these results at all locations. This is particularly the case for $St_W < 0.3$, where wake shedding and bubble pumping characteristic frequencies are typically expected **(Duell and George, 1999; Khalighi et al., 2001; Volpe, Devinant and Kourta, 2015; McArthur et al., 2016)**. Upon closer inspection, however, **Fig. 5.11** reveals subtle broad peaks at $St_W \approx 0.107$ and $St_W \approx 0.123$ for stationary and moving ground conditions, respectively. While particularly discernible at mid-height (25-40), these peaks are found at all base locations, suggesting a near global influence. Similar characteristics are described by Duell and George **(1993, 1999)** for the bubble pumping mechanism at $St_W \approx 0.069$, as well as Volpe et al. **(2015)** ($St_W \approx 0.11$), Khalighi et al. **(2001)** ($St_W \approx 0.098$), McArthur et al. **(2016)** ($St_W \approx 0.08$) and Pavia et al. **(2018)** ($St_W \approx 0.094$), at similar Strouhal numbers on various other models. Particularly interesting, is the increase in St_W with moving ground use, being approximately 17%; identical to the increase in the wake length indicated in **Fig. 5.10**.

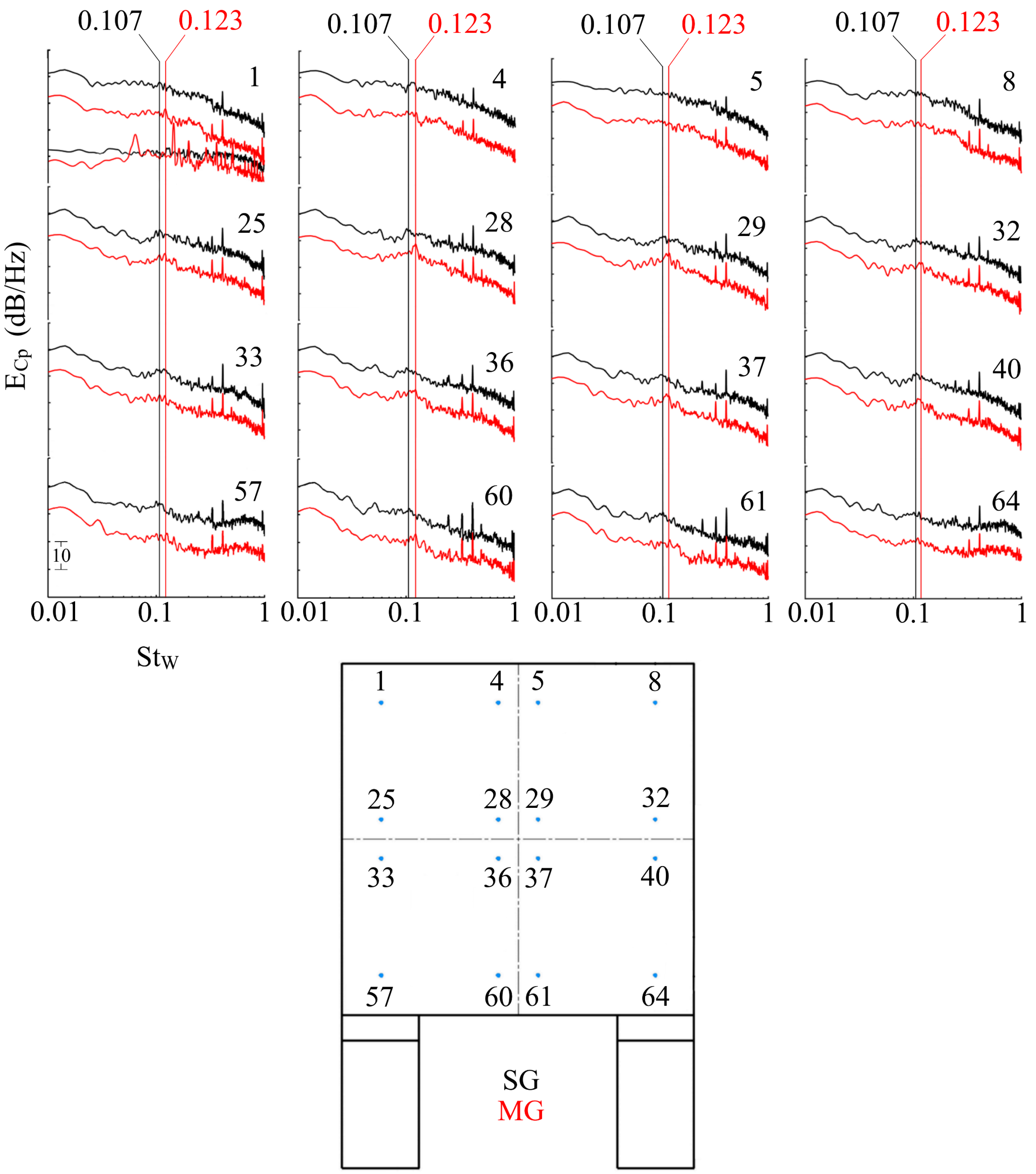

Fig. 5.11 Base pressure spectra (MG results offset by -10dB/Hz)

Further insight into the nature of these spectra is provided by the signal coherence (γ^2) and phase (ϕ) between symmetrical positions 25 and 32. These relationships were obtained using

$$\gamma^2_{1\text{-}2} = \frac{|S_{1\text{-}2}|^2}{|S_{1\text{-}1}\, S_{2\text{-}2}|} \qquad (5.1)$$

$$\phi_{1\text{-}2} = \arctan\left(\frac{\mathrm{Im}[S_{1\text{-}2}]}{\mathrm{R}[S_{1\text{-}2}]}\right) \qquad (5.2)$$

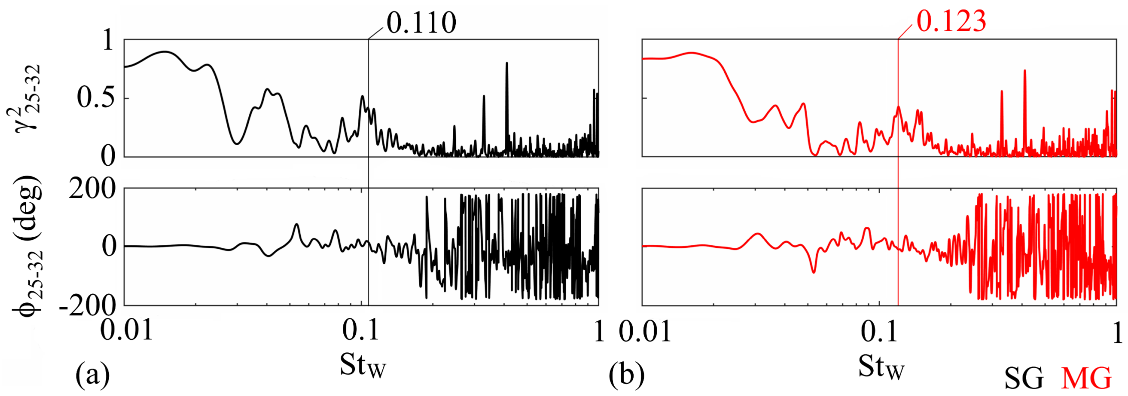

Fig. 5.12 Base pressure coherence (γ^2) and phase (ϕ) relationships between positions 25 and 32: (a) SG, (b) MG

where $S_{1\text{-}1}$ and $S_{2\text{-}2}$ are the auto-spectra of signals 1 and 2, respectively, and $S_{1\text{-}2}$, the cross-spectrum. In equation 5.2, Im and R indicate the imaginary and real parts of the function. Consequently, **Fig. 5.12** presents these results, indicating a strong coherence ($\gamma^2 \approx 0.5$) between mid-height positions 25 and 32 at the characteristic frequencies identified in **Fig. 5.11**. At these locations, the signals are also shown to act in-phase ($\phi \approx 0$), typical of the bubble pumping mode **(Duell and George, 1993, 1999; Khalighi et al., 2001)**.

5.4.2 General wake dynamics

The dynamic processes in the wake are further evaluated with velocity spectra (E_u, E_v, E_ω) presented in **Fig. 5.13**. **Figure 5.13(a)** confirms the existence of weak lateral wake shedding at $St_W \approx 0.228$ and $St_W \approx 0.279$ for the moving and stationary ground conditions, respectively. These frequencies are in general agreement with those found by Volpe, Devinant and Kourta **(2015)** ($St_W \approx 0.18$), McArthur et al. **(2016)** ($St_W \approx 0.17$), and Grandemange, Gohlke and Cadot **(2013b)** ($St_W \approx 0.17$). These results (**Fig. 5.13(a)**) also capture the bubble pumping mode for the moving ground case, identified in **Fig. 5.11** ($St_W \approx 0.121$), with the corresponding peak for stationary ground ($St_W \approx 0.107$) not clearly distinguishable. From these findings, three interesting insights can be inferred:

1. With the use of stationary ground, the bubble pumping mode is weaker.
2. At $St_W \approx 0.28$, the lateral shedding is less coherent for the stationary ground case.

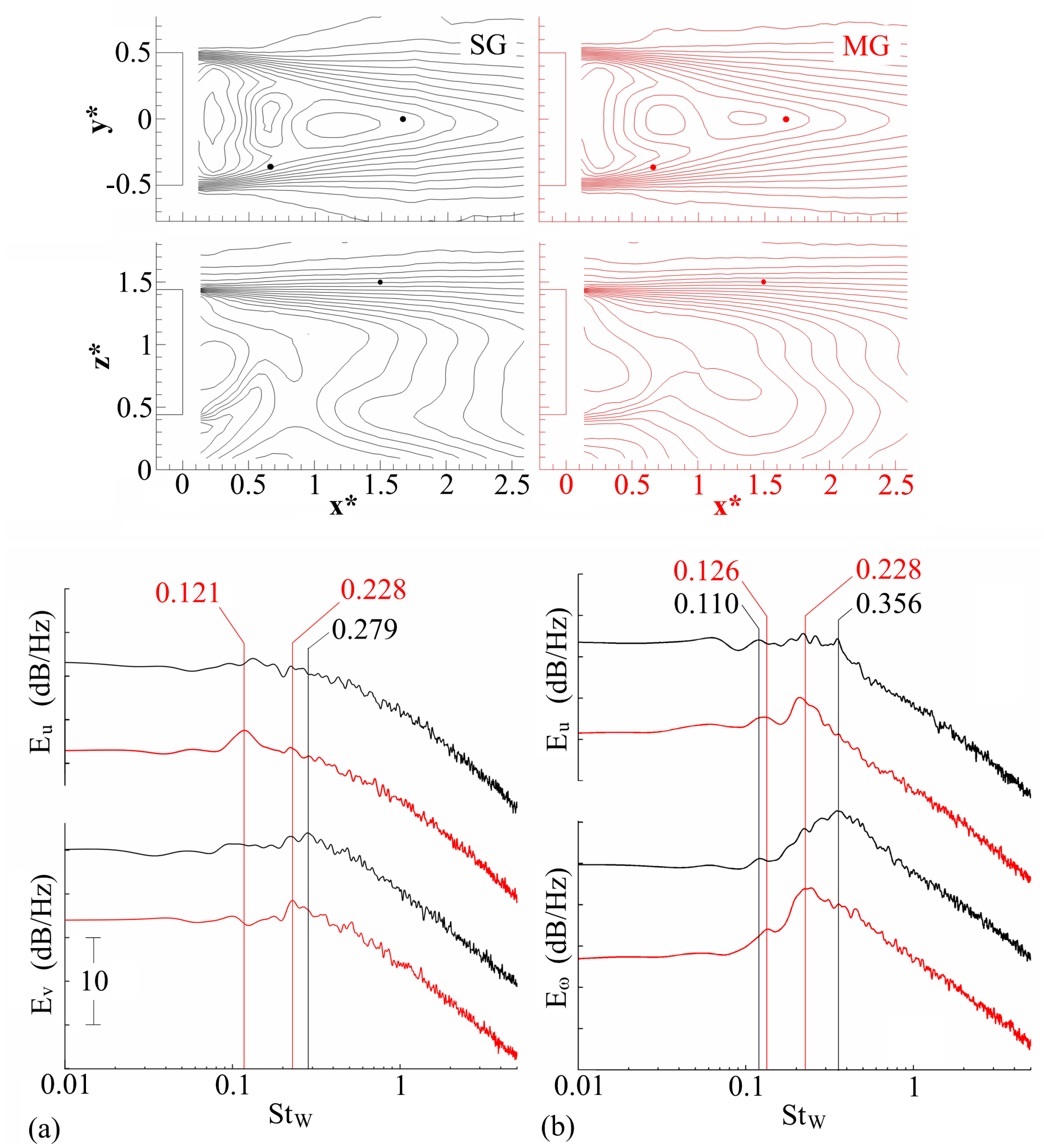

Fig. 5.13 Velocity spectra in the wake: (a) E_u at $x^*\approx 0.65$, $y^*\approx -0.35$ and E_v at $x^*\approx 1.65$, $y^*\approx 0$; (b) E_u and E_ω at $x^*\approx 1.5$, $z^*\approx 1.5$ (MG spectra offset by -10dB/Hz)

3. Lateral shedding is sensitive to the ground condition, with the characteristic frequency reduced by approximately 18% with moving ground use (from $St_W \approx 0.28$ to $St_W \approx 0.23$).

These results highlight the significant influence of the aspects of ground simulation, such as the development of the GSR, on the overall wake dynamics. Additionally, they show strong interdependency of these motions, with the reduction in frequency of lateral flapping (ΔSt_W

≈ 18%) being in good agreement with the variations observed for the bubble pumping (ΔSt_W ≈ 17%) and wake length (Δx_r^* ≈ 17%).

Figure 5.13(b) also presents both streamwise and heightwise velocity spectra (E_u, E_ω) at a central location within the top shear layer. Within these results, the frequencies representative of bubble pumping are present for both ground conditions ($St_W \approx 0.110$ (SG) and $St_W \approx 0.126$ (MG)). The frequency of heightwise shedding is also captured. With moving ground, this is found identical to the lateral flapping at $St_W \approx 0.228$, with a more intense, narrowband peak. In contrast, for the stationary ground case, the nature of both E_u and E_ω, appears more broadband, suggesting the processes to be less coherent **(Zdravkovich, 1997)**. This is particularly evident for E_u, where any clearly defined oscillatory behaviour is mostly absent. More importantly, however, the results (**Fig. 5.13(b)**) show a significant increase in heightwise shedding frequency with stationary ground use to $St_W \approx 0.356$, indicating this motion is also sensitive to the ground condition.

Further insights into the nature of the wake dynamics are provided using Proper Orthogonal Decomposition (POD) **(Lumley, 1967)** of the recorded base pressure. This technique allows the decomposition of a generic unsteady field into a set of dominant oscillatory modes that are ranked by their energy content. The first four modes obtained this way are presented in **Fig. 5.14** for both ground conditions. The first mode is shown to be an in-phase global wake oscillation, typical of bubble pumping **(Duell and George, 1993, 1999)**. This is the dominant mechanism, accounting for 32.6% and 40.6% of the base pressure energy content for the stationary and moving ground conditions, respectively. Of particular interest is the energy content for the moving ground case being almost a third higher than that for the stationary ground, providing further support for weaker bubble pumping with the latter, as identified in **Fig. 5.13**. Subsequent modes are significantly weaker. Modes 2 and 3 represent the heightwise and crosswise wake shedding processes, respectively, with Mode 4 being a symmetrically centred oscillation. For both ground conditions, the results show the energy of Mode 2 (SG - 9.85%, MG - 8.94%) subtly higher relative to Mode 3 (SG – 6.42%, MG – 6.89%). This confirms the heightwise flapping as the stronger one of the asymmetric shedding processes.

The most variation between the ground conditions is found within the topologies of the last two modes. For the stationary ground case, the crosswise shedding (Mode 3) topology appears chaotic and vertically asymmetric (**Fig. 5.14(a)(iii)**). With the inclusion of

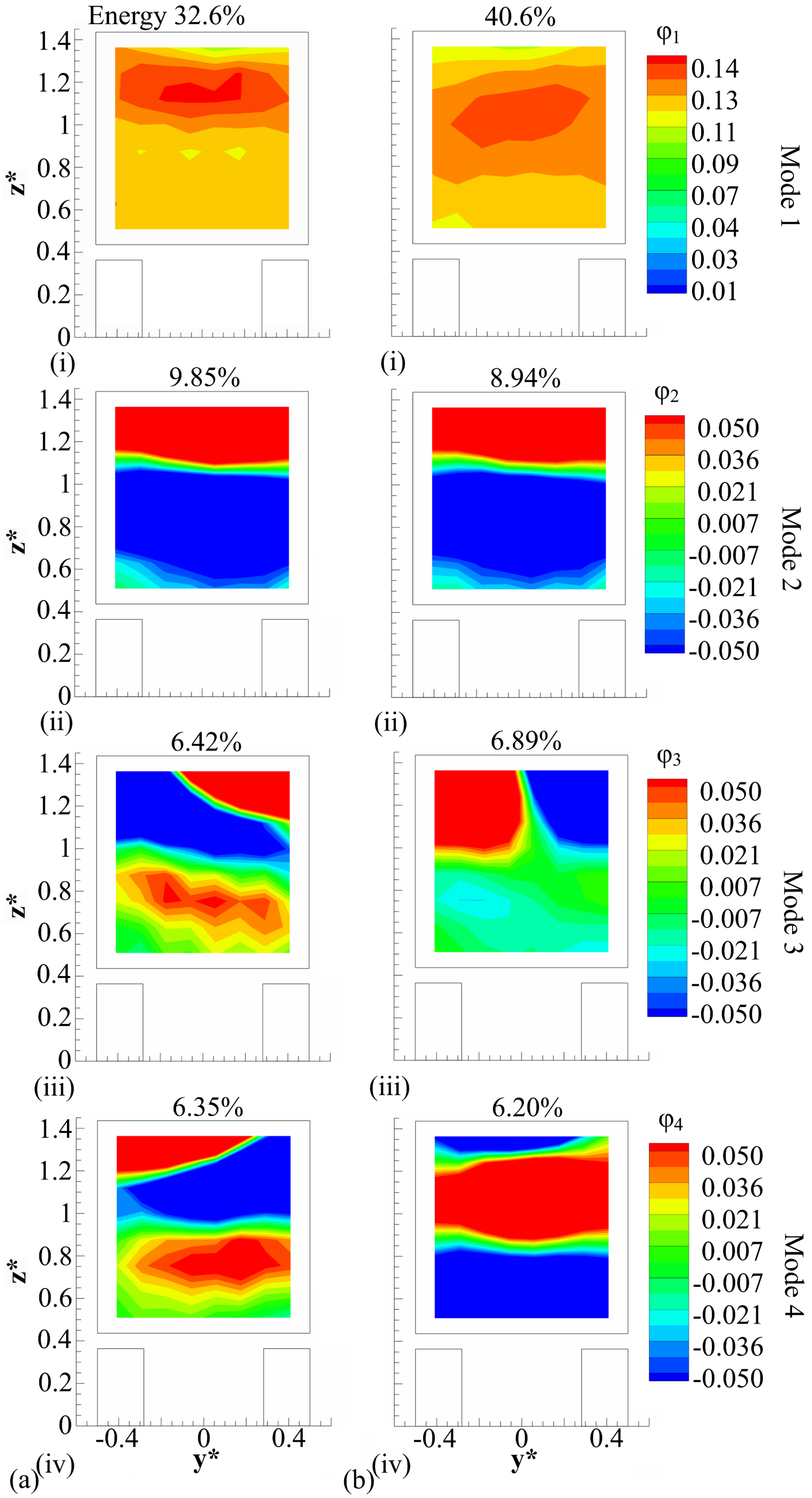

Fig. 5.14 The first 4 modes (i-iv) of POD of base pressure: (a) SG, (b) MG

moving ground, this is seen to be materially affected, replaced with more organised opposing cells dominating the top half of the base (**Fig. 5.14(b)(iii)**). These results show that the process is model-height dependent and support the change to a more coherent lateral shedding with moving ground, as indicated in **Fig. 5.13(a)**.

5.4.3 Influence of the GSR

This section considers the flow dynamics within the GSR to better understand its influence. **Figure 5.15** presents streamwise and heightwise velocity spectra (E_u, E_ω) at selected locations within, downstream, and above ((a)-(k)) the GSR in plane SV1. At position (a), closest to the underbody, E_u can be seen generally similar between the two ground conditions, with marginally higher magnitudes beyond $St_W \approx 0.3$ with moving ground use. This is expected to be a result of more effective underbody flow inducing additional higher-frequency turbulence within the exiting fluid, with this behaviour persisting further downstream to (b). At this location ((b)), a strong increase in E_u (≈5dB/Hz) below $St_W \approx 0.5$ is also observed for the stationary ground case, with these characteristics remaining consistent to position (e). These results suggest the GSR to be a source of lower-frequency, larger-scale turbulent structures. Upon exit at (f), these characteristics are seen to change. At all locations further downstream ((f)-(h)), the spectra for the moving ground condition are observed to exhibit a near-constant offset to lower magnitudes (≈2-5dB/Hz), reflective of suppressed boundary layer development.

The same streamwise evolution ((a)-(h)) for E_ω shows similar trends. Within these results, the influence of GSR is seen spatially narrower, limited to $0.3<x^*<0.8$ ((b)-(d)). At $x^* \approx 0.6$ ((c)), the flow-field appears most affected, with magnitude increases of more than 10dB/Hz ($St_W < 0.5$) with stationary ground. These characteristics are similar to those observed for E_u, further suggesting the GSR's influence to be almost omni-directional in nature with significant increases in the unsteadiness of the local flow-field. These findings offer an explanation for the particular Cp_{rms}, $\partial Cp_{rms}/\partial z$, u_{rms}^* and K trends observed in **Figs. 5.1, 5.3, 5.5, 5.7**. At (e), spectra become identical for both ground conditions. Further downstream, at positions (f)-(h), the trends show the inclusion of moving ground to suppress lower-frequency ($St_W < 0.5$) unsteadiness by up to 5dB/Hz. This is most likely a consequence of the removal of the GSR.

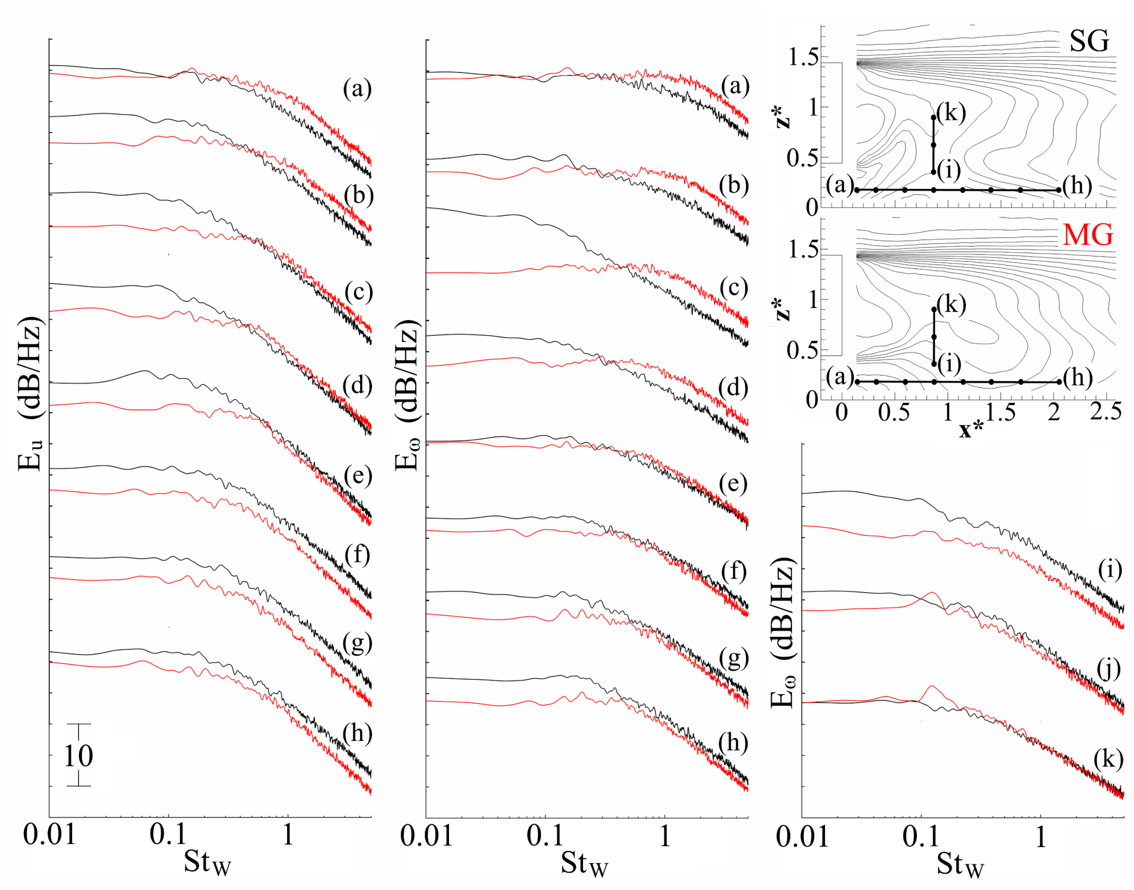

Fig. 5.15 Velocity spectra (E_u, E_ω) along $0.15<x^*<2.08$ at $y^* \approx 0$, $z^* \approx 0.18$ and $0.36<z^*<0.91$ at $x^* \approx 0.86$, $y^* \approx 0$

Heightwise evolution between positions (i) and (j) shows similar characteristics to those at lower locations. At (i), an offset to lower magnitudes for the moving ground case persists, with this influence weakening further up ((j)). No observable difference between the two ground conditions exists at (k), with the exception of a subtle peak, reflective of the bubble pumping mode, seen in the moving ground case ($St_W \approx 0.126$).

5.4.4 Influence of rotating wheels

Another important difference between the two ground conditions is the addition of rotating wheels with moving ground use; this influence is now considered. Overall, the flow-field has been shown symmetric about $y^* \approx 0$, thus, for brevity, only results for the left wheel are discussed. **Figure 5.16** presents crosswise evolution of velocity spectra behind the wheel profile ((a)-(e)) as well as heightwise evolution directly above ((f)-(h)). At position (a), E_u for the moving ground case is significantly reduced across the frequency range, reflective

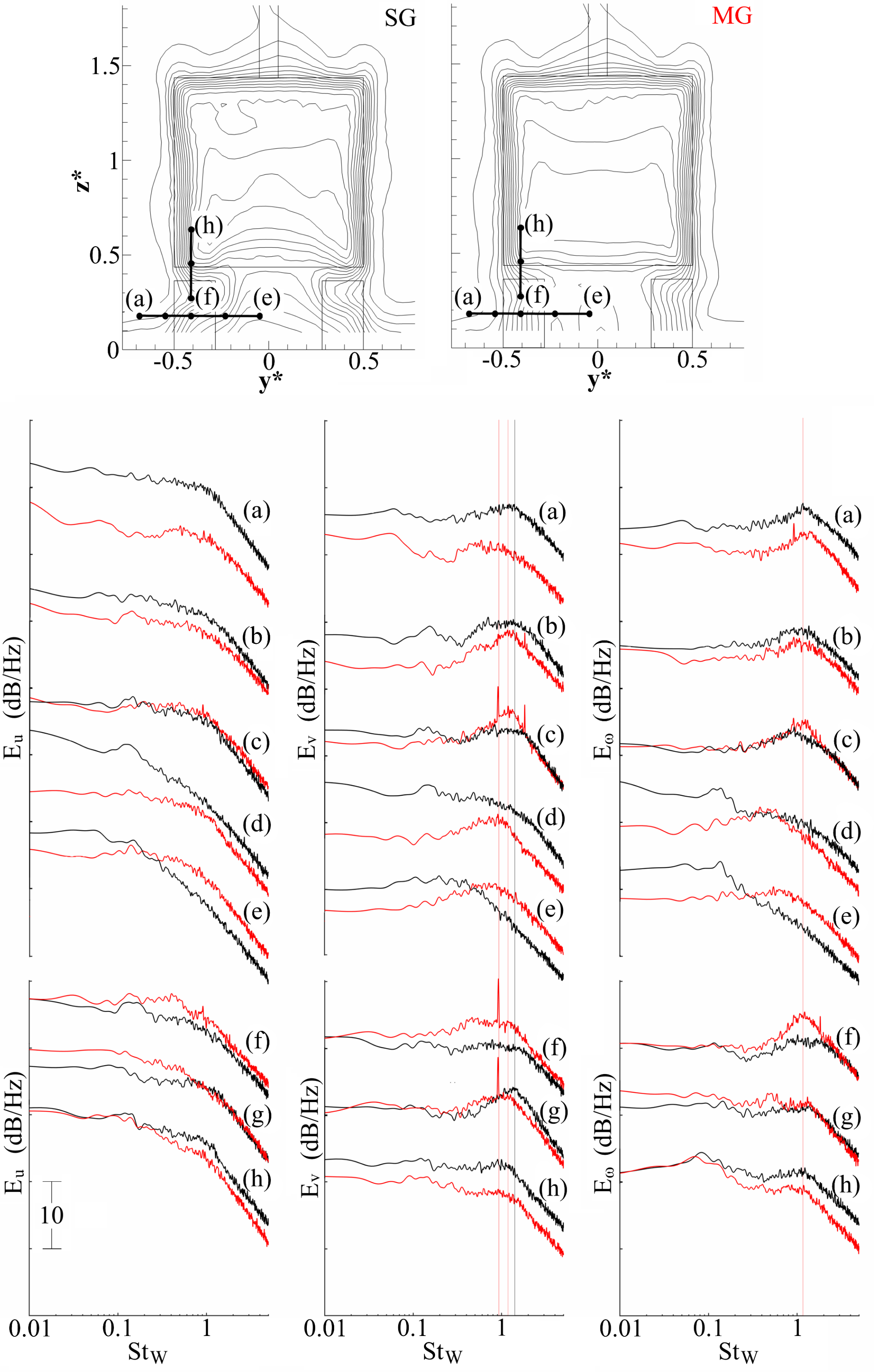

Fig. 5.16 Velocity spectra (E_u, E_v, E_ω) along $-0.68<y^*<-0.045$ at $z^* \approx 0.18$ ((a)-(e)) and $0.27<z^*<0.63$ at $y^* \approx -0.41$ ((f))-(h)) in plane T2

of the reduced influence of the boundary layer and subsequent interactions with the model. These characteristics are seen to dissipate further inboard, with position (c) exhibiting insensitivity to ground condition. At (d), the stationary ground case shows strong increases in E_u below $St_W \approx 1$, representative of the nearby GSR influence, as discussed in **Section 5.4.3**. This behaviour, albeit weaker, can be seen to persist to position (e). At higher locations (f)-(g), very little difference in E_u is observed, suggesting general insensitivity to the ground condition.

Spectra of crosswise velocity (E_v) are also considered in the same locations. The impact of the boundary layer interactions with the local flow is again evident for the stationary ground case, with higher magnitude offsets at (a)-(b). With moving ground use, elevated E_v is evident for $St_W > 0.3$, with a maximum found in position (c) at $St_W \approx 1.2$. Based on the wheel width and results indicated in **Fig. 5.13(a)**, this frequency appears to coincide with the expected characteristic frequency of lateral wheel wake shedding ($St_W \approx 1.1$). At the same position ((c)), two stronger distinct peaks are also shown at $St_W \approx 0.92$ and $St_W \approx 1.28$. The first corresponds to the wheel rotation frequency ($St_W \approx 0.87$), estimated using the belt speed and wheel size. The latter remains somewhat uncertain, possibly representing a resonant half-harmonic. The $St_W \approx 0.92$ peak is also clearly distinguishable at locations (f) and (g), directly above (c) and subsequently the wheel centre. Moving inboard toward the underbody region, positions (d)-(e) can also be seen to capture the crosswise wheel shedding for the moving ground case. At these points, however, these characteristics are observed to be much weaker, more broadband and at a reducing central frequency ($0.75 < St_W < 0.9$).

Vertical evolution of E_v ((c), (f)-(h)) shows a quicker transition to broader spectra for the moving ground case. As previously described, for this condition, the strongest and most defined spectral characteristics are evident at position (c). With stationary ground use, however, similar behaviour is observed at (g), suggesting the wheel wake to be uplifted under these conditions. This would be a consequence of the flow being entrained through the upwash generated by the GSR and is consistent with the results presented in **Fig. 5.7**.

Similar trends are also found for E_ω. The GSR influence is again evident at (d)-(e), further confirming its omni-directional impact. The lateral wheel wake shedding is also captured at (c)-(f).

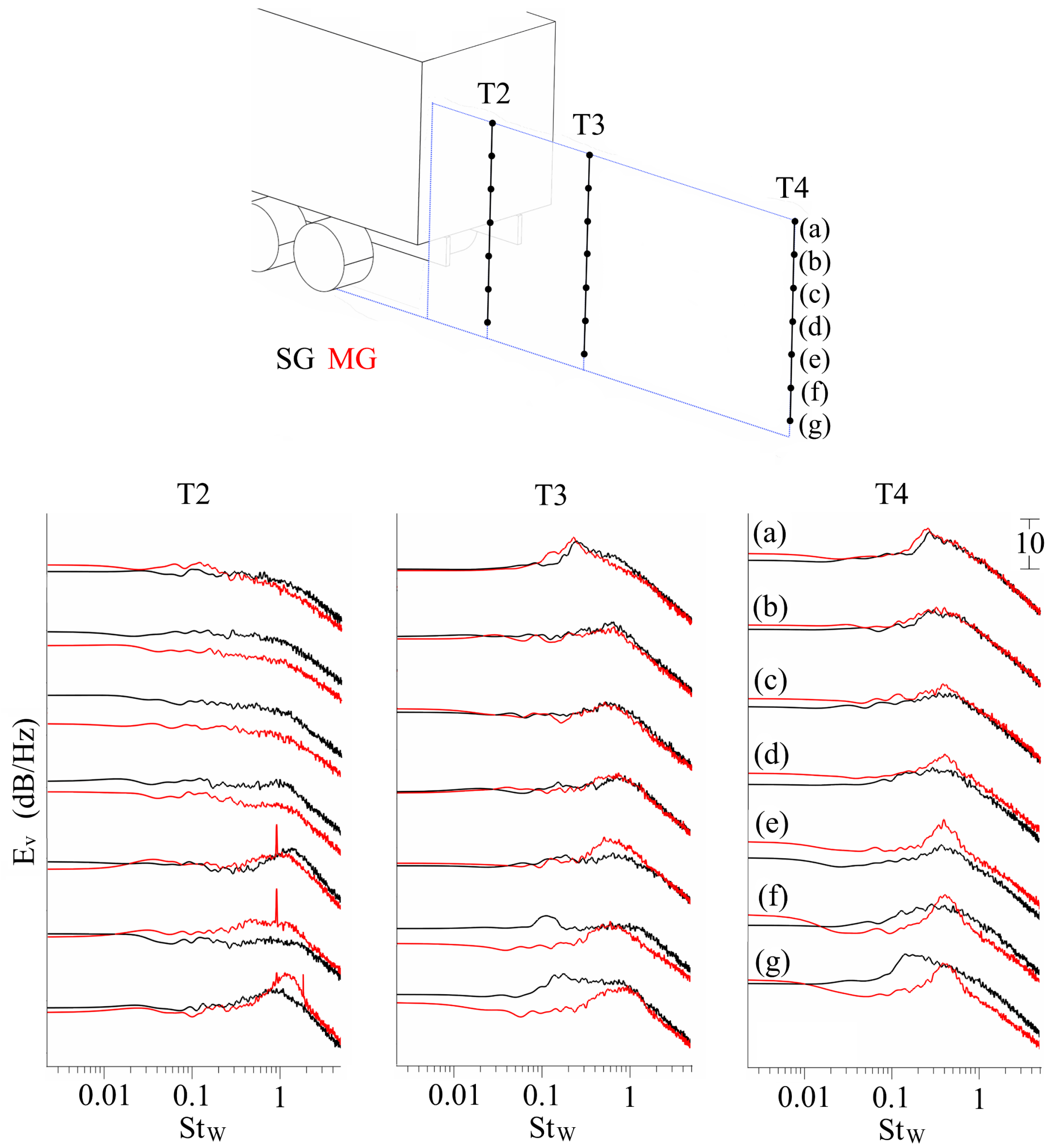

Fig. 5.17 Streamwise evolution (T2-T4) of wheel influence on E_v at $y^* \approx -0.41$ between $0.091<z^*<1.18$

Lastly, the streamwise evolution of the wheel influence on E_v is evaluated, with results presented in **Fig. 5.17**. In T2, the lower positions (e)-(g) can be seen dominated by the wheel wake shedding ($1 < St_W < 1.2$) as identified in **Fig. 5.16**. These characteristics are shown to extend vertically from the ground level to both bottom trailer base corners, confirming the impact of the wheel turbulence identified along the lower trailing edge in **Fig. 5.2** and **Fig. 5.3**. Further up, there exists no clear evidence of the wheel impact. However, for the stationary ground case, spectra are found offset to higher magnitudes behind the base, supporting the previously discussed increases in flow unsteadiness under these conditions. The differences dissipate at (a) with very little local variation.

At T3, with moving ground use, the wheel wake signature continues to dominate the lower positions (e)-(g), though markedly more narrowband and within a reduced frequency band ($0.6 < St_W < 0.8$). For the stationary ground case, similar behaviour is not observed. Instead, broader spectral characteristics are evident, closer in nature to turbulent fluctuations within a boundary layer. These results suggest the possibility such flow interactions, generated by strong boundary layer development, precipitate more rapid streamwise dissipation of the wheel wake.

The wheel wake continues to devolve further downstream, with frequencies reducing to $St_W \approx 0.4$ at T4. At this position, with moving ground use, the vertical propagation, also shows increasing wheel wake influence extending past model mid-height to (c). Additionally, spectra can be seen becoming progressively broader with increasing height. In contrast, for the stationary ground, the trends from T3 appear to persist to T4, with broader characteristics and lower magnitudes limited to the lower positions (in particular (e)-(g)). Streamwise development for each ground condition is shown decidedly different. In both cases, however, vertical evolution shows a clear transition from the prevalent wheel wake influence near the ground ((g)) to weak lateral base wake shedding closer to the top ((a)), identified in **Fig. 5.13** and **Fig. 5.14**.

5.5 Summary

In this chapter, the effects of moving ground use were discussed. From the time-averaged perspective, measurements of total model and trailer drag indicated small reductions in both with the use of moving ground, though the former was found within experimental uncertainty. Subtle increases in base pressure were also identified together with reduced unsteadiness. Wheel wakes were captured within the base pressure spatial gradient distributions, being most prominent close to the bottom base corners.

With stationary ground use, a large region of flow separation close to the ground and directly behind the model, previously identified in the literature, was shown to develop for the current model. Consequently, strong upwash in the lower wake portions close to the base was generated, with subsequent flow entrainment promoting enhanced crosswise flow within the wheel-trailer junction, resulting in local wake contractions disruptive to wheel wake formation. This characteristic was seen to persist downstream, promoting a more inconsistent wake width with height. In contrast, using moving ground was shown to inhibit the ground separation region, alleviating these effects, and allowing for undisturbed development of the trailer base and wheel wakes. Under these conditions, the mean wake length was found to increase.

While the differences between ground conditions may be perceived as subtle from the time-averaged perspective, wake dynamics were found markedly affected. Overall, no clearly defined oscillatory behaviour was found within the time-dependent wake aspects, with broader characteristics typical instead. The wake was shown dominated by the bubble pumping mode, which was found to be sensitive to the ground condition. Characteristic frequency of this mode was revealed to increase with moving ground, with this change in excellent agreement with the variation in the wake length. The crosswise and heightwise asymmetric shedding processes for the stationary ground case were identified at $St_W \approx 0.279$ and $St_W \approx 0.356$, respectively, with both reducing to $St_W \approx 0.228$ with moving ground use. For the latter, the characteristics were more defined, with lateral shedding also found to be height dependent.

With stationary ground, the ground separation region was revealed to be a source of low-frequency ($St_W < 0.5$) local disturbance, producing spectral magnitudes up to 10dB/Hz higher than those observed when absent. This feature was found to affect all directions, with additional unsteadiness contaminating the surrounding flow-field. The wheel wake development was also found affected by ground condition. For the moving ground case, relatively stronger and more defined shedding was identified, with the signatures found to extend upward past model mid-height far downstream. In contrast, with the use of stationary ground, wheel wakes were shown to have weaker heightwise impact, much broader characteristics, and to dissipate at shorter downstream distances.

Chapter 6

Assessment of the upstream model mounting

The second part of the setup optimisation concentrated on the assessment of the aerodynamic characteristics of various mounting techniques typical to ground vehicle models. With a particular focus on the effects at the model base, a novel front support sting was proposed and evaluated against more common methods of mounting from the top and sides. Details of all three support techniques are described in **Section 4.3**. The experiments were conducted using Baseline 1 and moving ground. All results presented in this chapter were corrected for blockage effects as outlined in **Section 4.8**.

The results presented in this chapter have been published as Rejniak and Gatto **(2020b)** and are reproduced here with some changes under the Creative Commons Attribution 4.0 International License (https://creativecommons.org/licenses/by/4.0/).

6.1 Drag coefficients

Recorded drag results for all three mounting configurations are presented in **Table 6.1**. Total model drag (C_{DM}) was determined in the top mounting configuration, as outlined in **Chapter 5** (here corrected for blockage). The small overall contribution of trailer (C_{DT}) to total drag is evident for all three configurations. This has been previously explained (**Section 5.1**) as the result of the small tractor-trailer gap. **Table 6.1** also shows that the trailer drag for the top setup ($C_{DT} \approx 0.017$) is larger relative to the side ($C_{DT} \approx 0.011$) and front ($C_{DT} \approx 0.006$) supports. These differences are very subtle, all lying within the experimental uncertainty.

	Top	**Side**	**Front**
C_{DM} (±0.018)	0.649	-	-
C_{DT} (±0.010)	0.017	0.011	0.006

Table 6.1 Total (C_{DM}) and trailer (C_{DT}) drag coefficients for the three mounting configurations

6.2 Time-averaged base pressure

Figure 6.1 presents Cp and Cp_{rms} distributions for all three configurations, with relative differences to front setup also included for comparison. All topologies show vertical symmetry and horizontal asymmetry. Maximum Cp is located close to the top trailing edge, with magnitudes seen to decrease towards lower base half. This distribution, corresponding to the typical positions of the upper recirculating flow impingement and lower wake vortex core, as discussed previously in **Chapter 5**, remains similar for all three configurations. For the side mounting (**Fig. 6.1(a)(iii)**), the upper flow impingement appears subtly more pronounced, with **Fig. 6.1(a)(iv)** indicating a local increase of $\Delta Cp \approx 0.007$ at $z^* \approx 1.36$ relative to the front setup (**Fig. 6.1(a)(i)**). The same comparison (**Fig. 6.1(a)(iv)**) between the top and front mountings shows the differences less localised and instead, more offset to lower magnitudes ($\Delta Cp \approx 0.01$). These results suggest two separate mechanisms are responsible for these relative changes. For the side setup, a shift in the vertical wake balance is evident, with wake length reductions for the top mounting. The latter is further supported by the results in **Table 6.1**. The implications of these observations are discussed further in **Section 6.3**.

Results for Cp_{rms} (**Fig. 6.1(b)**) show, again, the characteristic vertical symmetry and horizontal asymmetry. The top-mounted model (**Fig. 6.1(b)(ii)**) is shown to produce the highest Cp_{rms}, with the maximum relative increase of $\Delta Cp_{rms} \approx 0.004$ at $z^* \approx 1.24$ indicated in **Fig. 6.1(b)(iv)**. Results for the side setup are observed lower in comparison with the front mounting by a similar amount (**Fig. 6.1(b)(iv)**). These differences remain very subtle, with all variations within experimental uncertainty, suggesting general insensitivity to support configuration.

A more global perspective is explored with the average base pressure (Cp_b) and calculated trailer base drag (C_{DTb}) presented in **Table 6.2**. The significance of the small

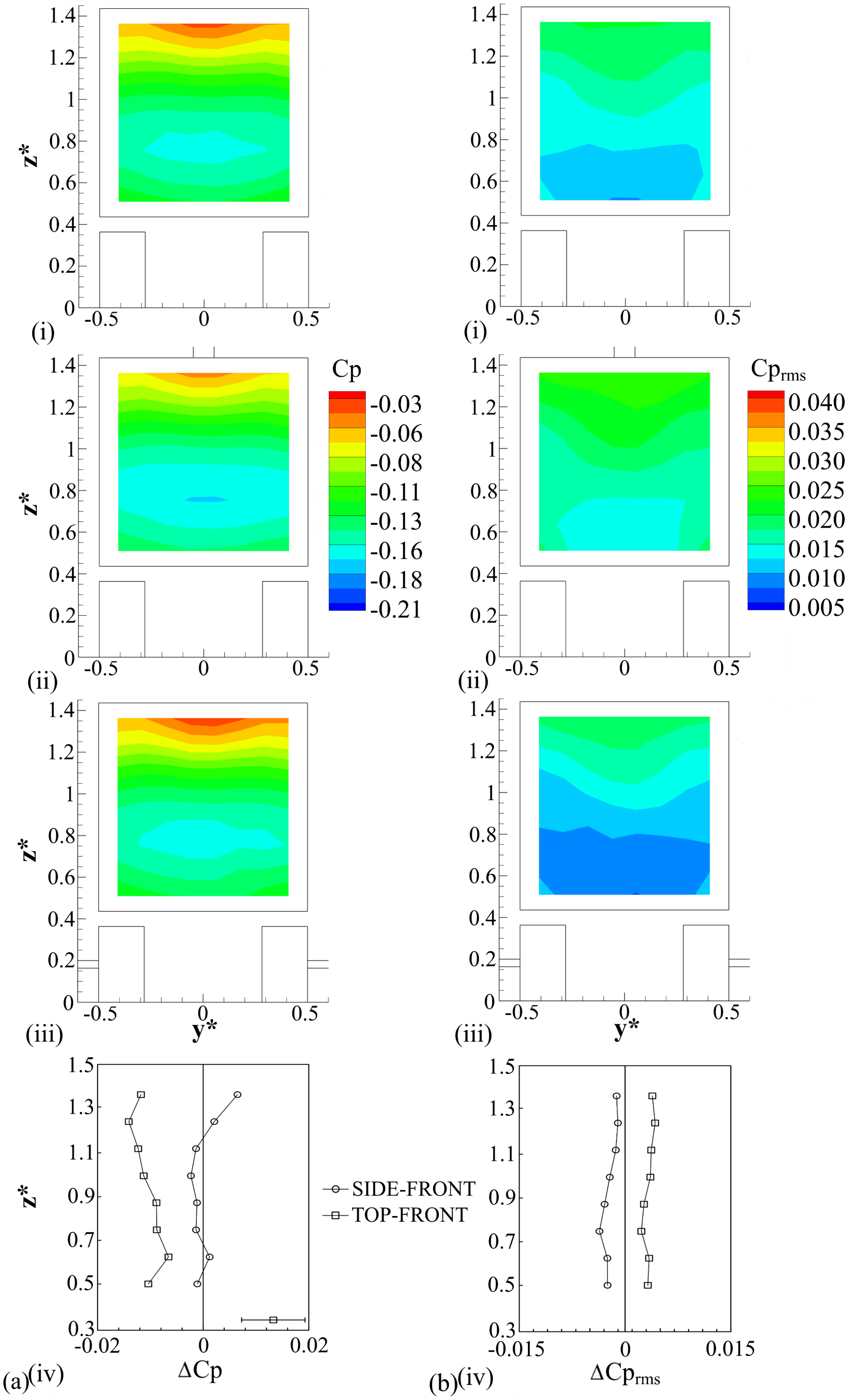

Fig. 6.1 Time-averaged base pressure data: (a) Cp and (b) Cp_{rms}; (i) front, (ii) top, (iii) side, (iv) plots of differences top-front and side-front along y* ≈ 0

tractor-trailer gap at reducing trailer drag is highlighted by these results, with C_{DTb} shown to contribute between 13.6% (front and side) to 14.8% (top) of total model drag (C_{DM}). For the side and front mounting configurations, Cp_b and C_{DTb} are found identical, with the model mounted from the top showing a relative reduction in Cp_b accompanied by a corresponding increase in C_{DTb} (9.1%). The latter generally agrees with the trend presented in **Table 6.1**. A similar behaviour was also reported by Hetherington and Sims-Williams **(2006)**, with a 7.5% increase in drag with the inclusion of a top strut. Additionally, no significant effect from side support struts was identified, with similar conclusions also drawn by Miao, Mack and Indinger **(2015)**. The present results support these findings, and therefore, indicate that the proposed front sting does not materially affect mean drag production.

	Top	**Side**	**Front**
Cp_b (±0.006)	-0.132	-0.121	-0.121
C_{DTb}	0.096	0.088	0.088

Table 6.2 Average base pressure (Cp_b) and calculated trailer base drag (C_{DTb}) coefficients for the three mounting configurations

6.3 Time-averaged wake flow-field

The following sections consider the time-independent flow characteristics. First, the general impact on the base wake is considered, with more detailed interrogations of the various support configurations presented thereafter.

6.3.1 Overall effects on the base wake

Figure 6.2 presents the u* contours in planes T2 and T4. In **Fig. 6.2(a)** within $|y^*|<0.4$, $0.45<z^*<1.35$, the common wake topology is shown for all configurations, with magnitudes decreasing from the trailer top to bottom. The minimum u* position again coincides with minimum Cp (**Fig. 6.1(a)**), commensurate with the central location of the lower wake vortex core. Within the underbody exiting flow ($|y^*|<0.25$, $z^*<0.45$ - **Fig. 6.2(a)**), the effect of moving ground can be seen unaffected by the various mounting methods, with no evidence of the GSR and similar u* magnitudes for all three configurations. In each case, the wake is shown to retain good vertical symmetry, with the typical horizontal asymmetry also characteristic, and closure attained by T4 (**Fig. 6.2(b)**).

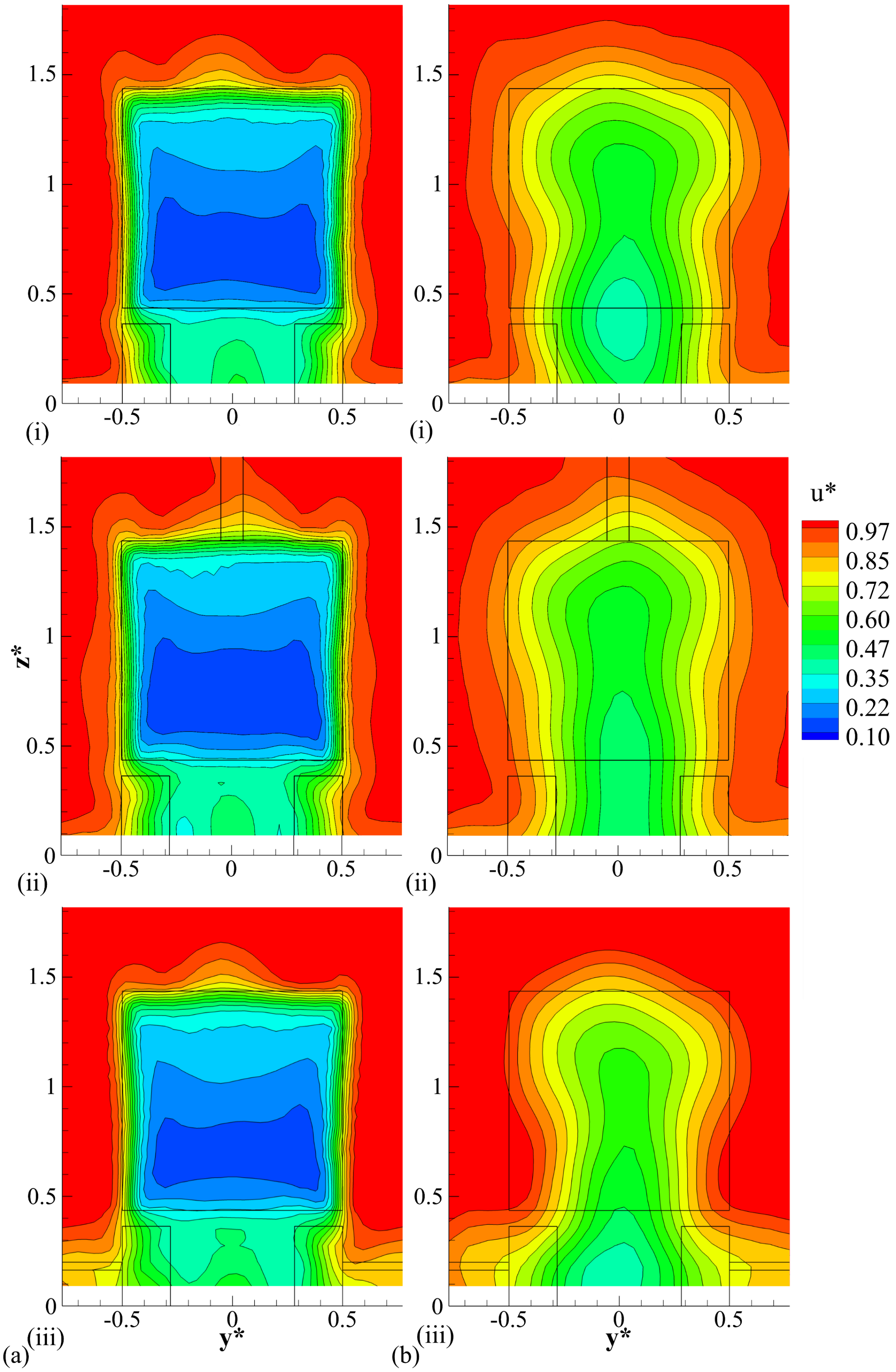

Fig. 6.2 Contours of u* in: (a) T2 and (b) T4; (i) front, (ii) top, (iii) side mounting

A more detailed inspection of **Fig. 6.2(a)** shows the u* topologies downstream of the trailer base relatively unchanged for the front and top mounting techniques. In contrast, the inclusion of side support struts is observed to prompt a small reduction in the size of the lowest u* magnitudes region (0.5<z*<0.8 - |y*|<0.4), suggesting a subtle change in vertical wake balance with this setup, consistent with **Fig. 6.1(a)(iv) (Perry et al. 2016)**. In **Fig. 6.2(a)(ii)**, the influence of the top support strut's wake is captured above the trailer (u*≈0.95 at y*≈0, z*≈1.8). The resultant local velocity deficit as well as general topology are similar to that reported by Strachan et al. **(2007)**. The influence of the side supports can also be observed in **Fig. 6.2(a)(iii)**, with regions close to the floor (|y*|>0.5, z*<0.3) dominated by significant flow retardation up to Δu*≈0.2, in general agreement with Hetherington **(2006)**. For the front mounting (**Fig. 6.2(a)(i)**), similar effects are not observed, suggesting no comparable interference exists locally.

Results from plane T4 (**Fig. 6.2(b)**) provide further insight. At this position, the top and front configurations show only limited impact on the mean wake, with both exhibiting approximately the same height and width. Minimum u* is located within |y*|<0.2 at z*<0.7. Distinctly, the side support configuration (**Fig. 6.2(b)(iii)**) appears to impart a significant impact to the wake development, with a marked reduction in width. Both the mean and unsteady aspects of wake development would be expected to be affected by this contraction, despite the base pressure differences appearing marginal (**Fig. 6.1**). The following sections explore this issue further, showing this change to be a result of additional wake blockage increasing the velocity magnitudes around the model profile sides. Additionally, with the trends being relatively similar at T2 (**Fig. 6.2(a)**), these results highlight the importance of considering wider data sets for accurate conclusions to be drawn.

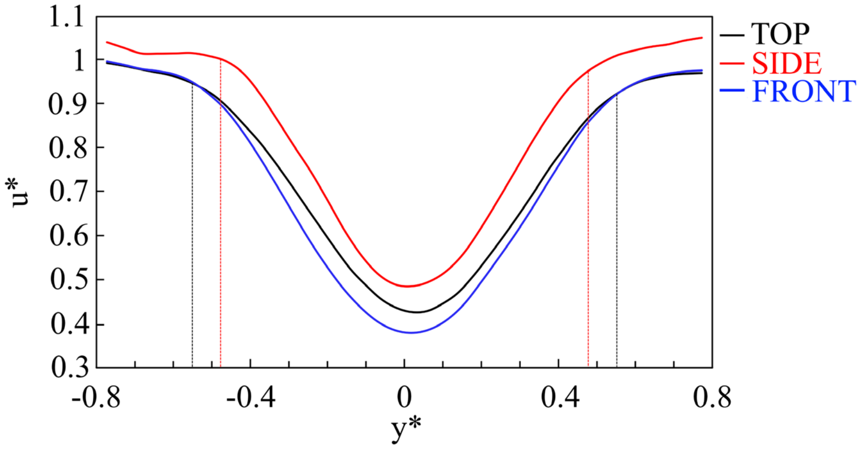

Fig. 6.3 Spanwise profiles of u* in T4 at z*≈0.5

The relative differences identified in **Fig. 6.2** are better quantified in **Fig. 6.3**, with profiles of u* in T4 at z*≈0.5. The reduced wake width for the model mounted from the sides is evident in this data (**Fig. 6.3**). Using the Δu*≈-0.05 relative to local freestream as the bounded criterion, a reduction from |y*|<0.55 (top and front) to |y*|<0.48 (side) is evident.

Further assessment is provided in **Fig. 6.4** with u* and ω* profiles at x*≈0.14, y*≈0 (SV1). The underbody exiting flow is shown generally insensitive to mounting method along the vehicle centreline. Below z*≈0.4, both the mean underbody mass flux (**Fig. 6.4(a)**) and relative upwash (**Fig. 6.4(b)**) show excellent agreement between the various setups. From this perspective, the results indicate no significant influence of the front sting on the performance of the moving ground, similar to the top and side setups typically used for these applications, suggesting the adopted design to be appropriate for this purpose.

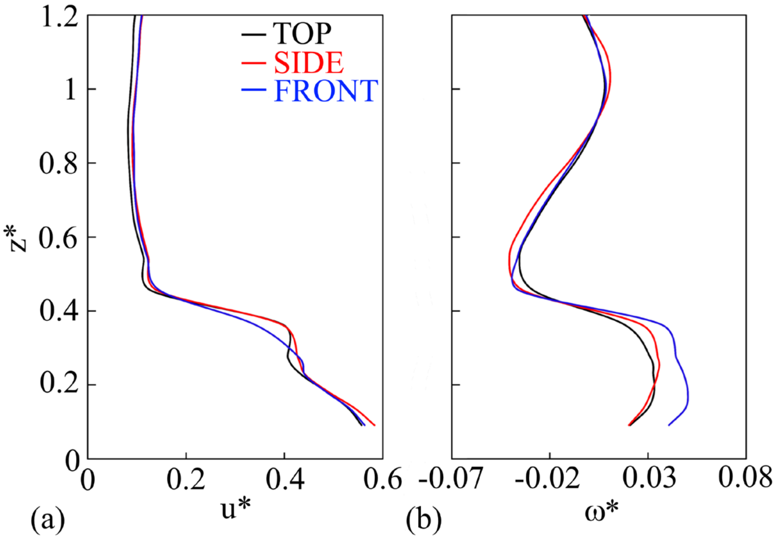

Fig. 6.4 Velocity magnitude profiles at x*≈0.14, y*≈0 (SV1): (a) u*, (b) ω*

6.3.2 Impact on mean turbulence production

Further insight into the effects of various mounting configurations on the nature of the separated wake is provided by considering the turbulent characteristics. Normal Reynolds stress $(u'^2)^*$ distributions within the planes SH1 and SV1 are presented in **Fig. 6.5**. The general topologies remain similar for all three configurations. In **Fig. 6.5(a)**, the maximum magnitudes indicate the development of separated shear layers from the trailer sides (0.1<x*<2, 0.2<|y*|<0.5). Correspondingly, the regions of elevated $(u'^2)^*$ in **Fig. 6.5(b)** map the top shear layers for each case. These results agree with the trends found by McArthur et

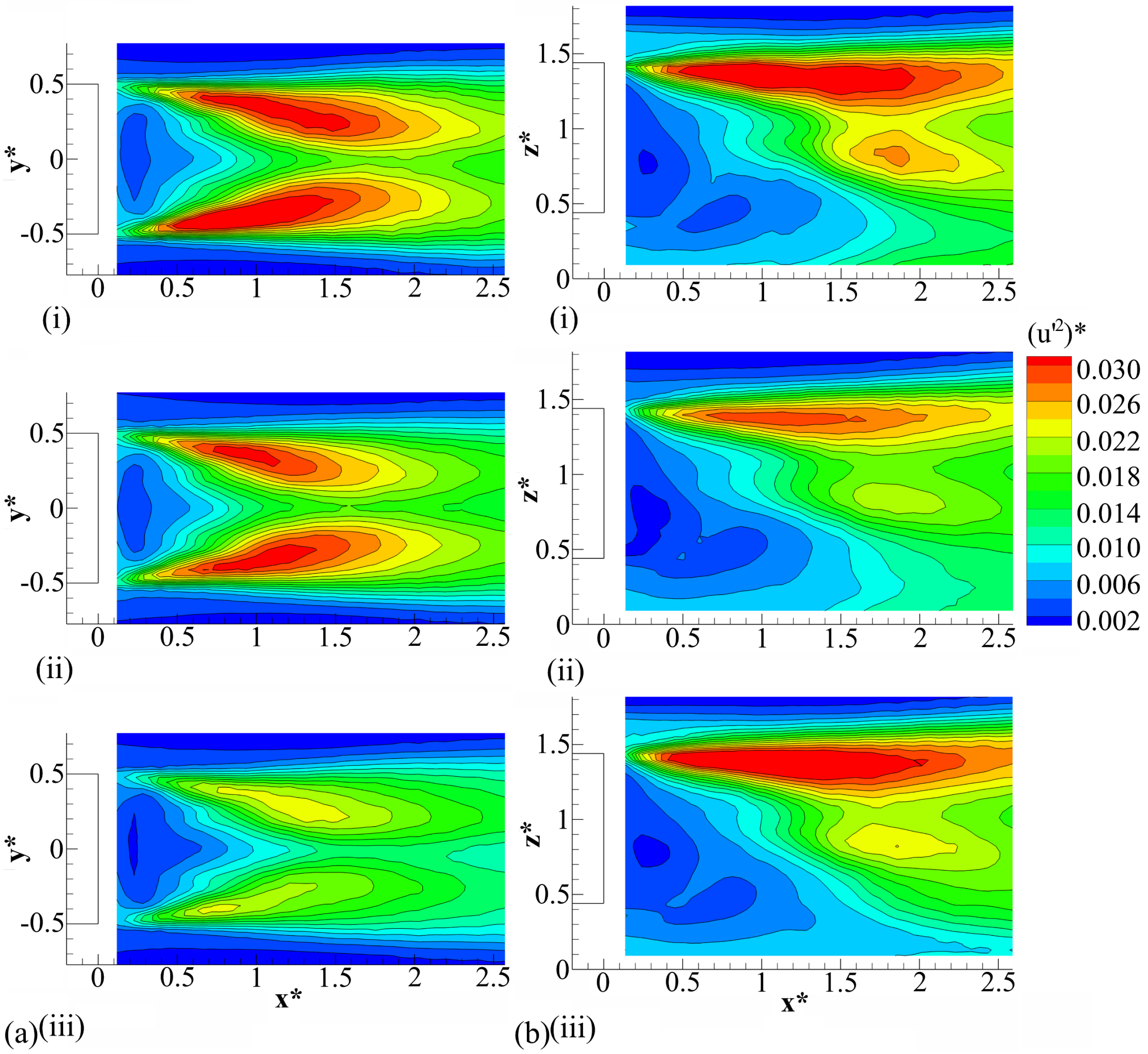

(i) (i)

(ii) (ii)

(a)(iii) (b)(iii)

Fig. 6.5 Normal Reynolds stress $(u'^2)^*$ distributions in SH1 (a) and SV1 (b): (i) front, (ii) top, (iii) side mounting

al. **(2016)** and provide an indication of the general size and shape of the model base wake. Upon closer examination, subtle differences in the shear layer development between various mounting methods are observed. Within the side shear layers at SH1 (**Fig. 6.5(a)**), the top and front setups show most intense magnitudes relative to the sides, with the front also marginally larger in size. From this perspective, support interference for the front and top configurations would be expected to be minimal, explaining the similarity. At SV1 (**Fig. 6.5(b)**), the closest resemblance is found for the front and side setups, with the top mounting exhibiting lower $(u'^2)^*$ within the top shear layer. Likewise, from this perspective, interference from the side and front supports should be minimal. These results show that mounting the model from the front maintains the benefits while minimising the deficiencies of the common top and side setups, for each perspective.

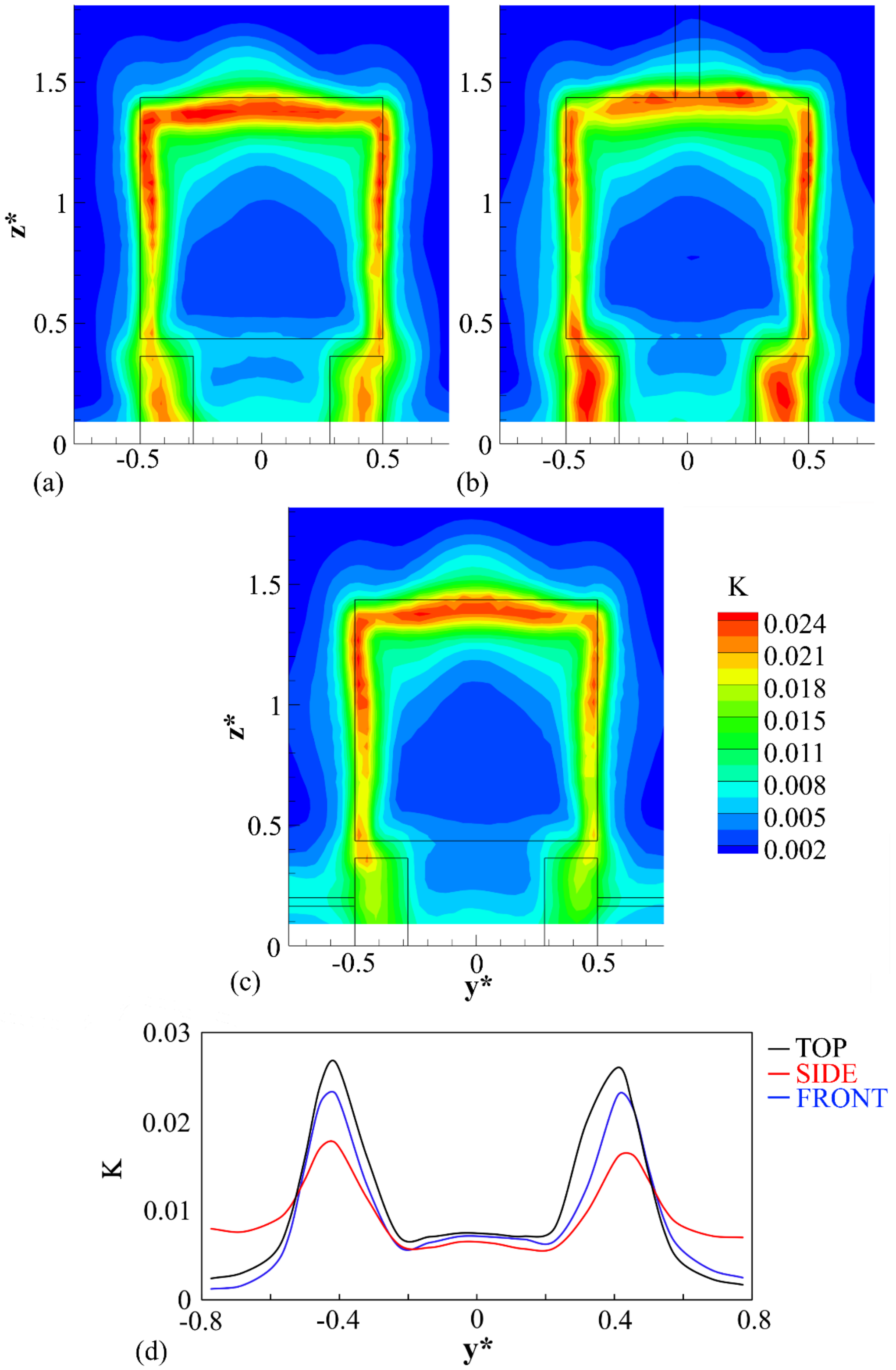

Fig. 6.6 Mean turbulent kinetic energy K in T2: (a) front, (b) top, (c) side mounting contours, and (d) profiles at z*≈0.18

Differences in turbulence production are further evaluated with the mean turbulent kinetic energy (K) within plane T2 presented in **Fig. 6.6**. All three topologies (**Fig. 6.6(a-c)**) show elevated K located mainly along the vehicle edges and directly behind the wheels. For the front support (**Fig. 6.6(a)**), most intense K are found around the top and upper portions of side trailer edges, as well as downstream of the wheels ($0.3<|y^*|<0.5$, $0.9<z^*<1.4$ and $0.3<|y^*|<0.5$, $0.1<z^*<0.35$ respectively). The top-mounted setup (**Fig. 6.6(b)**) can be seen to exhibit less intense K within the top separated shear layer ($|y^*|<0.5$, $1.3<z^*<1.4$). For this configuration, K is also stronger behind the wheels. Within this region (behind wheels), K magnitudes dissipate further for the side mounting configuration (**Fig. 6.6(c)**), with this disparity most evident in **Fig. 6.6(d)**. For this configuration, **Fig. 6.6(d)** also highlights the significant increase in turbulence production outside this region ($|y^*|>0.5$), resulting from the presence of the side struts. Generally, these results agree with Knowles, Saddington and Knowles **(2013)**, showing reduced regions of high turbulence intensity within the wheel wake when using side struts, and show that the front sting imparts no similar influence.

6.3.3 Localised influence of top support strut

With the global effects discussed in the previous sections, the influence of the top strut is now assessed more locally, within the transverse plane T1 positioned directly behind the support. **Figure 6.7(a)** presents the spanwise profiles of u^* at $z^*\approx1.8$. For the front and side mounting configurations, little overall variation is observed, as would be expected within undisturbed freestream flow. A similar trend can also be seen for the top-mounted setup for $|y^*|>0.1$, with differences within $\Delta u^*<0.05$, indicating only a limited influence within these areas. Within $|y^*|<0.1$, however, the presence of the top strut generates the characteristic velocity deficit discussed already in **Section 6.3.1**. This close to the support, this deficit is found higher, up to $\Delta u^*\approx0.1$ at $y^*\approx0$. Analogous trends are also found for u_{rms}^* (**Fig. 6.7(b)**), with very little variation for the front and side setups across the entire width, as well as the top mounting for $|y^*|>0.1$. Directly behind the top strut, in line with the u^* deficit seen in **Fig. 6.7(a)**, a local increase in u_{rms}^* is evident ($\Delta u_{rms}^*\approx0.03$ relative to freestream), indicating higher turbulence production. Within this region, a distinct disparity in the Reynolds shear stress $(u'v')^*$ profile (**Fig. 6.8**) is also observed with the top support present. This trend reflects the spanwise inboard momentum flux generated as the flow moves around the strut and becomes entrained into the local wake.

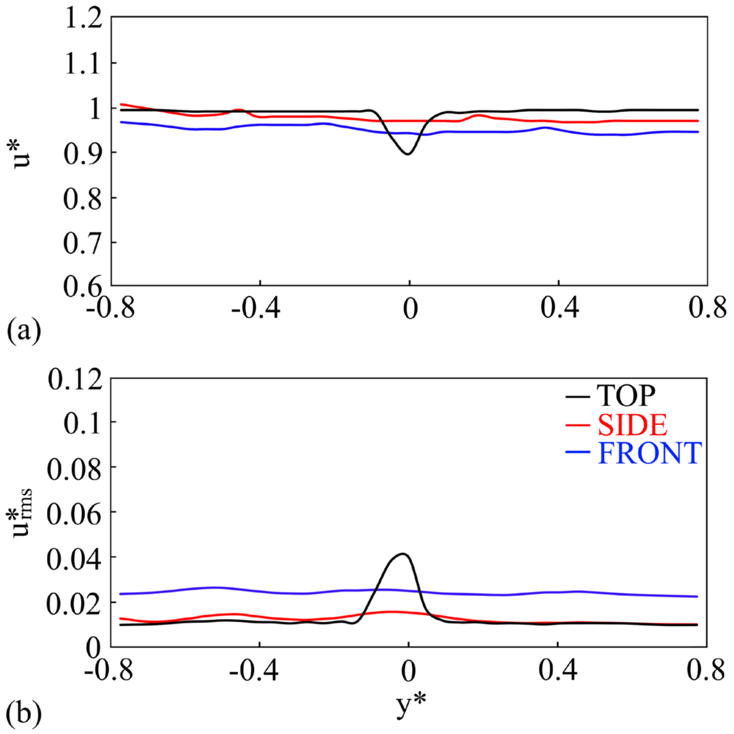

Fig. 6.7 Spanwise profiles at x*≈ -1.05 (T1) and z*≈1.8: (a) u* and (b) u_{rms}*

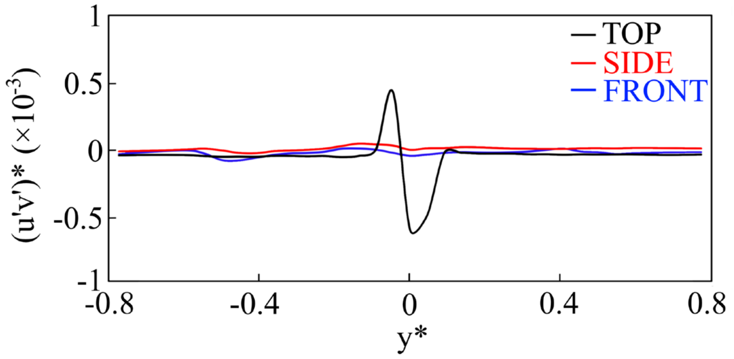

Fig. 6.8 Profiles of the Reynolds shear stress (u′v′)* at z*≈1.8 in T1

Further insight is gained with comparisons of K production at plane T1, as presented in **Fig. 6.9**. In all three cases, elevated K is found close to the trailer corners and along the trailer centre. For the front (**Fig. 6.9(a)**) and side (**Fig. 6.9(c)**) mounting configurations, the topologies remain very similar, with maxima of K≈0.011 and K≈0.010, respectively (y*≈0 – **Fig. 6.9(d)**). These results confirm a general insensitivity to these support configurations exists locally. In contrast, results for the top mounting (**Fig. 6.9(b)**) show centrally elevated

K over a subtly greater width (|y*|<0.15). This is most evident in **Fig. 6.9(d)** and is most likely a consequence of the flow negotiating the obstruction caused by the strut **(Simpson, 2001)**. For this configuration, a characteristic relative reduction in K (wake deficit) at the model centreline is also shown (**Fig. 6.9(b, d)**), with a similar relative increase also evident further up at z*>1.7 (**Fig. 6.9(b)**). The central reduction in K close to the trailer surface agrees with a local suppression of the roof boundary layer suggested by Strachan et al. **(2007)** using a comparable top support strut. Additionally, this observation offers some explanation for the reduced turbulence levels found within the top separated shear layer for this setup (**Fig. 6.5(b)(ii)**, **Fig. 6.6(b)**). Overall, the results within T1 show similar trends for the front and side setups, with Hetherington **(2006)** also reporting little influence from the side struts on the upper model portions.

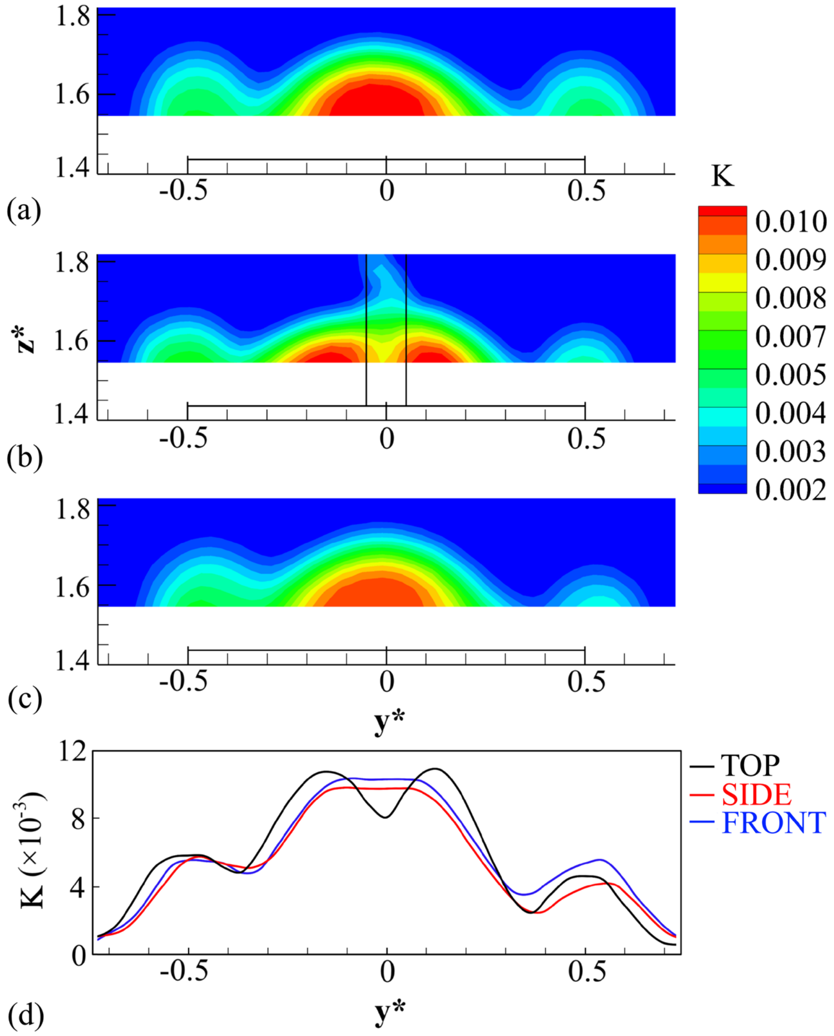

Fig. 6.9 Mean turbulent kinetic energy K in T1: (a) front, (b) top, (c) side, (d) profiles at z*≈1.55

6.3.4 Localised influence of side support struts

This section considers the local influence of the side support struts. The global results presented in **Sections 6.3.1** and **6.3.2** showed very good vertical symmetry, therefore, for brevity, only results for the left side are included in the following discussion. **Figure 6.10(a)** provides vertical profiles of u* and u_{rms}* at x*≈0.25 within plane SV2. Above z*≈0.4, all three configurations show a near-uniform velocity profile (**Fig. 6.10(a)(i)**), with values close to u*≈1, consistent with undisturbed freestream flow. Remains of the floor boundary layer are evident for the top and front setups below z*≈0.2. For the side mounting, the profile is seen to deviate markedly for z*<0.4, with a minimum of u*≈0.76 at z*≈0.2. This deficit is representative of the local wake generated by the side strut, with the strut's central axis coincident with minimum velocity magnitude position. The evidence of this deficit is also provided in **Fig. 6.2(a)(iii)**. This trend is seen to persist further downstream to T4 (**Fig. 6.10**

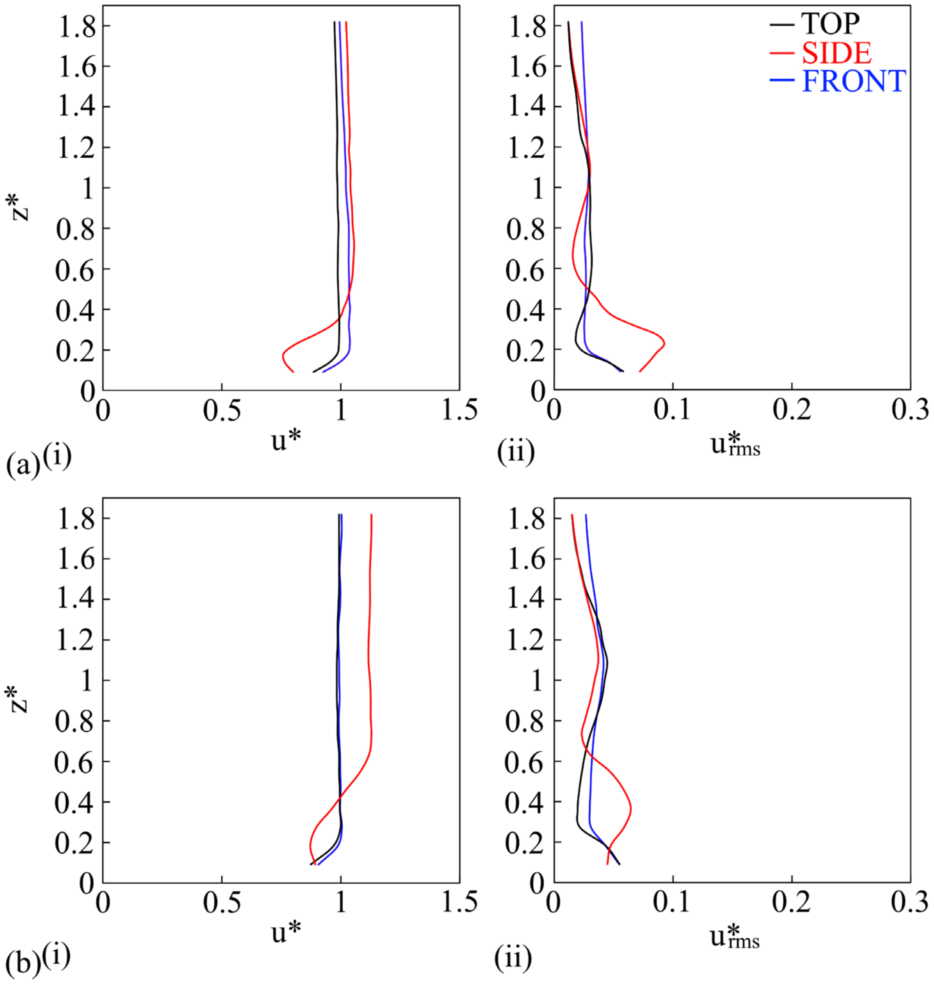

Fig. 6.10 Velocity profiles at: (a) x*≈ 0.25, y*≈-0.76 (SV2) and (b) x*≈ 2.59, y*≈-0.76 (T4); (i) u*, (ii) u_{rms}*

(b)(i)). At this position, the local velocity magnitudes adjacent to the model profile (z*>0.6) are shown to increase markedly, with this rise generated by the additional wake blockage produced by the side struts, evident in the lower parts (z*<0.6). Consequently, above z*≈0.6, magnitudes are up to Δu*≈0.13 higher, with this behaviour being responsible for the reduced wake width for this configuration, as discussed in **Section 6.3.1**. Further comparisons between **Fig. 6.10(a)(i)** and **(b)(i)** also suggest that as the strut wake evolves downstream, the impact of the local flow blockage grows, with little influence at z*>0.4 observed in **Fig. 6.10(a)(i)** followed by significant increases seen in **Fig. 6.10(b)(i)** (z*>0.4).

Similar variations are also found for u_{rms}* (**Fig. 6.10(a-b)(ii)**). Above z*≈0.5, a general insensitivity to mounting method is indicated, with u_{rms}*≈0.025 for all three cases. Closer to the ground, however, profiles for the side-mounted setup are seen to deviate (increase) in comparison to the other configurations. In **Fig. 6.10(a)(ii)**, u_{rms}* increases significantly up to the maximum of u_{rms}*≈0.093 found at z*≈0.22. This result is reflective of the rise in turbulence production adjacent to the model wake. Further downstream at T4 (**Fig. 6.10(b)(ii)**), the affected area is shown to widen (up to z*≈0.6), reducing subtly in maximum magnitude to u_{rms}*≈0.064. The spatial growth supports the additional wake blockage induced by this setup, with the results indicating the significant impact the side struts can impart to the surrounding flow-field.

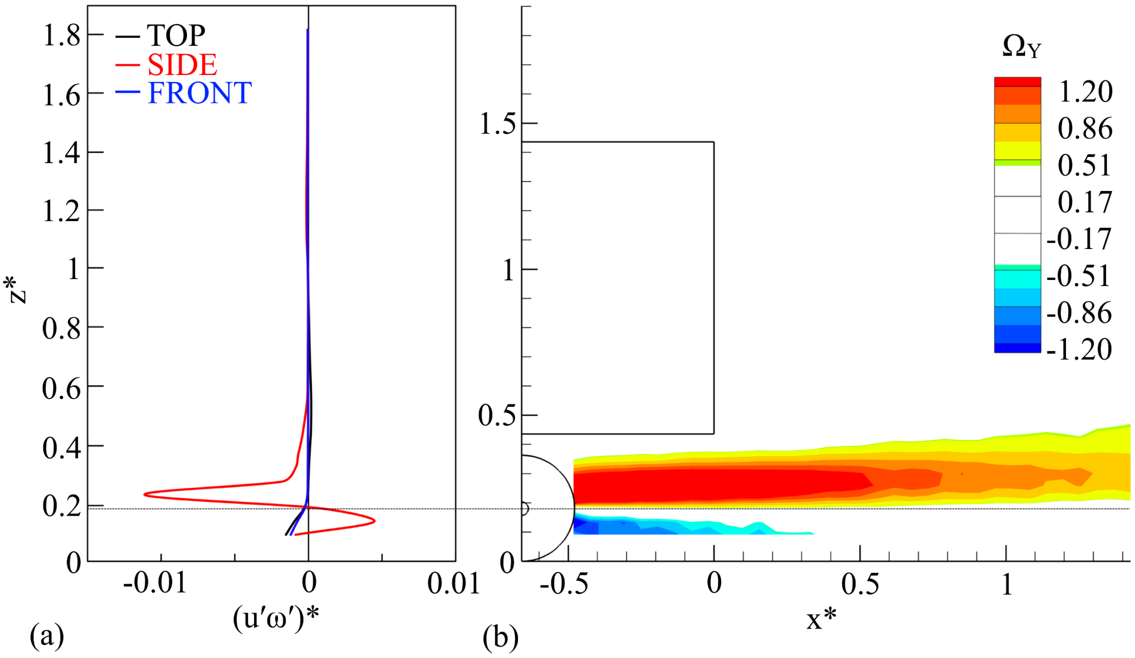

Fig. 6.11 Details of side strut wake: (a) (u′ω′)* profiles at x*≈-0.48 – SV2; (b) Ω_Y contours for the side mounting configuration in SV2 (contours -0.5< Ω_Y<0.5 omitted)

Further details of the nature of the side strut wake are provided with profiles of the Reynolds shear stress $(u'\omega')^*$ within SV2 (**Fig. 6.11(a)**). For the top and front mounting configurations, little variation exists locally, with $(u'\omega')^* \approx 0$. One exception is evident closer to the ground, where the stress magnitude increases subtly in the negative direction, reflective of the weak floor boundary layer influence. Results for the side-mounted setup, however, are distinctly different. Within $0.1<z^*<0.5$, significant $(u'\omega')^*$ magnitude increases centred around the strut axis are indicated in **Fig. 6.11(a)**, representative of strong momentum flux typical of a separated wake. Unlike an axisymmetric wake, however, the flow shed from these struts is dominated by substantially greater downward momentum due to the close proximity of the moving ground. This is reflected in the stress magnitudes within $0.2<z^*<0.3$ being more than twice as high as those within $0.1<z^*<0.2$ (**Fig. 6.11(a)**). Results for the crosswise vorticity (Ω_Y), presented in **Fig. 6.11(b)**, highlight this effect further, with vorticity magnitudes above the strut level being more intense and distributed than those below. Downstream propagation is also shown more significant, with relatively high magnitudes extending as far as $x^* \approx 1$. These results, once again, emphasise the substantial influence the side struts have on the nearby flow-field close to the base, as well as far downstream.

The effects of this asymmetric flow over the side strut are now explored further. **Figure 6.12** provides streamwise vorticity (Ω_X) contours behind the left wheel and the surrounding area at T2. Firstly, all three configurations reveal a common vortical structure centred around $y^* \approx -0.4$, $z^* \approx 0.45$. This vortex develops from the flow wrapping around the trailer bottom corner, being comparable in size and strength for all three cases ($\Delta y^* \approx 0.1$, $\Delta z^* \approx 0.1$ at $\Omega_{X\max} \approx 1.8$). Overall comparisons between the top and front setups suggest similar characteristics. In contrast, the side mounting configuration (**Fig. 6.12(c)**) is shown to produce secondary effects within the region. An additional structure is seen developing directly downstream of the wheel and closer to the ground ($y^* \approx -0.4$, $z^* \approx 0.15$) for this setup. Signatures of this vortex, albeit with a significantly lower magnitude, are also observable for the front-mounted case (**Fig. 6.12(a)**), being weaker still for the top mounting (**Fig. 6.12(b)**). This trend of locally decreasing Ω_X magnitude is reflective of the increasing difference in velocity magnitudes between the underbody exiting flow and the flow adjacent to the outside wheel profile. The former is shown invariant with mounting method (**Fig. 6.4(a)**), with the latter seen markedly reduced for the side-mounted setup through the deficit generated by the struts (**Fig. 6.10(a)(i)**). Finally, remnants of the vorticity generated over the side strut are also evident at y*≈-0.6, z*≈0.25 (Ω_X≈-0.55 - **Fig. 6.12(c)**). Overall, the similarities between the top and front setups from this perspective, indicate little influence from the upstream sting on the flow near the ground.

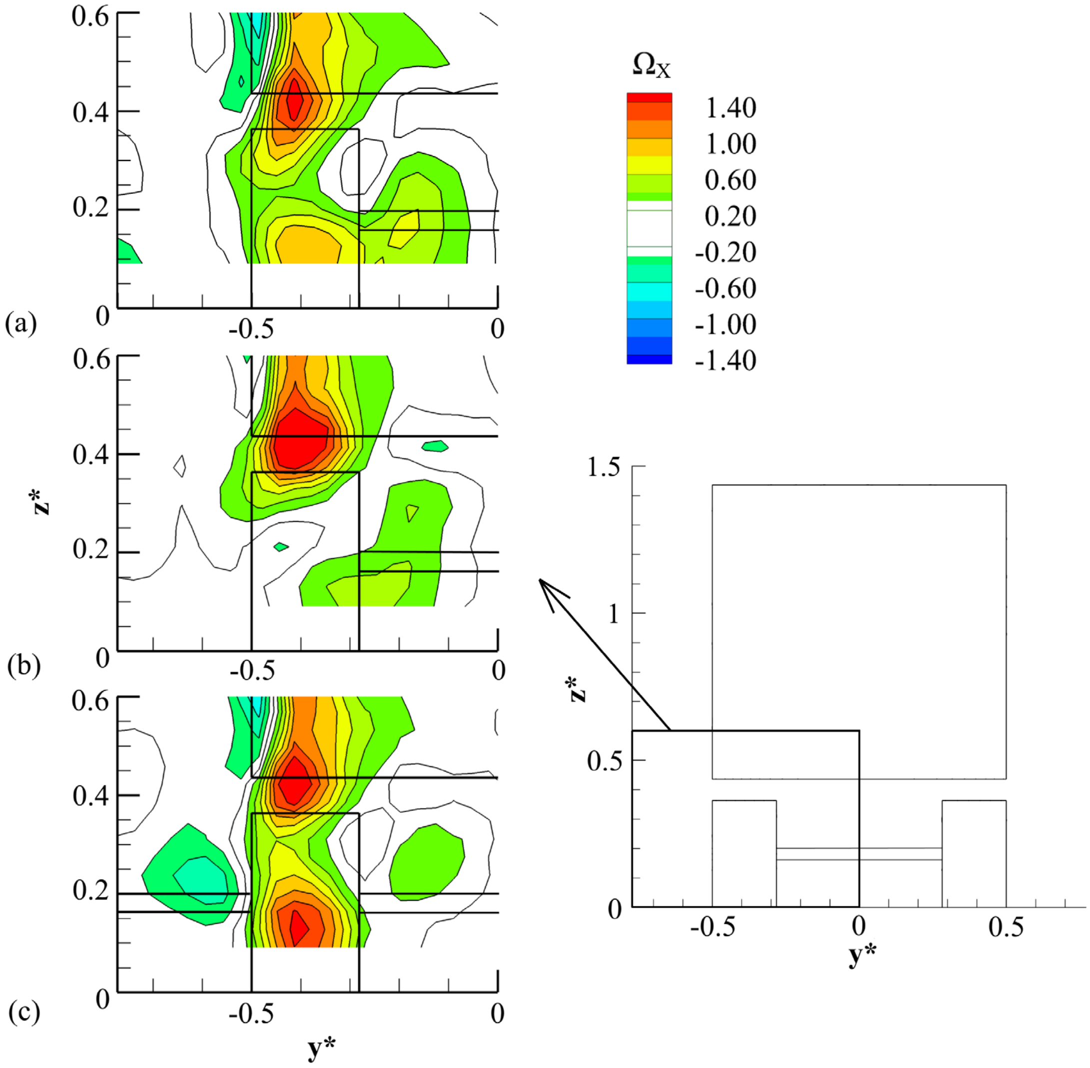

Fig. 6.12 Streamwise vorticity (Ω_X) contours behind the left wheel in T2: (a) front, (b) top, (c) side mounting (contours $-0.2<\Omega_X<0.2$ omitted for clarity)

6.4 Time-dependent flow characteristics

Results considered in the previous sections suggest that from a time-independent perspective, the proposed front-mounted support methodology is a viable alternative to the more established techniques. Time-dependent aspects are now compared to complete the analysis. Both base pressure and wake velocity spectra are considered, with the former averaged from 15 time-segments (1.25s duration) and the latter, 39 time-segments (0.5s duration). Bin widths are ΔSt_W≈0.0052 for both, with a 50% overlap. Selected results are presented with offset magnitudes to aid interpretation.

6.4.1 General wake dynamics

Selected pressure spectra on the model base are presented in **Fig. 6.13**, with a relative offset of 5dB/Hz between the setups. Little variation is shown between differing mounting methods, with no strongly defined peaks evident for all. However, for all configurations, a broad peak at $St_W \approx 0.107$ is indicated at most locations, in particular closer to the base centre (positions 25-32, **Fig. 6.13**). This frequency coincides with the characteristic frequency of the bubble pumping mode found in the pressure spectra of the top-mounted model with the use of moving ground as detailed in **Section 5.4.1** (here St_W lower due to applied blockage corrections). To validate the nature of this peak, **Fig. 6.14** provides coherence and phase information for positions 25 and 32, for all three mounting setups. These results, indeed, show the oscillations at this frequency to remain in-phase, characteristic of the bubble pumping mode **(Duell and George, 1999)**. Analogous to the results discussed in **Section 5.4.1**, comparisons to previous work, show good agreement to Duell and George **(1999)** ($St_W \approx 0.069$), Khalighi et al. **(2001)** ($St_W \approx 0.098$), Volpe, Devinant and Kourta **(2015)** (St_W

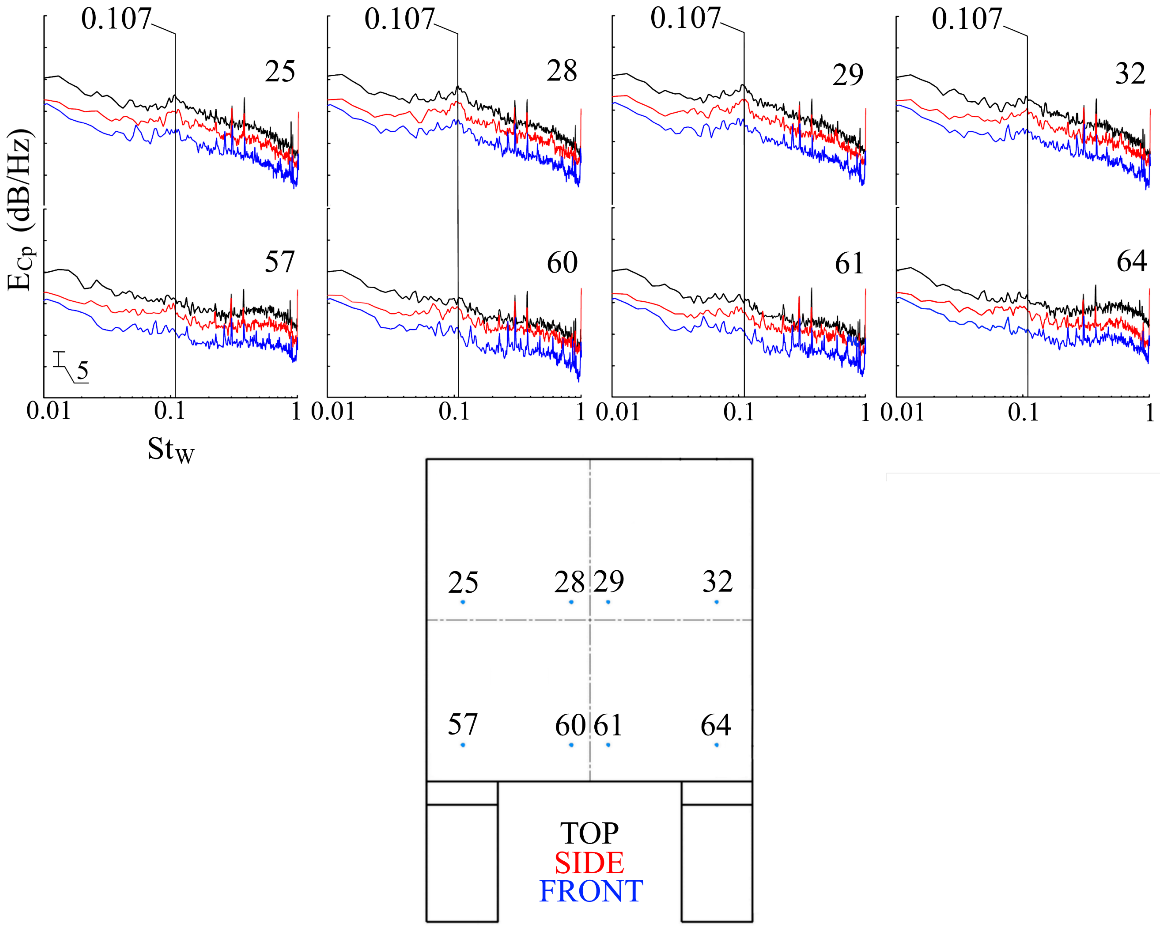

Fig. 6.13 Base pressure spectra at selected locations (relative offset of Δ5dB/Hz)

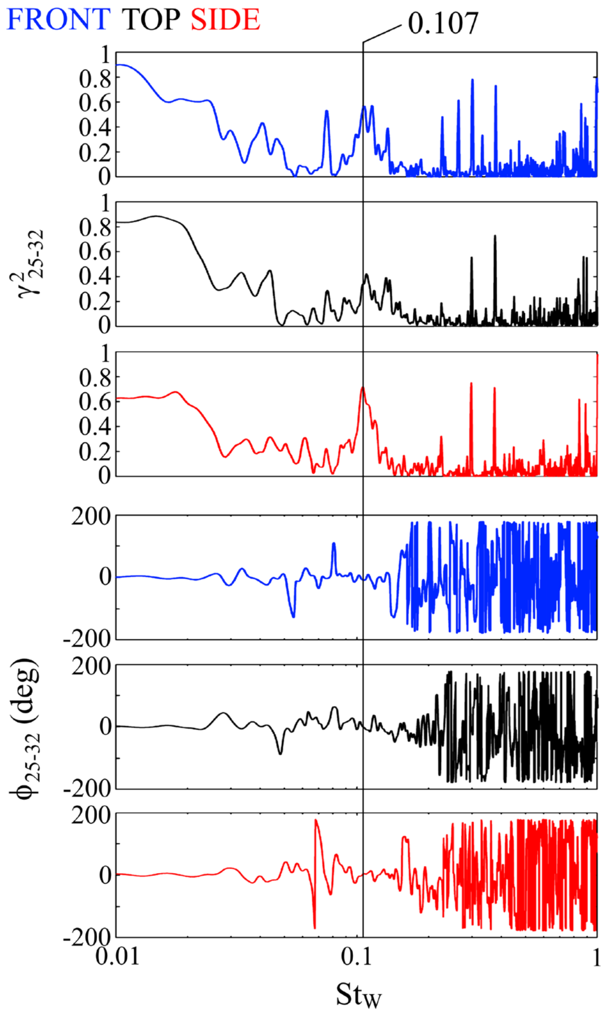

Fig. 6.14 Base pressure coherence (γ^2) and phase (ϕ) relationships between positions 25 and 32

≈0.11), McArthur et al. **(2016)** (St_W ≈0.08), and Pavia et al. **(2018)** (St_W ≈0.094). These results, therefore, suggest the characteristic frequency of the streamwise wake oscillation remains insensitive to the varying mounting method. Furthermore, the front and side mountings appear to promote the strongest coherence, suggesting the top strut may have an adverse impact on this mode.

The bubble pumping mode is also captured in the streamwise velocity spectra (E_u) within the side separated shear layers, with peaks at St_W ≈0.107 evident in **Fig. 6.15(a)** for all three configurations. Oscillations consistent with lateral wake shedding are also found within these results at a central far wake location (E_v – **Fig. 6.15(b)**). This mode, again, remains largely insensitive to mounting method (St_W ≈0.212), with similar lateral shedding characteristic frequencies also reported by Grandemange, Gohlke and Cadot **(2013b)**, Volpe, Devinant and Kourta **(2015)**, and McArthur et al. **(2016)**. One possible exception is the side-mounted configuration, shown to exhibit somewhat less defined spectral characteristics at this frequency. The time-averaged results (**Fig. 6.2(a-b)(iii)**, **Fig. 6.10**) identified strong localised disturbance produced by the side struts, which would be expected to impact this mechanism. Within the top separated shear layer (**Fig. 6.15(c)**), a broader heightwise shedding mode is also identified at $St_W \approx 0.22$. This behaviour can be seen mostly unaffected by mounting method, with all three configurations exhibiting largely similar characteristics.

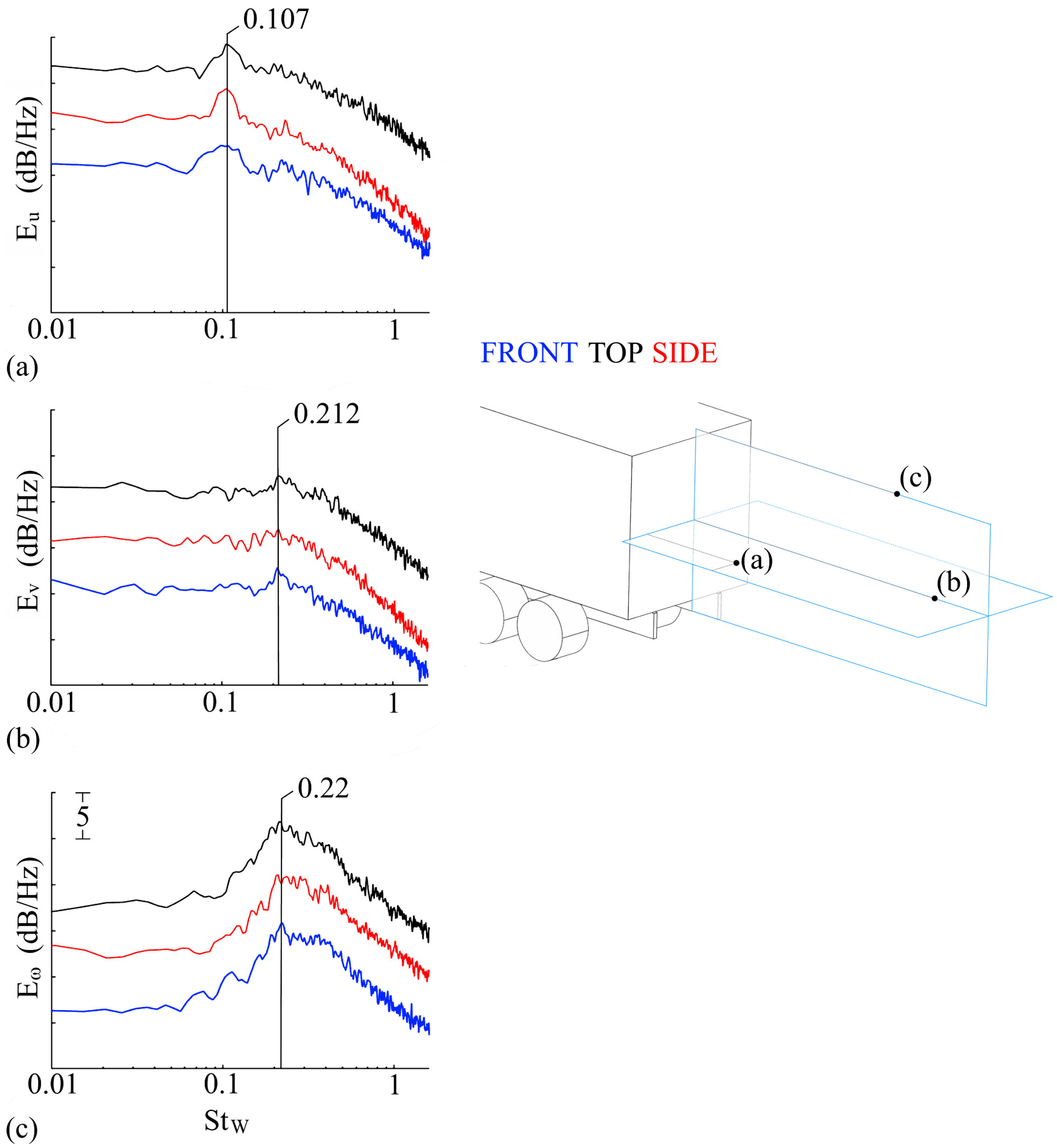

Fig. 6.15 Velocity spectra in the wake: (a) E_u at $x^* \approx 0.64$, $y^* \approx -0.36$, $z^* \approx 0.92$; (b) E_v at $x^* \approx 1.64$, $y^* \approx 0$, $z^* \approx 0.92$; (c) E_ω at $x^* \approx 1.36$, $y^* \approx 0$, $z^* \approx 1.5$ (relative offset of $\Delta 5$dB/Hz)

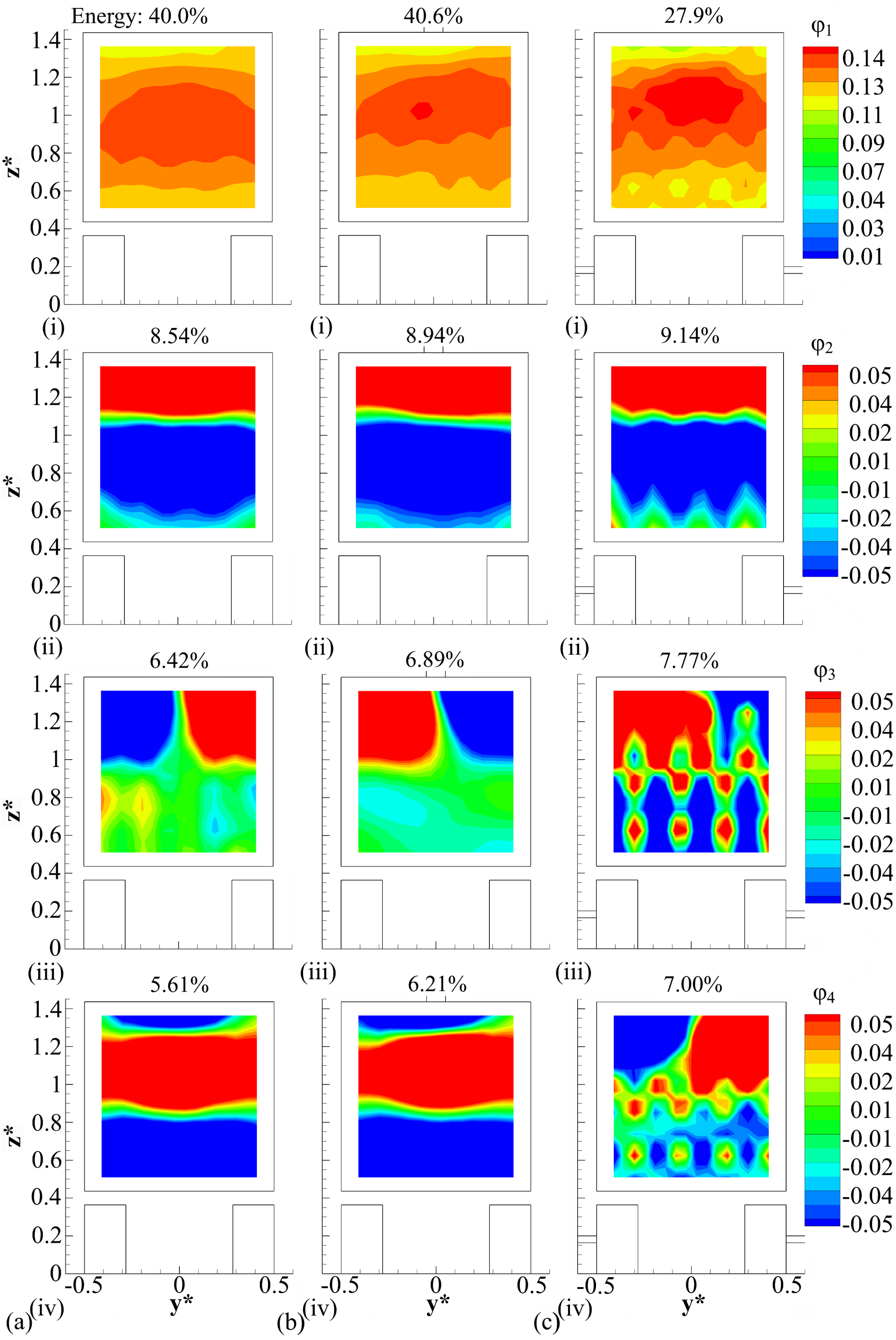

Fig. 6.16 The first 4 modes of POD of base pressure: (a) front, (b) top and (c) side mounting; (i) Mode 1; (ii) Mode 2; (iii) Mode 3; (iv) Mode 4

Further insight into the dynamic processes is gained by considering the POD modes of the unsteady base pressure signals. **Figure 6.16** presents the first four modes with a combined energy of just over half of the total budget, for all three configurations. In all three cases, the first mode (**Fig. 6.16(a-c)(i)**) is characterised by a near-uniform topology typical of a global streamwise wake oscillation, confirming the bubble pumping as the dominant mode. For the side-mounted model, reduced signal-to-noise ratio appears characteristic in these results, resulting most probably from the side struts being more susceptible to the transfer of tunnel vibration to the Scanivalve. Comparisons between the front (**Fig. 6.16(a)(i)**) and top (**Fig. 6.16(b)(i)**) configurations reveal near-identical energy levels (40.0% and 40.6% respectively), both being significantly higher relative to the side setup (**Fig. 6.16(c)(i)** – 27.9%). This reduction is a possible consequence of the impact the side support struts impart to the model base wake. This result is further supported by the lower $(u'^2)^*$ magnitudes within side shear layer development indicated for this method in **Fig. 6.5(a)(iii)**. The heightwise shedding mode identified in **Fig. 6.15(c)** is also confirmed within the POD results, evident as Mode 2, for all three configurations (**Fig. 6.16(a-c)(ii)**). The energy content of Mode 2 is approximately one-quarter that of Mode 1 (for front and top). As can be seen in **Fig. 6.16(a-c)(ii)**, this mode remains largely insensitive to mounting method, in agreement with the spectral characteristics presented in **Fig. 6.15(c)**.

Mode 3 confirms the lateral wake shedding mechanism for the front and top mounting configurations (**Fig. 6.16(a-b)(iii)**). The oscillation is centred around $y^*\approx 0$, with opposing cells dominating the upper base half. This trend has been previously described in **Section 5.4.2**, with the same height-dependency also evident here. These results suggest the crosswise shedding mode remains largely unaffected by the front sting, in agreement with the spectral characteristics identified in **Fig. 6.15(b)**. For the side support configuration, within Mode 3 (**Fig. 6.16(c)(iii)**), the opposing cells positioned in the top half of the base are less obvious. In this case, the topology is largely dominated by noise, with characteristically chaotic trends, supporting the spectral behaviour identified in **Fig. 6.15(b)** for this setup, indicating less defined, more incoherent lateral shedding characteristics.

The same symmetrically centred oscillation described in **Section 5.4.2** is again characteristic of Mode 4 for the top and front mounting configurations (**Fig. 6.16(a-b)(iv)**). The same is not observed for the side-mounted setup, which appears to exhibit an additional asymmetric mode, similar to the crosswise shedding. In this case, however, the topology again is mostly chaotic typical of increased noise levels.

6.4.2 Local spectral comparisons

As final means of assessment, velocity spectra at selected locations are compared to evaluate the local impact of the various mounting methods. Firstly, positions downstream of the top support strut are considered, with **Fig. 6.17** presenting the lateral ((a)-(d)) and vertical ((d)-(f)) evolution at plane T1. At (a), laterally furthest away from the strut, E_u shows little variation between the setups, indicating the local flow remains largely insensitive to support configuration. A subtle reduction in high-frequency turbulence for the top mounting is observed further inboard, at (b), with a decrease in magnitudes (≈3-5dB/Hz) beyond St_W ≈0.1. The opposite effect is evident with increasing proximity to the top strut, marked by significantly higher E_u magnitudes found at (c)-(d) for this setup. The maximum increase (≈15-20dB/Hz) is shown directly downstream of the strut centre at (d). This result confirms

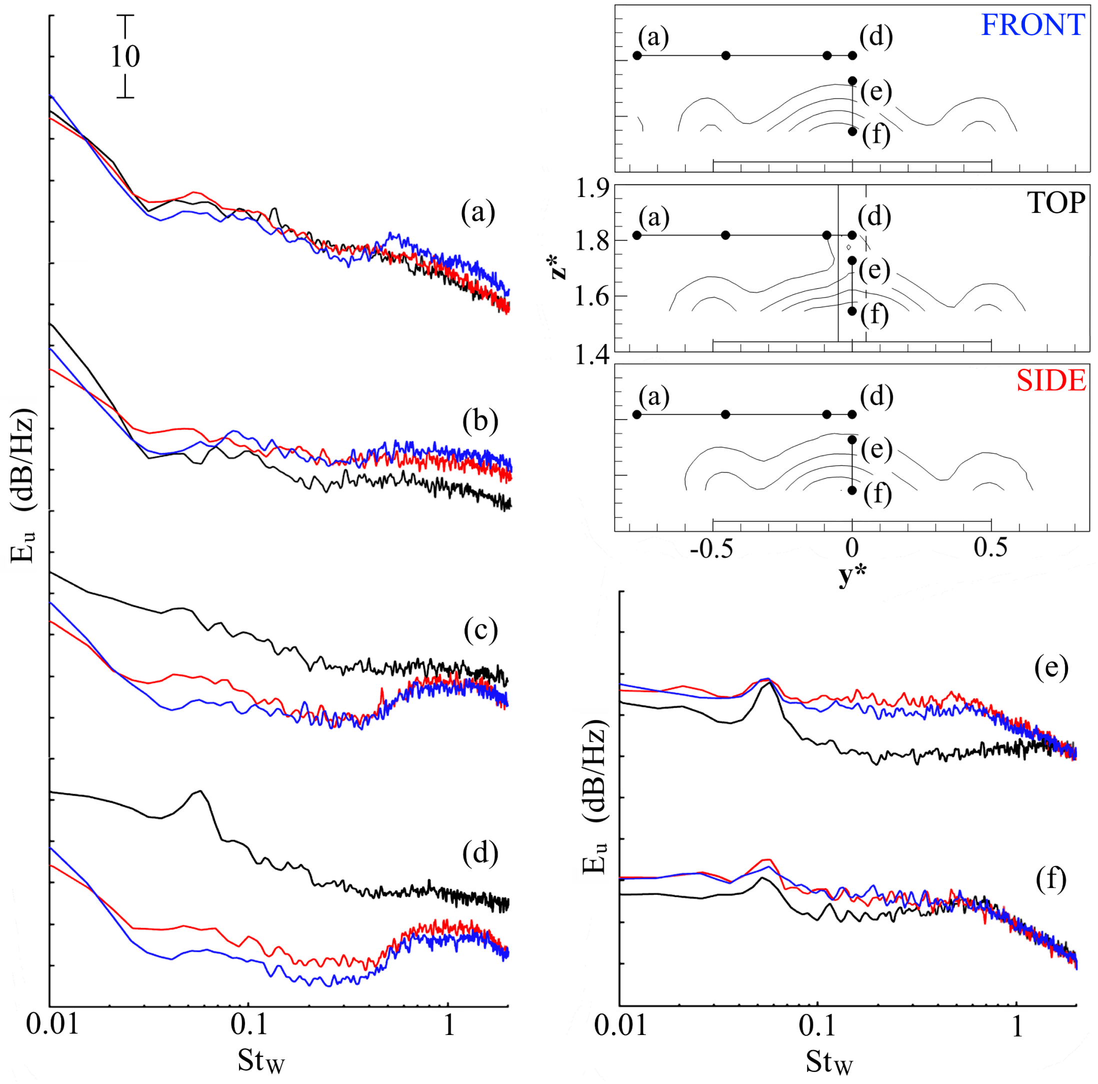

Fig. 6.17 Velocity spectra (E_u) at selected locations in T1 along $-0.76<y^*<0$ at $z^*\approx1.82$ (a-d), and $1.55<z^*<1.82$ at $y^*\approx0$ (d-f)

the wake generated by the top strut as a source of localised turbulence. At this distance away from the trailer roof ((d)), this is in agreement with the relatively elevated K identified in **Fig. 6.9(b)** at the same position. In contrast, closer to the roof surface, the vertical E_u evolution (**Fig. 6.17**) indicates relative reductions in magnitudes for the top mounting configuration at (e). This trend is shown to persist still to lower positions ((f)), albeit to a lesser degree, with reductions of up to 2.5dB/Hz for $St_W < 0.4$. These results tend to agree with Strachan et al. **(2007)**, who suggested a suppression of the roof boundary layer behind an overhead strut, with further support for this allegation also provided by the K results presented in **Fig. 6.9**.

Further insight is gained by assessing the downstream propagation of the top strut's influence. **Figure 6.18** provides vertical variations ((a)-(c)) of E_u above the base wake at two different streamwise locations (I-II). Closer to the model, at I, broad peaks centred around $St_W \approx 0.2$ are evident at positions (a) and (c) for all three configurations, corresponding to the heightwise wake shedding identified in **Fig. 6.15(c)**. Position (a) shows increases in magnitudes of up to 10dB/Hz below $St_W \approx 0.4$ for the top support setup. Comparisons to position (d) in **Fig. 6.17**, therefore, reveal the influence of the wake emanating from the top strut to persist downstream to I. This influence can be seen to weaken downward through (b), with no appreciable effect at (c). The impact of the top strut is completely inhibited further downstream at II (**Fig. 6.18**), where the spectra of all three configurations show near-identical trends at all points (a)-(c). One possible exception is found at (a), where the spectra for the front mounting configuration exhibit magnitude reductions at lower frequencies, indicating subtly less intense turbulence within the local flow. Overall, however, the results presented in **Fig. 6.17** and **Fig. 6.18** indicate general similarities exist between the front and side-mounted models from this perspective, suggesting little local impact from these methods.

The spectral characteristics within the side strut wake are now considered. **Figure 6.19** presents E_u at selected locations, with points (a)-(e) highlighting heightwise variations behind the strut and (f)-(j) located further downstream. At (a) positioned closest to the ground, E_u characteristics remain generally similar for all configurations, with marginal reductions in magnitude (≈1-5dB/Hz) for $St_W < 0.1$ evident for the side mounting. Both the front and side-mounted setups also show a discrete peak at $St_W \approx 0.82$, corresponding to the wheel rotation frequency ($St_W \approx 0.80$), as previously described in **Section 5.4.4**. For the front, this peak is discernible up to position (d), with positions (a)-(c) also showing a related harmonic at $St_W \approx 1.64$. Further up at (b), magnitudes beyond $St_W \approx 0.1$ are shown to increase by up to 10dB/Hz for the side setup. This relative increase becomes most significant within the strut's wake at (c), indicating E_u up to 20dB/Hz higher in comparison with the other configurations. These results confirm the side strut to be a source of substantial turbulence, affecting the local flow-field. Moving vertically upward, this influence is found to persist as high as $z^* \approx 0.4$, with magnitudes at position (d) still higher by up to 15dB/Hz relative to the front support configuration. Distinctly, the top-mounted model at the same position ((d)) also exhibits increased E_u ($\approx$10dB/Hz) in comparison with the front setup, indicating additional streamwise unsteadiness, with this effect shown to persist upward to (e). In

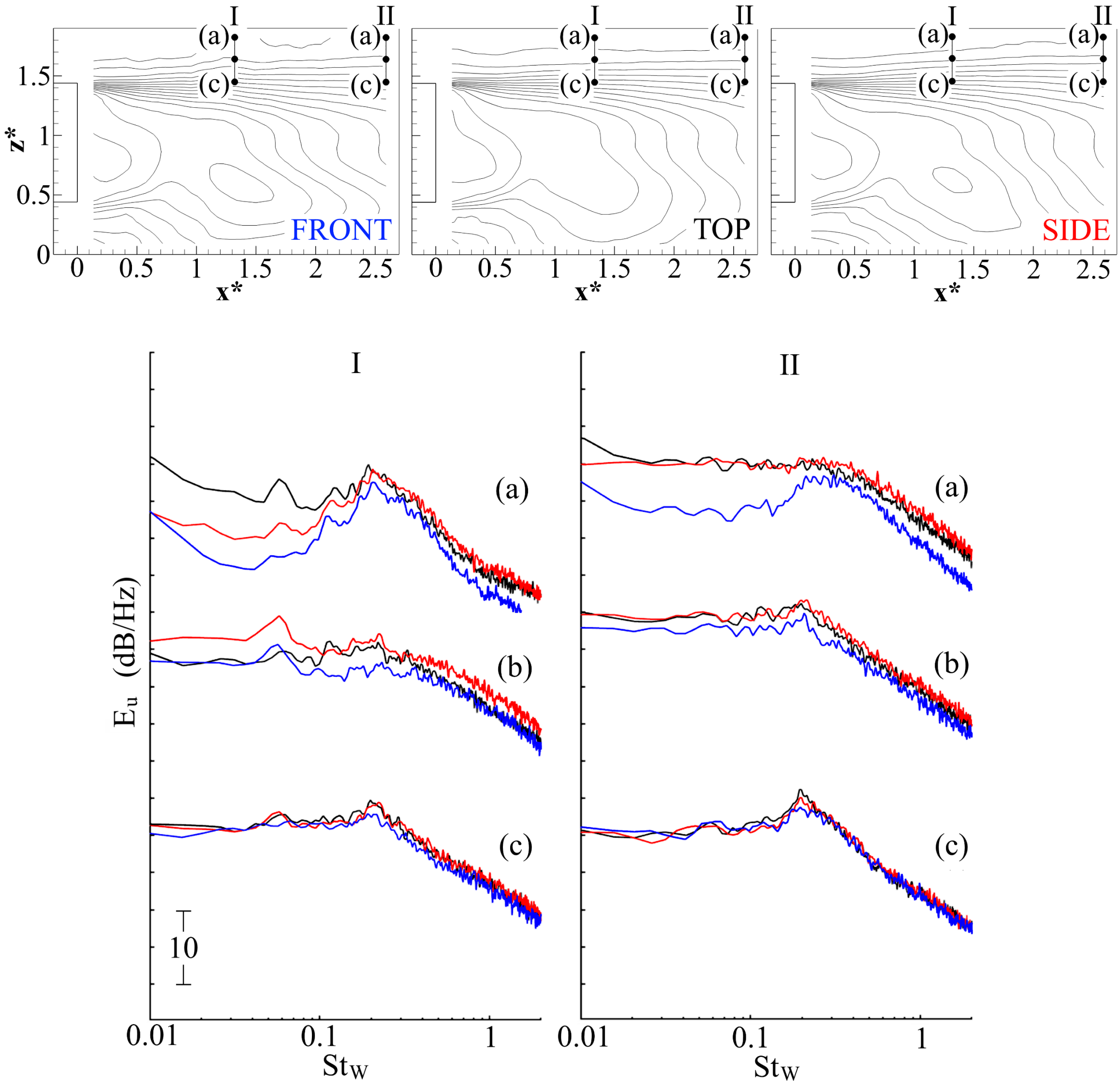

Fig. 6.18 Velocity spectra (E_u) at selected locations in SV1 along $1.45<z^*<1.82$ (a-c) at $x^* \approx 1.32$ (I) and $x^* \approx 2.59$ (II)

contrast, at the same location ((e)), E_u magnitudes for the side support are found to match those of the front configuration, suggesting general insensitivity at this position.

Close to the ground, downstream positions (f)-(g) show little sensitivity to streamwise position, with the E_u trends closely resembling those at (a)-(b). For the front mounting configuration, the wheel rotation signature ($St_W \approx 0.82$) is again evident at these

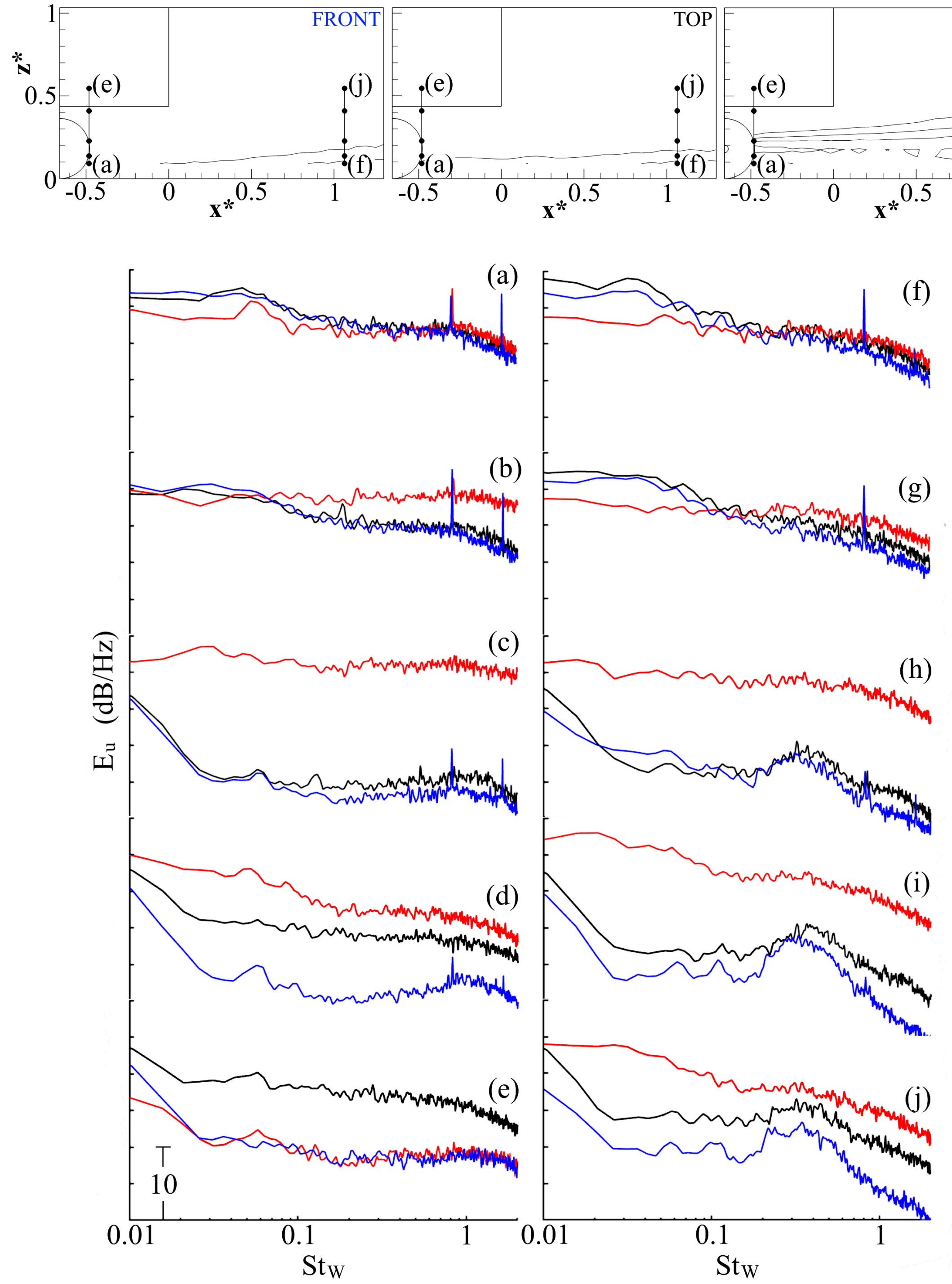

Fig. 6.19 Velocity spectra (E_u) at selected locations in SV2 along $0.09<z^*<0.55$ at $x^* \approx -0.48$ (a-e) and $x^* \approx 1.06$ (f-j)

locations. Further up, the offset in magnitudes between the top and front configurations identified at (d)-(e) is still evident at (i)-(j), albeit to a lesser degree (≈5dB/Hz), suggesting the same effect imparted by the former is weaker at these positions. Additionally, at (h)-(j), results for these two setups capture broad peaks centred around St_W ≈0.4, with a shift to a subtly lower frequency for the front. At this position, this increase in energy corresponds to the devolving lateral wheel wake shedding, as detailed in **Section 5.4.4**, indicating these characteristics to be retained when using the front sting. In contrast, with the model mounted from the sides, the wheel wake signature is shown completely inhibited by the overall increase in magnitudes ((h)-(j)), which is somewhat supported by the results presented in **Fig. 6.6**. Higher E_u magnitudes for the side support setup are evident at all positions (h)-(j). These results suggest the wake generated by the side strut propagates downstream and upwards, affecting the flow-field at higher locations, in agreement with **Fig. 6.2(a-b)(iii)**, **Fig. 6.10** and **Fig. 6.11**.

Qualitative comparisons to **Fig. 6.17** and **Fig. 6.18** suggest the impact imparted to the surrounding flow-field by the side strut wake is broader and more significant relative to that produced by the top support strut. Additionally, from this perspective, the trends of the front and top support setups remain largely similar, indicating little appreciable interference from the front sting.

6.5 Summary

The effects of the proposed front model-mounting method evaluated and compared to other well-established techniques (from top and sides) were discussed in this chapter. Recorded drag showed subtle variations, with increases, albeit within experimental uncertainty, in trailer drag for the top and side setups relative to the upstream configuration. Subtle differences in base pressure topologies were also found, with a small increase in the calculated trailer base drag coefficient for the top mounting. Overall, comparisons of recorded trailer drag and calculated trailer base drag revealed the inclusion of the front sting to have little influence on the mean drag production.

Some variations in the time-averaged base wake topologies between the three configurations were indicated in the results, with the turbulence production within the developing separated shear layers also found affected. Significant areas of flow retardation and increases in turbulence characterised the localised wakes generated by the top and side support structures. With the side struts, the vorticity production around the rear wheel profile was shown to be altered. Additionally, the propagating side strut wake was found to affect the flow-field far downstream of the base. The wake produced additional flow blockage close to the ground, with increases in velocity magnitudes further up and subsequent model wake contraction arising as a consequence.

Wake dynamics of all three setups were found dominated by the bubble pumping mode, with the corresponding characteristic frequency insensitive to mounting method. In the side-mounted setup however, this mode was found significantly weaker, with approximately a 12 percentage point reduction in the energy budget relative to the front and top configurations. The asymmetric shedding (flapping) characteristic frequencies were also indicated largely insensitive to different configurations. One exception was the lateral shedding mode, appearing much less defined and more incoherent for the side-mounted model. Additionally, POD of the base pressure signals revealed an additional asymmetric mode exists for this setup, absent in the other two cases.

Spectral analysis of selected regions of the flow-field showed the top support strut to increase turbulence levels within the flow over the trailer, with this influence weakening with downstream evolution. Within the regions closer to the model roof, this was shown reversed, with the top-mounted setup showing evidence of suppressed fluctuations within the central portions near the surface boundary layer. Downstream of the side strut, the increases in turbulence were found more intense still. With this setup, a significant influence on the surrounding flow was identified close to the model base, as well as further downstream. The results suggested downstream and upward propagation.

Overall, no significant interference was identified for the front sting within the flow-field at the model base. The results suggested the proposed technique to combine local benefits while minimising deficiencies of the other common mounting methods from top and sides. Therefore, the front sting was shown to provide an excellent alternative for ground vehicle studies, particularly those focusing on model rear.

Chapter 7

Preliminary investigation of lobed mixers

This chapter discusses the results of the initial investigation of lobed mixers. This investigation aimed to assess the suitability of the devices for drag reduction of boat-tailed ground vehicles. The experiments were conducted using Baseline 1 in the front mounting configuration, as presented in **Fig. 4.16**, with the inclusion of moving ground. Three base inserts (LB1-3) were studied, as discussed in **Section 4.4.1**. In addition to the different lobe geometries, a legacy boat-tail (BT), as well as standard baseline (no insert) were assessed for comparison. First, the relative changes in drag are presented. The baseline wake is discussed thereafter, followed by the influence of the legacy boat-tail. Finally, the effects of lobed mixers on the base wake are outlined, including the produced vorticity and impact on mixing.

The results presented in this chapter have been published as Rejniak and Gatto **(2019)** and are reproduced here with the permission of the copyright holder.

7.1 Average drag

The total drag coefficient of Baseline 1 in the current setup was determined as $C_{DM} \approx 0.72$, in excellent agreement with the results detailed in **Chapter 5**, demonstrating consistency in drag of Baseline 1 measured in various setups. Note that blockage corrections are not applied to these results, explaining the difference in comparison with the values presented in **Table 6.1** (**Chapter 6**). The change in C_{DM} (measured acting on the trailer) with the BT and LB1-3 is presented in **Table 7.1**. All configurations result in drag reduction, with the lobed boat-tails shown to produce further benefits relative to the BT. The highest drag reduction of 10.2% is produced by LB1, with the result of LB2 (9.6 ± 0.7%) within the experimental uncertainty. Among the lobed boat-tails, the smallest drag benefit is evident for LB3, but remains significantly more effective than the BT offering a 6.9% reduction.

For the three lobe configurations tested, the effect of lobe pitch and height can be evaluated. The drag results show decreasing pitch (LB1 to LB3) and increasing height (LB1 to LB2) marginally degrade performance, suggesting the optimum for this setup is likely near LB1. With the minimum pitch and height configuration (LB3) producing the lowest drag reduction, this decreasing trend ($p \to 0$, $h \to 0$) suggests further reductions would approach the benefit of the BT.

Overall, the results presented in **Table 7.1** show that in all cases (LB1-3), the addition of the lobed mixer profile can be effective in enhancing the drag reduction of a standard boat-tail characterised by higher α. Given this ability, it seems that integration onto existing boat-tails, or application to shorter, more extreme BT angle configurations, with similar overall aerodynamic benefit, may be possible.

	BT	**LB1**	**LB2**	**LB3**
ΔC_{DM} (%) (±0.7)	-6.9	-10.2	-9.6	-8.8

Table 7.1 Measured total drag reduction with the base inserts relative to Baseline 1

7.2 Base wake measurements

The measurements within the baseline wake are evaluated first to enable a direct comparison to the remaining configurations (BT, LB1-3). **Figure 7.1** presents u* contours at the model base in both measurement planes T2 and T3, with the wake characterised by lower u* magnitudes directly downstream of the model profile. At T2, within $|y^*|<0.5$, $0.45<z^*<1.4$, the velocities are distributed uniformly and decrease from the top base edge towards the lower positions, with the minimum ($u^* \approx 0.18$) at $|y^*|<0.4$, $0.55<z^*<0.8$, marking the central location of the lower wake vortex. Generally, the wake appears symmetric vertically about $y^* \approx 0$ and asymmetric horizontally, reflective of the typical vertical wake topology. These trends are in very good agreement with those already discussed in **Chapters 5** and **6**, despite the differences in HWA sampling rates and grid densities. Undisturbed freestream flow can

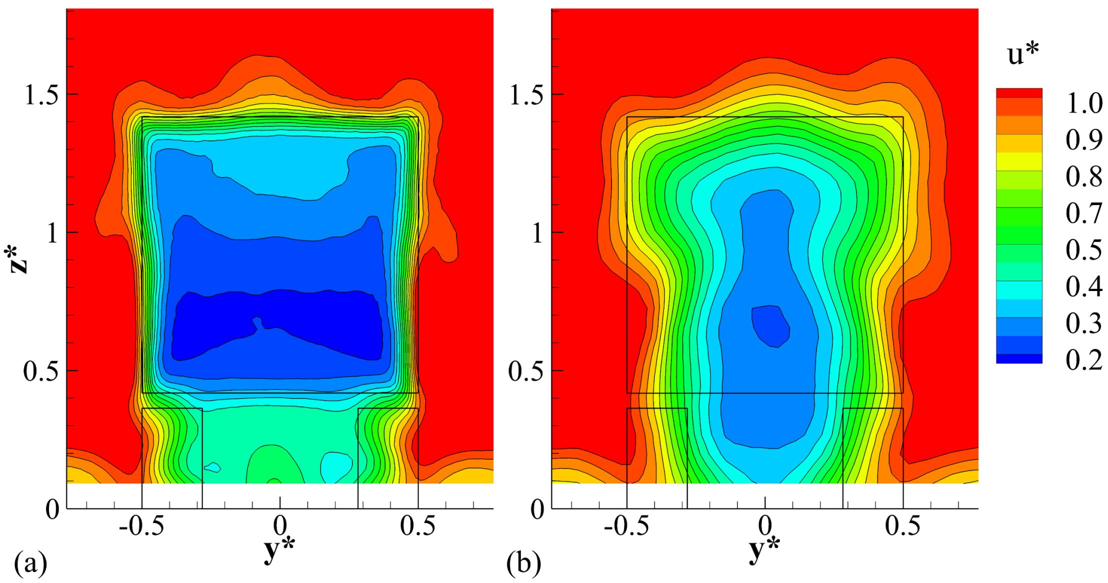

Fig. 7.1 Streamwise velocity contours within the baseline wake at: (a) T2, (b) T3

be seen surrounding the model profile in both planes, with one exception evident near the ground on both sides of the model ($u^*\approx0.9$ at $|y^*|>0.5$, $z^*<0.2$). This subtle flow retardation corresponds to the remnants of the upstream boundary layer. Nevertheless, given the distance to the base inserts and $u^*\approx1$, these areas are not expected to significantly influence the comparisons.

The vertical symmetry and horizontal asymmetry are maintained further downstream at T3 (**Fig. 7.1(b)**). At the same position, the vertical wake size (defined here as encompassing $u^*<0.8$) remains effectively unchanged from T2, as does the lateral wake size above $z^*\approx0.8$. However, as evident in **Fig. 7.1(b)**, for $z^*<0.8$, the wake width reduces to $|y^*|<0.4$ from the $|y^*|<0.5$ observed at T2. The minimum velocity magnitudes ($u^*<0.4$) are found within this narrower region, highlighting the most intense u* gradients extending down to the ground.

To better understand this transition between T2 and T3, areas of enhanced flow rotation are examined, with **Fig. 7.2** providing topologies of crosswise (Ω_Y) and heightwise (Ω_Z) vorticity. Note that these results were calculated and used for comparison without the X-direction component. As can be seen, highest Ω_Y and Ω_Z are evident in regions where the fixed flow separation from the trailer edges results in high velocity gradients and fluctuations, marking the top and side shear layers. The results compare well with those of McArthur et al. **(2016)** and Lo and Kontis **(2017)**. Ω_Z (**Fig. 7.2(b)**) indicates good symmetry

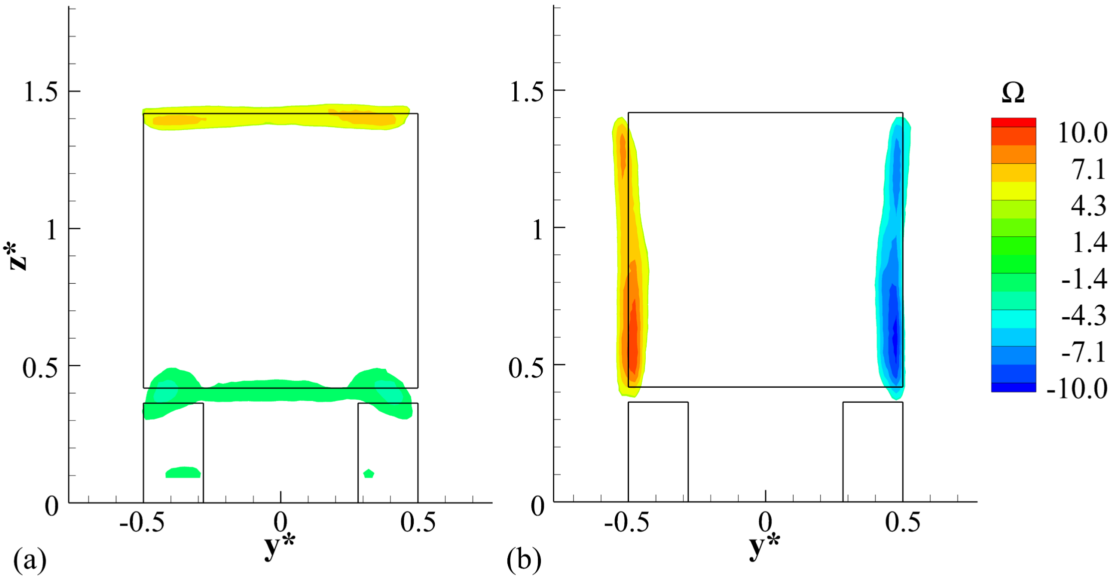

Fig. 7.2 Baseline wake vorticity at T2: (a) Ω_Y, (b) Ω_Z (ranges $-1.5<\Omega_Y<4$ and $-4<\Omega_Z<4$ omitted for clarity)

about y*≈0 with no significant maximum magnitude disparity ($\Omega_{Z\max}\approx|10|$). As expected, Ω_Y (**Fig. 7.2(a)**) shows opposite trends with higher magnitudes ($\Omega_{Y\max}\approx|6.7|$) along the top ($1.35<z^*<1.45$) and lower ($\Omega_{Y\max}\approx|3.7|$) closer to the bottom edge ($0.3<z^*<0.5$). This is a consequence of lower u* magnitudes within the exiting underbody (relative to freestream) flow, resulting in lower gradients. Considering **Fig. 7.2(a)** further, Ω_Y along the top edge is indicated strongest near the sides ($0.3<|y^*|<0.5$ at $z^*\approx1.4$) relative to the midsection ($|y^*|<0.3$). This result is most likely a consequence of the relative increase in local velocity gradients as presented in **Fig. 7.1(a)**. A similar trend, albeit more pronounced ($\Omega_{Z\max}\approx|10|$), is also observed at both sides ($|y^*|\approx0.5$ between $0.4<z^*<0.85$) in **Fig. 7.2(b)**. With the strongest vorticity apparent at these positions, **Fig. 7.2(b)** provides some explanation for the observed wake contraction below z*≈0.8 in **Fig. 7.1(b)**. Overall, these baseline results are in very good agreement with those presented in **Chapters 5 – 6** for similar setups.

7.3 Influence of standard boat-tail insert

Results for the BT are now considered and evaluated relative to the baseline discussed in **Section 7.2**. **Figure 7.3** presents the u* contours for the BT in T2 and T3. One immediate implication of adding this insert, evident in **Fig. 7.3(a)**, is the relative reduction in wake size, with $\Delta z^*\approx0.1$ from the top towards the model centreline and $\Delta y^*\approx0.1$ inboard from the sides.

The wake "boundary" now resides closer to the BT trailing edges, as would be expected from the boat-tailing effect **(Altaf et al. 2014; Kehs et al. 2013)**. Comparisons to **Fig. 7.1(a)**, also show minimum u* magnitudes to displace vertically into the upper base portions with the BT added ($0.7<z^*<1.3$ – **Fig. 7.3(a)**), with comparatively lower, more distributed magnitudes ($0.5<z^*<1.35$, $|y^*|<0.4$), likely to be a consequence of the trapped cavity flow. Another direct modification is evident in the lower region ($0.1<z^*<0.6$, $|y^*|<0.6$) in **Fig. 7.3(a)**, with a local increase in the wake width, reflective of the flow transitioning from the narrower boat-tail end to the wider flow near the ground.

Further downstream, (T3 - **Fig. 7.3(b)**), higher velocity magnitudes ($0.45<u^*<0.7$ within $0.7<z^*<1.25$, $|y^*|<0.3$) are seen directly behind the BT, accompanied by more significant spanwise and vertical wake contractions relative to **Fig. 7.1(b)**. One important implication which can be inferred from these results is that with the BT, the upper wake portion at this downstream position is nearer closure compared to the baseline. The opposite is found nearer ground level ($z^*<0.5$) with a distinct increase in the wake width ($\Delta y^*\approx0.3$ relative to baseline in **Fig. 7.1(b)**) and reduced u* magnitudes. Lowest velocity magnitudes ($u^*\approx0.23$) now reside in this region ($0.2<z^*<0.5$, $|y^*|<0.2$) relocating from $0.55<z^*<0.75$, $|y^*|<0.1$ (**Fig. 7.1(b)**). The inferred implications of these results are twofold. Firstly, the wake of the BT is tapered from the top and directed towards the ground relative to baseline. Secondly, the trends suggest that this increase in downward momentum for the BT results in faster and slower closure in the upper and lower wake portions, respectively. This offers some support for the drag measured for the BT (**Table 7.1**), given that decreases in wake size have been

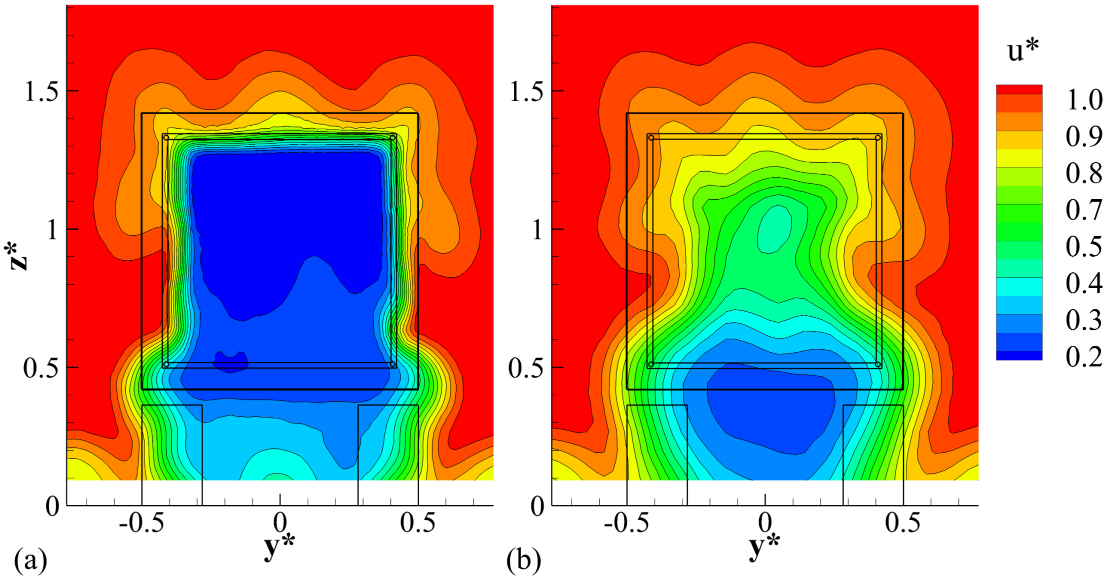

Fig. 7.3 Streamwise velocity contours within the BT wake at: (a) T2, (b) T3

linked to drag reductions **(Grandemange et al., 2013)**. Additionally, this significant rise in downward momentum is suggested to produce changes in the vertical wake balance, with the sizes of the top and bottom wake vortices expected to increase and decrease, respectively, making the former dominant. These characteristics would subsequently result in a downward shift of the rear stagnation point, with the new location likely downstream of the base bottom half.

The relative differences are further evaluated with comparisons of the wake vorticity (**Fig. 7.4**). For the BT (**Fig. 7.4(a,b)**), these are shown topologically similar to baseline **Fig. 7.4(a,b)**, though with spatial reductions in width and height, commensurate with corresponding trailing edge lengths. Markedly, **Fig. 7.4** shows higher Ω_Y ($\Omega_{Ymax} \approx |9|$) along the top edge ($1.3<z^*<1.4$), lower Ω_Y ($\Omega_{Ymax} \approx |1|$) along the bottom edge ($z^* \approx 0.4$), and similar $\Omega_{Zmax} \approx |10|$ along the sides. Increases in vorticity magnitudes at the top alongside comparable Ω_Z at the sides suggest stronger flow entrainment from above towards the wake centre. This observation is supported by the heightwise (towards the ground) and crosswise reductions of the BT wake size as shown in **Fig. 7.3(b)**. Below $z^* \approx 0.7$ (**Fig. 7.3(b)**), this influence can be seen limited, which is consistent with the relatively lower extent of the side shear layers identified in **Fig. 7.4(b)**.

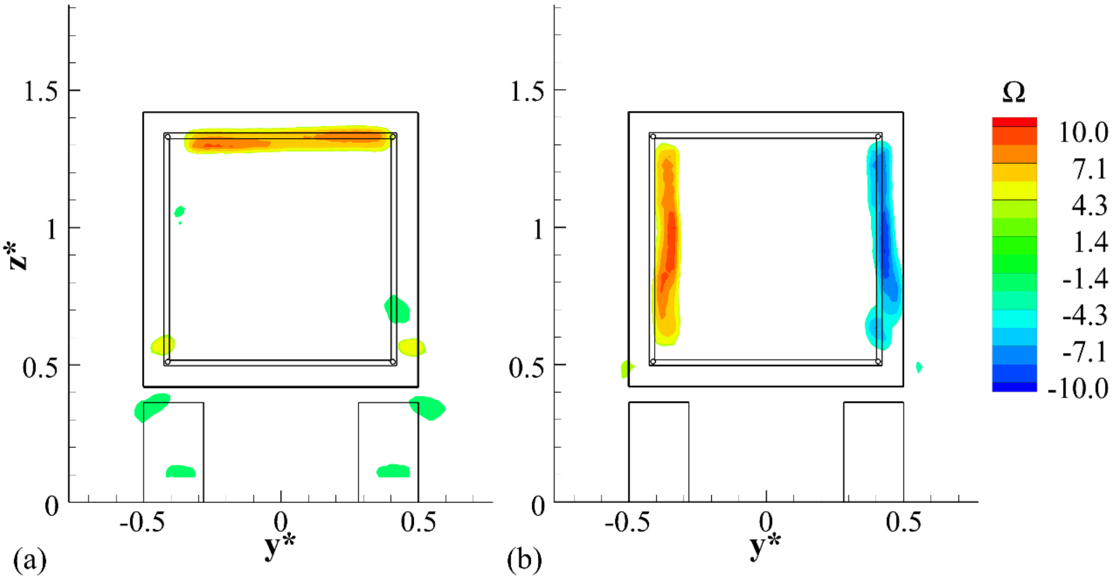

Fig. 7.4 BT wake vorticity at T2: (a) Ω_Y, (b) Ω_Z (ranges $-1.5<\Omega_Y<4$ and $-4<\Omega_Z<4$ omitted for clarity)

7.4 Influence of lobed mixers

Given the well correlated results for the baseline and the effects of the BT established, the influence of the lobed mixer profiles is now considered. **Figure 7.5** presents u* contours for LB1-3. At T2, topologies remain similar, which is somewhat expected due to the short relative distance to this measurement plane ($\Delta x^* \approx 0.13$ from insert's trailing edges). Generally, all configurations exhibit vertical symmetry and horizontal asymmetry, similar to the trends observed previously. Similar to the BT, here the lowest velocity areas are also found within the cavity ($|y^*|<0.4$, $0.4<z^*<1.3$), with a comparable increase in lower wake width (albeit marginally less by $\Delta y^* \approx 0.1$-0.2 compared to **Fig. 7.3(a)**) again evident ($0.1<z^*<0.4$).

Moving downstream, at T3 (**Fig. 7.5**), the results show very distinct transverse wake contractions fixed around $z^* \approx 0.8$. This feature, absent from the other configurations, is seen to contribute to an almost "hourglass" wake topology, with lower u* magnitudes evident both above and below the "waist". The bottom structure is generally spatially bigger with lower u* magnitudes in comparison to the upper segment. Additionally, velocity minima, which reside in these areas ($z^* \approx 0.6$), are lower relative to both the baseline (**Fig. 7.1(b)**) and the BT (**Fig. 7.3(b)**). These findings provide some support for the trend shown in **Table 7.1**, where lower velocities would indicate greater wake lengths with respect to the trailer base, and consequently, larger drag reductions as the low-pressure cores of the wake vortices are shifted further downstream ($u^* \approx 0.19$ within $|y^*|<0.1$, $0.46<z^*<0.6$ – LB1, $u^* \approx 0.19$ within $|y^*|<0.1$, $0.46<z^*<0.7$ – LB2, and $u^* \approx 0.20$ within $|y^*|<0.1$, $0.53<z^*<0.56$ – LB3) **(Duell and George, 1999)**. Above the "waist" ($z^*>0.8$), these differences are greater still with $u^* \approx 0.25$ for LB1, $u^* \approx 0.24$ for LB2, and $u^* \approx 0.27$ for LB3, demonstrating again general support for the results in **Table 7.1**.

Comparing **Fig. 7.5(a-c)** at T3 to **Fig. 7.3(b)** (BT) directly, the results show the addition of lobed profiling results in a clear shift in the wake topology. Perhaps most obvious is the re-establishment of a low-velocity wake ($u^*<0.5$) in the upper half. This suggests one influence of adding lobes to the standard boat-tail is a limited flow entrainment towards the ground. This is proposed to be a result of the confining effect imparted by the "waist" through enhanced crosswise flow, providing uplift, or support, against downward movement. Further evidence is provided in **Fig. 7.6**, which presents the u_{rms}^* profiles along $y^* \approx 0$ in both T2 and T3. For all configurations in **Fig. 7.6(a)**, the maxima are located

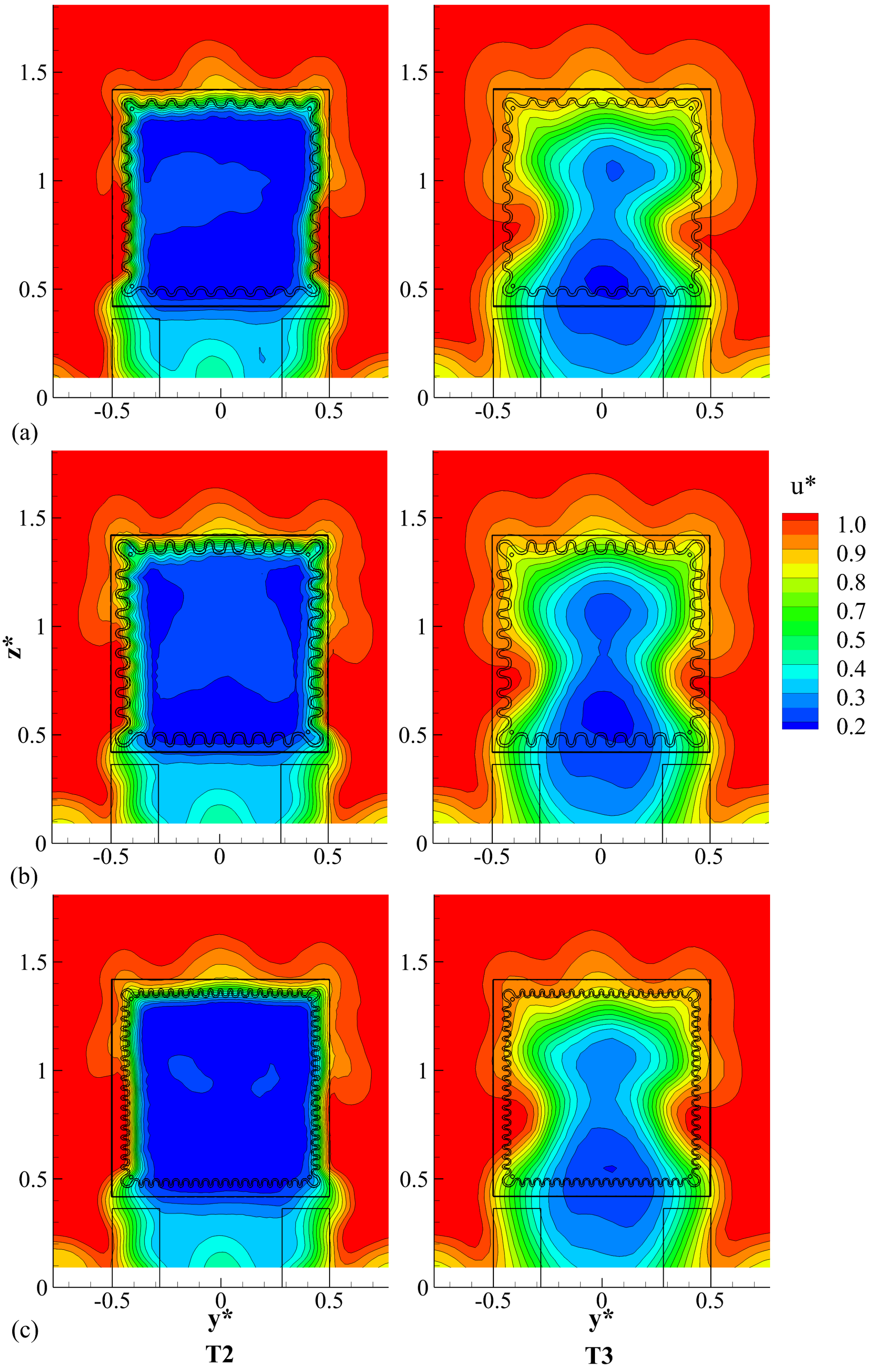

Fig. 7.5 Streamwise velocity contours at T2 and T3 for: (a) LB1, (b) LB2, (c) LB3

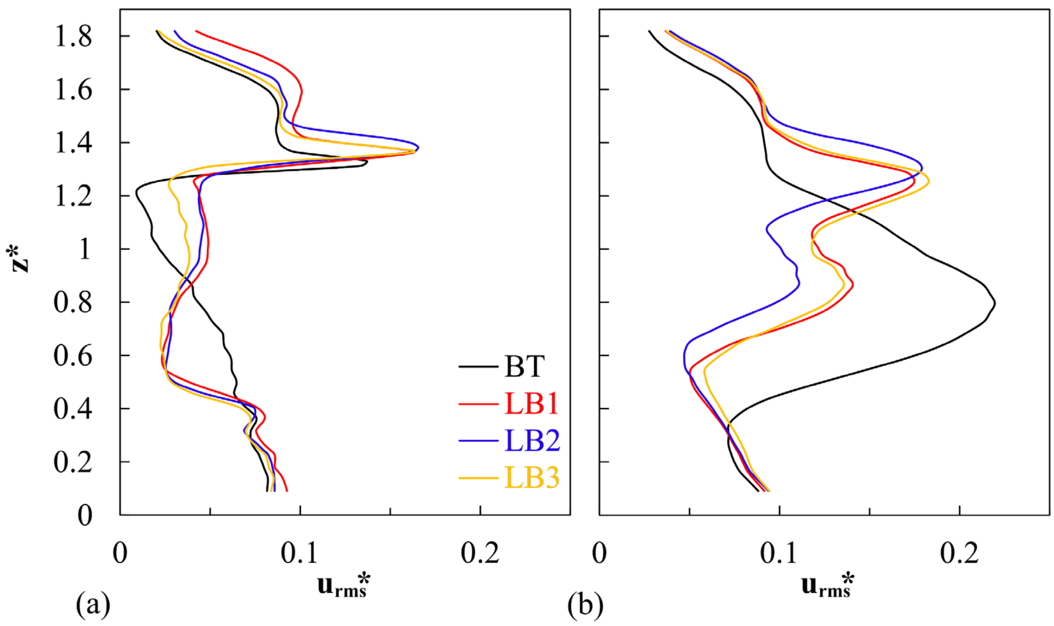

Fig. 7.6 Vertical profiles of u_{rms}* along y*≈0 at: (a) T2, and (b) T3

between 1.3<z*<1.5 marking the increased turbulence production within the separated top shear layer. One immediate observation is the subtle local increase in fluctuations (Δu_{rms}*≈0.026) for all LB1-3 in comparison with BT; the latter also appearing subtly shifted to a lower position (Δz*≈0.035). Between 0.9<z*<1.3, u_{rms}* magnitudes decrease rapidly for all configurations, with the lowest values evident for BT. In the lower base half (0.4<z*<0.9), this trend is reversed, with LB1-3 exhibiting up to Δu_{rms}*≈0.039 lower at z*≈0.58 relative to BT. Comparisons between **Fig. 7.6(a)** and **(b)** reveal that further downstream (T3), while u_{rms}* maxima for LB1-3 continue to occupy higher positions (z*>1.2), for the BT a significant shift can be observed, with the maximum now located closer to base mid-height (z*≈0.8). This trend supports the hypothesis of quicker closure in the upper wake half for the BT, as inferred earlier (**Fig. 7.3(b)**), and confirms the uplifted wake as one of the effects of the lobed mixer configurations. Additionally, in contrast with **Fig. 7.6(a)**, **Fig. 7.6(b)** shows the maximum u_{rms}* for the BT higher (Δu_{rms}*≈0.045) relative to LB1-3. The implications of this change in turbulence production between T2 and T3 are further discussed in **Section 7.4.2**.

Further evidence for the mechanism responsible for the uplifted wakes of LB1-3 is presented in **Fig. 7.7** (note the increased scale), which details both Ω_Y and Ω_Z for LB1 at T2 (LB2 and LB3 omitted for brevity since general topologies remain similar). For this

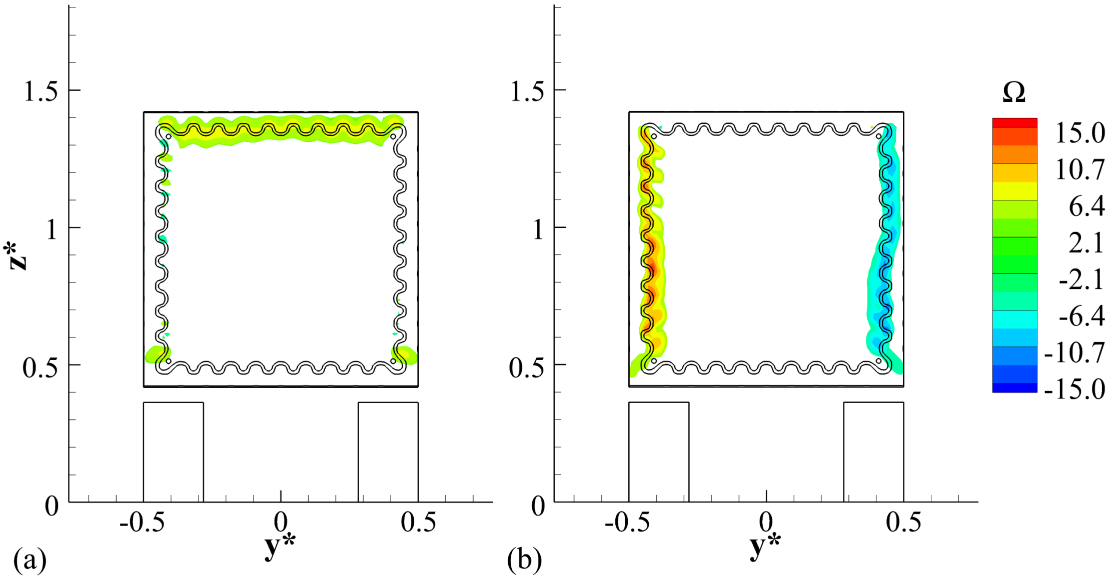

Fig. 7.7 Wake vorticity for LB1 at T2: (a) Ω_Y, (b) Ω_Z (ranges $-4<\Omega_Y<4$ and $-5<\Omega_Z<5$ omitted for clarity)

configuration, while comparable vorticity magnitudes exist along the top edge ($\Omega_{Ymax} \approx|9.3|$), significantly greater (almost 50% compared to **Fig. 7.4(b)**) Ω_Z develops at the sides ($\Omega_{Zmax} \approx|15|$). These magnitudes extend to $\Omega_{Ymax} \approx|11.5|$ and $\Omega_{Zmax}\approx|12|$ for LB2, and $\Omega_{Ymax} \approx|10.6|$ and $\Omega_{Zmax} \approx|11|$ for LB3, highlighting a correlation (when considered in conjunction with **Table 7.1**) between crosswise contractions (precipitated by Ω_Z production) and highest drag benefit. As changes in Ω_{Ymax} remain marginal between the cases, less impact on the drag reduction is inferred.

7.4.1 Streamwise vorticity

Streamwise vorticity contours (Ω_X) for LB1 and LB3 (LB2 omitted for brevity due to close similarities to LB1) are provided in **Fig. 7.8** to better understand their behaviour. Results for the BT are also included for comparison. Generally, all results exhibit relatively good vertical symmetry. One possible exception is above $z^*\approx1.1$ in **Fig. 7.8(b, c)**, where the vorticity magnitudes are significantly weaker, making detection more challenging. In the same area at T3, LB1 and LB3 exhibit weak co-rotating sets of vorticity ($y^*\approx-0.1$, $z^*\approx1.2$ and $y^*\approx0.3$, $z^*\approx1.3$ for **Fig. 7.8(b)**, and $y^*\approx-0.1$, $z^*\approx1.2$ and $y^*\approx0.4$, $z^*\approx1.1$ for **Fig. 7.8(c)**). The results in **Fig. 7.8(b)** at T2 indicate the source of these structures originates from the top

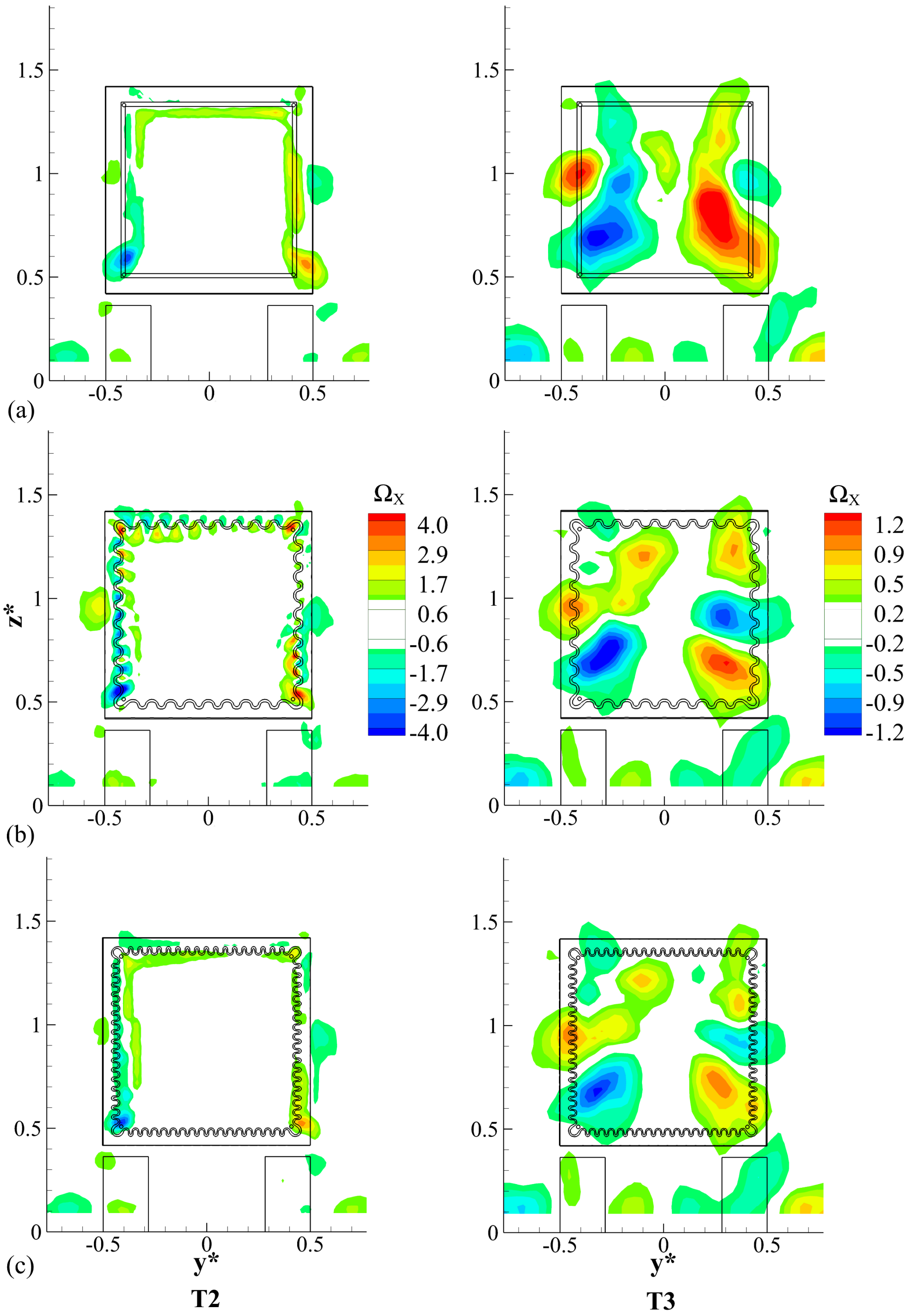

Fig. 7.8 Streamwise vorticity contours (Ω_X) at T2 and T3: (a) BT; (b) LB1; (c) LB3 (ranges $-0.7<\Omega_X<0.7$ for T2 and $-0.2<\Omega_X<0.2$ for T3 omitted for clarity)

corners of the base ($y^*\approx-0.45$, $z^*\approx1.35$ and $y^*\approx0.4$, $z^*\approx1.35$). In the lower base half at T2, all configurations indicate the development of pockets of counter-rotating vorticity near the bottom corners of the inserts ($0.4<|y^*|<0.5$ at $z^*\approx0.55$). The maximum magnitudes generated reside within these locations, with $\Omega_{X\max}\approx|3.8|$ for the BT (**Fig. 7.8(a)**), $\Omega_{X\max}\approx|5.8|$ for LB1 (**Fig. 7.8(b)** – $\Omega_{X\max}\approx|6.3|$ for LB2), and $\Omega_{X\max}\approx|4.2|$ for LB3 (**Fig. 7.8(c)**). These results suggest the bottom corners make a substantial contribution to the overall streamwise vorticity production. For the BT (**Fig. 7.8(a)**), the vorticity appears most prominent only at these locations, with small filaments of elevated Ω_X observed along the top ($1.3<z^*<1.4$), and side ($0.4<|y^*|<0.5$) trailing edges. Contrary to this, at the same locations, LB1 and LB3 (**Fig. 7.8(b, c)**) exhibit more pronounced (particularly LB1) Ω_X magnitudes. The case of LB1 is particularly interesting, showing evidence of small pairs of counter-rotating cells at each lobe (**Fig. 7.8(b)**). This topology agrees well with the flow-field seen downstream of a typical lobed mixer, as outlined in **Section 2.4.1**, with the small vorticity pockets in particular, mimicking the illustrative streamlines presented in **Fig. 2.20**. These cells appear variable in magnitude, being most intense near the bottom corners. Given some distance between the trailing edges and the measurement plane (T2) exists, they correlate spatially to the lobed profile relatively well, with vorticity direction switching at intervals of profile pitch. For each pair, there exists a dominant cell with higher magnitude acting in a direction to entrain flow towards the wake centre; this is predominantly found along the sides. This action supports the crosswise flow enhancement mechanism proposed (and subsequent confining effect imparted by the "waist") described in relation to **Fig. 7.5** at T3. For the LB3 case (**Fig. 7.8(c)**) at T2, these cells are not clearly visible, which is most likely due to insufficient spatial resolution relative to the small pitch of LB3.

Comparison of results from T2 and T3 (**Fig. 7.8**) indicates that with downstream propagation, the small counter-rotating cells observed at T2 coalesce into weaker, but larger counter-rotating pairs, centred near base mid-height at each side. Winant and Browand **(1974)** observed a similar phenomenon for controlling the mixing layer growth, with expanding vortices of the same sign tending to undergo a pairing process. Additionally, Zaman and Hussain **(1980)** also showed spatial expansions, coupled with a drop in maximum vorticity resulting from the same process. The results for the BT at T3 (**Fig. 7.8(a)**) show two main counter-rotating structures centred close to $|y^*|\approx0.3$ at $z^*\approx0.7$. Located nearby are induced counter-rotating counterparts ($|y^*|\approx0.4$ at $z^*\approx0.95$). Considering maximum magnitudes, the former is clearly dominant ($\Omega_{X\max}\approx|1.5|$) with the particular

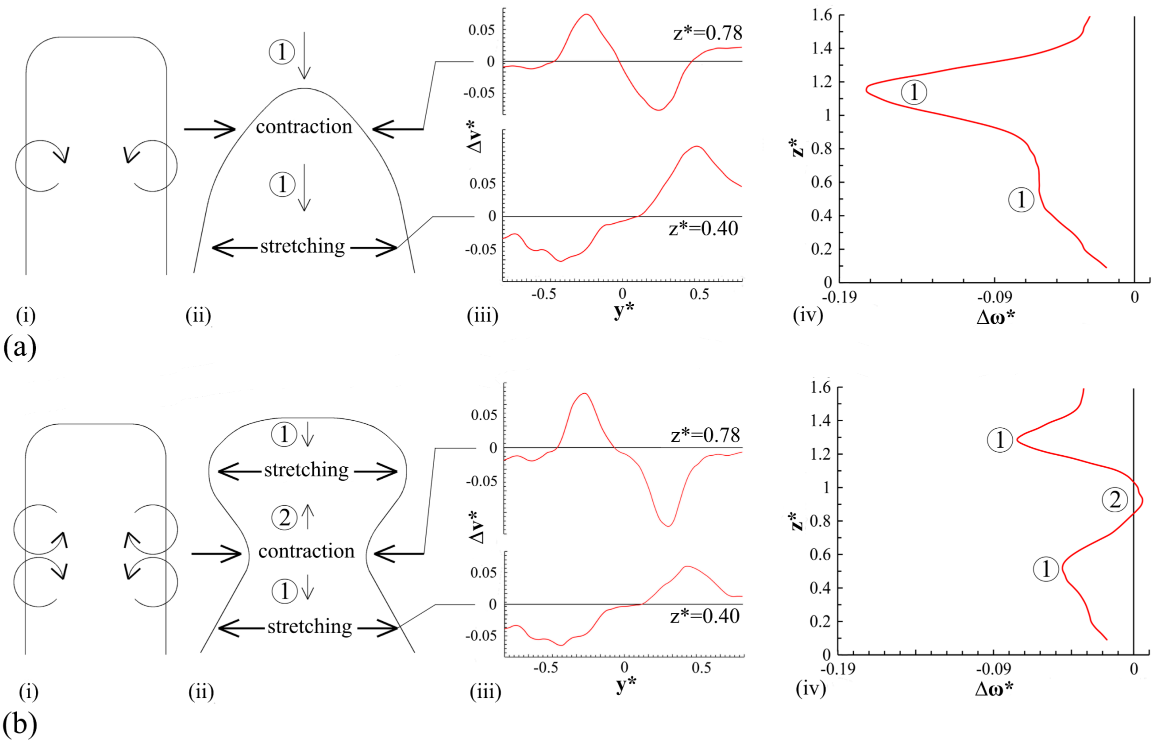

Fig. 7.9 Influence of Ω_X at T3 for: (a) BT, and (b) LB1; (i) schematic of unaltered wake and vortex arrangement, (ii) inferred influence on wake, (iii) relative crosswise velocity (Δv^*) referenced to Baseline for the BT and LB1 at $z^*=0.40$ and 0.78, (iv) relative heightwise velocity ($\Delta\omega^*$) referenced to Baseline for BT and LB1 at $y^*=0$

sense of rotation suggesting their main action is firstly to entrain flow transversely to the wake centre and then down towards the ground. This is represented in **Fig. 7.9(a)** showing a prevalent vortex-induced contraction at the top of the wake, and subsequent expansion, or stretching, in the lower parts. For LB1 and LB3 (including LB2), a slightly different mechanism is observed. With the vorticity produced at the lobed trailing edges, the wake at T3 is dominated by two sets of counter-rotating structures (a pair for each side) of near-equal magnitude ($\Omega_{X\max} \approx |1.2|$) and symmetrically positioned. As highlighted in **Fig. 7.9(b)(ii)**, the same central transverse contraction is induced by these structures as seen for the BT. However, each upper and lower cell also induces stretching at wake top and bottom, respectively. Direct evidence supporting this behaviour is presented in **Fig. 7.9(a-b)(iii)**. Differences in crosswise velocity magnitude (relative to the baseline) produced by the inclusion of BT and LB1 show both contraction, or relative inflow, at $z^*\approx 0.78$, and stretching, or relative outflow, closer to the ground at $z^*\approx 0.4$. Similar relative differences in heightwise velocity magnitude presented in **Fig. 7.9(a-b)(iv)** provide further evidence. For the BT case, the principal action of the main vortex pair is indicated as downward entrainment (labelled as 1) in agreement with **Fig. 7.9(a)(ii)**. In contrast, for LB1 both positive and negative relative heightwise velocities exist. With LB1, downward entrainment pervades nearer the ground ($z^*\approx0.4$) with a relative magnitude ($-\Delta\omega^*$) similar to adding the BT. At higher positions, however, specifically that co-incident with the "waist" ($z^*\approx0.78$), a small relative upwash is indicated (labelled as 2). This action is a consequence of having two sets of counter-rotating vortices (of near-equal magnitude) providing uplift to the wake (see **Fig. 7.9(b)(ii)**). Above this level ($z^*>0.78$), entrainment towards the ground is re-established, but at notably lower levels compared to the BT (**Fig. 7.9(a-b)(iv)**). This generally agrees with the results of Pavia, Passmore and Gaylard **(2016)**, who show that for the best drag reduction, the induced downwash and upwash in the wake should be balanced. In such cases, the wake is vertically balanced and centred behind the base, with the core of the toroidal wake vortex shifted away from the base. Overall, these results demonstrate that the addition of lobed mixer profiling to a high-angle boat-tail has the ability to fundamentally alter the structure of the wake resulting in additional drag benefits.

7.4.2 Mixing

Lobed mixers are primarily used for flow mixing enhancement. To assess the effects on mixing, the mean turbulent kinetic energy (K) is presented in **Fig. 7.10** and **Fig. 7.11** for LB1-3 and the BT. At T2, all four configurations show similar topologies, with increased K evident directly behind top and side trailing edges, the rear wheels, and within the transition region subtending the two. For the BT (**Fig. 7.10(a)**), most intense K can be seen located just above the bottom corners ($|y^*|\approx0.4$ at $z^*\approx0.6$), with the corresponding effect for LB1-3 indicated slightly lower ($z^*\approx0.5$). Strong turbulence production and equivalent flow mixing exists in these areas. Equally important are the differences in width affected by elevated K along the top ($1.3<z^*<1.4$) and side edges ($0.3<|y^*|<0.5$) of the inserts. For the BT, and to some extent LB3, lower K magnitudes acting over narrower regions are found. In contrast, with LB1 and LB2, higher, more distributed magnitudes are evident in the same areas. This difference in magnitudes within the side shear layers is most evident from **Fig. 7.10(e)**. Considered holistically, **Table 7.2**, which presents plane-averaged K (denoted as $\overline{K}$), confirms the implication of these results, with greater $\overline{K}$ for LB1 and LB2 (T2) providing direct evidence of enhanced flow mixing due to the lobed profiling. This has been described by Hu et al. **(2001, 2002)**, Cooper et al. **(2005)** and Mao et al. **(2006)** as a "stirring" effect

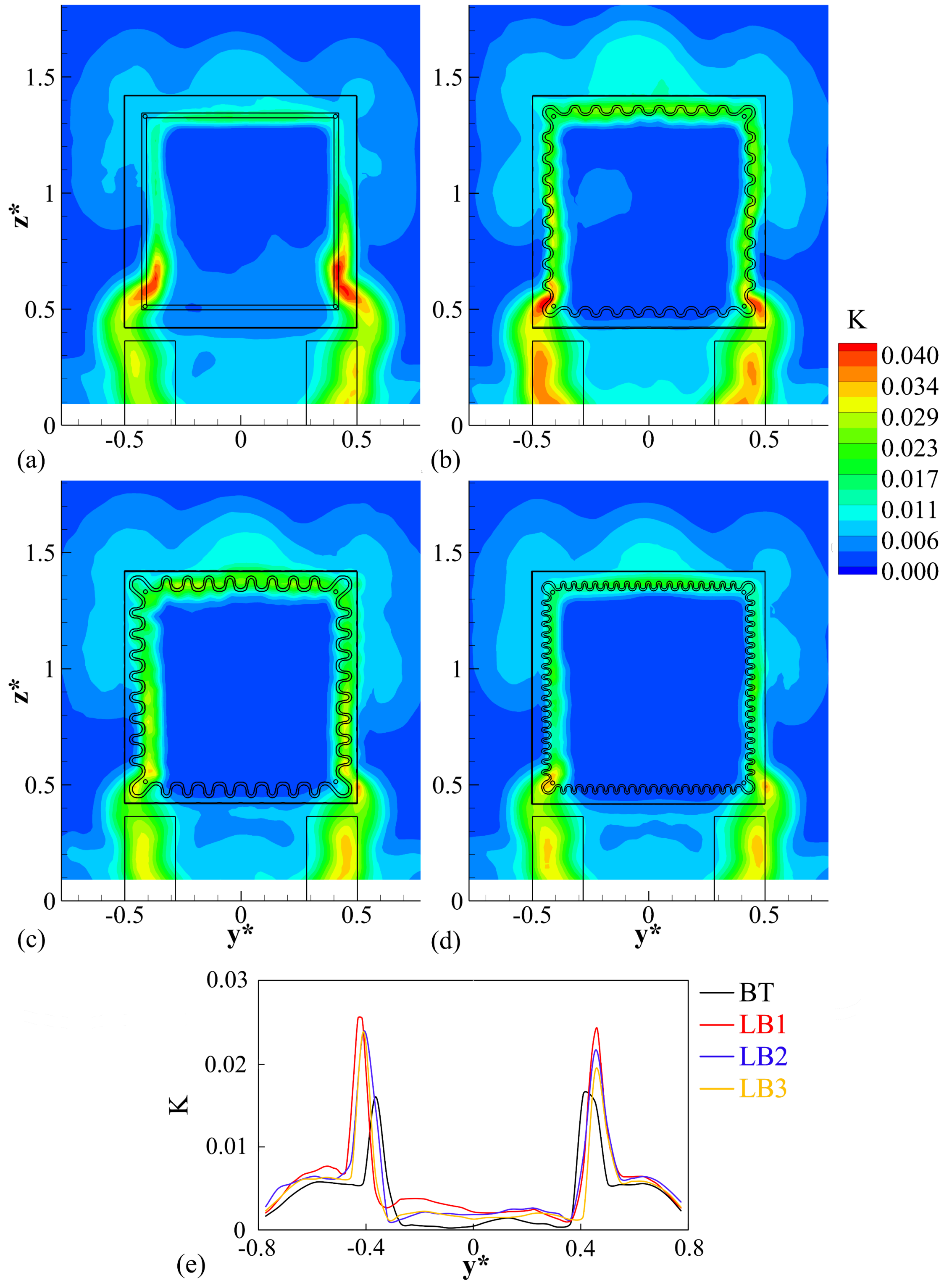

Fig. 7.10 Turbulent Kinetic Energy (K) at T2: (a) BT, (b) LB1, (c) LB2, (d) LB3, (e) spanwise plots at z*≈1

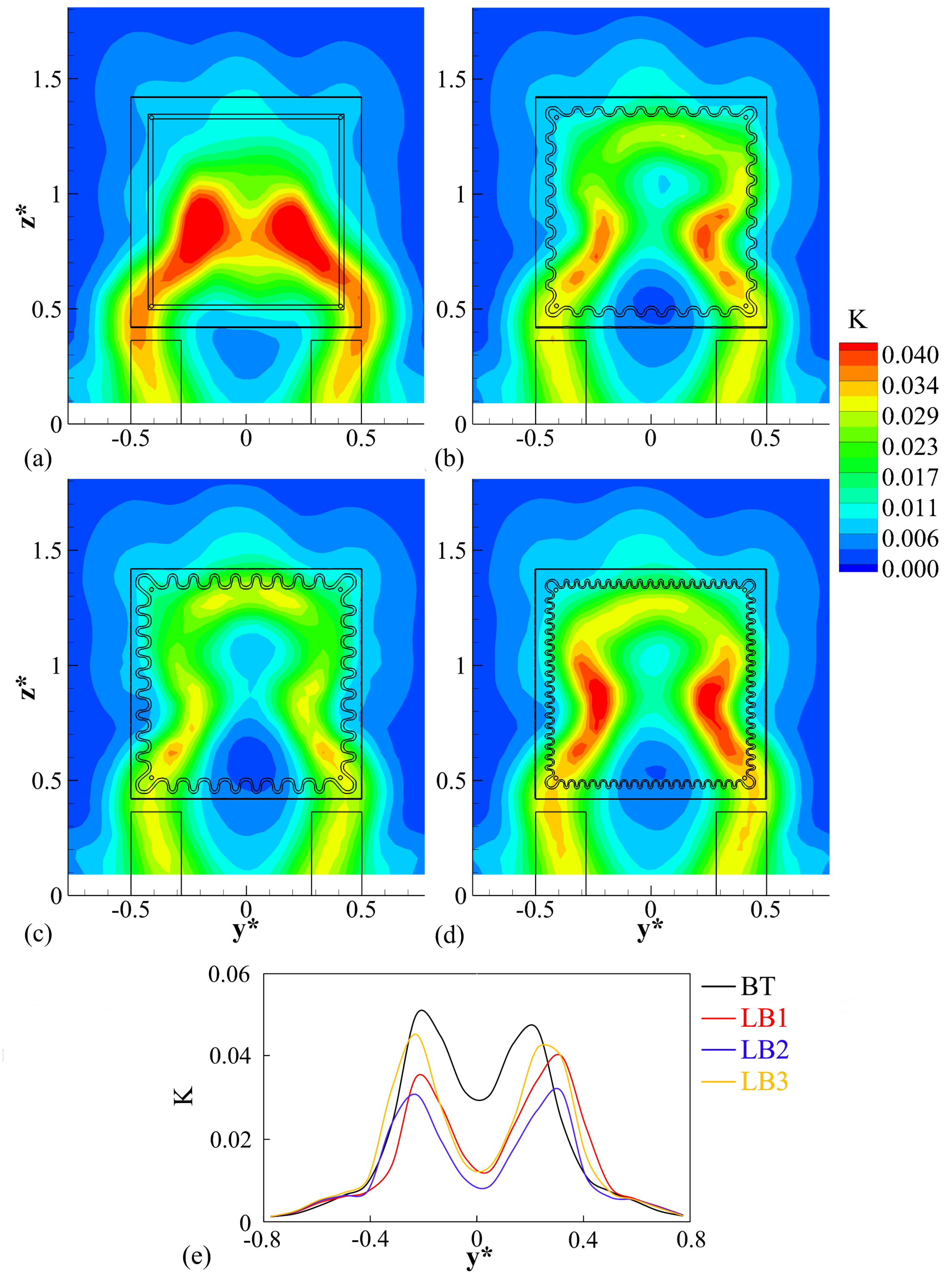

Fig. 7.11 Turbulent Kinetic Energy (K) at T3: (a) BT, (b) LB1, (c) LB2, (d) LB3, (e) spanwise plots at z*≈0.9

produced by large-scale vorticity shed from the lobes. These studies also highlight that most turbulent mixing occurs within short distances from the trailing edge (X/h<8, where h is the crest-trough height of lobed mixer profile; see **Section 2.4.1**). In these regions, vortical structures break down rapidly, significantly increasing the local levels of turbulence. Beyond X/h>8, K growth slows as the shear layers become weaker **(Hu et al., 2001)**. For unmodified surfaces (such as BT), the reverse is true, with K increasing almost linearly up to X/h≈11 (as described in **Section 2.4.2**). Results presented here (**Table 7.2**) support these findings.

Further evidence for this behaviour is found at T3. In **Fig. 7.11**, all four inserts exhibit elevated K acting over wider areas compared to **Fig. 7.10**. The BT (**Fig. 7.11(a)**) can be seen to indicate substantially higher, more concentrated K, developing near base mid-height. In contrast, LB1 and LB2 at this streamwise position (equivalent to X/h≈23.7 for LB1/LB3 and X/h≈14.2 for LB2) exhibit the lowest K, demonstrating the same enhanced mixing mechanisms exist for this application as others already identified. Also of interest in the cases of LB1-3, are the areas of maximum K located close to the "waist" (z*≈0.78) (**Fig. 7.11(b-d)**), as well as those of elevated K near the top edge (y*≈0, z*≈1.3). McCormick and Bennett **(1994)**, and Yu and Yip **(1997)** observed similar results near the "pinch-off" position of transverse structures (see **Section 2.4.1**), with Mao et al. **(2006)** identifying highest K near the top, where stretching is maximised.

	BT	**LB1**	**LB2**	**LB3**
T2 ($\times 10^3$)	6.4	7.3	6.7	5.8
T3 ($\times 10^3$)	12.4	11.1	10.5	19

Table 7.2 Plane-averaged turbulent kinetic energy ($\overline{K}$) for the BT and LB1-3

7.5 Summary

In this preliminary investigation, all lobed-mixing geometries tested were found to provide drag benefits compared to both the baseline (no device fitted) and legacy boat-tail device; the best drag reduction achieved was 10.2%. Assessment of the lobed profile pitch and height found that reducing pitch and increasing height within the tested range degrades performance (although within experimental uncertainty). From detailed wake measurements, the principal mechanism responsible for the improved drag reductions was found to be the production of additional vorticity at the lobes, which enhanced crosswise flow entrainment, and limited wake movement towards the ground. This action resulted in a spatially higher wake, with a characteristic “waist” producing an “hourglass” wake topology. Assessments of turbulent kinetic energy also showed the lobed profiling to enhance mixing in the wake, with similar trends identified in other applications also observed for this case.

Going forward, a more detailed investigation is necessary to fully understand the processes responsible for the specific streamwise vorticity evolution and subsequent wake modifications. Such an evaluation should provide more insight into the particular characteristics of these devices, contributing to enhanced drag benefits. Additionally, the results for LB3 presented in this chapter, lead to the important observation that subsequent tests should involve grids of finer spatial resolution for more accurate flow-field representation. These aspects are considered in the following chapter.

Chapter 8

Detailed assessment of trailing edge-integrated lobed mixers

Following the preliminary investigation, lobed-mixing geometries were integrated directly into the model trailing edges and the effects interrogated in detail. The geometric parameters of the examined configurations (LBT) are discussed in **Section 4.4.2**. For comparison, the baseline case as well as trailing edge tapers (BTT – **Section 4.4.2**) are also assessed. As outlined in **Section 4.2.2**, the model used for this study is Baseline 2. Front mounting (**Section 4.3.3**) and moving ground are used for all experiments. Results of load measurements and HWA are presented and considered from both time-averaged and time-dependent perspectives. Baseline and BTT cases are discussed first, with the LBT effects examined thereafter.

8.1 Baseline characteristics

Firstly, the characteristics of Baseline 2 are discussed. Measured drag coefficient (corrected for blockage) is detailed first, with the time-averaged flow-field considered thereafter.

8.1.1 Drag coefficient

The total model drag coefficient measured and corrected for blockage for Baseline 2 is C_{DM}≈0.579 (±0.017), in good agreement with similar model configurations in other studies, in particular Salati et al. **(2015)** (C_{DM} ≈0.586) and Wood **(2006)** (C_{DM} ≈0.5). Additionally, this result represents a reduction of up to 10.8% in total model drag relative to Baseline 1 (as detailed in **Chapter 6**). With the modifications limited to tractor reshaping, this decrease in drag is inferred to be a consequence of the rounded front of Baseline 2, likely promoting better flow attachment around the front corners.

8.1.2 Time-averaged wake

Figure 8.1(a) presents the contours of u* in planes SV1 **(i)** and SH1 **(ii)** for the baseline case. The wake is represented by the lower u* magnitudes directly behind the base, with **Fig. 8.1(a)(i)** showing the recirculation region contained within x*<1.5 and surrounded by undisturbed freestream flow (z*>1.5 in **Fig. 8.1(a)(i)** and |y*|>0.5 in **Fig. 8.1(a)(ii)**). From the vertical perspective (**Fig. 8.1(a)(i)**), the wake height is seen coincident with the model height. Minimum u* (**Fig. 8.1(a)(i)**) is positioned close to the model (0.2<x*<0.4) within the bottom base half (0.7<z*<0.9), commensurate with the position of the lower wake vortex **(Perry, Pavia and Passmore, 2016; Castelain et al., 2018; Pavia, Passmore and Sardu, 2018)**. Horizontally, **Fig. 8.1(a)(ii)** shows excellent symmetry around y*≈0 and wake width

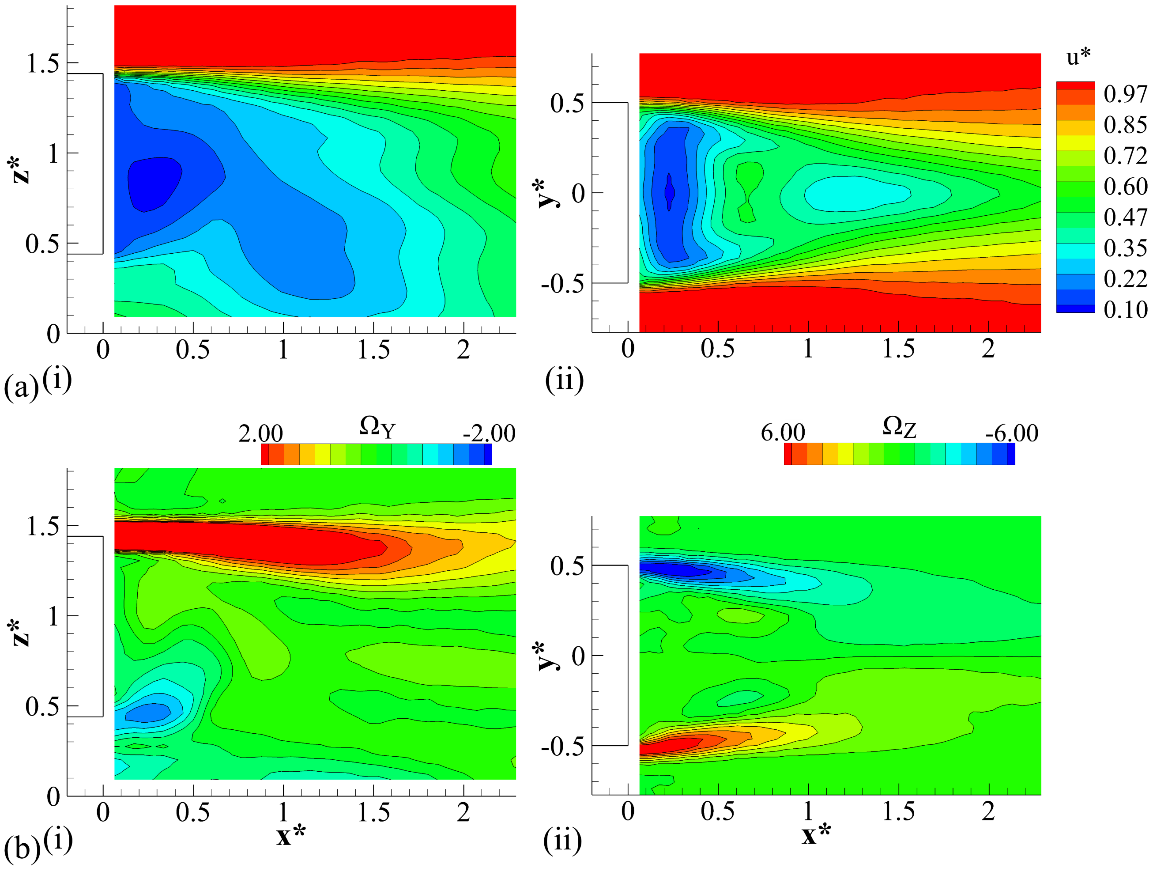

Fig. 8.1 Baseline wake: (a) streamwise velocity u* and (b) in-plane vorticity (Ω_Y and Ω_Z); (i) SV1 (Ω_Y), (ii) SH1 (Ω_Z)

being initially coincident with model width, with subtle inboard tapering evident further downstream.

Further insight into the nature of the separated wake is provided in **Fig. 8.1(b)** presenting the distribution of the in-plane vorticity (Ω_Y – crosswise, Ω_Z – heightwise) for SV1 **(i)** and SH1 **(ii)**. As would be expected, highest Ω_Y and Ω_Z coincide with the separated top and side shear layers, respectively, reflective of the wake tending to achieve closure and in line with the gradual downstream tapering of the region observed in **Fig. 8.1(a)**. Elevated Ω_Y is also evident in the portion of the flow exiting the underbody (**Fig. 8.1(b)(i)**), representative of the local upwash generated by the flow being entrained into the lower wake vortex. Small counter-rotating structures are also evident inboard of the side shear layers ($0.5<x^*<0.7$, $0.2<|y^*|<0.3$ – **Fig. 8.1(b)(ii)**).

Figure 8.2 presents u* and streamwise vorticity Ω_X contours in plane T3. At this position, the wake, represented by lower u* magnitudes, is seen to coincide with the model profile and extend to the ground level, with the minimum u* located within $|y^*|<0.2$, $0.2<z^*<0.4$. The wake width appears largely consistent with height, with weak crosswise contractions evident around $z^*\approx0.2$ and $z^*\approx0.8$. These contractions appear to result from the localised enhancement in the crosswise flow generated by the vorticity positioned directly above, as presented in **Fig. 8.2(b)**. This topology (**Fig. 8.2(b)**) presents two sets of counter-rotating structures positioned near-symmetrically around $y^*\approx0$. The vortices originate from the four base corners, generated by the differences in flow direction upon separation from the trailing edges. Rouméas, Gilliéron and Kourta **(2009)** have also shown similar bottom

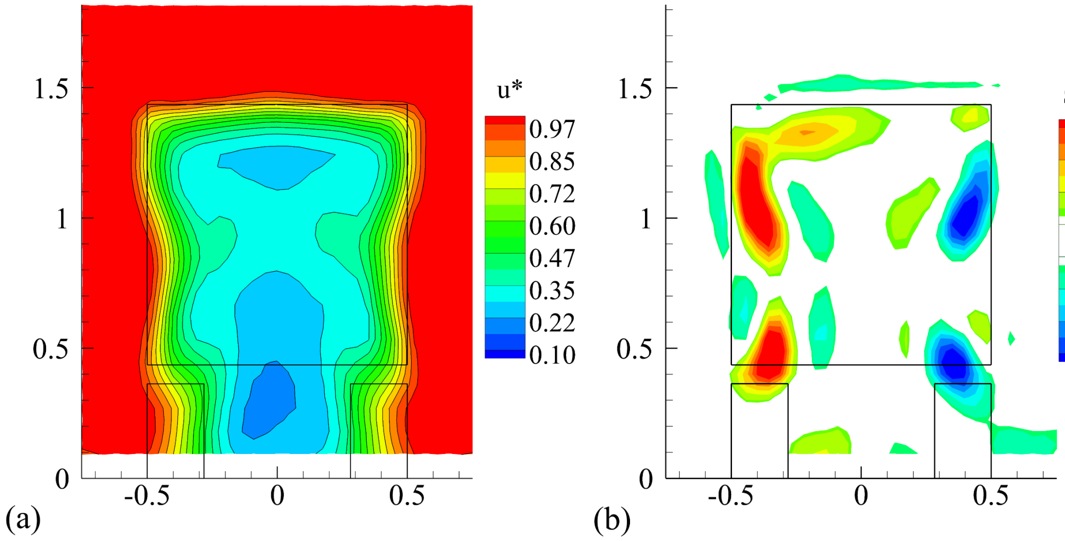

Fig. 8.2 Baseline wake at T3: (a) streamwise velocity u*, (b) streamwise vorticity Ω_X ($-0.25< \Omega_X<0.25$ omitted for clarity)

base corner vortices. Where the flow along the trailer sides would typically be characterised by a subtle downwash **(Lajos, Preszler and Finta, 1986)**, these vortices are generated such that on each side the vorticity is co-rotating. Overall, the wake topology for Baseline 2 appears largely similar to the trends previously identified for Baseline 1 (**Chapters 5 – 7**).

8.2 Effects of tapering

The effects of trailing edge tapering are now discussed. Changes in the drag coefficient relative to baseline are considered first, with the influence on the wake flow-field examined thereafter.

8.2.1 Impact on drag coefficient

Figure 8.3 presents the reduction in the drag coefficient ($-\Delta C_{DM}$) with respect to the drag measured in the baseline configuration ($C_{DM} \approx 0.579$) for the range of taper angles $5° < \alpha < 30°$. One immediate observation is that throughout this range, the best drag benefits are achieved with all (side and top) edges tapered relative to the sides or top alone. This is particularly evident within $5° < \alpha < 15°$ where tapering is most effective. Within this range, the drag reduction obtained with tapering at the sides is significantly lower, with this trend decreasing further when only the top edge is tapered. This is in general agreement with Perry, Passmore and Finney **(2015)**, as well as Hirz and Stadler **(2013)**.

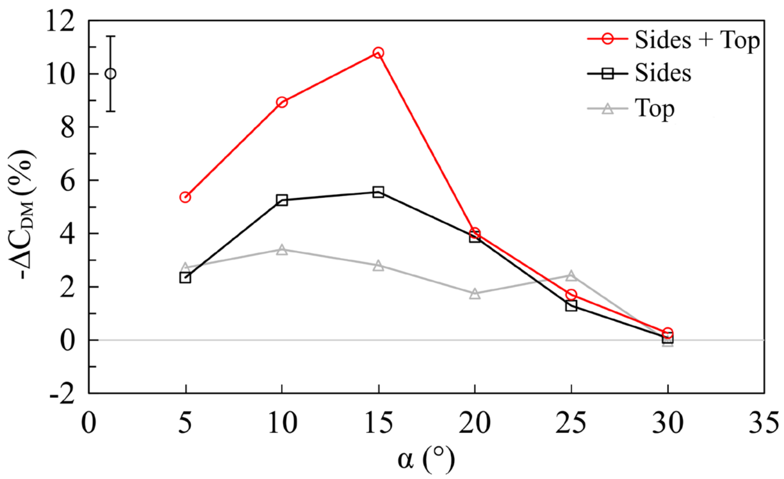

Fig. 8.3 Drag reduction with tapered edges (BTT) for angles $5° < \alpha < 30°$

Considering solely the results for all three edges tapered, for the lower angles, the drag reduction increases gradually with the angle up to α=15°, where the maximum benefit is achieved. Past α=15° however, a sharp drop is observed, with further increases approaching the results of the baseline. This is in excellent agreement with the trend found by Yi **(2007)**. Overall, the best drag reduction of 10.8% is achieved with BTT α=15°, in general agreement with Van Raemdonck and Van Tooren **(2010)**, and Salati, Cheli and Schito **(2015)**.

8.2.2 Impact on time-averaged wake flow-field

Figure 8.4 presents u* distribution in the wake of the low-drag taper configuration with α=15° on both sides and top. The results for BTT α=20° are also included to provide insight into the mechanisms responsible for the sharp decline in drag benefit. Firstly, from SV1 (**Fig. 8.4(a)(i)**), BTT α=15° can be seen to produce a wake which is markedly more tapered from the top in comparison with the baseline (**Fig. 8.1(a)(i)**), suggesting significant increases in downward momentum upon separation. This is an expected result, as the flow separates at the trailing edge of the tapered surface, and agrees with the results of Perry, Pavia and Passmore, **(2016)**, and Grandemange et al. **(2013)**. One consequence of this can be seen in the upper wake portions (z*>0.9), where the downstream evolution of u* for BTT α=15° shows a more rapid increase in magnitudes, suggesting these portions to close more quickly relative to the baseline. Below this level (z*<0.9) the opposite is evident, with lower u* magnitudes extending relatively further downstream to x*≈1.4. As a result, the overall wake topology from this perspective appears shifted towards the ground. One possible reason for this observation is a change in the vertical wake balance with BTT α=15°, precipitated by the growth of the top recirculating vortex and downward shift of the saddle point; both a consequence of the increase in downward momentum within the flow leaving the top tapered edge, in agreement with Perry, Pavia and Passmore **(2016)**. This is considered further in the remainder of this section. The lowest u* magnitudes within the wake are now located close to the base and extending its entire height. Considering **Fig. 8.4(b)(i)**, the increase in the taper angle to α=20° is seen to produce a significantly less tapered wake in comparison with α=15°. The upper portions (z*>0.9) no longer show faster closure, with the overall trend approaching that of the baseline (**Fig. 8.1(a)(i)**). These differences in wake height are highlighted further in **Fig. 8.5(a)**, with this figure (**Fig. 8.5(a)**) also emphasising the substantial reduction in the u* deficit at z*>0.9 for BTT α=15° discussed earlier.

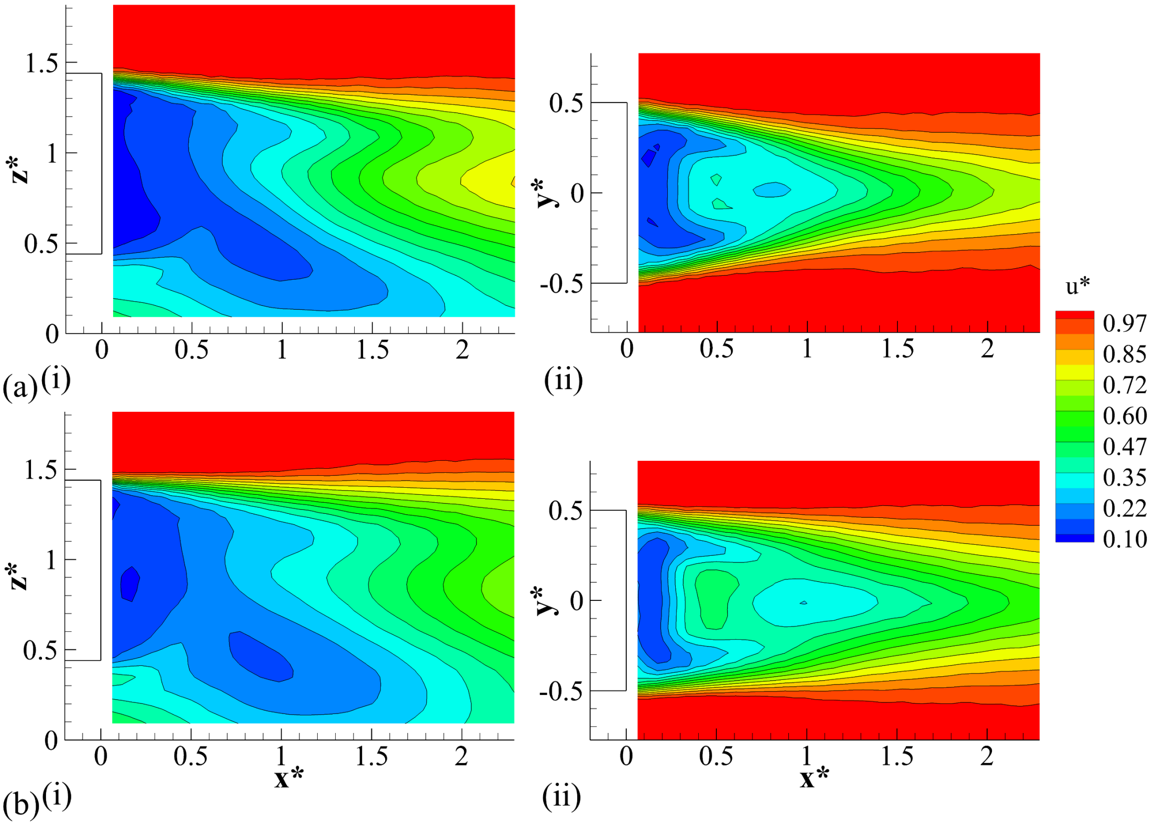

Fig. 8.4 Streamwise velocity contours (u*) for: (a) BTT α=15° (sides and top) and (b) BTT α=20° (sides and top); (i) SV1, (ii) SH1

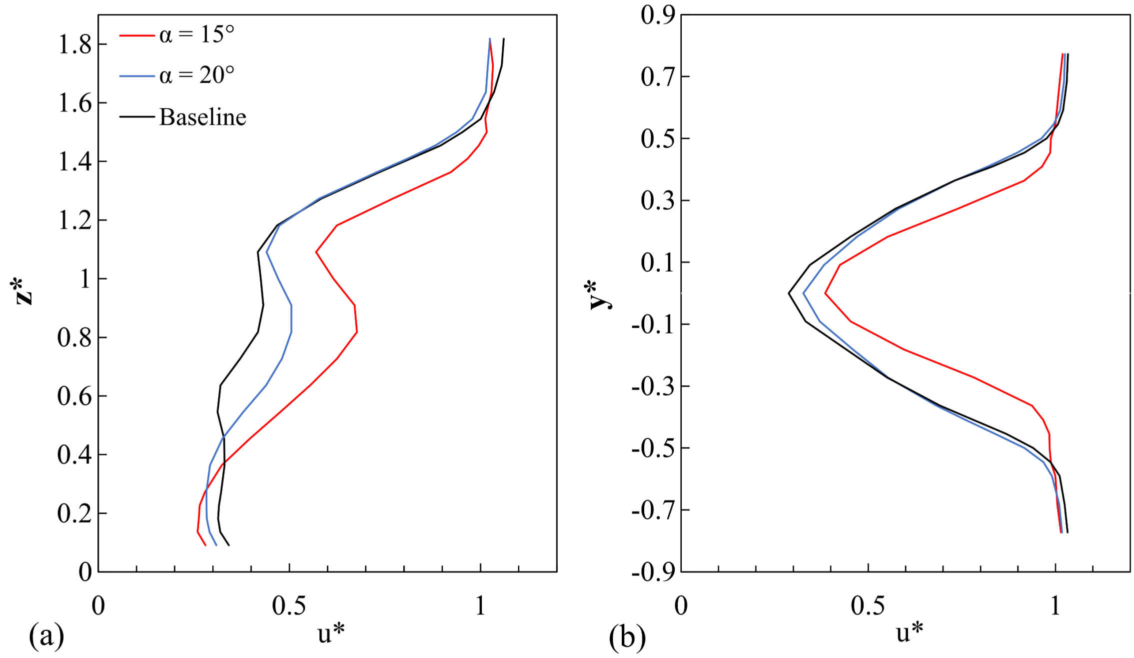

Fig. 8.5 Profiles of u* for Baseline, BTT α=15° and BTT α=20° (sides and top for both): (a) x*≈1.8, y*≈0 (SV1), (b) x*≈1.25, z*≈0.92 (SH1)

Further insight is gained from the horizontal perspective (SH1). **Figure 8.4(a)(ii)** (BTT α=15°) shows a substantial reduction in the wake width relative to the baseline (**Fig. 8.1(a)(ii)**), which is expected to be a result of the increase in inboard momentum generated by the tapered sides. In this position ($z^*\approx0.92$ – SH1), the lower u^* contours also suggest reduced wake length for BTT α=15°, consistent with a quicker local closure. **Figure 8.4(b)(ii)** (BTT α=20°) again exhibits similarities to the baseline topology, with a local increase in the wake width relative to BTT α=15°. This is further highlighted in **Fig. 8.5(b)**, showing a reduction in wake width for BTT α=15° from $|y^*|<0.5$ (baseline and BTT α=20°) to $|y^*|<0.4$, and $\Delta u^*\approx0.1$ increase at $y^*\approx0$, supporting the alleged enhancement in crosswise flow. In the same plane (SH1), the lowest velocity magnitudes ($u^*<0.2$) for BTT α=15° are seen to extend downstream to $x^*\approx0.55$ within $0.1<|y^*|<0.35$ (**Fig. 8.4(a)(ii)**). In contrast, in **Fig. 8.4(b)(ii)** (BTT α=20°) these are seen limited in both the spanwise and streamwise directions, to $x^*<0.35$, $0.2<|y^*|<0.35$. This trend is likely reflective of an increase in the size of the side portions of the toroidal wake vortex, or side wake vortices, for BTT α=15°. Perry, Passmore and Finney **(2015)** reported this as one of the results of effective trailing edge tapering, producing improved base pressure recovery. Results in **Fig. 8.3** support these findings.

Figure 8.6 presents crosswise and heightwise vorticity trends from the same planes, SV1 and SH1. In SV1, Ω_Y magnitudes generated along the top shear layer remain similar for both tapered configurations and the baseline. For BTT α=15° however, this region of high positive Ω_Y appears to arch subtly towards the wake centre, consistent with lower positions of the developing top shear layer and reductions in wake height (**Fig. 8.5(a)**). Additionally, the area of upwash generated from the exiting underbody flow appears to extend further downstream to $x^*\approx0.4$ for BTT α=15° relative to $x^*\approx0.3$ for BTT α=20°. For the latter, this portion of the flow also appears to be angled more significantly towards the wake centre, similar to the baseline case (**Fig. 8.1(b)(i)**), suggesting the average position of the lower wake vortex to be closer to the base. This observation further supports the inferred shift in vertical wake balance for BTT α=15°.

In SH1, Ω_Z results for the BTT α=15° (**Fig. 8.6(a)(ii)**) show stronger heightwise vorticity, consistent with enhanced inboard momentum. The regions of elevated vorticity are also shown located marginally closer to $y^*\approx0$, supporting the reduction in the wake width for this configuration (**Fig. 8.5(b)**). Analogously, for BTT α=20° (**Fig. 8.6(b)(ii)**), Ω_Z

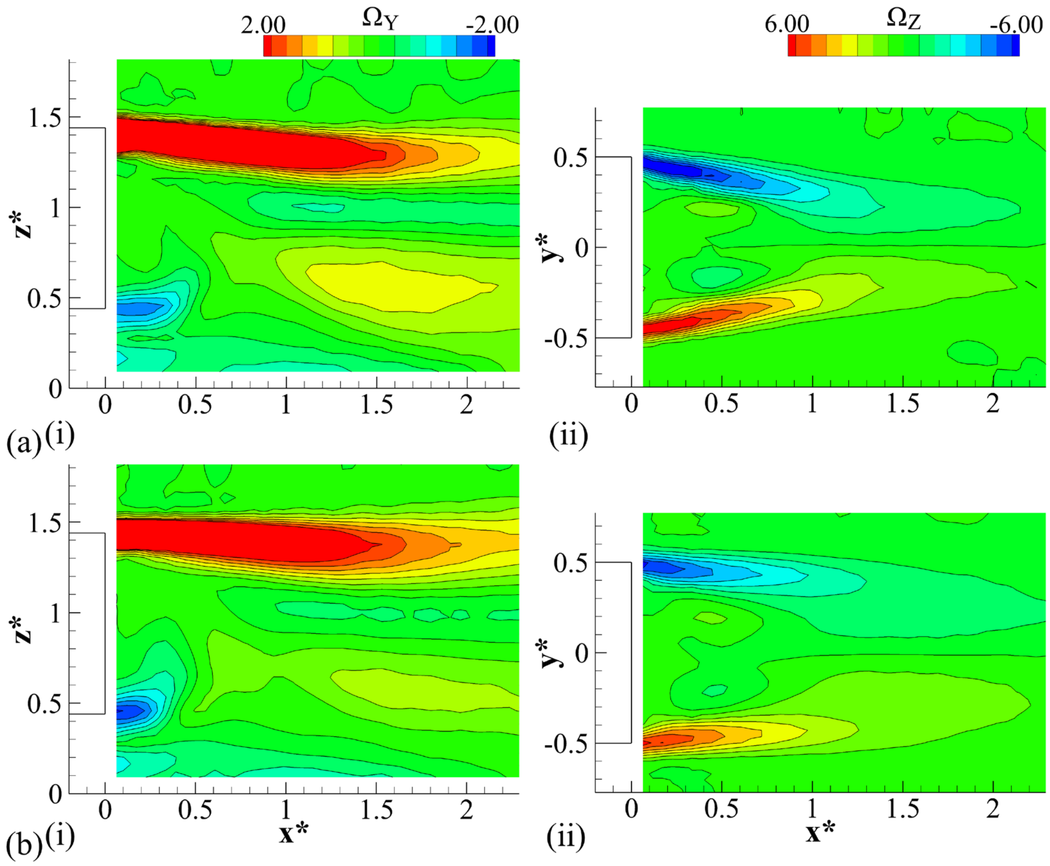

Fig. 8.6 Wake vorticity for: (a) BTT α=15° (sides and top) and (b) BTT α=20° (sides and top); (i) Ω_Y in SV1, (ii) Ω_Z in SH1

topology closely resembles that of the baseline (**Fig. 8.1(b)(ii)**), confirming degradation in performance with increasing α.

Figure 8.7(a-b)(i) presents u* contours for the BTTs α=15° and α=20° from the transverse perspective (T3). From **Fig. 8.7(a)(i)**, it is evident that the taper α=15° reduces the size of the wake downstream of the trailer base, providing support for the presented drag results (**Fig. 8.3**), as Grandemange et al. **(2013)** indicate reductions in wake size as a factor contributing to drag decrease. Additional insights are gained from **Fig. 8.7(a)(ii)** presenting the streamwise vorticity (Ω_X) in the same plane. These results show two pairs of counter-rotating structures centred around the middle of the base. The nature of these vortices is such that the pairs are counter-rotating horizontally, but also vertically along each side (all adjacent vortices are counter-rotating), resembling the topology produced by the lobed boat-tails, as detailed in **Chapter 7**, **Section 7.4.1**. The vortices originate from the four base corners, with Grandemange et al. **(2013)** suggesting the optimum drag reduction is achieved when all adjacent structures are counter-rotating, as is the case here. As described in **Section**

7.4.1, the principal action of these vortices is to contract the wake around the middle ($z^*\approx0.8$) with subsequent stretching occurring in the lower parts ($z^*<0.6$). This is indeed the case for the BTT α=15°, as presented in **Fig. 8.7(a)(i)**, with a maximum increase in the local wake width relative to baseline (**Fig. 8.2(a)**) of $\Delta y^*\approx0.2$ at $z^*\approx0.4$. Additionally, though the upper pair appears subtly elongated spatially (a result most likely of the downstream distance from the base), the maximum vorticity within each of the four structures is found near-identical being approximately $|\Omega_X|\approx1.1 - 1.2$. One consequence of this symmetry is reflected in **Fig. 8.8**, showing near-symmetric upwash and downwash around $z^*\approx0.9$, with maxima of $\omega^*\approx0.068$ and $\omega^*\approx-0.076$ at $z^*\approx0.36$ and $z^*\approx1.45$, respectively. This distribution of vertical velocity is in excellent agreement with the report of Pavia, Passmore and Gaylard **(2016)**, who associate such a balance in the upwash/downwash with the overall vertical wake balance and optimum drag conditions. These results, therefore, provide further support for the alleged shift in the vertical wake balance and subsequent high drag reduction obtained with the BTT α=15°.

For the BTT α=20°, the symmetry in Ω_X is lost as can be seen in **Fig. 8.7(b)(ii)**, with only one dominating pair of counter-rotating vortices evident. From their direction, the principal action of these structures is inferred to result in a subtle contraction at $z^*\approx0.7$, as can be seen in **Fig. 8.7(b)(i)**, as well as a relative enhancement in upwash, with increases in wake height (relative to BTT α=15°) in agreement with **Fig. 8.5(a)**. The characteristics presented in **Fig. 8.7(b)(ii)** are similar to those of the boat-tail (BT) discussed in **Section 7.4.1**, however, the vorticity direction and consequently the effects on the wake structure are opposite. This difference is suggested to stem from the disparity in the origin of the two vortices. While for the BTT α=20°, the vortices are seen to originate from the top corners, in the BT case the dominating structures were shown to originate from the bottom corners (**Section 7.4.1**). This is suggested to be the result of the inherent differences in the configurations, with the boat-tail constructed from four panels inclined inboard at equal angle (here bottom edge is straight). With the bottom base edge sloped inboard, the exiting underbody flow is typically characterised by higher local upwash **(Grandemange et al., 2013; Perry, Passmore and Finney, 2015; Perry, Pavia and Passmore, 2016)**, offering an explanation for the stronger flow circulation around the bottom corners for the BT. Furthermore, Perry, Passmore and Finney **(2015)** show that for side taper angles of α>16°, the lower portions of the sides are more prone to unsteady separation, explaining the sudden reduction, or loss, of the bottom corner vortices. The results presented in **Fig. 8.7(b)(ii)**

($|y^*|\approx0.4$, $z^*\approx0.5$) for the BTT α=20° support these findings. Ultimately, the top vortex pair presented in **Fig. 8.7(b)(ii)** results in a wake which is wider at $z^*>0.9$ and narrower at $z^*<0.6$ (**Fig. 8.7(b)(i)**) relative to the BTT α=15° (**Fig. 8.7(a)(i)**). Additionally, **Fig. 8.8** reflects the growing vertical imbalance consequent to the imbalance in Ω_X, showing an increase in upwash and reduction in downwash relative to the BTT α=15°, with local maxima of $\omega^*\approx0.110$ and $\omega^*\approx-0.043$ at $z^*\approx0.36$ and $z^*\approx1.45$, respectively. These results support the degradation in performance for the BTT α=20° **(Pavia, Passmore and Gaylard, 2016)**.

Finally, results for the BTT α=25° are also presented from this perspective (**Fig. 8.7(c)**). As can be seen in **Fig. 8.7(c)(ii)**, two pairs or counter-rotating vortices are again evident at $z^*\approx0.4$ and $z^*\approx1$. However, in this case, while the pairs are counter-rotating horizontally, along each side they are now co-rotating; a topology typically resulting in increased drag **(Grandemange et al., 2013)**. These characteristics now resemble those of the baseline (**Fig. 8.2(b)**), except close to the top base edge ($z^*\approx1.4$), where an additional pair of smaller counter-rotating vortices can be observed, positioned close to the base corners. These results suggest that a taper angle this high (α=25°) along the top edge produces substantial pressure gradients to generate these vortices, in general agreement with Perry, Passmore and Finney **(2015)**. One clear consequence of these structures is the enhanced downward momentum, producing evident reductions in wake height (**Fig. 8.7(c)(i)**). Below this level ($z^*<1.3$) however, the wake topology for the BTT α=25° largely resembles that of the baseline (**Fig. 8.2(a)**), with further reductions and increases in wake width relative to the BTT α=20° at $z^*<0.6$ and $z^*>0.9$, respectively. This trend of changing wake width with increasing α is further highlighted in **Fig. 8.9**, and supports the progressive shift in the vertical wake balance.

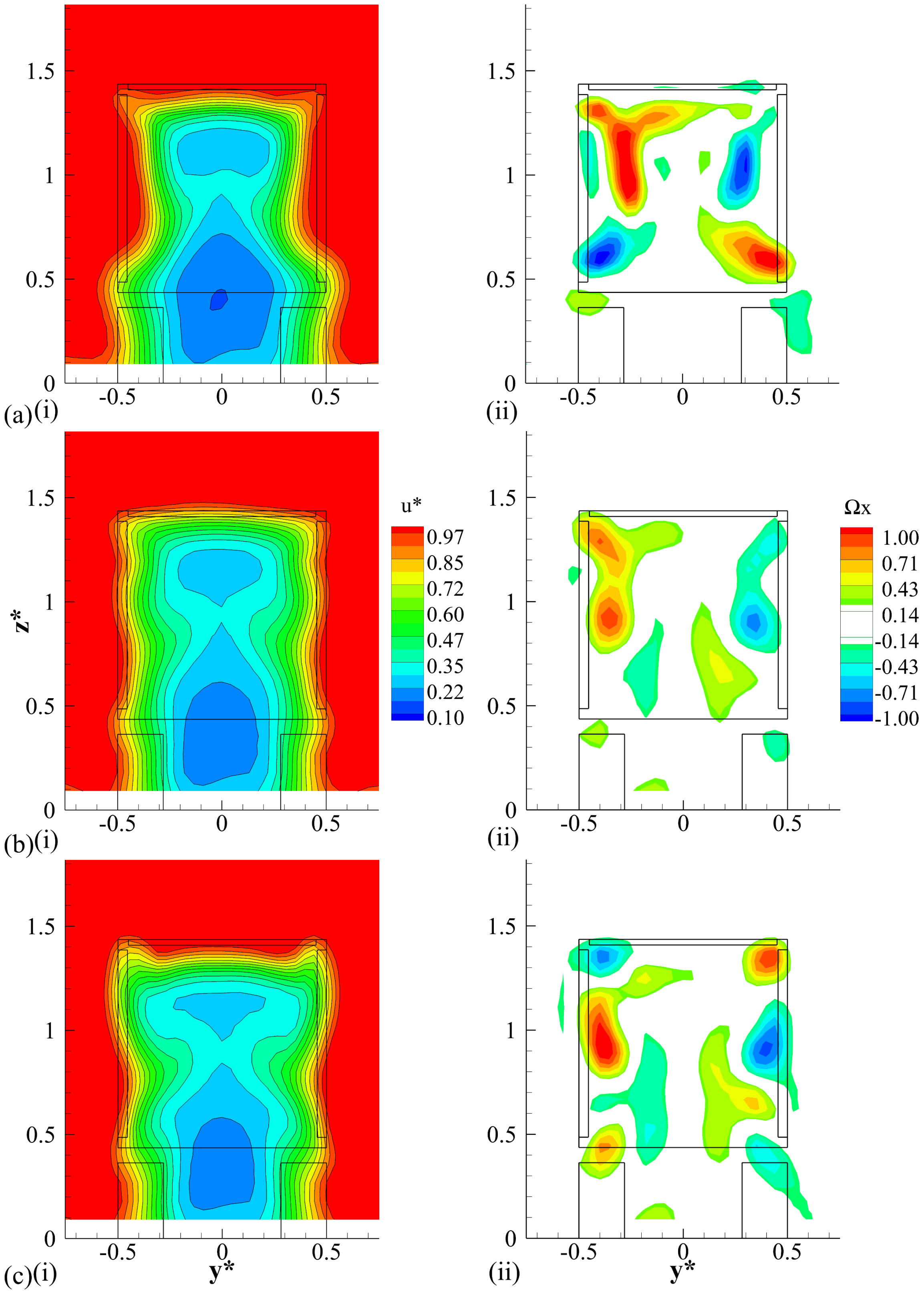

Fig. 8.7 Contours of streamwise velocity (i) and vorticity (ii) in T3 for: (a) BTT α=15° (sides and top), (b) BTT α=20° (sides and top), (c) BTT α=25° (sides and top) ($-0.25< \Omega_X<0.25$ omitted for clarity)

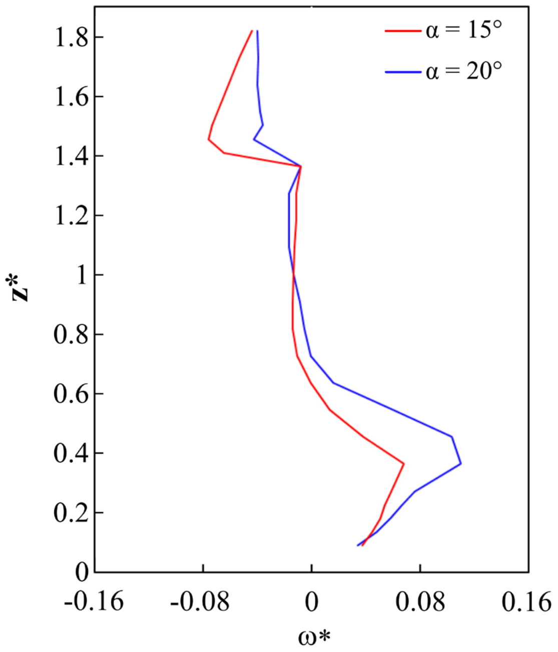

Fig. 8.8 Plots of vertical velocity ω* in SV1 at x*≈0.25 for BTT α=15° and BTT α=20° (sides and top for both)

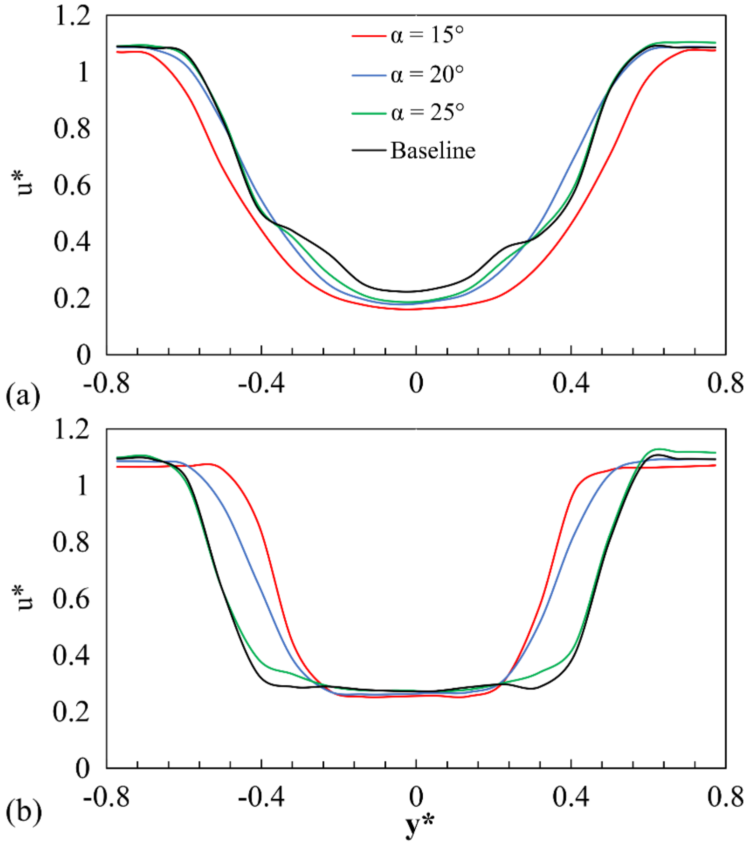

Fig. 8.9 Plots of u* in T3 for Baseline, BTT α=15° (sides and top), BTT α=20° (sides and top) and BTT α=25° (sides and top) at: (a) z*≈0.45, (b) z*≈1.18

8.2.2.1 Isolated influence of top and sides

In this section, the isolated influence of top and side tapers on the wake topology is evaluated. Configuration BTT α=20° is selected for this purpose, with **Fig. 8.10** presenting the results for the two variations in T3. At first inspection, u* topology for the side tapers (**Fig. 8.10(a)(i)**) is found near-identical to that of the full (sides and top) configuration (**Fig. 8.7(b)(i)**). In contrast, the results for the top taper (**Fig. 8.10(b)(i)**) closely resemble those of the baseline (**Fig. 8.2**). This somewhat supports the drag results for BTT α=20° (**Fig. 8.3**), whereby the drag reduction for sides varies only marginally from the full configuration, with the top tapering exhibiting drag values within experimental uncertainty of the baseline drag.

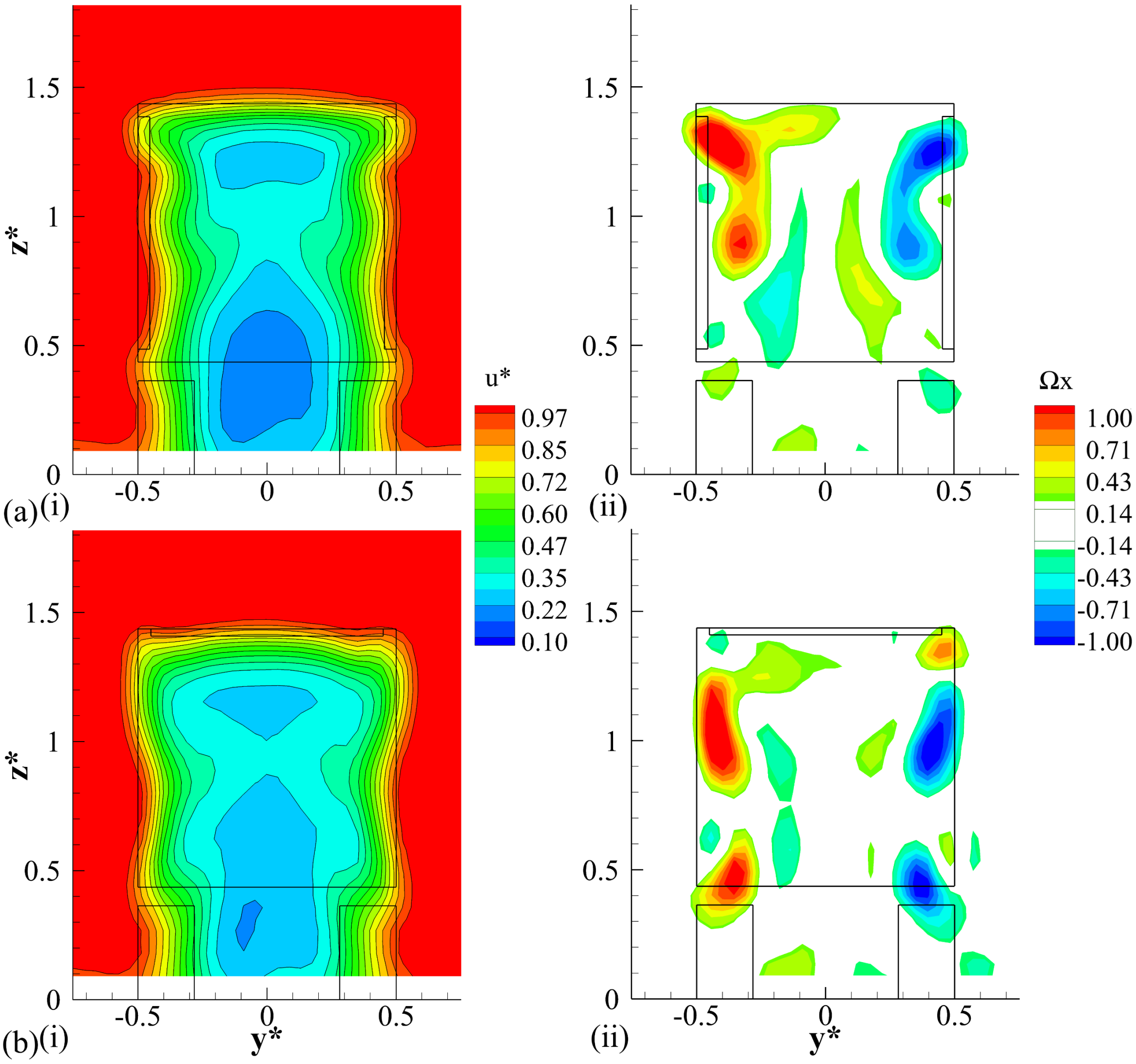

Fig. 8.10 Contours of streamwise velocity (i) and vorticity (ii) in T3 for: (a) BTT α=20° - sides only, (b) BTT α=20° - top only (-0.25< Ω_X<0.25 omitted for clarity)

Upon further examination, some subtle but distinct differences can be found. Above $z^*\approx1.2$, **Fig. 8.10(a)(i)** shows widening of the wake relative to **Fig. 8.7(b)(i)**. This is likely a result of the increase in the strength of the local vortices (**Fig. 8.10(a)(ii)** – $|y^*|=0.4$, $z^*=1.3$) up to $|\Omega_X|\approx1.5$, in comparison with $|\Omega_X|\approx0.9$ found in **Fig. 8.7(b)(ii)**. This suggests that the inclusion of both, side and top tapers, acts to reduce the strength of the longitudinal vortices shed from the corners of the side tapers. The Ω_X topology for the BTT $\alpha=20°$ top taper (**Fig. 8.10(b)(ii)**) is found generally similar to the BTT $\alpha=25°$ case presented in **Fig. 8.7(c)(ii)**, further supporting the hypothesis that for the latter, the flow along the trailer sides separates early at the taper's leading edge. Unlike the BTT $\alpha=25°$ however, for the BTT $\alpha=20°$ top taper, the pair of counter-rotating vortices shed from the top taper corners is barely detectible at $|y^*|\approx0.45$, $z^*\approx1.4$, being substantially lower for this case. As a result, these structures can be seen to make little difference to wake height.

8.3 Effects of lobed-mixing geometries

The influence of the inclusion of lobed mixers at the base edges is now evaluated. Different lobed mixer geometries are investigated, with variation in pitch and penetration angle in the ranges of $0.027W < p < 0.105W$ and $5° < \beta < 30°$, respectively. Firstly, changes in the drag coefficient are discussed. The impact on the wake flow-field for varying pitch (p) and penetration angle (β) is discussed thereafter.

8.3.1 Impact on drag coefficient

Figure 8.11 presents the reduction in drag coefficient ($-\Delta C_{DM}$; relative to baseline) for the different pitches tested. For each pitch, the effect of varying penetration angle is also captured. At first inspection, most configurations can be seen to reduce drag, with only a few cases of drag increase, found mainly at the extremes of the $5° < \beta < 30°$ range. **Figure 8.11** shows most LBT configurations perform best with all sides and top modified, with the benefit reducing with decreasing number of affected edges. This trend is similar to that observed for the BTTs, suggesting some similarities in the drag reduction processes exist between these configurations. Considering only the results of all three base edges modified, for each presented pitch (**Fig. 8.11(a-f)**) there exists a β which produces the best drag benefit; $\beta=20°$ for $p=0.027W$, $\beta=15°$ for $p=0.044W$; $\beta=7.5°$ for $p=0.055W$; $\beta=5°$ for $p=0.067W$, β=12.5° for p=0.086W, β=15° for p=0.105W. Therefore, for higher aspect ratio modifications, characterised by higher β, the trend suggests smaller pitches to be more suitable. Further inspection also reveals that, unlike the BTT, for the LBT configurations (sides and top), the drag variations with changing β are significantly more moderate, mostly devoid of severe increases/decreases such as that seen between the BTT α=15° and α=20°. This is especially the case for p=0.044W, p=0.055W and p=0.067W (**Fig. 8.11(b-d)**). Consequently, most LBT configurations continue to exhibit significant drag reductions at higher angles past β=15°. LBT p=0.044W (**Fig. 8.11(b)**) presents a particularly good trend, with drag reductions of up to 7.0% at β=20°, 5.5% at β=25° and 2.8% at β=30°. Overall, these results suggest that the drag reduction may be proportional to the streamwise vorticity

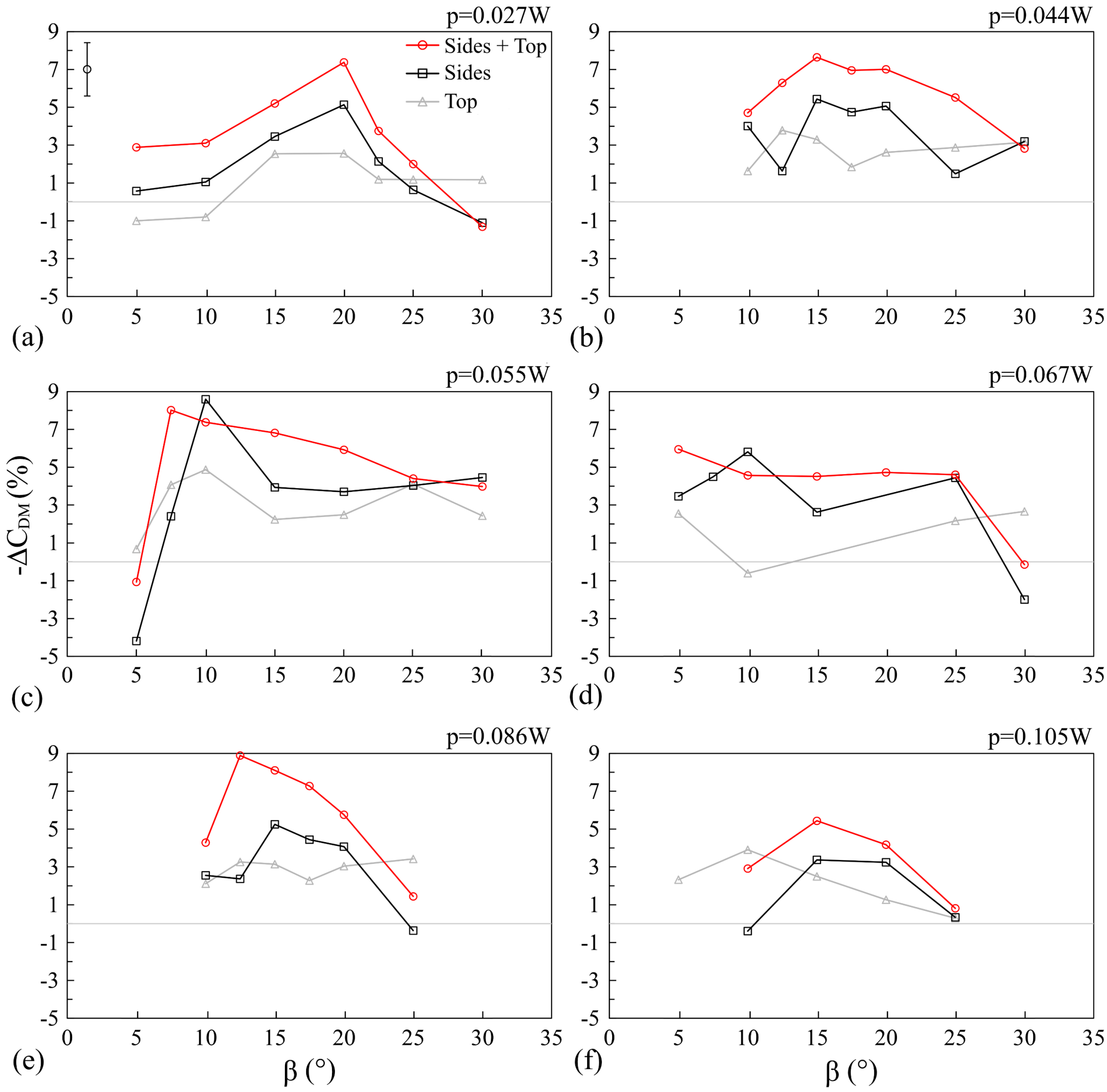

Fig. 8.11 Drag reduction for the LBT configurations at penetration angles within 5° < β < 30° and various pitches: (a) p=0.027W, (b) p=0.044W, (c) p=0.055W, (d) p=0.067W, (e) p=0.086W, (f) p=0.105W

generated by the lobes, with smaller pitches tending to produce higher average vorticity per lobe, as explained in **Section 2.4.1**. Additionally, the upper limit for the penetration angle is typically between 20°<β<30° **(Qiu, 1992; O'Sullivan et al., 1996; Yu, Hou and Chan, 2000)**, with further increases normally having negative impact on circulation strength.

Further insight is gained by comparing the results of LBTs at selected β, with the BTT at equivalent α=β. This allows comparisons between all configurations of identical aspect ratio modifications. These results are presented in **Fig. 8.12** and include only the instances where all, side and top, edges are modified, as the results in **Fig. 8.3** and **Fig. 8.11** show these to generally produce the highest drag benefits. **Figure 8.12(a-b)** shows that at β=10° and β=15°, while all LBTs reduce drag across the pitch range, the reductions are

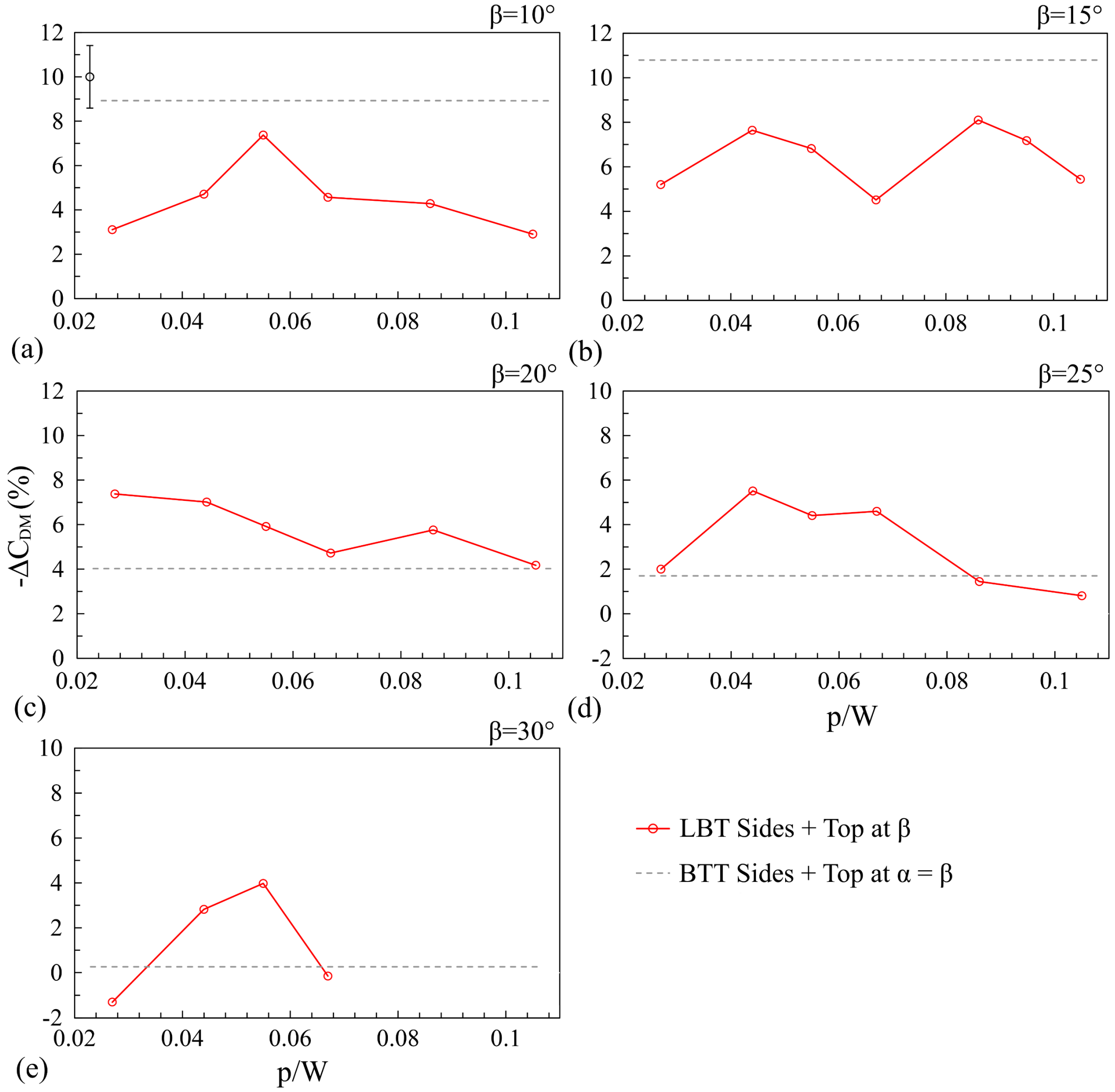

Fig. 8.12 Drag reduction for the LBT configurations of pitches within 0.027W < p < 0.105W at a constant β compared with BTT at equivalent α=β: (a) β=α=10°, (b) β=α=15°, (c) β=α=20°, (d) β=α=25°, (e) β=α=30°

generally lower in comparison with the BTT at equivalent α. The worst relative performance is found at β=15°, the angle of the optimum taper BTT (**Fig. 8.3**). At the same angle (**Fig. 8.12(b)**), the LBT results show an interesting, almost symmetric pattern, with the ΔC_{DM} for p=0.044W and p=0.086W near-identical. The implications of this trend are explored further in the following sections. Interesting results are discovered at higher angles exceeding β=α=15° (**Fig. 8.12(c-e)**). These trends show that as the angle increases and BTT's drag reduction capability reduces radically, most LBT configurations continue to exhibit substantial drag reductions persisting up to β=30°. These results suggest that with the addition of lobes, significant drag reductions can be achieved at much higher angles and thus, higher aspect ratios, significantly decreasing the impact on the vehicle's internal space.

8.3.1.1 Results of the non-linear LBT configurations

This section considers the effects of the non-linear LBT configurations (LBT-MOD) summarised in **Appendix A**. **Table 8.1** presents the model drag reduction ($-\Delta C_{DM}$) with respect to the baseline ($C_{DM}\approx0.579$) for all LBT-MOD variations. As can be seen, all non-linear configurations reduce drag, but none of the variations exceeds the reduction of the equivalent linear LBT (within experimental uncertainty). Of particular interest, however, are selected modifications applied to the top edge only generating relatively high drag benefits. Specifically, the configurations LBT-MOD2-1 (5.02%), LBT-MOD3-1 (4.56%) and LBT-MOD4-1 (5.15%) are found to reduce drag by approximately 5%, almost double the benefit for the linear (top only) LBT p=0.044W-β=20° (2.61%) and β=25° (2.88%). Additionally, these results are also shown better than those obtained with the top edge taper BTT α=20° (1.75%) and BTT α=25° (2.43%). These results suggest that the application of variable penetration angle to the lobes along the top trailing edge may be a promising method for achieving a relatively high drag reduction at low cost in internal space. Whether β is increasing or decreasing towards the base corners appears to make little difference to the overall drag benefit, suggesting the resulting interactions between the asymmetrically generated vortices remain similar for all.

Non-linear configuration	**$-\Delta C_{DM}$ (%)** (±1.4)
LBT-MOD1-1	2.68
LBT-MOD1-2	5.07
LBT-MOD1-3	6.07
LBT-MOD2-1	5.02
LBT-MOD2-2	5.19
LBT-MOD2-3	6.42
LBT-MOD3-1	4.56
LBT-MOD3-2	5.32
LBT-MOD3-3	5.84
LBT-MOD4-1	5.15
LBT-MOD4-2	5.47
LBT-MOD4-3	5.59
LBT-MOD5.1-2	4.49
LBT-MOD5.1-3	4.27
LBT-MOD5.2-2	5.72
LBT-MOD5.2-3	5.09
LBT-MOD6.1-2	4.97
LBT-MOD6.1-3	6.01
LBT-MOD6.2-2	5.27
LBT-MOD6.2-3	6.53
LBT-MOD7-2	2.85
LBT-MOD7-3	6.12

Table 8.1 Drag reduction results for the non-linear LBT configurations

8.3.2 Impact on time-averaged wake flow-field

The lobed mixer configuration selected for the flow-field evaluation is the LBT p=0.044W for its ability to produce significant drag reductions across the range of angles $15° < \beta < 25°$ (**Fig. 8.11(b)**). The configuration LBT p=0.044W-β=15° is considered first, with u* topologies in SV1 and SH1 presented in **Fig. 8.13(a)**. In SV1 (**Fig. 8.13(a)(i)**), the overall wake topology is similar to that of BTT α=15°, with the lowest u* magnitudes residing close to the base. One exception is the weaker tapering from the top, suggesting relatively lower downward momentum exists locally. This is also evident in the velocity deficit in the upper parts (z*>0.9) extending further downstream, with u*<0.3 at x*<1.3 in comparison with x*<1 for BTT α=15° (**Fig. 8.4(a)(i)**). From the horizontal perspective (SH1 – **Fig. 8.13(a)(ii)**), the wake is seen narrower than the baseline (**Fig. 8.1(a)(ii)**), indicating a relative enhancement in the crosswise flow. In comparison with the BTT α=15° however, the reductions in wake width are smaller, suggesting a relatively weaker inboard momentum; this is most evident in **Fig. 8.14(a)**. The lowest velocity magnitudes (u*<0.2) are again seen to extend further downstream to x*≈0.6 within 0.1<|y*|<0.35 (**Fig. 8.13(a)(ii)**), similar to BTT α=15° (**Fig. 8.4(a)(ii)**), suggesting a comparable increase in the size of the side wake vortices.

The in-plane vorticity (**Fig. 8.13(b)**) shows analogous trends. In SV1 (**Fig. 8.13(b)(i)**) the topology remains similar to that of the BTT α=15° (**Fig. 8.6(a)(i)**), except along the top shear layer (1.3<z*<1.5), which does not exhibit the same arching towards the wake centre as is seen in **Fig. 8.6(a)(i)**; consistent with weaker downward momentum. Close

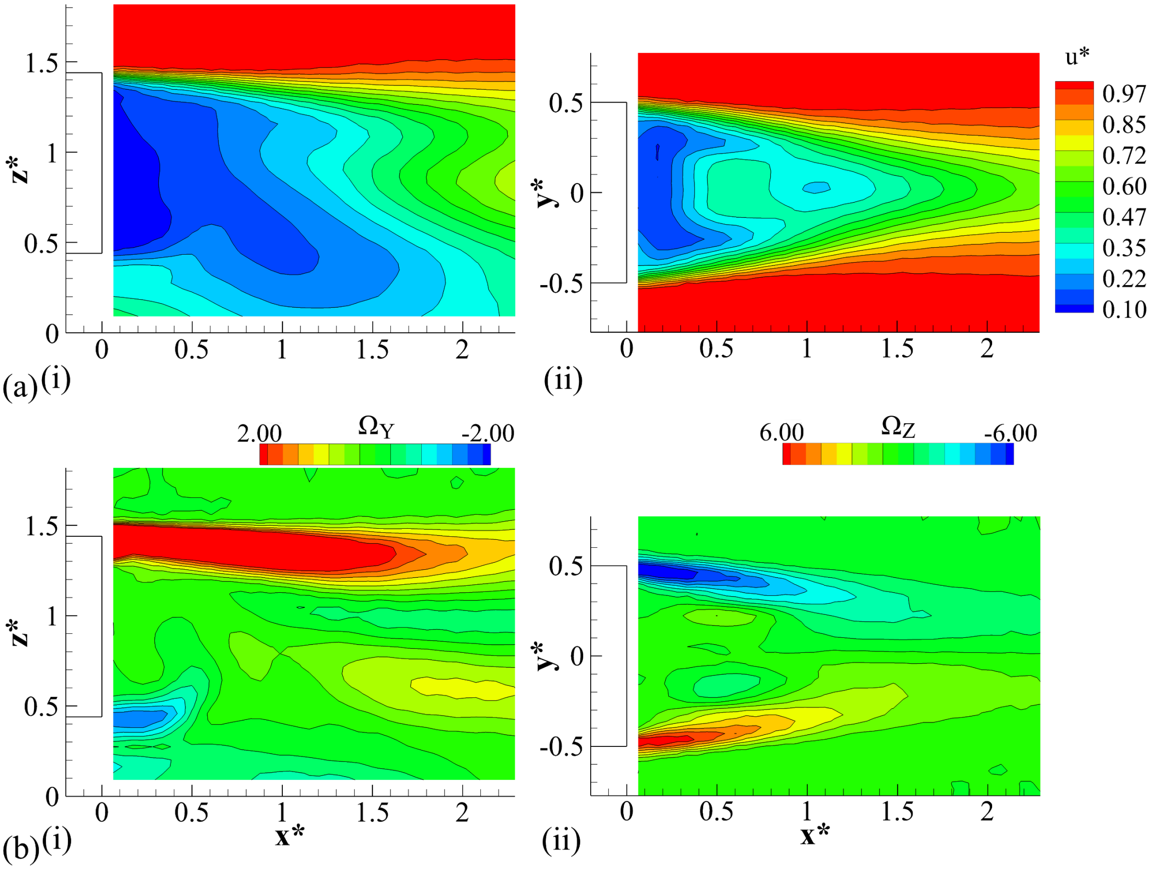

Fig. 8.13 LBT p=0.044W-β=15° (sides and top) wake: (a) streamwise velocity u* and (b) in-plane vorticity (Ω_Y and Ω_Z); (i) SV1 (Ω_Y), (ii) SH1 (Ω_Z)

to the underbody region (0.3<z*<0.5), the area of strong upwash appears near identical to that of the BTT α=15° (**Fig. 8.6(a)(i)**), extending to x*≈0.4. From these results, a similar shift in the vertical wake balance may be inferred, with the position of the lower wake vortex moved away from the base relative to the baseline case (**Fig. 8.1(b)(i)**). This is explored further in the remainder of this section. From the horizontal perspective (SH1 – **Fig. 8.13(b)(ii)**), Ω_Z supports a subtly wider wake for LBT p=0.044W-β=15° relative to BTT α=15°, with similar magnitudes, but less severe arching towards y*≈0. Overall, these findings support the drag results for these configurations, showing a tendency for smaller wakes to produce lower drag **(Grandemange et al., 2013)**.

Further insight is gained considering the LBT p=0.044W-β=20° wake topology presented in **Fig. 8.15**. **Figures 8.15(a-b)** show near-identical trends in u* and in-plane vorticity to those in **Fig. 8.13**, suggesting that the increase from β=15° to β=20° makes little difference to the overall wake size and distribution. These results imply that within this β range, strong flow entrainment from the side and top trailing edges is sustained, despite the increase in penetration angle. This finding supports the small variation in drag reduction between these configurations, changing from 7.6% (LBT p=0.044W-β=15°) to 7.0% (LBT p=0.044W-β=20°) (within experimental uncertainty; **Fig. 8.11(b)**). Furthermore,

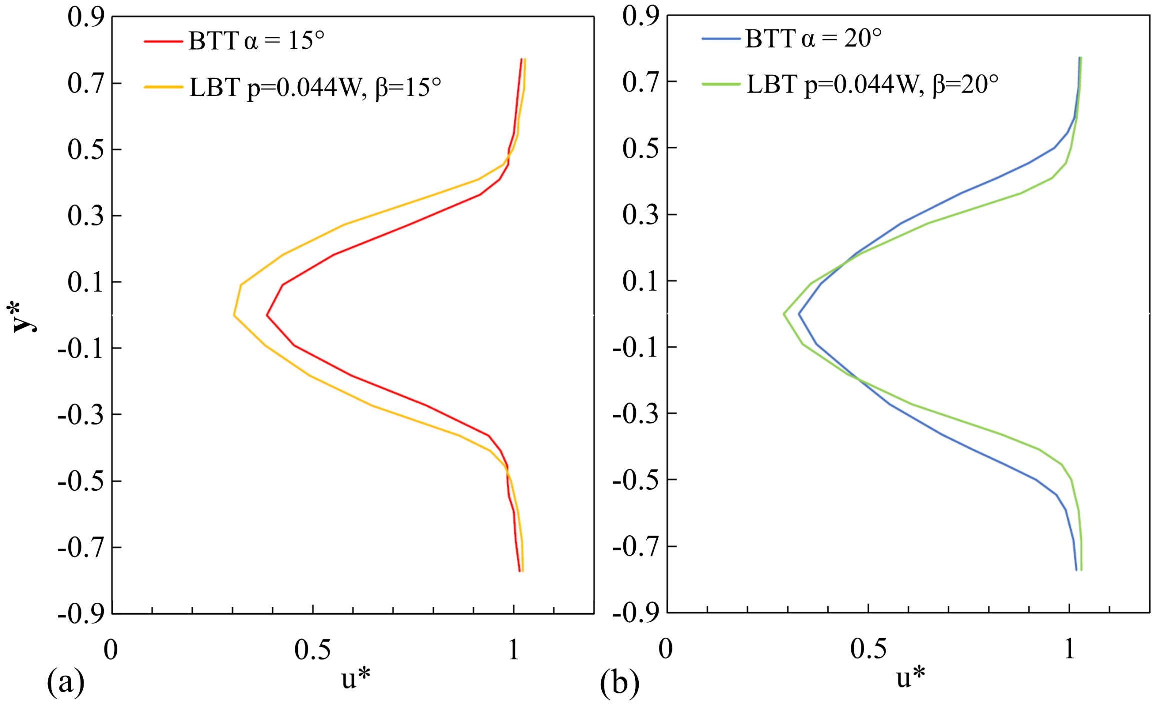

Fig. 8.14 Profiles of u* at x*≈1.25, z*≈0.92 (SH1) for: (a) BTT α=15° and LBT p=0.044W-β=15°, (b) BTT α=20° and LBT p=0.044W-β=20° (sides and top for all)

comparisons to the BTT α=20° (**Fig. 8.4(b)** and **Fig. 8.6(b)**), whose trends approach those of the baseline, suggest that LBT p=0.044W-β=20° generates stronger inboard momentum from the sides. This is most evident in the relative reduction in the wake width indicated in **Fig. 8.14(b)**. This again supports the drag reduction trends, with the benefit measured for the BTT α=20° limited to approximately 4% (**Fig. 8.3**).

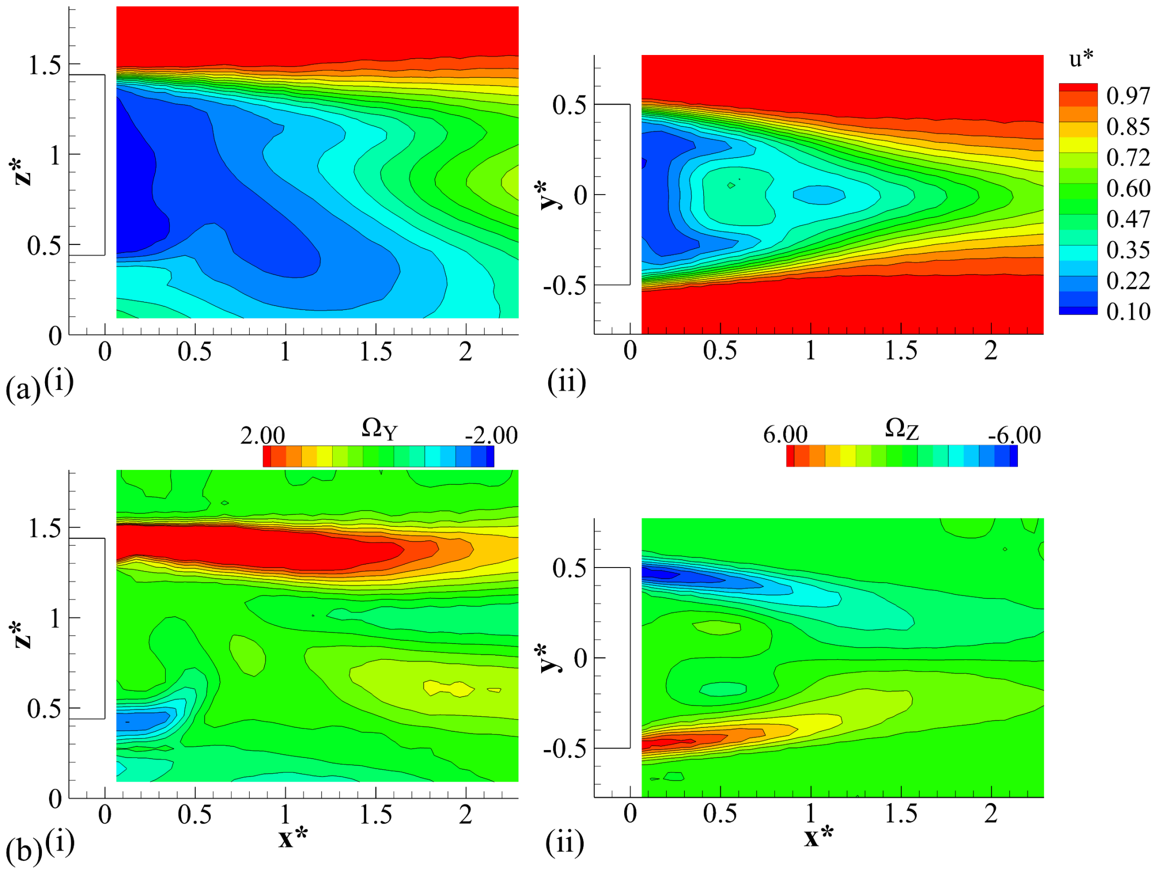

Fig. 8.15 LBT p=0.044W-β=20° (sides and top) wake: (a) streamwise velocity u* and (b) in-plane vorticity (Ω_Y and Ω_Z); (i) SV1 (Ω_Y), (ii) SH1 (Ω_Z)

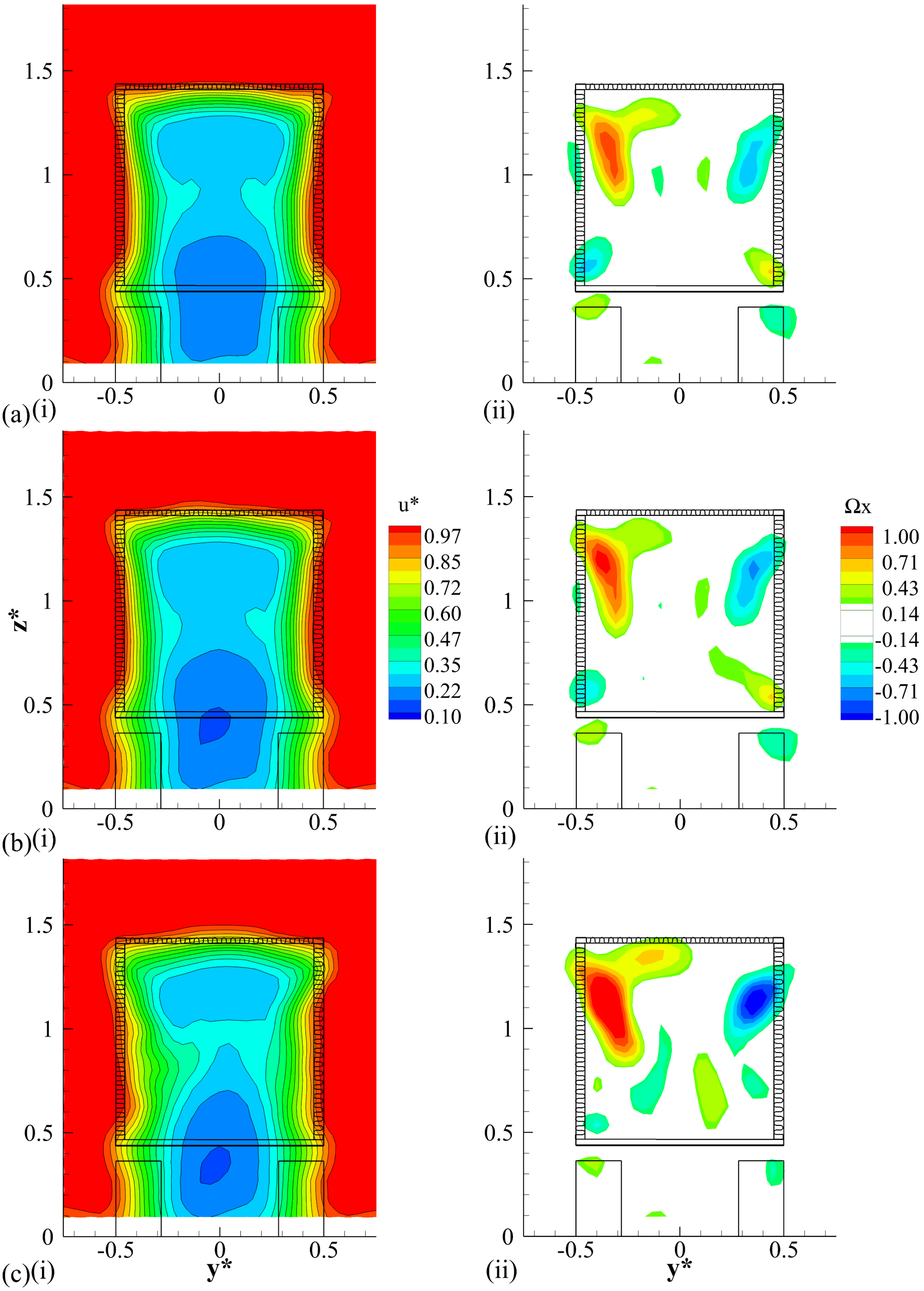

Fig. 8.16 Contours of streamwise velocity (i) and vorticity (ii) in T3 for LBT p=0.044W (sides and top) at: (a) β=15°, (b) β=20°, (c) β=25° ($-0.25<\Omega_X<0.25$ omitted for clarity)

Figure 8.16 considers the configurations LBT p=0.044W at β=15°, 20°, 25° in the transverse plane T3. The u* topology for the LBT p=0.044W-β=15° (**Fig. 8.16(a)(i)**) confirms reductions in wake size downstream of the trailer base (z*>0.5) and increases in the lower portions (z*<0.5), relative to the baseline (**Fig. 8.2(a)**). The lowest velocity magnitudes are contained within |y*|<0.3, z*<1.25, and the shape of the wake is seen to generally reflect the shape of the base, with small spanwise contractions visible around z*≈0.8. In comparison with the BTT α=15° (**Fig. 8.7(a)(i)**), the wake size reductions are evidently less significant, further supporting the variation in drag results for these two configurations. In the same plane, the topology of Ω_X (**Fig. 8.16(a)(ii)**) shows two pairs of counter-rotating structures around the base centre, similar to the trend observed for the BTT α=15° (**Fig. 8.7(a)(ii)**). For LBT p=0.044W-β=15°, the overall magnitudes are found subtly weaker ($|\Omega_X| \approx 0.6 - 1.0$) and the magnitude disparity between the individual structures higher, albeit limited to $|\Delta\Omega_X| \approx 0.4$. These results are reflected in **Fig. 8.17**, showing only marginal reductions in the upwash and downwash around z*≈0.9 (in comparison with the analogous trend for BTT α=15° in **Fig. 8.8**) and excellent retention of the balance, with the local maxima of ω*≈0.058 and ω*≈-0.057 at z*≈0.36 and z*≈1.45, respectively. These findings provide further support for the correlation between the vertical wake balance and drag benefit **(Grandemange et al., 2013; Pavia, Passmore and Gaylard, 2016)**.

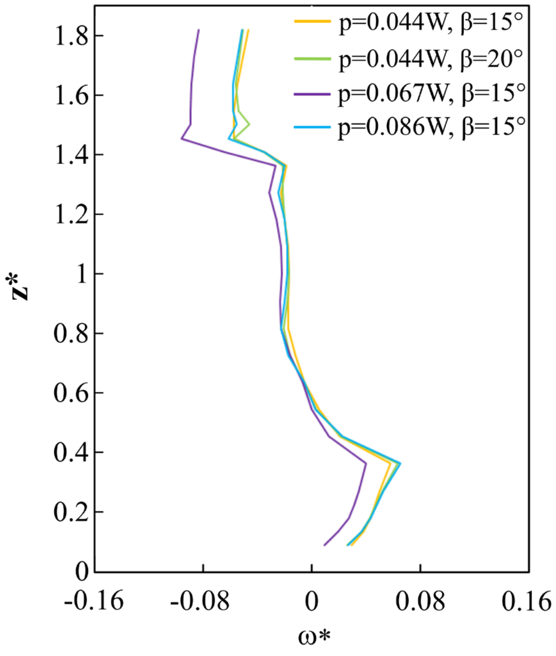

Fig. 8.17 Plots of vertical velocity ω* in SV1 at x*≈0.25 for LBT p=0.044W-β=15° and β=20°, p=0.067-β=15°, and p=0.086-β=15° (sides and top for all)

The effects of increasing penetration angle are evident by considering the results of LBT p=0.044W-β=20° (**Fig. 8.16(b)**). From this perspective, the u* topology (**Fig. 8.16(b)(i)**) is again seen nearly unaffected, being near-identical to **Fig. 8.16(a)(i)**. One exception is the minimum magnitude of u*≈0.16 at |y*|<0.1, 0.3<z*<0.45 in comparison with u*≈0.17 (within experimental uncertainty) in **Fig. 8.16(a)(i)**. These results agree with the trends presented in **Fig. 8.13** and **Fig. 8.15**, showing analogous similarities in planes SV1 and SH1. Correspondingly, the Ω_X topology (**Fig. 8.16(b)(ii)**) also continues to exhibit the four counter-rotating structures discussed earlier. For LBT p=0.044W-β=20°, the upper pair (z*≈1.2 - **Fig. 8.16(b)(ii)**) can be seen subtly stronger, with the maximum magnitudes now within $|\Omega_X|\approx0.6 - 1.1$ and a marginal increase in the magnitude disparity to $|\Delta\Omega_X|\approx0.5$. These trends support the variations in the drag reduction for these two configurations being within experimental uncertainty (**Fig. 8.11(b)**). More importantly, however, comparisons between **Fig. 8.16(b)** and BTT α=20° (**Fig. 8.7(b)**) reveal that for the same aspect ratio modifications (β=α=20°), the addition of lobed mixers continues to produce significant wake size reductions as well as the lower pair of streamwise vortices (0.5<z*<0.6). Consequently, the vertical wake balance is also seen retained in **Fig. 8.17**, in contrast with the overwhelming upwash found for the BTT α=20° in **Fig. 8.8**. These results support the significantly better drag reduction measured for the LBT configurations of β=20° relative to BTT α=20° (**Fig. 8.12(c)**).

Further increases in penetration angle (LBT p=0.044W-β=25° – **Fig. 8.16(c)(i)**) can be seen to continue producing reductions in wake size relative to the baseline (**Fig. 8.2(a)**) and BTT α=25° (**Fig. 8.7(c)(i)**). Some degradation is evident close to the top trailing edge (z*>1.1 - **Fig. 8.16(c)(i)**), where the wake appears to widen in comparison with **Fig. 8.16(a-b)(i)**. Additionally, between 0.5<z*<1, **Fig. 8.16(c)(i)** shows some degradation in symmetry about y*≈0, with stronger spanwise contractions apparent at y*<0 relative to y*>0. Furthermore, **Fig. 8.16(c)(ii)** shows increasing β to produce further increases and reductions in magnitudes of the upper and lower vortex pairs, respectively, with the magnitude disparity between adjacent structures of up to $|\Delta\Omega_X|\approx1$. Nonetheless, this topology remains more favourable than that of the BTT α=25° (**Fig. 8.7(c)(ii)**), which shows trends similar to the baseline with strong co-rotating structures along each model side. Overall, these results (**Fig. 8.16**) suggest that one effect of increasing β is a gradual loss in symmetry between the counter-rotating vortex pairs, explaining the steady degradation in drag reduction. Additionally, with increasing α, the redistribution of Ω_X appears very sudden, with a complete loss of the lower vortex pair from BTT α=15° to α=20°, supporting the severe increase in drag between the two. With the addition of lobed mixers however, this change can be seen to be more progressive, with both upper and lower vortex pairs sustained for higher aspect ratios.

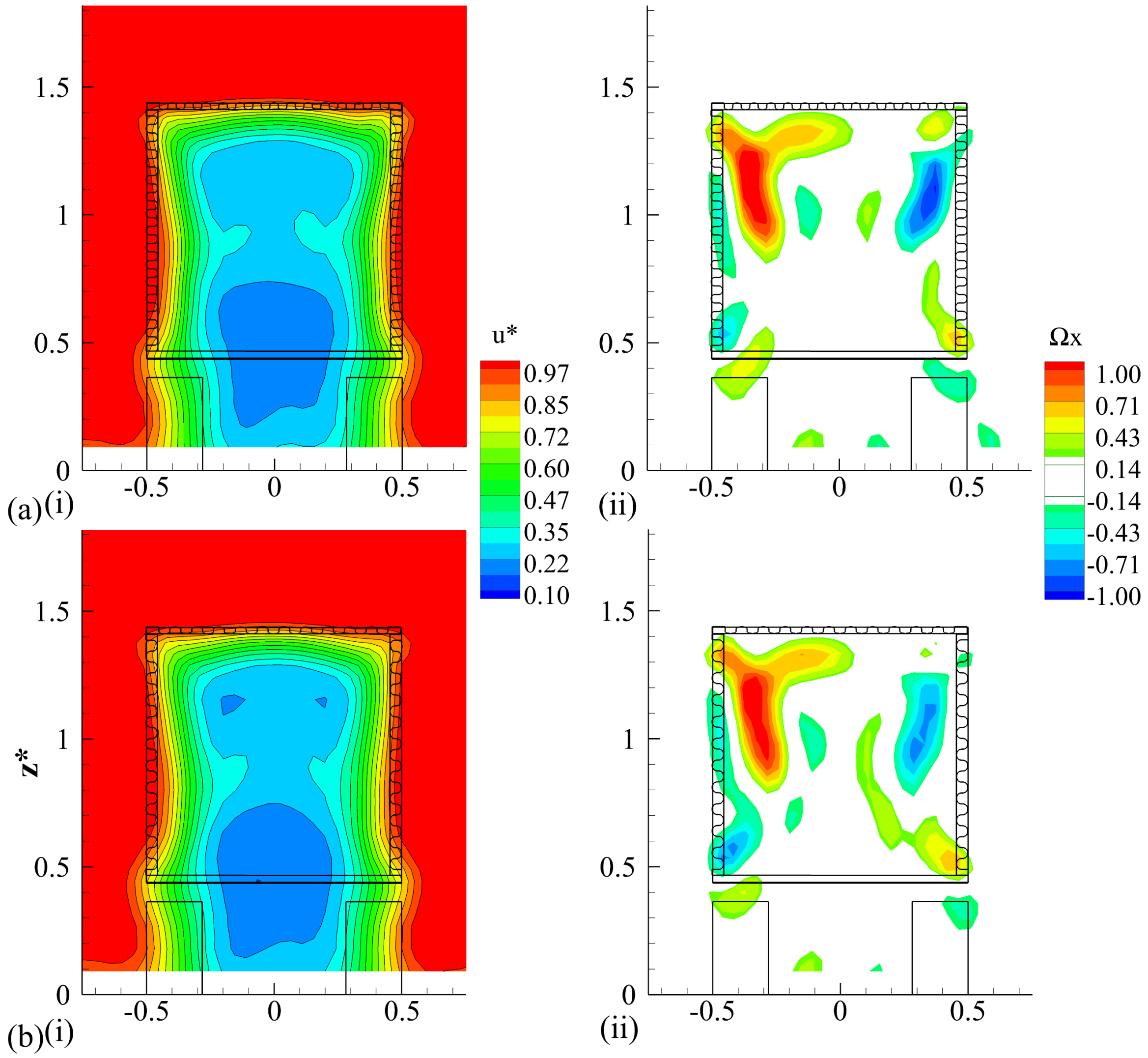

Fig. 8.18 Contours of streamwise velocity (i) and vorticity (ii) in T3 for: (a) LBT p=0.067W-β=15° (sides and top), (b) LBT p=0.086W-β=15° (sides and top) ($-0.25<\Omega_X<0.25$ omitted for clarity)

Effects of varying pitch are evaluated considering the results for LBT p=0.067W and p=0.086W at β=15° (**Fig. 8.18**). In both cases, u* topology (**Fig. 8.18(a-b)(i)**) closely resembles that of LBT p=0.044W-β=15° presented in **Fig. 8.16(a)(i)**, with observable reductions in wake size downstream of the trailer base and the lowest magnitudes contained within $|y^*|<0.3$, $z^*<1.25$. The similarities in the wake size between these three configurations are most evident in **Fig. 8.19**, showing near-identical vertical and spanwise u* profiles. More distinct differences, albeit still subtle, are found in the Ω_X distributions at T3 (**Fig. 8.18(a-b)(ii)**). In comparison with LBT p=0.044W-β=15° (**Fig. 8.16(a)(ii)**), LBT p=0.067W-β=15° (**Fig. 8.18(a)(ii)**) shows an increase in vorticity strength. While four counter-rotating structures are still evident, the maximum magnitudes are now within $|\Omega_X|\approx0.7 - 1.3$, representing a growth in magnitude disparity between the adjacent vortices up to $|\Delta\Omega_X|\approx0.6$. Further increases in pitch to p=0.086W (**Fig. 8.18(b)(ii)**) also result in stronger vorticity relative to p=0.044W, with maximum magnitudes of $|\Omega_X|\approx0.8 - 1.2$. In this instance however, the relative increase in the strength of the upper and lower structures is identical, resulting in a similar magnitude disparity ($|\Delta\Omega_X|\approx0.4$) as that found for p=0.044W. Considering these results in conjunction with the drag trends presented in **Fig. 8.12(b)** offers further support for the increasing drag with growing vortex imbalance, despite all of the configurations providing reductions in wake size. These results are also reflected in the vertical velocity trends in **Fig. 8.17**, showing a retention of the vertical wake balance for p=0.086W along with an increase in downwash and a subtle reduction in upwash for p=0.067W ($\omega^*\approx-0.096$ at $z^*\approx1.45$ and $\omega^*\approx0.040$ at $z^*\approx0.36$).

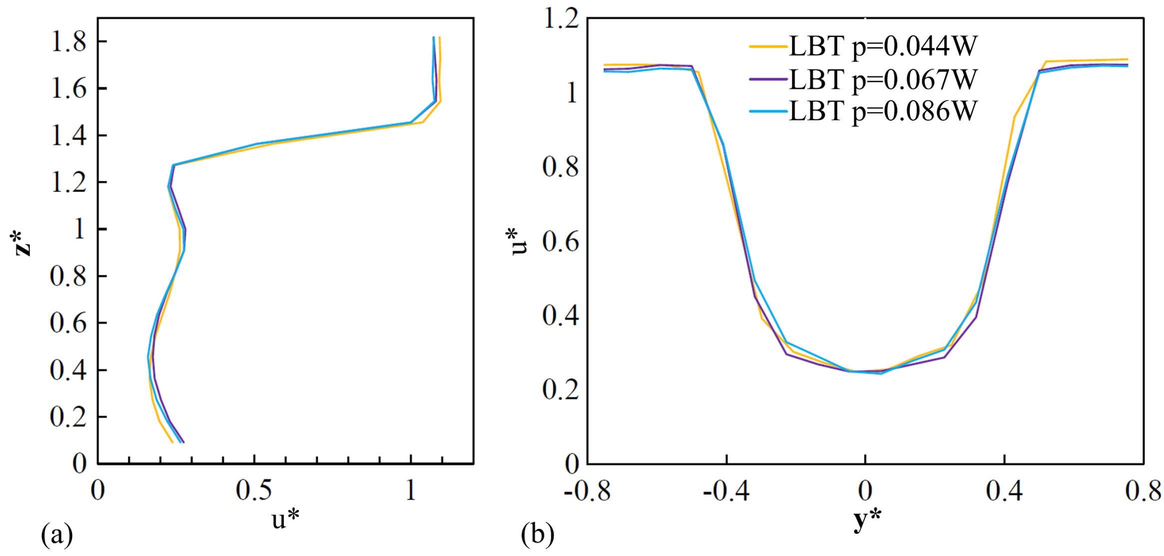

Fig. 8.19 Profiles of u* for LBTs p=0.044W, p=0.067W, p=0.086W (all β=15°) in T3 at: (a) y*≈0, (b) z*≈0.82 (sides and top for all)

8.3.2.1 Isolated influence of top and sides

The isolated influence of lobed-mixing geometries applied to the side and top trailing edges is evaluated on the LBT p=0.044W-β=20°, with the results presented in **Fig. 8.20**. In **Fig. 8.20(a)(i)**, the u* topology shows the trends to be generally similar at $z^*<1.2$ to those presented in **Fig. 8.16(b)(i)** for the same configuration with the top modification included. The sides (**Fig. 8.20(a)(i)**) can be seen to produce similar wake width reductions of approximately $\Delta y^*\approx 0.1$ from each side ($\Delta y^*\approx 0.2$ overall). Without the lobes along the top edge (**Fig. 8.20(a)(i)**), the wake above $z^*\approx 1.2$ is seen to expand both spanwise and upwards. For the same configuration, the Ω_X topology (**Fig. 8.20(a)(ii)**) again shows the four main counter-rotating vortices, much like with the inclusion of the top (**Fig. 8.16(b)(ii)**). In this case however (**Fig. 8.20(a)(ii)**), the maximum magnitudes within the upper vortices are found to increase up to $|\Omega_X|\approx 1.4$, with the lower structures seen almost unchanged relative to **Fig. 8.16(b)(ii)**. This results in a higher disparity in strength between the adjacent vortices of up to $|\Delta\Omega_X|\approx 0.9$, almost double that in **Fig. 8.16(b)(ii)**, which agrees with the lower drag reduction measured using sides only (**Fig. 8.11(b)**). Additionally, this disparity is near-equal to that found for the LBT p=0.044W-β=25° (sides and top – **Fig. 8.16(b)(ii)**), with both configurations resulting in similar drag reductions of approximately 5 – 5.5% (within experimental uncertainty – **Fig. 8.11(b)**), providing further support for the relationship between drag and vortex balance. From the results in **Fig. 8.20(a)(ii)** it can also be inferred that the inclusion of lobes along both sides and top weakens the upper vortices, producing a favourable effect on the overall wake. This is similar to the corresponding effects for the tapers BTT discussed in **Section 8.2.2.1**.

Further insight is gained considering the use of lobed mixers along the top edge only (**Fig. 8.20(b)**). The topology of u* (**Fig. 8.20(b)(i)**) shows reductions in the wake height of $\Delta z^*\approx 0.1$, with the wake width similar to that of the baseline (**Fig. 8.2(a)**). Comparisons between **Fig. 8.20(b)** and **Fig. 8.10(b)** (BTT α=20° top only) show the differences in both u* and Ω_X to be only marginal, with near-identical wake heights and vorticity distributions. Considered in conjunction with the relative differences observed with side modifications (**Fig. 8.10(a)** and **Fig. 8.20(a)**), these results suggest the application of lobed mixers to be more effective along the side trailing edges.

Overall, the trends presented in **Fig. 8.20** show that the global effects of lobed mixers on the base wake are principally similar to those of tapering, in that in both cases the role of the modification along the top edge is to reduce the wake's height, with modifications along the sides tending to reduce the wake width. This is also consistent with the drag reduction trends (**Fig. 8.3** and **Fig. 8.11**), showing the combination of both to be most beneficial.

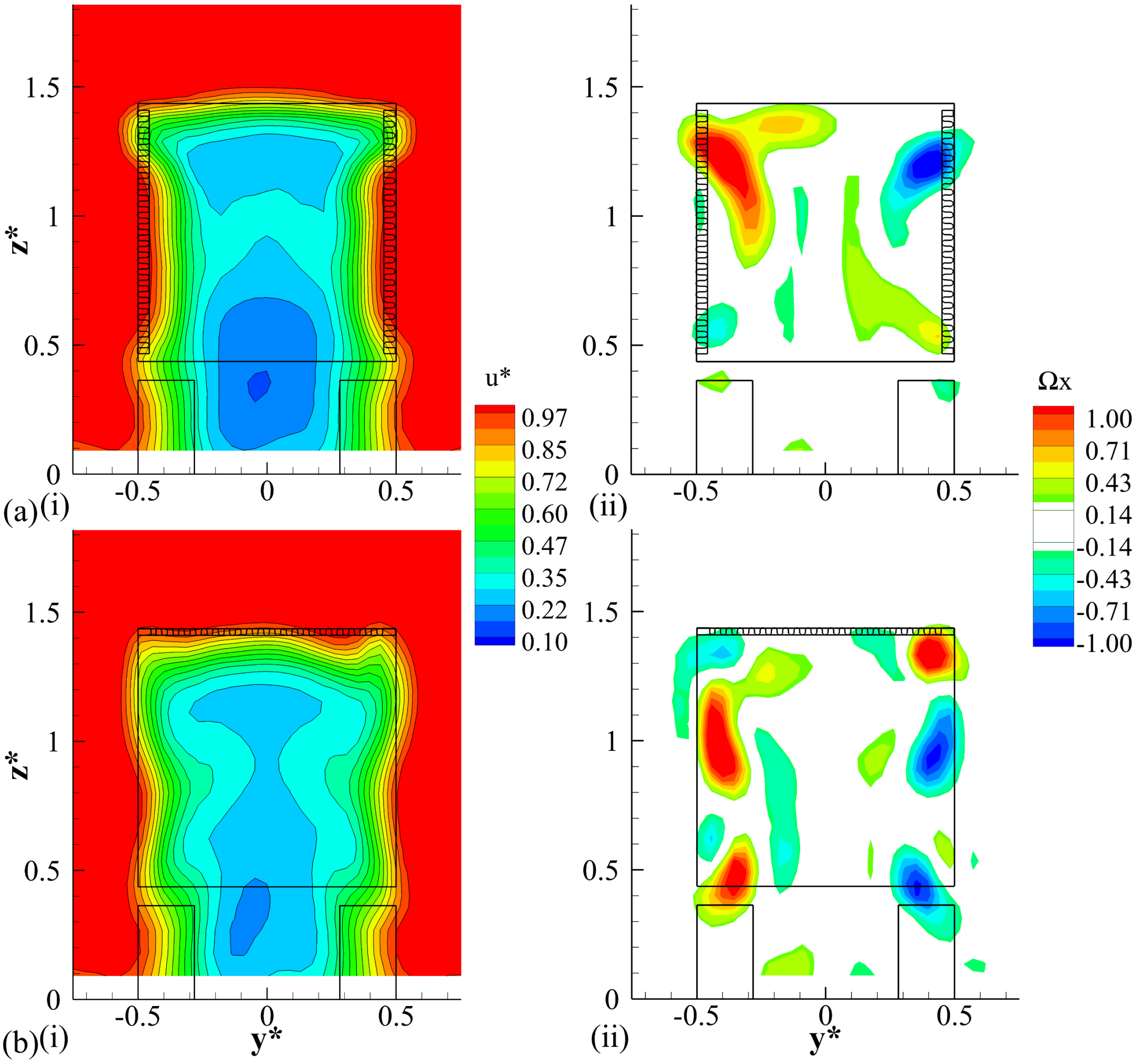

Fig. 8.20 Contours of streamwise velocity (i) and vorticity (ii) in T3 for: (a) LBT p=0.044W-β=20° - sides only, (b) LBT p=0.044W-β=20° - top only (-0.25<Ω_X<0.25 omitted for clarity)

8.3.2.2 Lobe vorticity

To assess the flow-field characteristics close to the trailing edge, the LBT p=0.044W-β=15° is considered in plane TS1, as presented in **Fig. 8.21**. In **Fig. 8.21(a)**, the u* topology can be seen to be characteristically non-uniform, closely resembling the lobed profile. This non-uniformity is a key condition for the production of streamwise vorticity at each lobe **(Skebe, Paterson and Barber, 1988; Qiu, 1992)** and suggests that the geometries studied here fulfil this requirement. Subtle deformation of the velocity field downstream of each lobe can also be observed, with small increases in magnitude around the middle of the lobe relative to the position closer to the peak. This trend is typical and reflective of the deformation caused by the streamwise vorticity presented in **Fig. 8.21(b) (McCormick and Bennett, 1994; Yu and Yip, 1997; Hu et al., 2001, 2002)**. In **Fig. 8.21(b)**, the pairs of counter-rotating vortices are evident, as expected, with each pair centred around the lobe's profile. From this perspective, each clockwise vortex (blue) is located close to the upper lobe side, with the anticlockwise (red) vortex positioned beneath, consistent with the high-speed freestream flow entering the profile from the left-hand side. Additionally, the former can be seen (**Fig.**

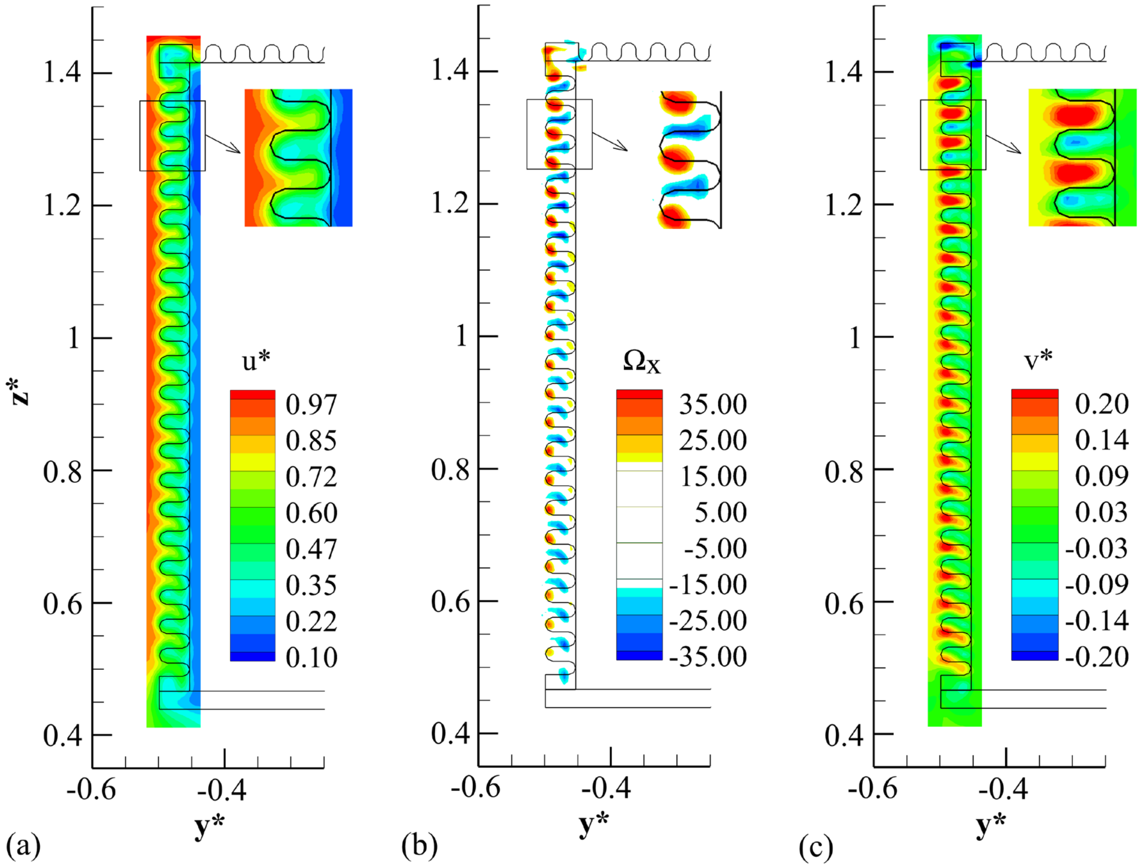

Fig. 8.21 Contours within plane TS1 for LBT p=0.044W-β=15° of: (a) streamwise velocity, (b) streamwise vorticity, (c) crosswise velocity ($-15<\Omega_X<15$ omitted for clarity)

8.21(b)) to be more elongated, with the maximum vorticity position closer to the trough, whereas the latter is found to be rounder and located towards the peak. This asymmetry is inferred to stem from the inherent asymmetry in the flow over the model sides. For a road vehicle model with moving ground use, the flow over the sides is expected to experience subtle downwash **(Lajos, Preszler and Finta, 1986)** and thus, result in the fluid entering the lobe profile at an angle as opposed to parallel. This is expected to shift the line of maximum pressure from the peak to a position marginally higher along the lobe's profile, as presented in the schematic in **Fig. 8.22**. As a result, the fluid is unable to reach the "underside" of the lobe and the anticlockwise vortex is formed closer to the crest.

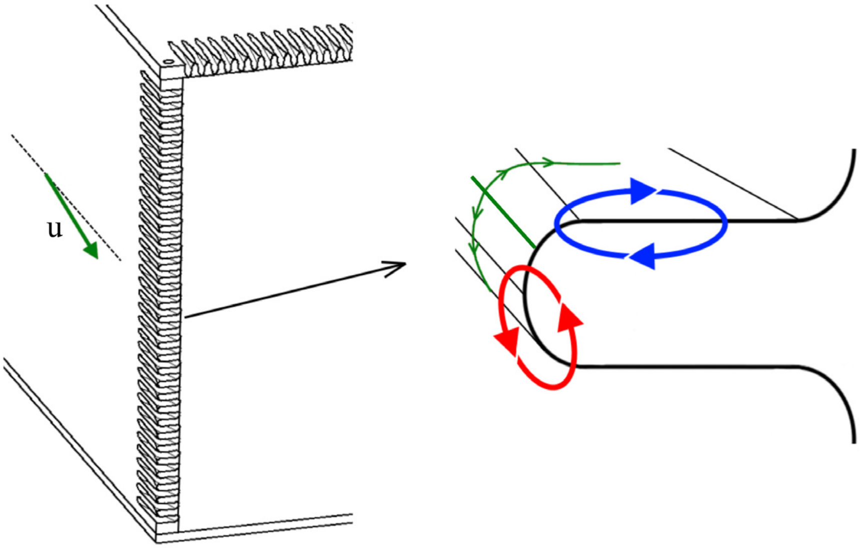

Fig. 8.22 Schematic of the vortex formation over the lobes located along the model's side trailing edges

Another result of this asymmetry is reflected in the variable strength of the adjacent vortices. As the line of maximum pressure moves upwards, the pressure gradients over the upper lobe surface are expected to become less severe in comparison with the peak, as the effective slope reduces. Consequently, the anticlockwise vortex is expected to be stronger (higher pressure gradients). Within the upper base half (**Fig. 8.21(b)**), the maximum vorticity is found to be $\Omega_{X\max} \approx 49.5$ and $\Omega_{X\max} \approx -39.1$ for the anticlockwise and clockwise structures, respectively, supporting this hypothesis, with a similar asymmetry in the vortex strength also observed by Eckerle, Sheibani and Awad **(1990)**. Furthermore, towards the ground, where the local downwash becomes more significant due to moving ground proximity, the line of maximum pressure is expected to shift progressively closer to the upper lobe side. This would continue to reduce the local pressure gradients, weakening the clockwise structures further, as indeed seen in **Fig. 8.21(b)**. Simultaneously, on the other side of the line, the pressure gradients become so severe that the anticlockwise structures are formed increasingly closer to the peak and weaker, as they form over a shorter effective height (smaller surface). This is reflected in the overall gradual weakening of the vorticity towards the base bottom, with the clockwise structures also seen larger and better defined.

Figure 8.21(c) also presents the contours of crosswise velocity v* in the same position (TS1). One important effect of the counter-rotating vortex pairs is observed at each trough of the profile, with pockets of strong inboard crossflow generated locally, consistent with the reductions in the wake width found for the LBT configurations (**Fig. 8.13**, **Fig. 8.16**). Behind each lobe a small area of outboard crossflow is also induced, in agreement with the direction of the adjacent vortices. The latter, however, are considerably weaker, which is expected due to the overall stronger inboard entrainment produced by the low-pressure wake.

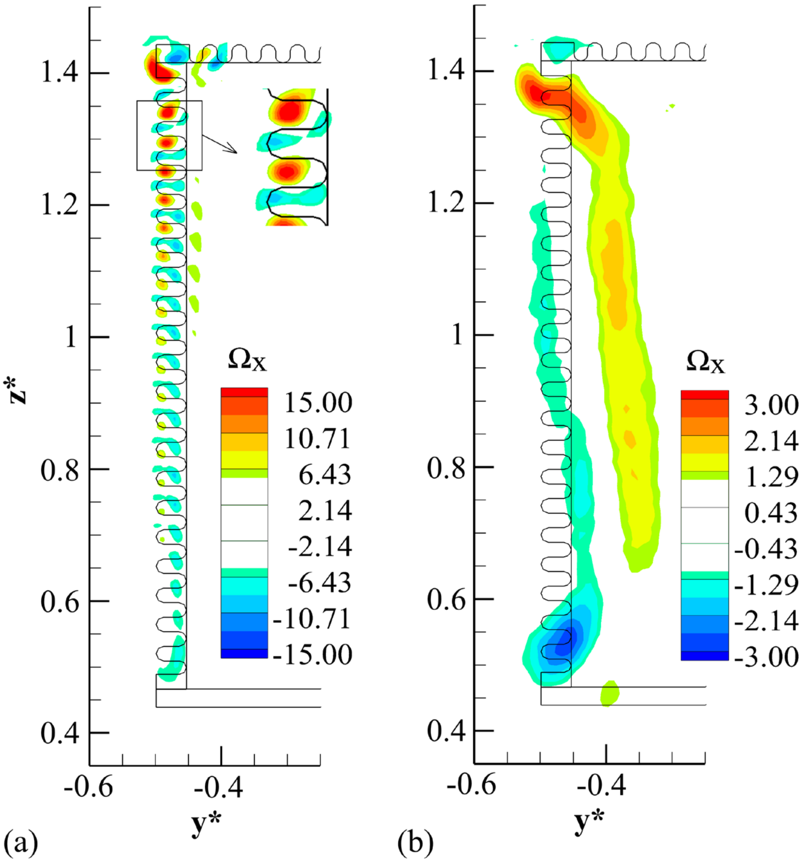

(a) (b)

Fig. 8.23 Streamwise vorticity contours for LBT p=0.044W-β=15° in:
(a) TS2 ($-5<\Omega_X<5$ omitted for clarity), (b) TS3 ($-1<\Omega_X<1$ omitted for clarity)

Further insight is gained with the streamwise vorticity data from the planes TS2 and TS3 (**Fig. 8.23**). In TS2 (**Fig. 8.23(a)**) the distinct cells of counter-rotating vorticity are still discernible. One immediate observation however, is the significant reduction in magnitudes, with $\Omega_{X\max}\approx 27.1$ and $\Omega_{X\max}\approx -10$, consistent with a downstream vortex breakdown **(Hu et al., 2001, 2002)**. Hu et al. **(2001, 2002)** showed that as the streamwise vortices travel downstream, they tend to break down rapidly into increasingly smaller structures occupying random positions. Although instantaneous results revealed the strength of the smaller vortices to be consistent with the upstream locations, within the time-averaged results the distribution remained more organised with the mean strength reduced **(Hu et al., 2001, 2002)**. The results here support these findings (**Fig. 8.23(a)**). Additionally, the vortices which are originally (at the trailing edge) smaller and weaker are typically found to diffuse more rapidly **(Eckerle, Sheibani and Awad, 1990; Waitz et al., 1997)**. Results in **Fig. 8.23(a)** again agree, with the weak anticlockwise vortices seen in **Fig. 8.21(b)** in the lower base half now almost indiscernible at $z^*<0.8$ (**Fig. 8.23(a)**). This region ($z^*<0.8$ – **Fig. 8.23(a)**) is now dominated by the clockwise structures. Similarly, in the upper base half ($z^*>1.1$) the anticlockwise cells are observed to be dominant, consistent with the pattern in **Fig. 8.21(b)**.

As the vortices evolve further, they continue to diffuse, with the maximum vorticity in TS3 (**Fig. 8.23(b)**) at $\Omega_{X\max}\approx 3.5$ and $\Omega_{X\max}\approx -2.8$ for the anticlockwise and clockwise structures, respectively. Additionally, only two distinct regions of counter-rotating vorticity are observed at this position. For the anticlockwise structure, the highest magnitudes are located in the upper base half ($z^*>1$ – **Fig. 8.23(b)**), whereas the most elevated clockwise magnitudes are positioned at $z^*<0.8$. This trend is consistent with the upstream planes (TS1 – **Fig. 8.21(b)**, TS2 – **Fig. 8.23(a)**), whereby the former was found dominant in the upper base half, with the latter, dominating lower portions. Hu et al. **(2001)** showed that the adjacent vortices of the same sign tend to spread around their counter-rotating neighbours and merge together as they travel downstream, producing larger areas of like-sign circulation. Results in **Fig. 8.23** are reflective of a similar behaviour. Additionally, Hu et al. **(2001)** also showed that through the downstream diffusion, vortices have the tendency to spread toward the low-velocity region, which is evident in **Fig. 8.23(b)** with the structures found to shift toward the wake centreline. Finally, further downstream diffusion of these structures is observed to produce the previously discussed topology within T3 (**Fig. 8.16(a)(ii)**), with the elevated magnitudes of anticlockwise and clockwise circulation found at -0.4<y*<-0.3, 1<z*<1.2 and -0.5<y*<-0.4, 0.5<z*<0.7, respectively. Overall, these results indicate the evolution of the streamwise vorticity (from TS1 to T3) to contribute to the production of vertical wake balance discussed previously (**Fig. 8.17**), resulting in enhanced drag reductions.

Additional detail regarding the downstream decay of the maximum streamwise vorticity magnitude for the LBT p=0.044W-β=15° is presented in **Fig. 8.24**. Close to the trailing edges (X/h<1), the Ω_{Xmax} magnitude is very high, as would be expected with a small pitch and high-speed upstream flow. Further downstream, the vorticity diffuses rapidly, reducing by almost 50% within the distance equivalent to approximately 3h. This trend (**Fig. 8.24**) is in general agreement with that reported by Hu et al. **(2001)** for larger lobes at lower Reynolds numbers, and suggests that the breakdown of large-scale streamwise vortices into smaller structures occurs within short distances from the trailing edges.

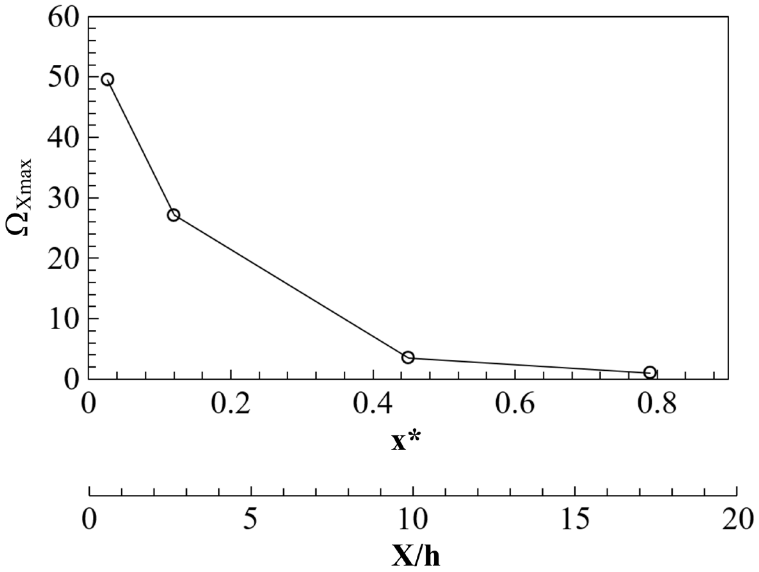

Fig. 8.24 Downstream decay of the maximum streamwise vorticity magnitude for the LBT p=0.044W-β=15°

The effects of penetration angle on the vorticity production and evolution are considered with the results of LBT p=0.044W-β=20° (**Fig. 8.25**). One immediate observation in **Fig. 8.25(a)** is a similar asymmetric generation of vorticity as explained previously for LBT p=0.044W-β=15° (**Fig. 8.22**). Correspondingly, the vorticity is also found to be strongest in the upper base half and weakening toward the floor. Further inspections reveal that the initial maximum vorticity within the anticlockwise structures is subtly higher (Ω_{Xmax}≈52.4) for this configuration (**Fig. 8.25(a)**) in comparison with **Fig.**

8.21(b). This finding is in general agreement with the theory that higher penetration angles generate stronger circulation **(Barber, Paterson and Skebe, 1988)**. In contrast, the clockwise vortices in **Fig. 8.25(a)** are observed to be weaker, with $\Omega_{Xmax} \approx -36.4$. The relative reduction in the latter is near-equivalent to the increase found for the anticlockwise structures, suggesting perhaps that a link exists between the asymmetry and increasing penetration angle. The growing disparity in strength of the counter-rotating vortices is also somewhat consistent with the trend observed previously at T3 (**Fig. 8.16(a-b)(ii)**).

Further downstream through TS2 and TS3, similar trends of the vortex diffusion (TS2 – **Fig. 8.25(b)**) and merging (TS3 – **Fig. 8.25(c)**) are also observed. Interestingly, in **Fig. 8.25(b)** the vorticity is found weaker relative to **Fig. 8.23(a)**, which is reflective of a higher initial maximum vorticity decay rate, with the magnitude reducing by 55% over $\Delta x^* < 0.09$ (TS1 to TS2), in comparison with the 45% found for LBT p=0.044W-β=15°. This suggests that with higher penetration angles, the initial vorticity is stronger and breaks down more rapidly. At TS3 (**Fig. 8.25(c)**) trends are similar to **Fig. 8.23(b)**, with the maximum vorticity within the anticlockwise structures once again subtly higher at $\Omega_{Xmax} \approx 3.7$.

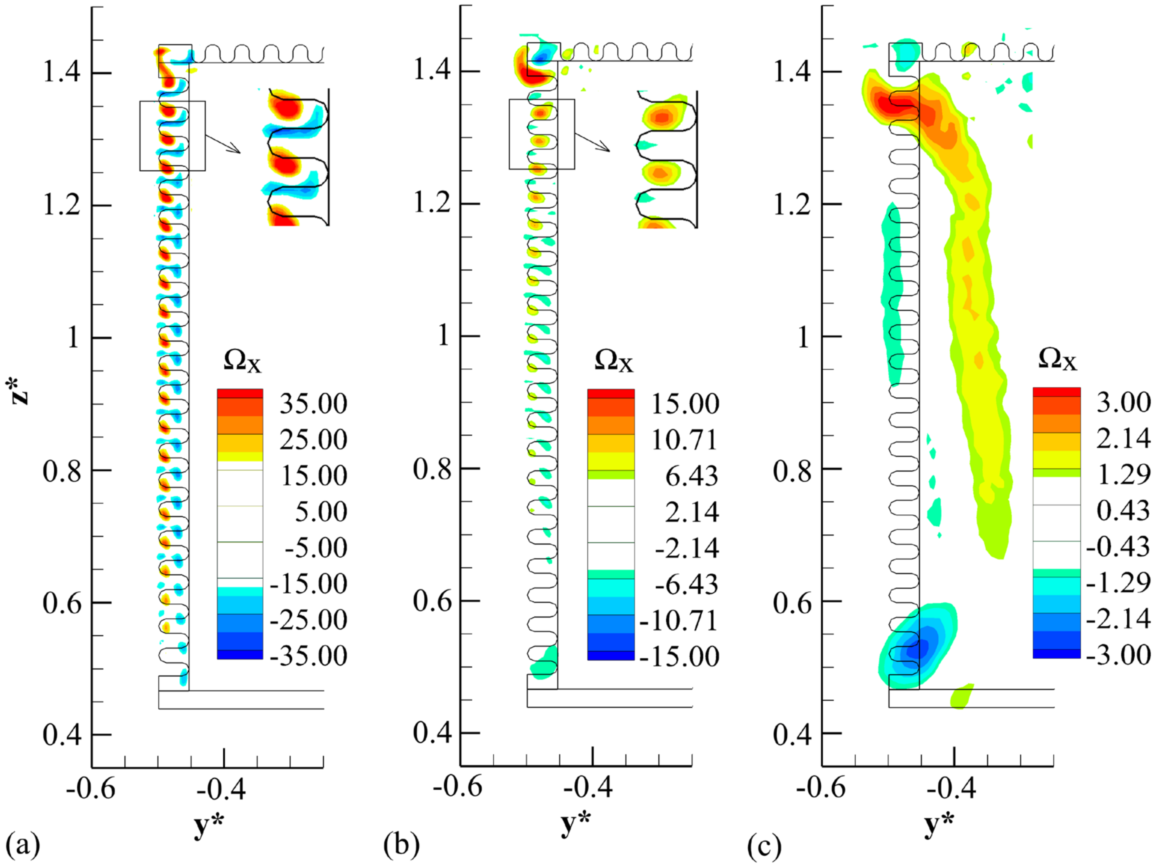

Fig. 8.25 Streamwise vorticity contours for LBT p=0.044W-β=20° in: (a) TS1 ($-15<\Omega_X<15$ omitted for clarity), (b) TS2 ($-5<\Omega_X<5$ omitted for clarity), (c) TS3 ($-1<\Omega_X<1$ omitted for clarity)

Further insight is gained by considering the higher pitch configurations LBT p=0.067W-β=15° and LBT p=0.086W-β=15° (**Fig. 8.26**). Firstly, in the closest plane TS1, the asymmetry in the vorticity production is again evident for both (**Fig. 8.26(a-b)(i)**). Considering all presented results from TS1 for varying penetration angle and pitch, these trends support the hypothesis that the asymmetry is a result of the inherent upstream flow conditions (**Fig. 8.22**) rather than any modifications of lobe profiles, with all exhibiting a similar behaviour. Another consistency between all presented geometries is the overall reduction in vorticity strength from the top towards the floor (**Fig. 8.26(a-b)(i)**). With increasing pitch (p=0.067W – **Fig. 8.26(a)(i)**, p=0.086W – **Fig. 8.26(b)(i)**) the relative spacing between the adjacent vortices shed from the lobes is seen to increase, as would be expected. Additionally, the initial maximum vorticity magnitudes are also found weaker in comparison with LBT p=0.044W-β=15° (**Fig. 8.21(b)**), with $\Omega_{Xmax}\approx41.7$ and $\Omega_{Xmax}\approx-32.1$ for p=0.067W, and $\Omega_{Xmax}\approx45.1$ and $\Omega_{Xmax}\approx-35.8$ for p=0.086W. These results (**Fig. 8.26(a-b)(i)**) suggest that the average vorticity per lobe segment reduces with increasing pitch, in agreement with Barber, Paterson and Skebe **(1988)**. Interestingly however, unlike the trend for increasing penetration angle, which showed growing disparity between anticlockwise and clockwise structures' strength, increasing the pitch appears to reduce the magnitude of all structures, with the disparity remaining near-identical, further supporting the relationship between the growth in asymmetry and penetration angle.

Further downstream at TS2 (**Fig. 8.26(a-b)(ii)**), the overall vorticity magnitudes reduce in comparison with TS1 for both pitches, as expected. For these two configurations however, the vortices are also seen to expand spatially (**Fig. 8.26(a-b)(ii)**), which is not observed for the p=0.044W profiles. Waitz et al. **(1997)** explained that after being shed from the trailing edges, the streamwise vortices grow spatially as they diffuse, eventually beginning to cancel each other out as the distance between adjacent structures reduces. Considering this in conjunction with the results presented here, the following can be inferred. For the smaller pitches (p=0.044W), the vortices are packed more tightly, and their outermost sections begin to interact relatively rapidly, which is reflected in the higher rates of Ω_{Xmax} decay. With the higher pitches (p=0.067W, p=0.086W) however, the larger spacing between the adjacent vortices allows them to expand initially as they begin to diffuse. This again is supported by the relatively lower initial Ω_{Xmax} decay rates showing reductions of 39% (p=0.067W) and 41% (p=0.086W) within the $\Delta x^*<0.09$ from TS1 to TS2.

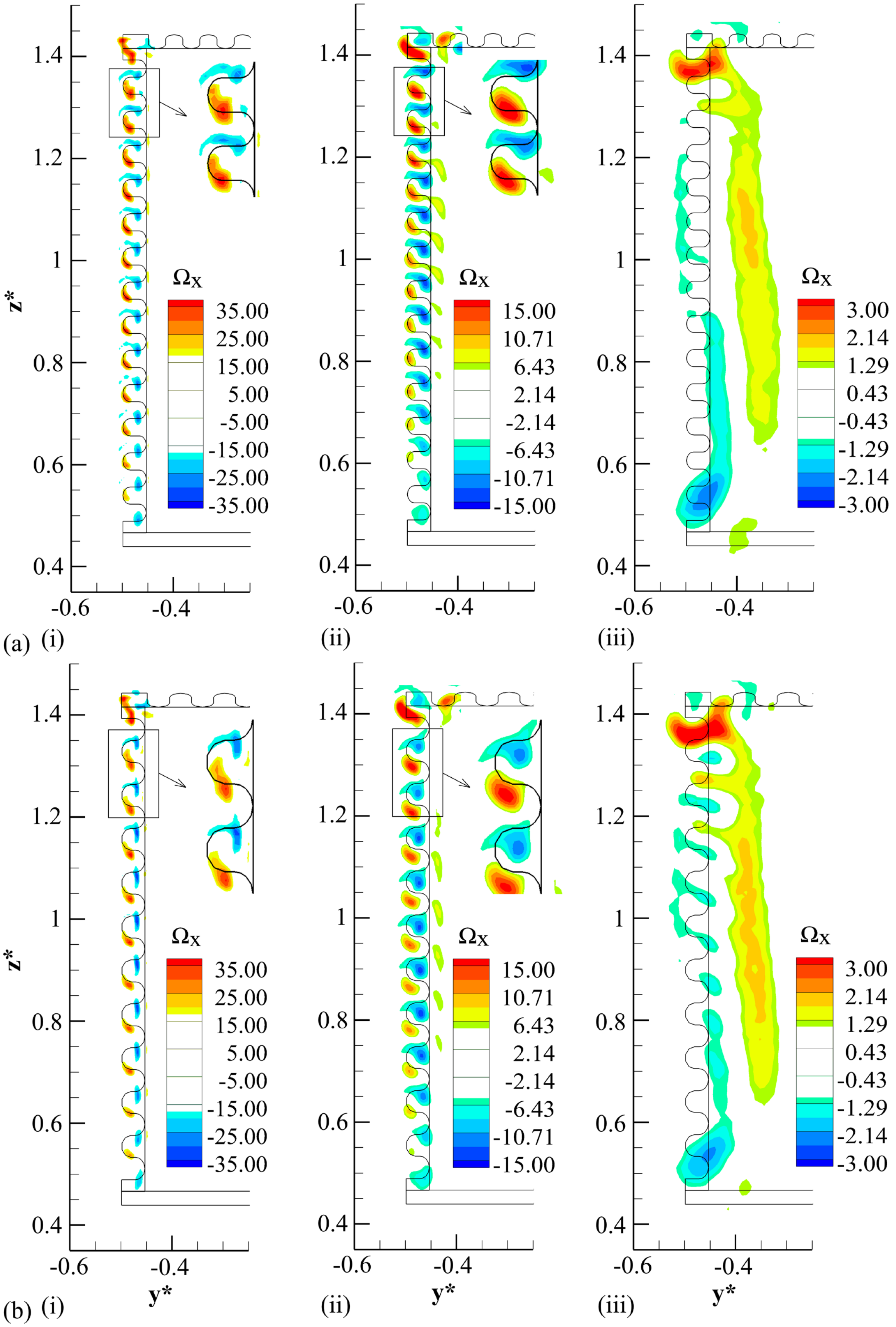

Fig. 8.26 Streamwise vorticity contours for LBT p=0.067W-β=15° (a) and LBT p=0.086W-β=15° (b) in: (i) TS1 ($-15<\Omega_X<15$ omitted for clarity), (ii) TS2 ($-5<\Omega_X<5$ omitted for clarity), (iii) TS3 ($-1<\Omega_X<1$ omitted for clarity)

Slower vorticity diffusion for the higher pitches is also evident at TS3 (**Fig. 8.26(a-b)(iii)**). In this position, the merging of like-sign structures is again observed for both p=0.067W and p=0.086W, suggesting this process to take place irrespective of pitch and penetration angle values. With the higher pitches however, some signatures of the distinct vortices are still distinguishable this far downstream, particularly for p=0.086W between $0.7<z^*<1.35$ (**Fig. 8.26(b)(iii)**).

8.4 Time-dependent flow characteristics

The effects of the different configurations on the time-dependent aspects of the wake flow-field are now considered. Velocity spectra are averaged from 39 and 9 time-segments (0.5s duration) for the 20-second and 5-second measurements, respectively, with a 50% overlap. Bin widths are $\Delta St_W \approx 0.0042$ for both. Selected results are presented with offset magnitudes to aid interpretation.

8.4.1 General wake dynamics

Velocity spectra at selected locations within the base wake for the baseline as well as the lower-drag configurations previously discussed from the time-averaged perspective are presented in **Fig. 8.27**. **Figure 8.27(a)** presents the streamwise velocity spectra (E_u) within the side shear layer. For the baseline, these signals capture the characteristic bubble pumping frequency, with a subtle broad peak observed at $St_W \approx 0.105$, in very good agreement with that found for Baseline 1 model (**Section 6.4.1**), indicating the changes in forebody geometry and flow Reynolds number have little influence on this mode. With BTT $\alpha=15°$, **Fig. 8.27(a)** shows the pumping peak to be fully suppressed, accompanied by a reduction in magnitudes for $St_W > 0.2$, with the former also observed for BTT $\alpha=20°$. This is in good agreement with the reports of Khalighi et al. **(2001)** and Martín-Alcántara et al. **(2014)** who demonstrated a similar bubble pumping suppression for straight cavities contributing to drag reduction. Similar behaviour is also found for the LBT configurations, all observed to suppress the bubble pumping peak in a similar manner to the tapering. These trends, therefore, generally support the measured reductions in drag and suggest the low-drag configurations act to stabilise the wake by weakening the global streamwise oscillation.

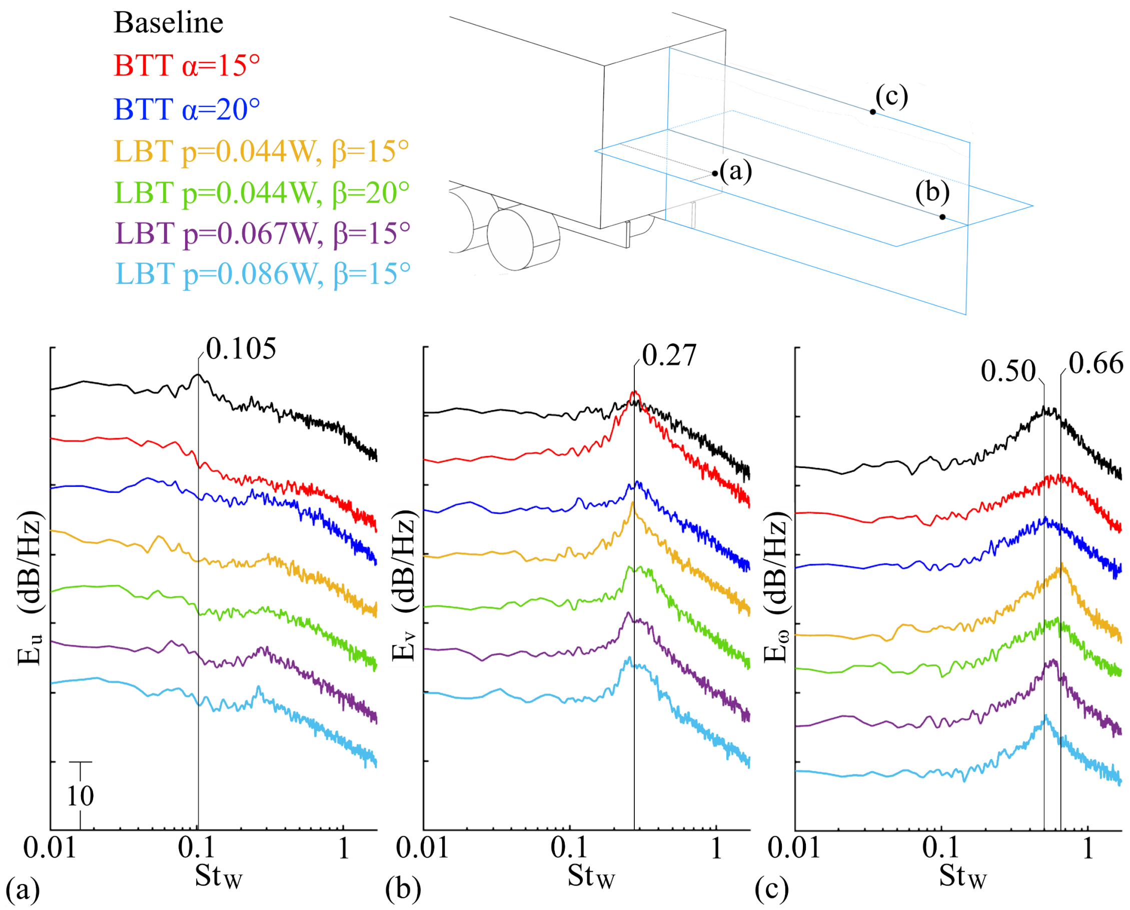

Fig. 8.27 Velocity spectra in the wake: (a) E_u at x*≈0.70, y*≈-0.36, z*≈0.92; (b) E_v at x*≈2.06, y*≈0, z*≈0.92; (c) E_ω at x*≈1.34, y*≈0, z*≈1.41 (relative offset of Δ7dB/Hz)

The lateral shedding (flapping) mode is also captured within E_v at a central wake position for all configurations (**Fig. 8.27(b)**). For the baseline, a broad weak peak centred around $St_W \approx 0.27$ is evident, reflective of the low levels of energy and coherence which exist for the crosswise shedding mode. This behaviour is similar to that observed previously for Baseline 1 (**Section 6.4.1**), further outlining the similarities between the two models. One exception is the subtle increase in characteristic frequency of this mode for Baseline 2 (**Fig. 8.27(b)**). Fan et al. **(2020)** noted the dependency of the Strouhal number associated with asymmetric shedding processes on the boundary layer characteristics prior to separation, which can subsequently be influenced by the forebody conditions and flow Reynolds number. This therefore suggests the characteristic frequency of lateral shedding increases for Baseline 2 as the forebody becomes more streamlined and the Reynolds number higher. This frequency remains insensitive to the inclusion of BTT α=15° (**Fig. 8.27(b)**), however, a considerably narrower and higher peak is observed instead, suggesting the lateral shedding to be significantly more coherent and energetic for this case. This is likely a result of the enhancement in inboard momentum upon separation from the trailing edges, acting to strengthen the side wake vortices and local shear layers **(Perry, Passmore and Finney, 2015)**. Increasing the taper angle (BTT α=20° – **Fig. 8.27(b)**) results in characteristics similar to those of the baseline, with only a marginally more defined peak. With the use of LBT p=0.044W-β=15°, a trend similar to BTT α=15° is again evident, with a strong distinct peak at $St_W \approx 0.27$. With increasing penetration angle (LBT p=0.044W-β=20°), this peak becomes subtly less defined, being broader and weaker, albeit continuing to exhibit higher energies in comparison with the corresponding BTT α=20°. Analogous changes are also observed for increasing pitch (LBT p=0.067W-β=15° and p=0.086W-β=15°), with all LBT configurations showing similar trends. For the LBT configurations, the lateral shedding mode is also captured in **Fig. 8.27(a)** with subtle broad peaks within $0.26 < St_W < 0.30$. Overall, the results (**Fig. 8.27(b)**) show that the use of the BTT α=15° as well as the lobed mixers does not affect the characteristic frequency of lateral shedding, but instead has a marked impact on the nature of this mode, which becomes more energetic and coherent.

Figure 8.27(c) also captures the vertical shedding mode within E_ω for all presented configurations, with the baseline results showing broadband behaviour with a peak centred around $St_W \approx 0.50$. This is again higher than the corresponding characteristic frequency for Baseline 1 (**Section 6.4.1**), with this increase being analogous with that described for the lateral shedding mode. Nevertheless, similar to Baseline 1 (**Section 6.4.1**), the heightwise shedding characteristics can be seen subtly more energetic and better defined relative to the lateral shedding, indicating this to be the dominant asymmetric shedding mode. With the inclusion of BTT α=15°, a similar broad peak is observed at a higher frequency of $St_W \approx 0.66$, reflective of an increase in the vertical shedding characteristic frequency, likely generated by the reduction in the distance between the opposing shear layers, consequent to the inboard shift of the top shear layer **(Grandemange, Gohlke and Cadot, 2013b; Fan et al., 2020)**. Increasing the taper angle results in characteristics largely similar to the baseline, with BTT α=20° (**Fig. 8.27(c)**) exhibiting, again, a broad peak centred around $St_W \approx 0.50$. Further interrogation shows similar peaks for the LBT configurations to be generally subtly narrower relative to the baseline and both BTTs, suggesting further increases in the coherence of this mode with the use of lobed mixers. For LBT p=0.044W-β=15°, the peak is centred around $St_W \approx 0.66$, indicating a similar increase in the vertical shedding frequency as that observed for BTT α=15°. This frequency marginally reduces with increasing penetration angle, with LBT p=0.044W-β=20° showing $St_W \approx 0.62$. Similarly, increases in pitch also result in further reductions in the characteristic frequency, with $St_W \approx 0.55$ for LBT p=0.067W-β=15° and $St_W \approx 0.52$ for LBT p=0.086W-β=15°.

Considering the results in **Fig. 8.27** holistically, the inclusion of drag-reducing techniques is observed to suppress the streamwise wake oscillation, while enhancing, to differing degrees, the asymmetric shedding modes. Additionally, for the baseline, vertical shedding is shown stronger relative to lateral shedding, consistent with the previous results for Baseline 1 (**Section 6.4.1**). For the BTT α=15° and the LBTs however, lateral shedding appears to be the dominant one among the two asymmetric shedding modes, reflecting a marked influence of these configurations on the general wake dynamic processes.

8.4.2 Local influence of lobed mixers

Local effects of the lobed mixing geometries are now considered, with **Fig. 8.28(a)** presenting the E_v at selected locations downstream of the lobed trailing edge (TS1) for LBT p=0.044W-β=15°. At position (i) behind a trough, E_v shows an increase in the low-frequency ($St_W < 0.1$) activity with a distinct peak found at $St_W \approx 0.092$. The same trend is also observed downstream of the adjacent trough at (iii), with little defined oscillatory behaviour and a general reduction in magnitudes (up to 10dB/Hz) at (ii) coincident with the lobe. Positions (i) and (iii) correspond to the locations of increased inboard momentum, as shown in **Fig. 8.21(c)**, being a direct result of the generated streamwise vorticity (**Fig. 8.21(b)**). These well-defined peaks ($St_W \approx 0.092$) therefore, suggest a coherent vortex-induced crosswise oscillation, likely reflecting the shedding frequency of the structures. Analogously, the E_v trend at (ii) is consistent with the weaker local crossflow observed in **Fig. 8.21(c)**. Further down towards the floor, the trends downstream of a trough in the lower base half ((iv)) again exhibit similar characteristics to (i) and (iii), with the exception of the peak at $St_W \approx 0.092$ being marginally weaker and less defined through the overall increase in magnitudes (up to 5dB/Hz) for $St_W < 0.1$. This trend reflects the non-uniform flow characteristics along the side trailing edge, previously observed in the time-averaged results with streamwise vortices as well as inboard momentum weakening from the top towards the floor (**Fig. 8.21(b-c)**).

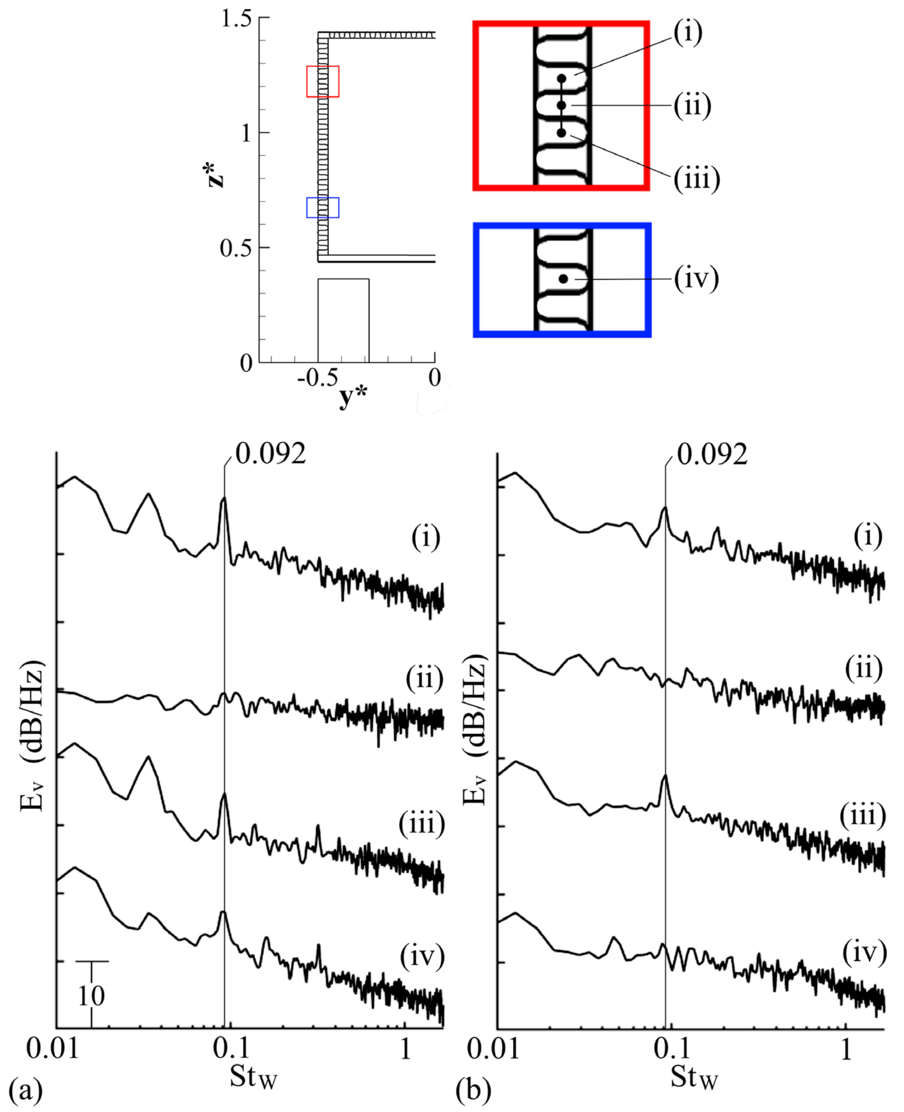

Fig. 8.28 Velocity spectra (E_v) in TS1 along $y^* \approx -0.47$ between $0.67 < z^* < 1.25$ for: (a) LBT p=0.044W-β=15°, (b) LBT p=0.044W-β=20°

Velocity spectra in the same positions are also presented for LBT p=0.044W-β=20° in **Fig. 8.28(b)**. In the upper base half ((i)-(iii)) the trends are generally similar to the corresponding positions in **Fig. 8.28(a)**, with the same peaks at $St_W \approx 0.092$ again captured downstream of the troughs ((i) and (iii)) and no distinct oscillatory characteristics behind the lobe ((ii)). With increasing penetration angle (**Fig. 8.28(b)**) however, the peaks at $St_W \approx 0.092$ appear subtly less defined with an overall increase in lower-frequency magnitudes (≈2dB/Hz; $St_W < 0.1$). This is somewhat consistent with the growing disparity in strength of the adjacent streamwise vortices, as shown in **Fig. 8.25(a)**, generating less coherent crosswise oscillations. In the bottom base half ((iv) – **Fig. 8.28(b)**), the same peak ($St_W \approx 0.092$) is observed almost entirely inhibited, again in agreement with the trends presented in

Fig. 8.25(a). Overall, **Fig. 8.28** shows that with increasing penetration angle the oscillations in the crossflow become less coherent at all locations, with the transition from the upper to lower edge positions remaining largely similar. Considering this in conjunction with **Fig. 8.17**, a correlation between the side edge flow characteristics and vertical wake balance can be inferred, offering further support for the little difference observed between these two configurations.

Figure 8.29 presents E_v at analogous positions for configurations LBT p=0.067W-β=15° and p=0.086W-β=15°. **Figure 8.29(a)** shows the same peaks at $St_W \approx 0.092$ exist for p=0.067W, as in **Fig. 8.28**, downstream of the troughs in the upper base half ((i) and (iii)), indicating the frequency of vortex-induced crosswise oscillations is insensitive to lobe pitch. Considered holistically, this is in general agreement with Mao et al. **(2009)**, who show vortex shedding frequency to vary with the flow Reynolds number; here constant for all configurations. Position (ii) (**Fig. 8.29(a)**) again shows no defined oscillatory behaviour with more general increases in magnitudes (up to 10dB/Hz) for $St_W < 0.2$ evident instead, suggesting less coherent characteristics exist locally. Moving towards the floor, position (iv) (**Fig. 8.29(a)**) shows diminishing crosswise oscillations with magnitude reductions of up to 5dB/Hz and a significant suppression of the energy around $St_W \approx 0.092$. Comparisons to LBT p=0.044W-β=15° (**Fig. 8.28(a)**) reveal that with LBT p=0.067W-β=15° the oscillations at the upper edge positions ((i-iii)) are stronger by up to 10dB/Hz, with the signals closer to the floor ((iv)) showing reductions of up to 20dB/Hz. Considering this in conjunction with the time-averaged results suggests the growing non-uniformity in the flow characteristics along the side trailing edge to be related to the degrading vertical wake balance (**Fig. 8.17**).

Further increases in pitch to LBT p=0.086W-β=15° (**Fig. 8.29(b)**) again show similar characteristics in positions (i) – (iii) with the distinct peak at $St_W \approx 0.092$. One exception is position (ii) downstream of the lobe, where the $St_W \approx 0.092$ peak is also captured. Closer to the floor, higher magnitudes for $St_W < 0.1$ can be seen re-established (relative to LBT p=0.067W-β=15°), with a defined peak at $St_W \approx 0.092$. Overall, the trends in **Fig. 8.29(b)** show similar characteristics and transition from the upper to lower edge portions to those found for LBT p=0.044W-β=15° (**Fig. 8.28(a)**), further supporting the similarities in vertical wake balance between the two configurations (**Fig. 8.17**).

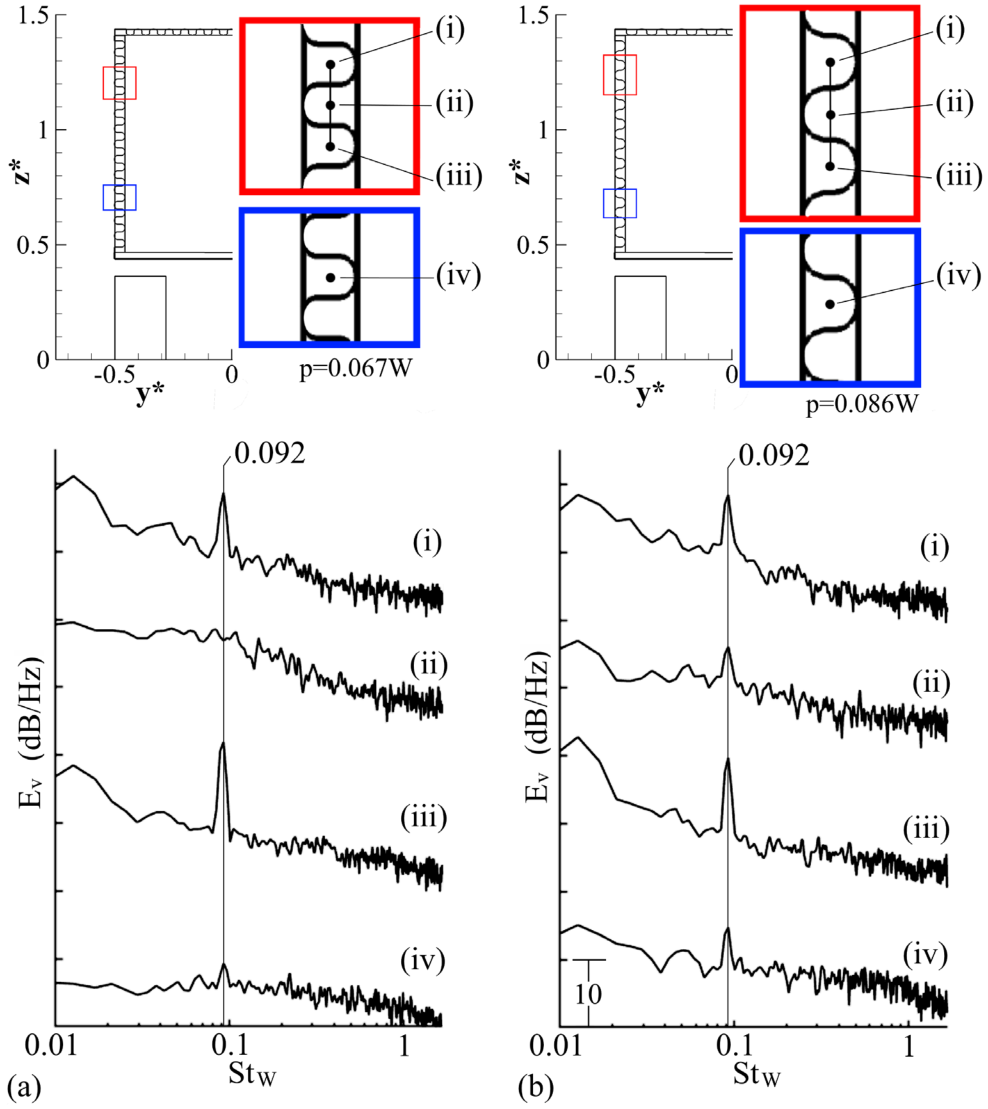

Fig. 8.29 Velocity spectra (E_v) in TS1 along y*≈-0.47 for: (a) LBT p=0.067W-β=15° between 0.70<z*<1.25, (b) LBT p=0.086W-β=15° between 0.68<z*<1.19

Velocity spectra (E_v) further downstream (TS2) are also presented in **Fig. 8.30**. No defined oscillatory behaviour is found at any of the positions (i) – (iv) from the top towards the bottom of the base, with all four LBT configurations exhibiting similar characteristics and the peak at $St_W \approx 0.092$ no longer observable. These results are consistent with the significant vortex breakdown occurring within short distances from the trailing edges, as indicated in **Fig. 8.24**. Towards the bottom of the base, at position (iv), all configurations show increases in higher-frequency activity ($St_W > 0.2$), likely reflective of the proximity to the moving ground and rotating wheel. Overall, these results suggest the strongest impact of the lobed mixers on the inboard flow at the model base to be limited to within x*<0.1.

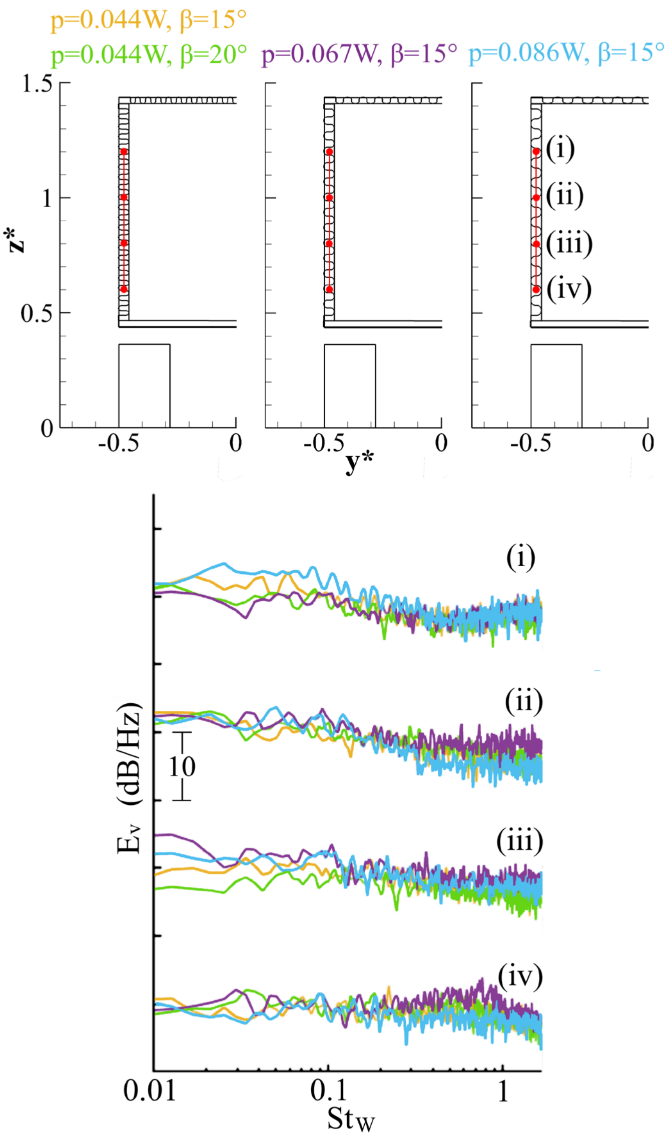

Fig. 8.30 Velocity spectra (E_v) in TS2 along y*≈-0.47 between 0.60<z*<1.20 for LBT p=0.044W-β=15°, p=0.044W-β=20°, p=0.067W-β=15°, and p=0.086W-β=15°

8.5 Summary

Within this chapter, the effects of trailing edge integrated lobed mixers were discussed and compared to the optimised baseline model as well as rear tapers. For the latter, the measured drag reduction trends were found to be in good agreement with the literature, showing the highest benefits with the side and top edges tapered, with the optimum taper angle of α=15° reducing drag by up to 10.8%. Beyond this angle, the performance was observed to degrade rapidly with a drag reduction of approximately 4.0% at α=20° and no further benefit thereafter. With the use of lobed mixing geometries, drag was also observed to reduce, with the smallest pitches producing the best trends resulting in drag reductions of up to 7.4% for p=0.027W and 7.6% for p=0.044W. Importantly, for the lobed mixer configurations, significant drag reductions were found to persist with increasing penetration angle up to β=30°. A particularly good trend was found for the configuration of p=0.044W, with drag reductions of up to 7.0% at β=20°, 5.5% at β=25°, and 2.8% at β=30°. Therefore, the lobed mixing configurations were shown to be effective for vehicle drag reduction at higher aspect ratios and therefore lower costs in internal space. Additionally, drag reductions of up to 5% were also measured for configurations including only the top trailing edge modifications with p=0.044W and symmetrically variable penetration angle.

The time-averaged results revealed the drag reduction obtained with the optimum tapering was a result of reductions in the wake size through enhanced inboard momentum and a shift in the vertical wake balance; the latter reflected in the symmetry of the longitudinal vorticity and a balance in the generated upwash and downwash. Increasing the taper angle was observed to produce less significant wake size reductions and degrade the vertical wake balance. Additionally, tapering of the side trailing edges was found instrumental to the production of vertical wake balance, with the top taper alone found to result in characteristics largely similar to those of the baseline model.

The results for the lobed mixer configurations showed the mechanisms responsible for the drag reduction to be analogous to those observed for tapering, i.e., reductions in wake size and shift in vertical wake balance. For these configurations, however, the effects on the base wake were found retained at higher penetration angles, with the changes observed to be more subtle compared with tapering. The lobes were shown to produce pairs of counter-rotating streamwise vortices, which produced enhanced inboard crossflow responsible for the reductions in base wake size. The streamwise vortices were found to break down with downstream evolution, weakening and coalescing with neighbouring structures of the same sign. At a distance equivalent to half-model-width downstream of the base, the individual structures were found no longer discernible, with the formation of larger and weaker counter-rotating structures centred around the middle of the base evident instead. The results showed the balance between these structures to be associated with the retention of the overall vertical wake balance and consequently higher drag reductions. Increasing the penetration angle was observed to degrade the magnitude symmetry within the counter-rotating vortex pairs shed from the lobes, with increases in pitch resulting in overall reductions in vorticity magnitudes locally. Additionally, for the former, the initial rate of vorticity decay was found to be higher, with the opposite observed for increasing pitch.

Evaluation of the time-dependent results showed the low-drag configurations to suppress the bubble pumping mode. In contrast, the lateral shedding mode was found to be stronger and more coherent, with the characteristic frequency insensitive to varying configurations. Vertical shedding frequency, however, was found to increase with both the optimum tapering and lobed mixer configurations relative to the baseline case. Increasing both pitch and penetration angle was also observed to marginally reduce the heightwise shedding frequency. Additionally, the inclusion of lobed mixers was shown to produce more coherent heightwise oscillations compared with both the baseline and tapering. Overall, the configurations associated with highest drag reductions were found to have a marked impact on the wake dynamics, with lateral shedding found to be the dominant one among the two asymmetric shedding modes.

A detailed interrogation of the velocity spectra closer to the lobed trailing edges showed the streamwise vortices to induce a coherent crosswise oscillation at $St_W \approx 0.092$ within short downstream distances from the base, with the corresponding energy reducing from the top towards the floor along the side trailing edge. No clearly defined oscillatory behaviour was found at further downstream positions, reflective of rapid vortex breakdown and indicating the impact of these configurations on the inboard flow at the model base to be limited to within $x^*<0.1$.

Chapter 9

Conclusion

The work presented in this thesis investigated the application of lobed-mixing geometries for base drag reduction of ground vehicles using a novel wind tunnel upstream model-mounting method. First, the effects of moving ground on the unsteady base wake were evaluated to determine the optimal experimental environment for similar models, with the proposed front mounting technique evaluated thereafter. The effects of lobed mixers were preliminarily investigated on a boat-tailed model to validate the hypothesis of drag reduction capabilities. The following detailed interrogation included a more realisable adaptation of lobed mixers, integrated directly into the vehicle's trailing edges. Multiple model configurations were tested and compared using load and base surface pressure measurements, with hot-wire anemometry employed for the flow-field interrogation. The key findings from each experimental phase are summarised in this chapter.

The experiments with stationary ground use revealed a large region of flow separation at the base of the model close to the ground, identified previously in literature for passenger cars. This area was found to strengthen the upwash in the lower wake portions, with subsequent crosswise flow enhancement within the trailer-wheel junction, resulting in localised wake width contractions and disruptions to the wheel wake formation. With the use of moving ground, these effects were alleviated through the inhibition of the ground separation region, enabling undisturbed development of the trailer base and wheel wakes. The mean wake length and characteristic bubble pumping frequency were found to increase under these conditions. Additionally, with ground simulation, the frequencies of the lateral and vertical asymmetric shedding processes were shown to reduce, with the spectral characteristics also found generally more defined. For higher ride-height vehicles, such as HGVs, the ground simulation is typically omitted based on the belief that the larger distance to the floor minimises any serious impact on the body aerodynamics. This work showed that while the differences between ground conditions may be perceived as subtle from the time-averaged perspective, wake dynamics are markedly affected, making moving ground use increasingly important for correct representation.

Subsequently, the effects of the proposed upstream fixture method were evaluated and compared to mounting from the top and sides using moving ground. The inclusion of the front sting was found to have little influence on the mean drag production. Regions of significant velocity deficit and turbulence increase were found downstream of the top and side supports, characterising the local wakes generated by the struts. The side mounting was shown to alter the vorticity production around the rear wheel, with the local wake propagating downstream and upward, resulting in additional flow blockage close to the floor. The top strut was also found to increase turbulence within the flow above the trailer, with the central regions near the roof boundary layer exhibiting suppressed fluctuations. This influence, however, was shown to be relatively less significant in comparison with the side mounting, with the effect weakening more rapidly with downstream evolution. Correspondingly, with the upstream sting, no significant interference was identified within the flow-field at the model base. Additionally, little impact on the general wake dynamics was identified, with the bubble pumping and asymmetric shedding characteristic frequencies largely insensitive to mounting method. The only exception was found for the side configuration, showing significant reductions in the energy of wake pumping and more incoherent lateral shedding characteristics. This study showed the local characteristics of the upstream mounting technique to combine the benefits and minimise shortcomings of the top and side methods, proving to be a good alternative for similar studies concentrating on the base flow.

The upstream model mounting methodology was used in the experiments conducted on lobe mixers. The preliminary investigation showed the lobed-mixing geometries to reduce model drag relative to both the baseline and the high-angle boat-tail used. The lobes were found to produce additional streamwise vorticity at the trailing edges, which enhanced the crosswise flow entrainment and uplifted the wake. This action was identified as the principal mechanism responsible for enhanced drag reduction, producing a more vertically balanced wake relative to that of the boat-tail which was dominated by a strong downwash.

Following this initial assessment, the lobe geometries were adapted and integrated directly into the model’s trailing edges, providing a more realisable configuration, without modifications to the model’s overall width and length. Multiple lobe pitches and penetration angles were evaluated and compared to high-aspect-ratio rear tapers. The lobe configurations characterised by smaller pitch were found to produce substantial drag reductions at higher angles (20°-30°), improving the performance compared with the tapering of corresponding aspect ratios. The mechanisms responsible for drag reduction were identified to be a reduction in wake size and shift in the vertical wake balance. The former was shown to be a result of the enhancement in inboard momentum close to the trailing edges through the generation of pairs of counter-rotating streamwise vortices, with the latter attributed to the downstream evolution of the vortices. The principal processes associated with the edge-integrated lobed mixers were found to be similar to the lobed boat-tails. Increasing the penetration angle degraded the magnitude symmetry within the counter-rotating vortex pairs near the lobes, with increases in pitch reducing the overall vorticity magnitudes locally. The initial rate of vorticity decay was also higher for the former, with the latter found to exhibit the opposite. The evaluation of the time-dependent aspects also revealed a marked impact on the wake dynamics. The configurations associated with highest drag reductions were found to suppress the wake pumping mode and enhance the asymmetric shedding modes, with lateral shedding also found to be dominant. Overall, the results presented in this work showed the trailing edge-integrated lobe mixers to be effective for road vehicle drag reduction. Furthermore, with significant benefits obtained at higher aspect ratios, where regular tapering’s performance is found substantially degraded, these qualities highlight the possibility that such geometries may be suitable for improving fuel consumption while minimising the losses in internal space.

9.1 Future work

This section recommends the areas which the future research within the scope of this thesis should aim to address.

9.1.1 Upstream model mounting

In this thesis, the method of upstream model mounting was shown to be an excellent alternative for ground vehicle testing with a potential for widespread use; however, more studies are required to understand the full extent of its effects. This work assessed the influence of such a support on the flow-field around the vehicle base; therefore, future studies should focus on the evaluation of the sting's impact on the upstream portions of the model, as well as the underbody. It would be beneficial to study additional sting shapes as well as the optimal fixture position on the model's front face as other, more suitable, variations of the method may exist.

9.1.2 Lobed-mixing geometries for drag reduction

The use of lobed-mixing geometries has been shown in this thesis to be effective for base drag reduction of ground vehicles. Nevertheless, this topic appears very complex and, therefore, there exists a broad scope for future studies. The experiments presented in this work were conducted at a relatively low Reynolds number and although the drag coefficient was shown to only vary marginally, the evaluation of the effects of these devices at higher Reynolds numbers would be beneficial. Correspondingly, future studies should also focus on the application of similar geometries to larger-scale models, with the present work showing evidence for effectiveness at a 1/24th-scale. Another aspect directly related to this is the matter of appropriate scaling of the devices; for instance, based on the number of lobes, upstream boundary layer thickness, or model dimensions.

All experiments presented in this work were conducted at zero yaw. While this provides a valuable insight into the general effects of the devices and remains a crucial benchmark for any configuration, the introduction of crosswinds would offer a broader perspective. It is, therefore, suggested that future studies consider the application of lobed-mixing geometries in variable yaw. Additionally, based on such results at larger-scales and including crosswinds, other non-linear configurations, not included in this thesis, may be proposed for improved performance.

Finally, it is suspected that the performance of the devices may vary in real conditions due to increases in freestream turbulence **(McAuliffe and D'Auteuil, 2016)**, therefore, it would be beneficial to study these geometries in a controlled wind tunnel environment with elevated turbulence levels.

References

1. Aeroserve Technologies Ltd. (2019) *Airtab*. Available at: http://www.airtab.com/index.htm.

2. Ahmed, S. R., Ramm, G. and Faltin, G. (1984) 'Some Salient Features of the Time-Averaged Ground Vehicle Wake', *SAE Transactions*, 93(2), pp. 473–503.

3. Allan, J. W. (1981) 'Aerodynamic drag and pressure measurements on a simplified tractor-trailer model', *Journal of Wind Engineering and Industrial Aerodynamics*, 9(1–2), pp. 125–136. doi: 10.1016/0167-6105(81)90083-0.

4. Altaf, A., Omar, A. A. and Asrar, W. (2014) 'Passive drag reduction of square back road vehicles', *Journal of Wind Engineering and Industrial Aerodynamics*. Elsevier, 134, pp. 30–43. doi: 10.1016/j.jweia.2014.08.006.

5. Anbarci, K. *et al.* (2013) 'Development of an Aerodynamic Analysis Methodology for Tractor-Trailer Class Heavy Commercial Vehicles', *SAE International Journal of Commercial Vehicles*, 6(2), pp. 441–452. doi: 10.4271/2013-01-2413.

6. Barber, T., Paterson, R. W. and Skebe, S. A. (1988) *Turbofan forced mixer lobe flow modeling. I - Experimental and analytical assessment*.

7. Barlow, J. B., Guterres, R. and Ranzenbach, R. (2001) 'Experimental parametric study of rectangular bodies with radiused edges in ground effect', *Journal of Wind Engineering and Industrial Aerodynamics*, 89(14–15), pp. 1291–1309. doi: 10.1016/S0167-6105(01)00146-5.

8. Bartow, W. B. *et al.* (2014) 'Experimental Investigations of Vehicle Base Drag Reduction Using Passive Jet Boat-Tail Flow Control', *SAE Technical Paper 2014-01-2448*. doi: 10.4271/2014-01-2448.Copyright.

9. Bauer, S. and Wood, R. (2001) 'Base Passive Porosity for Drag Reduction'. USA.

10. Bayraktar, I. *et al.* (2005) 'An assessment of drag reduction devices for heavy trucks using design of experiments and computational fluid dynamics', *SAE Technical Papers*, 114(2005), pp. 134–146. doi: 10.4271/2005-01-3526.

11. Bayraktar, I. and Bayraktar, T. (2006) 'Guidelines for CFD simulations of ground vehicle aerodynamics', *SAE Technical Papers*, (724). doi: 10.4271/2006-01-3544.

12. Bearman, P. W. and Owen, J. C. (1998) 'Reduction of bluff-body drag and suppression of vortex shedding by the introduction of wavy separation lines', *Journal of Fluids and Structures*, 12, pp. 123–130. doi: 10.1006/jfls.1997.0128.

13. Berta, C. and Bonis, B. (1980) *Experimental Shape Research of Ideal Aerodynamic Characteristics for Industrial Vehicles*. Warrendale, Pa.

14. Bolgar, I., Scharnowski, S. and Kähler, C. J. (2016) 'Control of the reattachment length of a transonic 2D backward-facing step flow', in Segalini, A. (ed.) *Proceedings of the 5th International Conference on Jets, Wakes and Separated Flows (ICJWSF2015). Springer Proceedings in Physics*. Springer, Cham, pp. 241–248. doi: 10.1007/978-3-319-30602-5_30.

15. Bolgar, I., Scharnowski, S. and Kähler, C. J. (2019) 'Passive flow control for reduced load dynamics aft of a backward-facing step', *AIAA Journal*, 57(1), pp. 120–131. doi: 10.2514/1.J057274.

16. Browand, F., Radovich, C. and Boivin, M. (2005) 'Fuel savings by means of flaps attached to the base of a trailer: Field test results', *SAE Technical Paper 2005-01-1016*. doi: 10.4271/2005-01-1016.

17. Bruneau, C. H. *et al.* (2012) 'Active and Passive Flow Control around Simplified Ground Vehicles', *Journal of Applied Fluid Mechanics*, 5(1), pp. 89–93.

18. Bruneau, C. H. and Mortazavi, I. (2008) 'Numerical modelling and passive flow control using porous media', *Computers and Fluids*, 37(5), pp. 488–498. doi: 10.1016/j.compfluid.2007.07.001.

19. Bruneau, C. H., Mortazavi, I. and Gilliéron, P. (2008a) 'Flow regularisation and drag reduction around blunt bodies using porous devices', in *European Drag Reduction and Flow Control Meeting*. Ischia, Italy. doi: 10.1007/978-1-4020-6858-4_50.

20. Bruneau, C. H., Mortazavi, I. and Gilliéron, P. (2008b) 'Passive control around the two-dimensional square back Ahmed body using porous devices', *Journal of Fluids Engineering, Transactions of the ASME*, 130(6), pp. 1–12. doi: 10.1115/1.2917423.

21. Buckley, F. T. (1995) 'ABCD - An improved coast down test and analysis method', *SAE Transactions*, 104, pp. 1136–1148. doi: 10.4271/950626.

22. Burgin, K., Adey, P. C. and Beatham, J. P. (1986) 'Wind tunnel tests on road vehicle models using a moving belt simulation of ground effect', *Journal of Wind Engineering and Industrial Aerodynamics*, 22, pp. 227–236.

23. Butcher, L. (2009) 'Lorry sizes and weights', *House of Commons SN/BT/654*.

24. Cai, J. and Chng, T. L. (2009) 'On vortex shedding from bluff bodies with base cavities', *Physics of Fluids*, 21. doi: 10.1063/1.3099334.

25. Cai, J., Chng, T. L. and Tsai, H. M. (2008) 'On vortical flows shedding from a bluff body with a wavy trailing edge', *Physics of Fluids*, 20. doi: 10.1063/1.2931682.

26. Cartieri, A. *et al.* (2010) 'Study of Support Interference Effects at S1MA Wind Tunnel Within the "SAO" Project', in *27TH INTERNATIONAL CONGRESS OF THE AERONAUTICAL SCIENCES*.

27. Castelain, T. *et al.* (2018) 'Identification of flow classes in the wake of a simplified truck model depending on the underbody velocity', *Journal of Wind Engineering and Industrial Aerodynamics*, 175, pp. 352–363. doi: 10.1016/j.jweia.2018.02.004.

28. Castellucci, P. J. and Salari, K. (2005) 'Computational Simulation of Tractor-Trailer Gap Flow with Drag-Reducing Aerodynamic Devices', *Methods*, (724). doi: 10.4271/2005-01-3625.

29. Chandrsuda, C. and Bradshaw, P. (1981) 'Turbulence structure of a reattaching mixing layer', *Journal of Fluid Mechanics*, 110, pp. 171–194. doi: 10.1017/S0022112081000670.

30. Chao, H., Huanli, Y. and Jian, D. (2020) 'Mixing and combustion augmentation of the RBCC with different mixer configurations in ejector mode', *Acta Astronautica*, 174, pp. 281–293. doi: 10.1016/j.actaastro.2020.05.018.

31. Choi, H., Lee, J. and Park, H. (2014) 'Aerodynamics of Heavy Vehicles', *Annual Review of Fluid Mechanics*, 46(1), pp. 441–468. doi: 10.1146/annurev-fluid-011212-140616.

32. Christoffersen, L., Landström, C. and Walker, T. (2010) 'A wind tunnel study correlating the aerodynamic effect of cooling flows for full and reduced scale models of a passenger car', *SAE Technical Papers*. doi: 10.4271/2010-01-0759.

33. CIFOR (2016) 'BREXIT and the Paris Agreement', *Asia-Pacific Rainforest summit*, (June), pp. 1–3.

34. Coon, J. D. and Visser, K. D. (2004) 'Drag Reduction of a Tractor-Trailer Using Planar Boat Tail Plates', pp. 249–265. doi: 10.1007/978-3-540-44419-0_24.

35. Cooper, K. (1998) 'Bluff-body Blockage Corrections in Closed- and Open-Test-Section Wind Tunnels', *Agard Ag-336*, 6.

36. Cooper, K. R. (1985) 'The effect of front-edge rounding and rear-edge shaping on the aerodynamic drag of bluff vehicles in ground proximity', *SAE Transactions*, 94, pp. 727–757. doi: 10.4271/850288.

37. Cooper, K. R. (2004) ‘Commercial Vehicle Aerodynamic Drag Reduction: Historical Perspective as a Guide’, in McCallen, R., Browand, F., and Ross, J. C. (eds) *The Aerodynamics of heavy vehicles: Trucks, Buses, and Trains*. Berlin: Springer, pp. 9–27.

38. Cooper, N. J., Merati, P. and Hu, H. (2005) ‘Numerical simulation of the vortical structures in a lobed jet mixing flow’, *43rd AIAA Aerospace Sciences Meeting and Exhibit - Meeting Papers*, pp. 13455–13467.

39. Crouch, R. W., Coughlin, C. L. and Paynter, G. C. (1977) ‘Nozzle exit flow profile shaping for jet noise reduction’, *Journal of Aircraft*, 14(9), pp. 860–867. doi: 10.2514/3.58866.

40. Cyr, S., Ih, K. D. and Park, S. H. (2011) ‘Accurate reproduction of wind-tunnel results with CFD’, *SAE 2011 World Congress and Exhibition*. doi: 10.4271/2011-01-0158.

41. Dantec Dynamics (2013) *StreamWare Pro Installation and User Guide*. Skovlunde.

42. Dantec Dynamics (2018) *Hot-wire & Hot-film Probe Usage Recommendations*. Skovlunde.

43. Deere, K. A. and Hunter, C. A. (1999) ‘Experimental Investigation of Convoluted Contouring for Aircraft Afterbody Drag Reduction’, in *35th AIAA/ASME/SAE/ASEE Joint Propulsion Conference & Exhibit*. Los Angeles, CA: AIAA.

44. Department for Business Energy & Industrial Strategy (2016) ‘2016 UK Greenhouse Gas Emissions MtCO’, 1990, p. 8090.

45. Department for Transport (2003) *A simplified guide to lorry types and weights*.

46. Department for Transport (2017a) *Road Traffic Estimates: Great Britain 2016*.

47. Department for Transport (2017b) *Table RFS0141: Fuel consumption by type and weight of vehicle: annual 2004 - 2016*.

48. Department for Transport (2018) *Table TSGB0306 (ENV0201): Greenhouse gas emissions by transport mode, United Kingdom: 2003 to 2015*.

49. Depuru Mohan, N. K., Prakash, K. R. and Panchapakesan, N. R. (2015) ‘Mixing Augmentation by Multiple Lobed Jets’, *American Journal of Fluid Dynamics*, 5(2), pp. 55–64. doi: 10.5923/j.ajfd.20150502.03.

50. Devesa, A. and Indinger, T. (2012) ‘Fuel Consumption Reduction by Geometry Variations on a Generic Tractor-Trailer Configuration’, *SAE International Journal of Commercial Vehicles*, 5(1), pp. 18–28. doi: 10.4271/2012-01-0105.

51. Drollinger, R. A. (1987) ‘Heavy duty truck aerodynamics’, *SAE Technical Paper Series*.

52. Duell, E. G. (1994) *Experimental investigation of unsteady near wakes of ground vehicle bodies*. Thesis, Cornell University.

53. Duell, E. G. and George, A. R. (1993) ‘Measurements in the unsteady near wakes of ground vehicle bodies’, *SAE Technical Paper 930298*.

54. Duell, E. G. and George, A. R. (1999) ‘Experimental Study of a Ground Vehicle Body Unsteady Near Wake’, *SAE Technical Paper 1999-01-0812*. doi: 10.4271/1999-01-0812.

55. Duriez, T., Aider, J. L. and Wesfreid, J. E. (2006) *Base flow modification by streamwise vortices: Application to the control of separated flows*, *Proceedings of FEDSM2006-98514*. Miami, FL.

56. Eckerle, W. A., Sheibani, H. and Awad, J. (1990) ‘Experimental measurement of the vortex development downstream of a lobed forced mixer’, in *Proceedings of the ASME 1990 International Gas Turbine and Aeroengine Congress and Exposition. V003T06A005*. Brussels, Belgium. doi: 10.1115/90-GT-027.

57. Ecoscore (2018) *How to calculate the CO2 emission from the fuel consumption?* Available at: http://ecoscore.be/en/info/ecoscore/co2 (Accessed: 4 July 2018).

58. Elofsson, P. and Bannister, M. (2002) 'Drag reduction mechanisms due to moving ground and wheel rotation in passenger cars', *SAE Technical Papers*, (724). doi: 10.4271/2002-01-0531.

59. European Commission (2018a) *EU Climate Action*. Available at: https://ec.europa.eu/clima/citizens/eu_en (Accessed: 4 July 2018).

60. European Commission (2018b) *Paris Agreement*, *Climate Action*. Available at: https://ec.europa.eu/clima/policies/international/negotiations/paris_en#tab-0-0 (Accessed: 4 July 2018).

61. Evrard, A. *et al.* (2017) 'Comparative effects of vortex generators on Ahmed's squareback and minivan car models', *Proceedings of the Institution of Mechanical Engineers, Part D: Journal of Automobile Engineering*, 231(9), pp. 1287–1293. doi: 10.1177/0954407016681696.

62. Fago, B., Lindner, H. and Mahrenholtz, O. (1991) 'The effect of ground simulation on the flow around vehicles in wind tunnel testing', *Journal of Wind Engineering and Industrial Aerodynamics*, 38(1), pp. 47–57. doi: 10.1016/0167-6105(91)90026-S.

63. Falchi, M. *et al.* (2006) 'Experimental and numerical investigation of flow control on bluff bodies by passive ventilation', *Experiments in Fluids*, 41(1), pp. 21–33. doi: 10.1007/s00348-006-0141-x.

64. Fan, Y. *et al.* (2020) 'Experimental and numerical analysis of the bi-stable turbulent wake of a rectangular flat-backed bluff body', *Physics of Fluids*, 32, 105111. doi: 10.1063/5.0019794.

65. Fang, X. X. *et al.* (2020) 'Turbulent structures and mixing enhancement with lobed mixers in a supersonic mixing layer', *Physics of Fluids*, 32, 041701. doi: 10.1063/5.0005156.

66. Feng, J. H. *et al.* (2015) 'Experimental and numerical study of mixing characteristics of a rectangular lobed mixer in supersonic flow', *Aeronautical Journal*, 119(1216), pp. 701–725. doi: 10.1017/S0001924000010782.

67. Feuvrier, A., Mazellier, N. and Kourta, A. (2013) 'Self-adaptive control of a bluff body wake by means of porous flaps', *International Journal of Engineering Systems Modelling and Simulation*, 5(1–3), pp. 57–67. doi: 10.1504/IJESMS.2013.052379.

68. Frank, T. and Turney, J. (2016) 'Aerodynamics of commercial vehicles', in Dillmann, A. and Orellano, A. (eds) *The Aerodynamics of Heavy Vehicles III*. Cham: Springer, pp. 195–210. doi: https://doi.org/10.1007/978-3-319-20122-1_12.

69. Garry, K. P. (1981) 'Development of container-mounted devices for reducing the aerodynamic drag of commercial vehicles', *Journal of Wind Engineering and Industrial Aerodynamics*, 9(1–2), pp. 113–124. doi: 10.1016/0167-6105(81)90082-9.

70. Garry, K. P. *et al.* (1994) 'The effect on aerodynamic drag of the longitudinal position of a road vehicle model in a wind tunnel test section', *SAE Technical Paper Series*.

71. Garry, K. P. and Le Good, G. M. (2005) 'An investigation of the sensitivity of rear wing orientation for saloon race cars', *SAE Technical Papers*, 2005(724). doi: 10.4271/2005-01-1018.

72. Gatto, A. and Babinsky, H. (2018) 'Investigation of Passive Porosity as a Means for Bluff-Body Drag Reduction', *SAE International Journal of Commercial Vehicles*, 11(1). doi: 10.4271/02-11-01-0006.

73. Geropp, D. and Odenthal, H. (2000) 'Drag reduction of motor vehicles by active flow control using the Coanda effect', *Experiments in Fluids*, 28, pp. 74–85.

74. Glauert, H. (1933) *Wind tunnel interference on wings, bodies and airscrews*.

75. Gleason, M. E. *et al.* (2015) 'Comparison of Computational Simulation of Automotive Spinning Wheel Flow

Field with Full Width Moving Belt Wind Tunnel Results', *SAE International Journal of Passenger Cars - Mechanical Systems*, 8(1), pp. 275–293. doi: 10.4271/2015-01-1556.

76. Le Good, G. M. *et al.* (1998) 'A comparison of on-road aerodynamic drag measurements with wind tunnel data from pininfarina and MIRA', *SAE Transactions*, 107, pp. 967–976. doi: 10.4271/980394.

77. Le Good, G. M. and Garry, K. P. (2004) 'On the use of reference models in automotive aerodynamics', *SAE Technical Paper 2004-01-1308*. doi: 10.4271/2004-01-1308.

78. Goodyer, M. J., Henderson, R. I. and Judd, M. (1975) 'The measurement of magnus force and moment using a magnetically suspended wind tunnel model', *IEEE Transactions on Magnetics*. IEEE, 11(5), pp. 1514–1516. doi: 10.1109/TMAG.1975.1058853.

79. Götz, H. and Mayr, G. (1998) 'Commercial Vehicles', in Hucho, W. (ed.) *Aerodynamics of Road Vehicles*. 4th edn. Warrendale, Pa.: Society of Automotive Engineers, pp. 415–488.

80. Grandemange, M. *et al.* (2013) 'Effect on drag of the flow orientation at the base separation of a simplified blunt road vehicle', *Experiments in Fluids*, 54:1529. doi: 10.1007/s00348-013-1529-z.

81. Grandemange, M., Cadot, O. and Gohlke, M. (2012) 'Reflectional symmetry breaking of the separated flow over three-dimensional bluff bodies', *Physical Review E - Statistical, Nonlinear, and Soft Matter Physics*, 86, pp. 1–4. doi: 10.1103/PhysRevE.86.035302.

82. Grandemange, M., Gohlke, M. and Cadot, O. (2013a) 'Bi-stability in the turbulent wake past parallelepiped bodies with various aspect ratios and wall effects', *Physics of Fluids*, 25(9). doi: 10.1063/1.4820372.

83. Grandemange, M., Gohlke, M. and Cadot, O. (2013b) 'Turbulent wake past a three-dimensional blunt body. Part 1. Global modes and bi-stability', *Journal of Fluid Mechanics*, 722, pp. 51–84. doi: 10.1017/jfm.2013.83.

84. Grover, K. and Visser, K. D. (2006) 'Over-the-Road Tests of Sealed Aft Cavities on Tractor Trailers', *SAE Technical Paper 2006-01-3529*. doi: 10.4271/2006-01-3529.

85. Gutierrez, W. T. *et al.* (1996) 'Aerodynamics overview of the Ground Transportation Systems (GTS) project for heavy vehicle drag reduction', *SAE Paper 960906*.

86. Guzman, A. *et al.* (2017) 'Further Analyses on Prediction of Automotive Spinning Wheel Flowfield with Full Width Moving Belt Wind Tunnel Results', *SAE International Journal of Passenger Cars - Mechanical Systems*, 10(2). doi: 10.4271/2017-01-1519.

87. Hackett, J. E. and Cooper, K. R. (2001) 'Extensions to Maskell's Theory for Blockage Effects on Bluff Bodies in a Closed Wind Tunnel', *The Aeronautical Journal*, pp. 409–417.

88. Hackett, J. E., Wilsden, D. J. and Lilley, D. E. (1979) *Estimation of tunnel blockage from wall pressure signatures: A review and data correlation*.

89. Hammache, M. and Browand, F. (2004) 'On the aerodynamics of tractor-trailers', in McCallen, R., Browand, F., and Ross, J. C. (eds) *The Aerodynamics of Heavy Vehicles: Trucks, Buses, and Trains*. Berlin: Springer, pp. 185–205. doi: 10.1007/978-3-540-44419-0_20.

90. Haque, A. U. *et al.* (2017) 'Effect of diamond shaped strut with cylindrical pitch rod in subsonic wind tunnel testing', *Measurement*. Elsevier Ltd, 99, pp. 1–6. doi: 10.1016/j.measurement.2016.12.016.

91. Heisler, H. (2002) *Advanced vehicle technology*. 2nd edn. Elsevier.

92. Hetherington, B. (2006) *Interference of supports used for ground vehicle wind tunnel testing*. Thesis, Durham University.

93. Hetherington, B. and Sims-Williams, D. B. (2004) 'Wind tunnel model support strut interference', *SAE Technical Papers*, 2004(724). doi: 10.4271/2004-01-0806.

94. Hetherington, B. and Sims-Williams, D. B. (2006) ‘Support strut interference effects on passenger and racing car wind tunnel models’, *SAE Technical Papers*, 2006(724). doi: 10.4271/2006-01-0565.

95. Hinterberger, C., Garcia-Villalba, M. and Rodi, W. (2004) ‘Large eddy simulation of flow around the Ahmed body’, in McCallen, R., Browand, F., and Ross, J. (eds) *The Aerodynamics of Heavy Vehicles: Trucks, Buses, and Trains*. Springer-Verlag Berlin Heidelberg, pp. 77–87.

96. Hirst, T. *et al.* (2015) ‘Bluff Body Drag Reduction Using Passive Flow Control of Jet Boat Tail’, *SAE International Journal of Commercial Vehicles*, 8(2), pp. 713–721. doi: 10.4271/2015-01-2891.

97. Hirz, M. and Stadler, S. (2013) ‘A New Approach for the Reduction of Aerodynamic Drag of Long-Distance Transportation Vehicles’, *SAE International Journal of Commercial Vehicles*, 6(2), pp. 453–458. doi: 10.4271/2013-01-2414.

98. Horrigan, K. *et al.* (2007) ‘Aerodynamic simulations of a class 8 heavy truck: Comparison to wind tunnel results and investigation of blockage influences’, *SAE Journal of Commercial Vehicles*, 116(2007), pp. 372–383. doi: 10.4271/2007-01-4295.

99. Howard, F. G. and Goodman, W. L. (1985) ‘Axisymmetric bluff-body drag reduction through geometrical modification’, *Journal of Aircraft*, 22(6), pp. 516–522. doi: 10.2514/3.45158.

100. Howell, J. *et al.* (2002) ‘Aerodynamic drag of a compact SUV as measured on-road and in the wind tunnel’, *SAE Technical Paper 2002-01-0529*. doi: 10.4271/2002-01-0529.

101. Howell, J. *et al.* (2012) ‘Bluff Body Drag Reduction with Ventilated Base Cavities’, *SAE International Journal of Passanger Cars - Mechanical Systems*, pp. 152–160. doi: 10.4271/2012-01-0171.

102. Howell, J., Sheppard, A. and Blakemore, A. (2003) ‘Aerodynamic Drag Reduction for a Simple Bluff Body Using Base Bleed’, *SAE International*, (3), pp. 2003-01–0995. doi: 10.4271/2003-01-0995.

103. Hu, H. *et al.* (2000) ‘Research on the vortical and turbulent structures in the lobed jet flow using laser induced fluorescence and particle image velocimetry techniques’, *Measurement Science and Technology*, 11(6), pp. 698–711. doi: 10.1088/0957-0233/11/6/313.

104. Hu, H. *et al.* (2001) ‘A study on a lobed jet mixing flow by using stereoscopic particle image velocimetry technique’, *Physics of Fluids*, 13(11), pp. 3425–3441. doi: 10.1063/1.1409537.

105. Hu, H. *et al.* (2002) ‘Mixing process in a lobed jet flow’, *AIAA Journal*, 40(7), pp. 1339–1345. doi: 10.2514/3.15201.

106. Hunter, C. A., Delore, P. and Presz, W. M. (1991) *Drag reduction and wake minimization on marine vehicles*. Springfield, Massachussetts.

107. Hwang, B. G. *et al.* (2016) ‘Reduction of drag in heavy vehicles with two different types of advanced side skirts’, *Journal of Wind Engineering and Industrial Aerodynamics*. Elsevier, 155, pp. 36–46. doi: 10.1016/j.jweia.2016.04.009.

108. Irving Brown, Y. A., Windsor, S. and Gaylard, A. P. (2010) ‘The effect of base bleed and rear cavities on the drag of an SUV’, *SAE Technical Paper 2010-01-0512*. doi: 10.4271/2010-01-0512.

109. Jørgensen, F. E. (2002) *How to measure turbulence with hot-wire anemometers - a practical guide*. Skovlunde: Dantec Dynamics.

110. Kawamura, Y. and Mizota, T. (2013) ‘Wind tunnel experiment of bluff body aerodynamic models using a new type of magnetic suspension and balance system’, *Journal of Fluids Engineering*, 135(10), pp. 1–5. doi: 10.1115/1.4024793.

111. Kehs, J. P. *et al.* (2013) ‘A Comparison of Full Scale Aft Cavity Drag Reduction Concepts With Equivalent Wind Tunnel Test Results’, *SAE International Journal of Commercial Vehicles*, 6(2), pp. 486–497. doi:

10.4271/2013-01-2429.

112.Khalighi, B. *et al.* (2001) 'Experimental and Computational Study of Unsteady Wake Flow Behind a Bluff Body with a Drag Reduction Device', *SAE Technical Paper 2001-01-1042*. doi: 10.4271/2001-01-1042.

113.Knowles, R. D., Saddington, A. J. and Knowles, K. (2013) 'On the near wake of a Formula One front wheel', *Proceedings of the Institution of Mechanical Engineers, Part D: Journal of Automobile Engineering*, 227(11), pp. 1491–1502. doi: 10.1177/0954407013491903.

114.Knowles, R., Saddington, A. and Knowles, K. (2002) 'On the near wake of rotating, 40%-scale champ car wheels', *SAE Transactions*, 111, pp. 2245–2253.

115.Koike, M., Nagayoshi, T. and Hamamoto, N. (2004) 'Research on aerodynamic drag reduction by vortex generators', *Technical Report*, (2), pp. 11–16. doi: 10.1109/ICCET.2010.5485956.

116.Krajnović, S. and Davidson, L. (2004) 'Large-Eddy Simulation of the Flow around Simplified Car Model', *SAE Technical Paper*.

117.Krajnović, S. and Davidson, L. (2005) 'Influence of floor motions in wind tunnels on the aerodynamics of road vehicles', *Journal of Wind Engineering and Industrial Aerodynamics*, 93(9), pp. 677–696. doi: 10.1016/j.jweia.2005.05.002.

118.Lajos, T., Preszler, L. and Finta, L. (1986) 'Effect of moving ground simulation on the flow past bus models', *Journal of Wind Engineering and Industrial Aerodynamics*, 22, pp. 271–277.

119.Lanser, W. R., Ross, J. C. and Kaufman, A. E. (1991) 'Aerodynamic performance of a drag reduction device on a full-scale tractor/trailer', *SAE Technical Paper 912125*. doi: 10.4271/912125.

120.Lav, C. (2013) 'Three Dimensional CFD Analysis on Aerodynamic Drag Reduction of a Bluff Tractor Trailer Body using Vortex Generators', *SAE Technical Paper 2013-01-2458*. doi: 10.4271/2013-01-2458.

121.Leuschen, J. (2013) 'The Effects of Ground Simulation on Tractor-Trailer Combinations', *SAE International Journal of Commercial Vehicles*, 6(2), pp. 510–521. doi: 10.4271/2013-01-2454.

122.Lin, J. C., Howard, F. G. and Selby, G. V. (1990) 'Control of turbulent separated flow over a rearward-facing ramp using longitudinal grooves', *Journal of Aircraft*, 27(3), pp. 283–285. doi: 10.2514/3.45931.

123.Littlewood, R. and Passmore, M. (2010) 'The optimization of roof trailing edge geometry of a simple square-back', *SAE Technical Paper 2010-01-0510*. doi: 10.4271/2010-01-0510.

124.Lo, K. H. and Kontis, K. (2017) 'Flow around an articulated lorry model', *Experimental Thermal and Fluid Science*, 82, pp. 58–74. doi: 10.1016/j.expthermflusci.2016.11.003.

125.Lumley, J. L. (1967) 'The structure of inhomogeneous turbulent flow', in Yaglom, A. M. and Tatarski, V. I. (eds) *Atmospheric turbulence and radio wave propagation*. Moscow: Nauka, pp. 166–178.

126.Mack, S. *et al.* (2012) 'The ground simulation upgrade of the large wind tunnel at the Technische Universität München', *SAE Technical Papers*. doi: 10.4271/2012-01-0299.

127.Mao, R. *et al.* (2009) 'On the vorticity characteristics of lobe-forced mixer at different configurations', *Experiments in Fluids*, 46(6), pp. 1049–1066. doi: 10.1007/s00348-009-0613-x.

128.Mao, R. H., Yu, S. C. M. and Chua, L. P. (2006) 'Kelvin - Helmholtz and Streamwise Vortices in the Near Wake of a Single-Lobe Forced Mixer', *Proceedings of the Institution of Mechanical Engineers, Part G: Journal of Aerospace Engineering*, 220(4), pp. 279–298. doi: 10.1243/09544100G00104.

129.Martín-Alcántara, A. *et al.* (2014) 'Drag reduction induced by the addition of a multi-cavity at the base of a bluff body', *Journal of Fluids and Structures*, 48, pp. 347–361. doi: 10.1016/j.jfluidstructs.2014.03.013.

130. Maskell, E. C. (1965) ‘A Theory of Blockage Effects on Bulff Bodies and Stalled Wings in a Closed Wind Tunnel’, *Her Majesty’s Stationery Office*, pp. 1–27. doi: AD-A955 243.

131. Mason, Jr, W. T. and Beebe, P. S. (1978) ‘The Drag Related Flow Field Characteristics of Trucks and Buses’, in Sovran, G., Morel, T., and Mason, Jr, W. T. (eds) *Aerodynamic Drag Mechanisms of Bluff Bodies and Road Vehicles*. New York-London: Plenum Press, pp. 45–93.

132. McArthur, D. *et al.* (2016) ‘On the near wake of a simplified heavy vehicle’, *Journal of Fluids and Structures*, 66, pp. 293–314. doi: 10.1016/j.jfluidstructs.2016.07.011.

133. McAuliffe, B. R. and D’Auteuil, A. (2016) ‘A System for Simulating Road-Representative Atmospheric Turbulence for Ground Vehicles in a Large Wind Tunnel’, *SAE International Journal of Passenger Cars - Mechanical Systems*, 9(2). doi: 10.4271/2016-01-1624.

134. McCallen, R. *et al.* (1999) ‘Progress in reducing aerodynamic drag for higher efficiency of heavy duty trucks (Class 7-8)’, *SAE Technical Paper 1999-01-2238*. doi: 10.4271/1999-01-2238.

135. McCormick, D. C. and Bennett, J. C. J. (1994) ‘Vortical and turbulent structure of a lobed mixer free shear layer’, *The American Institute of Aeronautics and Astronautics Journal*, 32(9), pp. 1852–1859.

136. Mercker, E. (1986) ‘A blockage correction for automotive testing in a wind tunnel with closed test section’, *Journal of Wind Engineering and Industrial Aerodynamics*, 22(2–3), pp. 149–167. doi: 10.1016/0167-6105(86)90080-2.

137. Mercker, E. and Knape, H. W. (1989) ‘Ground simulation with moving belt and tangential blowing for full-scale automotive testing in a wind tunnel’, *SAE Journal of Passenger Cars*, 98, pp. 401–420. doi: 10.4271/890367.

138. Miao, L., Mack, S. and Indinger, T. (2015) ‘Experimental and numerical investigation of automotive aerodynamics using DrivAer model’, in *Proceedings of the ASME Design Engineering Technical Conference*. Boston, Massachusetts. doi: 10.1115/DETC2015-47805.

139. Mohammadikalakoo, B., Schito, P. and Mani, M. (2020) ‘Passive flow control on Ahmed body by rear linking tunnels’, *Journal of Wind Engineering and Industrial Aerodynamics*. Elsevier Ltd, 205. doi: 10.1016/j.jweia.2020.104330.

140. Muirhead, V. U. (1976) *An Investigation Of Drag Reduction On Box-Shaped Ground Vehicles*. KU-FRI#180. The University of Kansas.

141. Muscroft, R. J. M., Sims-Williams, D. B. and Cardwell, D. A. (2006) ‘The Development of a Passive Magnetic Levitation System for Wind Tunnel Models’, *SAE Technical Paper Series*.

142. NASA (2020) *Global surface temperature*, *Global Climate Change: Vital Signs of the Planet*. Available at: https://climate.nasa.gov/vital-signs/global-temperature/ (Accessed: 14 August 2020).

143. North American Council for Freight Efficiency (2016) *Confidence Report on Trailer Aerodynamic Device Solutions*.

144. O’Sullivan, M. N. *et al.* (1996) ‘Computational study of viscous effects on lobed mixer flow features and performance’, *Journal of Propulsion and Power*, 12(3), pp. 449–456. doi: 10.2514/3.24056.

145. Ocokoljić, G., Rašuo, B. and Kozić, M. (2017) ‘Supporting system interference on aerodynamic characteristics of an aircraft model in a low-speed wind tunnel’, *Aerospace Science and Technology*, 64, pp. 133–146. doi: 10.1016/j.ast.2017.01.021.

146. Ortega, J. M. *et al.* (2004) ‘Computational Simulation of a Heavy Vehicle Trailer Wake’, pp. 219–233. doi: 10.1007/978-3-540-44419-0_22.

147. Page, M. *et al.* (2002) ‘Recent upgrades to the Swift 8ft × 9ft rolling-road wind tunnel’, *SAE Technical Paper*

2002-01-3341. doi: 10.4271/2002-01-3341.

148. Pankajakshan, R., Hilbert, C. and Whitfield, D. (2010) 'Passive Devices for Reducing Base Pressure Drag in Class 8 Trucks', in Dillmann, A. and Orellano, A. (eds) *The Aerodynamics of Heavy Vehicles III*. Springer, Cham, pp. 227–235.

149. Park, H. *et al.* (2006) 'Drag reduction in flow over a two-dimensional bluff body with a blunt trailing edge using a new passive device', *Journal of Fluid Mechanics*, 563, pp. 389–414. doi: 10.1017/S0022112006001364.

150. Paterson, R. W., Werle, M. J. and Presz, W. M. (1989) 'Projectile with Reduced Base Drag (US4813635)'. United States. doi: 10.1057/9780230607156.

151. Pavia, G. and Passmore, M. (2018) 'Characterisation of Wake Bi-stability for a Square-Back Geometry with Rotating Wheels', *Progress in Vehicle Aerodynamics and Thermal Management*, pp. 93–109. doi: 10.1007/978-3-319-67822-1_6.

152. Pavia, G., Passmore, M. and Gaylard, A. (2016) 'Influence of Short Rear End Tapers on the Unsteady Base Pressure of a Simplified Ground Vehicle', *SAE Technical Paper 2016-01-1590*. doi: 10.4271/2016-01-1590.

153. Pavia, G., Passmore, M. and Sardu, C. (2018) 'Evolution of the bi-stable wake of a square-back automotive shape', *Experiments in Fluids*, 59(1), pp. 1–20. doi: 10.1007/s00348-017-2473-0.

154. Perry, A. K. (2016) *An investigation into the base pressure of simplified automotive squareback geometries*. Thesis, Loughborough University.

155. Perry, A. K., Passmore, M. and Finney, A. (2015) 'Influence of Short Rear End tapers on the Base Pressure of a Simplified Vehicle', *SAE International Journal of Passenger Cars - Mechanical Systems*, 8(1), pp. 317–327. doi: 10.4271/2015-01-1560.

156. Perry, A. K., Pavia, G. and Passmore, M. (2016) 'Influence of short rear end tapers on the wake of a simplified square-back vehicle: wake topology and rear drag', *Experiments in Fluids*, 57(11), pp. 1–17. doi: 10.1007/s00348-016-2260-3.

157. Peterson, R. (1981) *Drag Reduction Obtained by the Addition of a Boattail to a Box Shaped Vehicle*.

158. Pujals, G., Depardon, S. and Cossu, C. (2010) 'Drag reduction of a 3D bluff body using coherent streamwise streaks', *Experiments in Fluids*, 49(5), pp. 1085–1094. doi: 10.1007/s00348-010-0857-5.

159. Qiu, Y. J. (1992) *A Study of Streamwise Vortex Enhanced Mixing in Lobed Mixer Devices*. Thesis, Massachusetts Institute of Technology.

160. Van Raemdonck, G. M. R. and Van Tooren, M. J. L. (2008a) 'Design of an Aerodynamic Aid for the Underbody of a Trailer within a Tractor-Trailer Combination', in *Bluff Body Aerodynamics and Application VI Conference*. Milan, Italy, pp. 20–24.

161. Van Raemdonck, G. M. R. and Van Tooren, M. J. L. (2008b) 'Time-averaged phenomenological investigation of a wake behind a bluff body', in *Bluff Body Aerodynamics and Application VI Conference*. Milan, Italy. doi: 10.1.1.667.9620.

162. Van Raemdonck, G. M. R. and Van Tooren, M. J. L. (2010) 'Numerical and Wind Tunnel Analysis Together with Road Test of Aerodynamic Add-Ons for Trailers', in Dillmann, A. and Orellano, A. (eds) *The Aerodynamics of Heavy Vehicles III*. Springer, Cham, pp. 237–252.

163. Rejniak, A. A. and Gatto, A. (2019) 'Application of Lobed Mixers to Reduce Drag of Boat-Tailed Ground Vehicles', *Journal of Applied Fluid Mechanics*, 12(6), pp. 1729–1744. doi: 10.29252/jafm.12.06.29742.

164. Rejniak, A. A. and Gatto, A. (2020a) 'Influence of Rotating Wheels and Moving Ground Use on the Unsteady Wake of a Small - Scale Road Vehicle', *Flow, Turbulence and Combustion*. Springer Netherlands, 106(1), pp.

109–137. doi: 10.1007/s10494-020-00180-8.

165. Rejniak, A. A. and Gatto, A. (2020b) 'Upstream wind tunnel model mounting: The forgotten method for road vehicle aerodynamics', *Proceedings of the Institution of Mechanical Engineers, Part D: Journal of Automobile Engineering*. doi: 10.1177/0954407020978017.

166. Rodriguez, O. (1991) 'Base drag reduction by control of the three-dimensional unsteady vortical structures', *Experiments in Fluids*, 11(4), pp. 218–226. doi: 10.1007/BF00192747.

167. Rouméas, M., Gilliéron, P. and Kourta, A. (2009) 'Analysis and control of the near-wake flow over a square-back geometry', *Computers and Fluids*, 38(1), pp. 60–70. doi: 10.1016/j.compfluid.2008.01.009.

168. SAE International (2012) *Wind Tunnel Test Procedure for Trucks and Buses (J1252)*. SAE International. doi: 10.4271/J1252_201207.

169. Salati, L., Cheli, F. and Schito, P. (2015) 'Heavy Truck Drag Reduction Obtained from Devices Installed on the Trailer', *SAE International Journal of Commercial Vehicles*, 8(2), pp. 747–760. doi: 10.4271/2015-01-2898.

170. Saltzman, E. and Meyer, Jr., R. (1999) *A Reassessment of Heavy-Duty Truck Aerodynamic Design Features and Priorities*. California: NASA National Technical Information Service.

171. Sardou, M. (1986) '"Reynolds Effect" and "Moving Ground Effect" tested in a quarter scale wind tunnel over a high speed moving belt', *Journal of Wind Engineering and Industrial Aerodynamics*, 22, pp. 245–270.

172. Schaut, N. and Sengupta, R. (2015) 'Aerodynamic Optimization of Trailer Add-On Devices Fully- and Partially-Skirted Trailer Configurations', *SAE International Journal of Commercial Vehicles*, 8(2), pp. 695–704. doi: 10.4271/2015-01-2885.

173. Schneider, W. C. (1955) 'Development of a new flutter testing technique using a towed dynamic airplane model equipped with an automatic stabilizing system', *NACA Research Memorandum*.

174. Schreyer, A.-M. and Taskin, G. (2018) 'Separation Control with Lobe Mixers in the Wake of an Axisymmetric Space-Launcher Model', in *New Results in Numerical and Experimental Fluid Mechanics XI*, pp. 315–325.

175. Simpson, R. L. (2001) 'Junction flows', *Annual Review of Fluid Mechanics*, 33, pp. 415–433. doi: https://doi.org/10.1146/annurev.fluid.33.1.415.

176. Sims-Williams, D. B. and Dominy, R. G. (1998) 'Experimental investigation into unsteadiness and instability in passenger car aerodynamics', *SAE Technical Papers*. doi: 10.4271/980391.

177. Sirenko, V., Pavlovs'ky, R. and Rohatgi, U. S. (2012) 'Methods of reducing vehicle aerodynamic drag', in *ASME 2012 Summer Heat Transfer Conference*. Puerto Rico, USA. doi: 10.1115/FEDSM2012-72491.

178. Skebe, S., Paterson, R. and Barber, T. (1988) 'Experimental investigation of three-dimensional forced mixer lobe flow fields', in *1st National Fluid Dynamics Conference*. Cincinnati, OH: AIAA. doi: 10.2514/6.1988-3785.

179. Smith, L. L. *et al.* (1997) 'Mixing enhancement in a lobed injector', *Physics of Fluids*, 9(3), pp. 667–678. doi: 10.1063/1.869224.

180. Söderblom, D. *et al.* (2009) 'An investigation of the aerodynamic drag mechanisms due to ground simulation in yawed flow conditions for heavy trucks', in *ASME 2009 Fluids Engineering Division Summer Meeting*, pp. 1–7.

181. Söderblom, D. *et al.* (2012) 'Experimental and Numerical Investigation of Wheel Housing Aerodynamics on Heavy Trucks', *SAE International Journal of Commercial Vehicles*, 5(1), pp. 2012-01–0106. doi: 10.4271/2012-01-0106.

182. Söderblom, D., Elofsson, P. and Hyvärinen, A. (2016) 'Numerical Investigation of Blockage Effects on Heavy Trucks in Full Scale Test Conditions', *SAE Technical Paper 2016-01-1607*. doi: 10.4271/2016-01-1607.

183. Stephens, R. G. and Babinsky, H. (2016) 'An Experimental Study on Truck Side-Skirt Flow', *SAE International Journal of Passenger Cars - Mechanical Systems*, 9(2). doi: 10.4271/2016-01-1593.

184. Storms, B. L. *et al.* (2001) *An experimental study of the ground transportation system (GTS) model in the NASA Ames 7-by 10-ft wind tunnel*. Ames Research Centre, Moffett Field, California.

185. Storms, B. L. *et al.* (2005) 'Detailed experimental results of drag-reduction concepts on a generic tractor-trailer', *SAE Technical Paper 2005-01-3525*. doi: 10.4271/2005-01-3525.

186. Storms, B. L. and Ross, J. C. (2006) 'Aerodynamic drag reduction of the underbody of a class-8 tractor-trailer', *SAE Technical Papers*, 115(2006), pp. 181–194. doi: 10.4271/2006-01-3532.

187. Strachan, R. *et al.* (2012) 'Force and moment measurements for a generic car model in proximity to a side wall', *Proceedings of the Institution of Mechanical Engineers, Part D: Journal of Automobile Engineering*, 226(10), pp. 1352–1364. doi: 10.1177/0954407012443643.

188. Strachan, R. K., Knowles, K. and Lawson, N. J. (2004) 'A CFD and experimental study of an Ahmed reference model', *SAE Technical Paper 2004-01-0442*. doi: 10.4271/2004-01-0442.

189. Strachan, R. K., Knowles, K. and Lawson, N. J. (2007) 'The vortex structure behind an Ahmed reference model in the presence of a moving ground plane', *Experiments in Fluids*, 42(5), pp. 659–669. doi: 10.1007/s00348-007-0270-x.

190. Surcel, M. D., Michaelsen, J. and Provencher, Y. (2008) 'Track-test evaluation of aerodynamic drag reducing measures for class 8 tractor-trailers', *SAE Technical Paper 2008-01-2600*. doi: 10.4271/2008-01-2600.

191. Suryanarayana, G. K., Pauer, H. and Meier, G. E. A. (1993) 'Bluff-body drag reduction by passive ventilation', *Experiments in Fluids*, 16(2), pp. 73–81. doi: 10.1007/BF00944909.

192. Tecplot Inc. (2013) *Tecplot 360 User's Manual*. Bellevue, WA.

193. The Council of The European Union (1996) *Council Directive 96/53/EC*.

194. Titchener, N., Colliss, S. and Babinsky, H. (2015) 'On the calculation of boundary-layer parameters from discrete data', *Experiments in Fluids*. Springer Berlin Heidelberg, 56(159). doi: 10.1007/s00348-015-2024-5.

195. Tombazis, N. and Bearman, P. W. (1997) 'A study of three-dimensional aspects of vortex shedding from a bluff body with a mild geometric disturbance', *Journal of Fluid Mechanics*. Brunel University London, 330, pp. 85–112. doi: 10.1017/S0022112096003631.

196. Tortosa, N. *et al.* (2017) 'General Motors' New Reduced Scale Wind Tunnel Center', *SAE International Journal of Passenger Cars - Mechanical Systems*, 10(1). doi: 10.4271/2017-01-1534.

197. Tropea, C., Yarin, A. and Foss, J. (2007) *Springer Handbook of Experimental Fluid Mechanics*. 1st edn. Verlag Berlin Heidenberg: Springer.

198. Tsui, Y. Y. *et al.* (2000) 'Heat transfer enhancement by multilobe vortex generators: Effects of lobe parameters', *Numerical Heat Transfer, Part A: Applications*, 37(6), pp. 653–672. doi: 10.1080/104077800274136.

199. Vallina Garcia, I. and Babinsky, H. (2018) 'An Experimental Study of the Impact of Underbody Roughness on the Instantaneous Wake Flow Topology behind a Truck Geometry', *SAE Technical Paper 2018-01-0714*, pp. 1–32. doi: 10.4271/2018-01-0714.

200. Varshney, H. and Guru, M. (2017) 'Aerodynamic drag reduction of tractor-trailer using wishbone type vortex generators', *International Journal for Research in Applied Science & Engineering Technology*, 5(9), pp. 1833–

1846.

201. Volpe, R., Devinant, P. and Kourta, A. (2015) ‘Experimental characterization of the unsteady natural wake of the full-scale square back Ahmed body: flow bi-stability and spectral analysis’, *Experiments in Fluids*, 56(5), pp. 1–22. doi: 10.1007/s00348-015-1972-0.

202. Waitz, I. A. *et al.* (1997) ‘Enhanced mixing with streamwise vorticity’, *Prog. Aerospace Sci.*, 33, pp. 323–351.

203. Waldmann, A., Lutz, T. and Krämer, E. (2018) ‘Wind tunnel support system influence on NASA common research model at low-speed conditions’, *Journal of Aircraft*, 55(5), pp. 1762–1772. doi: 10.2514/1.C034440.

204. Walter, J. *et al.* (2012) ‘The Windshear Rolling Road Wind Tunnel’, *SAE International Journal of Passenger Cars - Mechanical Systems*, 5(1), pp. 265–288. doi: 10.4271/2012-01-0300.

205. Wang, J. *et al.* (2014) ‘Low Drag Automotive Mirrors Using Passive Jet Flow Control’, *SAE International Journal of Passenger Cars - Mechanical Systems*, 7(2), pp. 538–549. doi: 10.4271/2014-01-0584.

206. Wang, Y. *et al.* (2020) ‘Experimental study of wheel-vehicle aerodynamic interactions’, *Journal of Wind Engineering and Industrial Aerodynamics*, 198(May 2019), pp. 1–15. doi: 10.1016/j.jweia.2019.104062.

207. Wäschle, A. (2007) ‘The influence of rotating wheels on vehicle aerodynamics - Numerical and experimental investigations’, *SAE Technical Papers*, 2007(724), pp. 776–790. doi: 10.4271/2007-01-0107.

208. Wickern, G., Zwicker, K. and Pfadenhauer, M. (1997) ‘Rotating wheels - Their impact on wind tunnel test techniques and on vehicle drag results’, *SAE Technical Papers*, 106(1997), pp. 254–270. doi: 10.4271/970133.

209. Wiedemann, J. and Potthoff, J. (2003) ‘The New 5-Belt Road Simulation System of the IVK Wind Tunnels - Design and First Results’, *SAE International Journal of Passenger Cars - Mechanical Systems*, 112, pp. 356–374. doi: 10.4271/2003-01-0429.

210. Willemsen, E. *et al.* (2011) ‘Automotive Testing in the German-Dutch Wind Tunnels’, *New Trends and Developments in Automotive Industry*. doi: 10.5772/13177.

211. Winant, C. D. and Browand, F. K. (1974) ‘Vortex pairing: The mechanism of turbulent mixing layer growth’, *Journal of Fluid Mechanics*, \bf 63, pp. 237–255. doi: 10.1017/S0022112074001121.

212. Wittmeier, F. *et al.* (2016) ‘The New Interchangeable Three-belt System in the IVK Full-Scale Wind Tunnel of University of Stuttgart: Design and First Results’, *SAE Technical Paper 2016-01-1581*. doi: 10.4271/2016-01-1581.

213. Wood, R. (2015) ‘Reynolds number impact on commercial vehicle aerodynamics and performance’, *SAE International Journal of Commercial Vehicles*, 8(2), pp. 590–667. doi: 10.4271/2015-01-2859.

214. Wood, R. M. (2006) ‘A Discussion of a Heavy Truck Advanced Aerodynamic Trailer System’, in *Int Symp Heavy Veh Weights Dimens*. University Park, PA.

215. Yang, Y. *et al.* (2015) ‘Large Eddy Simulation of Base Drag Reduction with Jet Boat-Tail Passive Flow Control’, in *Procedia Engineering*. Elsevier Ltd, pp. 150–157. doi: 10.1016/j.proeng.2015.11.200.

216. Yang, Y. *et al.* (2020) ‘Large eddy simulation of base drag reduction using jet boat tail passive flow control’, *Computers and Fluids*. Elsevier Ltd, 198. doi: 10.1016/j.compfluid.2019.104398.

217. Yang, Z., Nastov, A. and Schenkel, M. (2013) ‘Further Assessment of Closed-Wall Wind Tunnel Blockage Using CFD Reprinted From : Vehicle Aerodynamics 2005’, 2005(724).

218. Yang, Z. and Schenkel, M. (2010) ‘Assessment of Closed-Wall Wind Tunnel Blockage using CFD’, *Library*, 2004(724). doi: 10.4271/2004-01-0672.

219. Yi, W. (2007) *Drag reduction of a three-dimensional car model using passive control device*. Thesis, Seoul

National University.

220.Yu, S. C. M., Hou, Y. and Chan, W. K. (2000) ‘Scarfing and Scalloping Effects on Lobed Forced Mixer at Low-Speed Conditions’, *Journal of Propulsion and Power*, 16(3), pp. 440–448. doi: 10.2514/2.5608.

221.Yu, S. C. M. and Yip, T. H. (1997) ‘Measurements of velocities in the near field of a lobed forced mixer trailing edge’, *The Aeronautical Journal - Royal Aeronautical Society*, 101(2165), pp. 121–129.

222.Zaman, K. B. M. Q., Bridges, J. E. and Huff, D. L. (2011) ‘Evolution from “Tabs” to “Chevron Technology” - A Review’, *International Journal of Aeroacoustics*, 10(5–6), pp. 685–709. doi: 10.1260/1475-472X.10.5-6.685.

223.Zaman, K. B. M. Q. and Hussain, A. K. M. F. (1980) ‘Vortex pairing in a circular jet under controlled excitation. Part 1. General jet response’, *Journal of Fluid Mechanics*, 101(3), pp. 449–491. doi: 10.1017/S0022112080001760.

224.Zdravkovich, M. M. (1997) *Flow around circular cylinders: Volume I: Fundamentals.* Oxford: Oxford University Press.

225.Zdravkovich, M. M. (2003) *Flow around circular cylinders: Volume II: Applications*. Oxford: Oxford University Press.

226.Zhang, J., Pan, C. and Shan, Y. (2014) ‘Progress in helicopter infrared signature suppression’, *Chinese Journal of Aeronautics*. Chinese Society of Aeronautics and Astronautics, 27(2), pp. 189–199. doi: 10.1016/j.cja.2014.02.007.

227.Zhang, Y.-C. *et al.* (2014) ‘Aerodynamic Characteristics of Sedan with the Rolling Road Ground Effect Simulation System’, *Vehicle Engineering*, 2, pp. 31–35.

228.Zhang, Y. *et al.* (2013) ‘Test process and correction of automotive wind tunnel in Jilin university China’, *SAE Technical Paper 2013-01-1351*. doi: 10.4271/2013-01-1351.

Appendix A

In addition to the standard lobed mixer trailing edge configurations, several “non-linear” modifications are designed and tested. To enable comparison, these modifications are based on selected standard configurations. The first non-linear configuration (LBT-MOD1) is a variation of normal LBT characterised by p=0.086W and β=15° with the two central lobes replaced by a flat taper of α=15°, as presented in **Fig. A1**. As with the standard configurations, for LBT-MOD1, the influence of top and sides is isolated by testing with the top (LBT-MOD1-1) and sides (LBT-MOD1-2) only, as well as all sides and top together (LBT-MOD1-3).

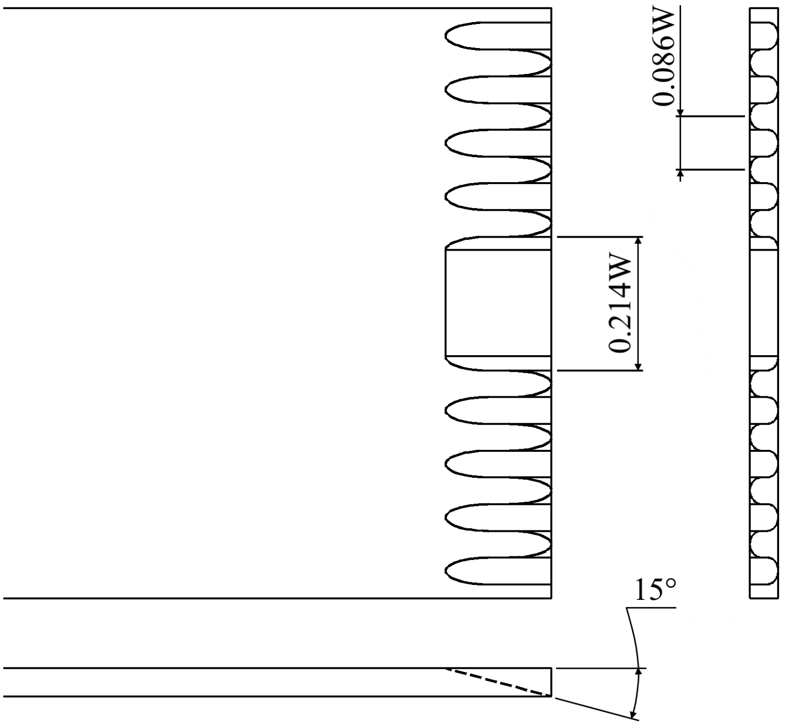

Fig. A1 Schematic of the non-linear configuration LBT-MOD1

The standard LBT configuration corresponding to p=0.044W is used to study the effects of variable penetration angle. **Fig. A2** presents configuration LBT-MOD2, characterised by the penetration angle decreasing from the sides towards the centre in the range of 10°<β<20° (1° increments). The modification is applied to the side and top trailer

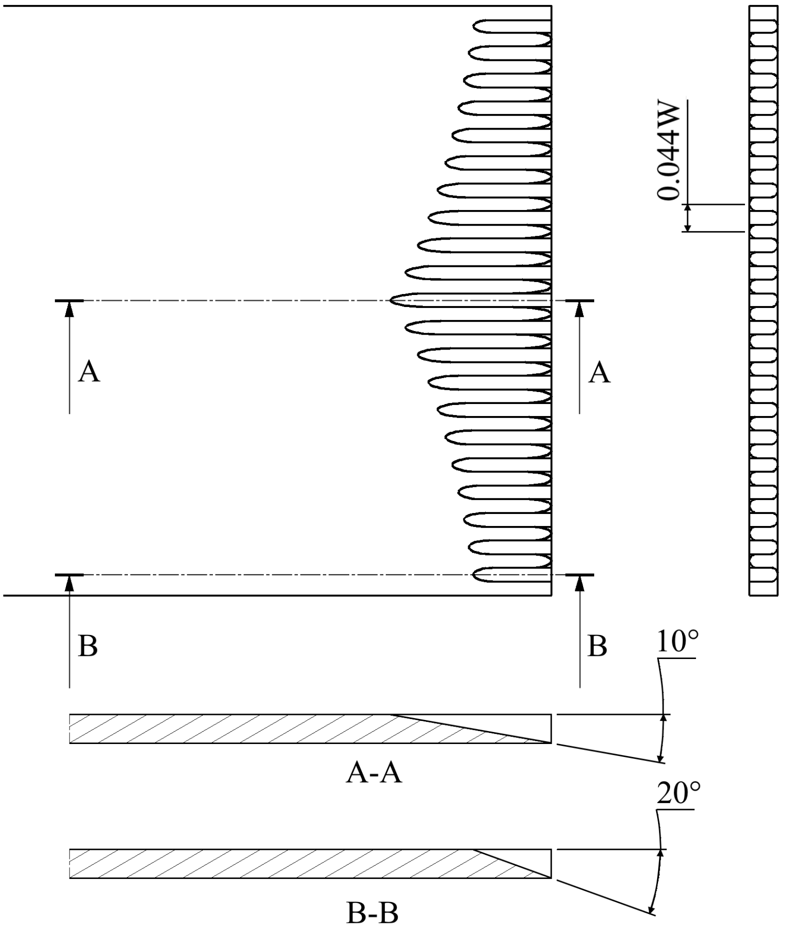

Fig. A2 Schematic of the non-linear configuration LBT-MOD2

surfaces and variations LBT-MOD2-1 (top only), LBT-MOD2-2 (sides only), LBT-MOD2-3 (sides and top) are all studied.

The same penetration angle range (10°<β<20°) is also used with the angle increasing from the sides towards the centre resulting in LBT-MOD3, as presented in **Fig. A3**. The isolated influence of the sides and top is also studied for this configuration, with the three variations denoted as LBT-MOD3-1 (top), LBT-MOD3-2 (sides), and LBT-MOD3-3 (sides and top).

A similar concept (penetration angle increasing towards the centre) is also studied for a larger penetration angle range, within 5°<β<25° (2° increments), denoted as LBT-MOD4 and presented in **Fig. A4**. This configuration is also tested in the three variations LBT-MOD4-1 (top), LBT-MOD4-2 (sides), and LBT-MOD4-3 (sides and top).

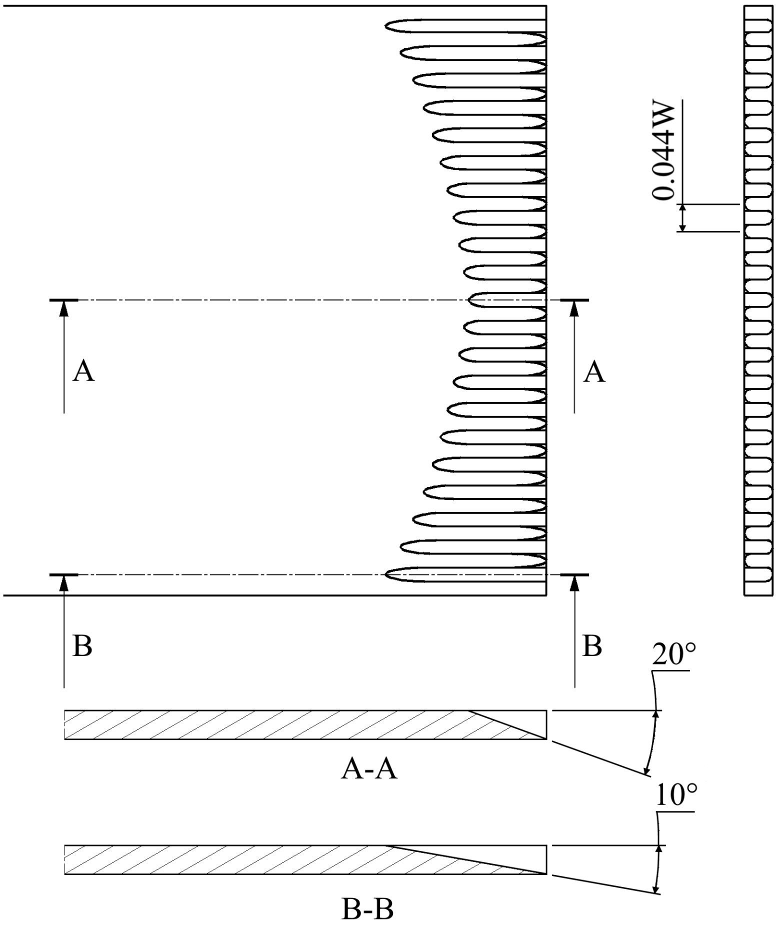

Fig. A3 Schematic of the non-linear configuration LBT-MOD3

Another configuration (LBT-MOD5) consists of a linear change in penetration angle in the range 10°<β<20° (0.5° increments), as presented in **Fig. A5**. This modification is applied exclusively to the side panels of the trailer. The studied variations include the penetration angle increasing towards the ground (LBT-MOD5.1-2), as well as decreasing towards the ground (LBT-MOD5.2-2); both with normal trailer top. Additionally, LBT-MOD5.1 sides are tested with the top panel of LBT-MOD3 for penetration angle decreasing towards the top trailer corners (LBT-MOD5.1-3), as well as top panel of LBT-MOD2 for β increasing towards the top trailer corners (LBT-MOD5.2-3).

A similar linear angle variation (LBT-MOD6) is also tested for a larger range of 5°<β<25° (1° increments), as presented in **Fig. A6**. Correspondingly, this configuration is also studied in the following variations:

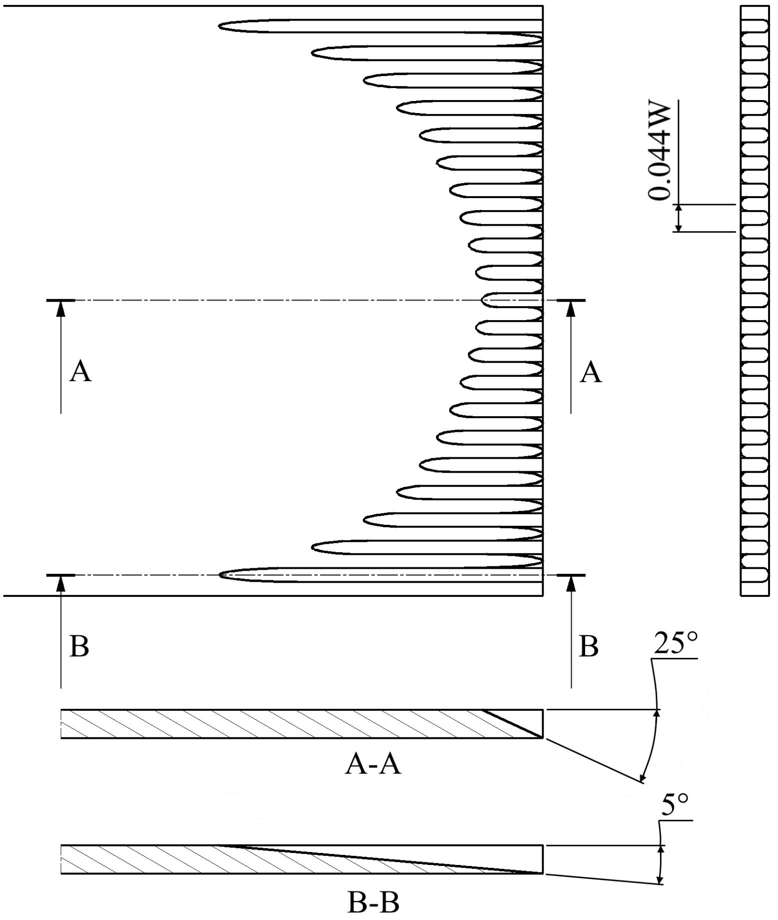

Fig. A4 Schematic of the non-linear configuration LBT-MOD4

- penetration angle increasing towards the ground on the sides with normal trailer top (LBT-MOD6.1-2)
- penetration angle decreasing towards the ground on the sides with normal trailer top (LBT-MOD6.2-2)
- penetration angle increasing toward the ground on the sides with LB-MOD4 trailer top (LBT-MOD6.1-3)
- penetration angle decreasing towards the ground on the sides with LB-MOD2 trailer top (LBT-MOD6.2-3).

In all tested LBT configurations, the lobe axis is always parallel to the streamwise direction. The influence of a variable lobe axis angle is evaluated with configuration LBT-MOD7 consisting of all lobes along the trailer sides skewed by -5° with respect to the streamwise direction (**Fig. A7**). Such side panels are tested alone with the normal flat trailer top (LBT-MOD7-2). Additionally, the LBT-MOD7 sides are tested together with a standard LBT top characterised by p=0.044W and β=20°, denoted by LBT-MOD7-3.

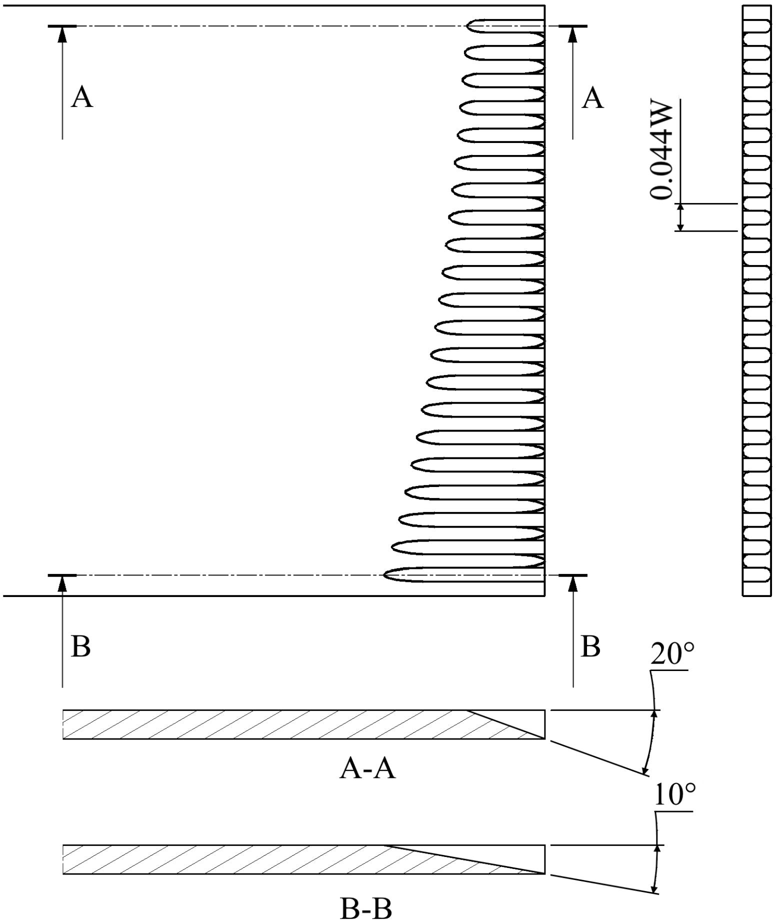

Fig. A5 Schematic of the non-linear configuration LBT-MOD5

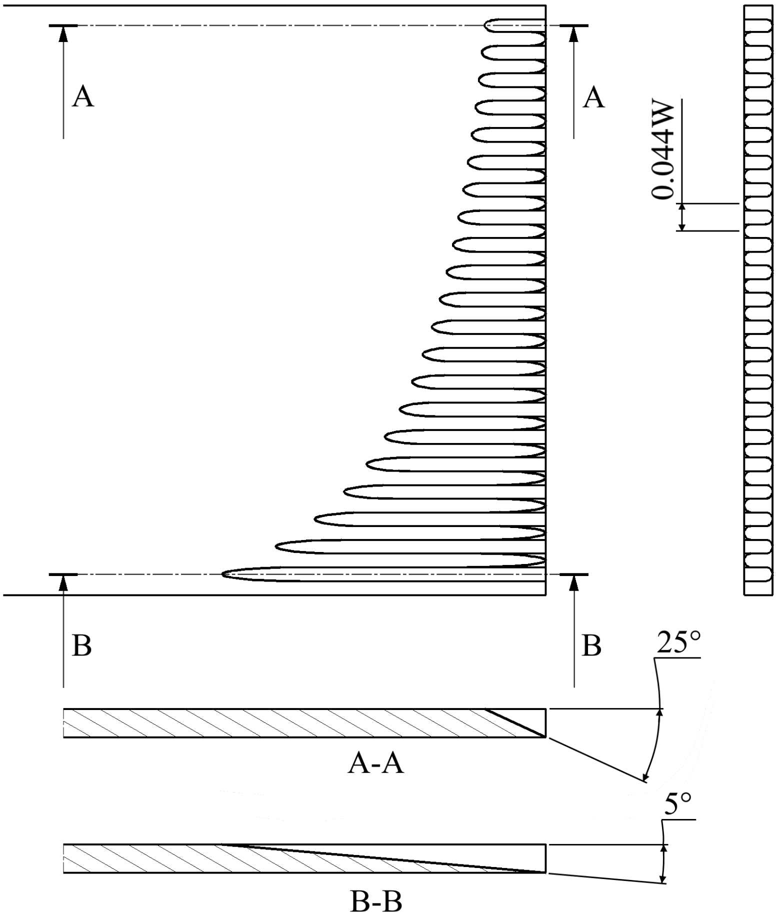

Fig. A6 Schematic of the non-linear configuration LBT-MOD6

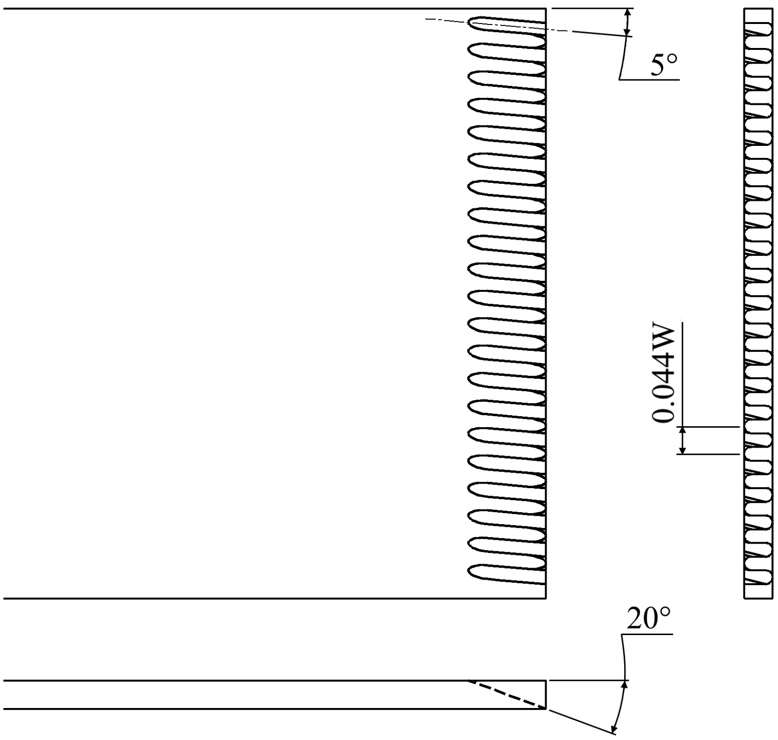

Fig. A7 Schematic of the non-linear configuration LBT-MOD7